NASA Contractor Report 3998

A Constitutive Model for the Inelastic Multiaxial Cyclic Response of a Nickel Base Superalloy René 80

V. G. Ramaswamy

NASA

NASA Contractor Report 3998

A Constitutive Model for the Inelastic Multiaxial Cyclic Response of a Nickel Base Superalloy René 80

V. G. Ramaswamy
University of Cincinnati
Cincinnati, Ohio

NASA

National Aeronautics
and Space Administration

Scientific and Technical
Information Branch

1986

ABSTRACT

The objective of this research was to develop unified constitutive equation which can model a variety of nonlinear material phenomena observed in Rene' 80 between 538 °C and 982 °C.

Five unified constitutive models were reviewed in detail to evaluate their capabilities and limitations. Two models, a generic back stress drag stress model and the Bodner model, were then used to model the behavior of Rene' 80 at 982 °C. Both models were found to have some advantageous features, however, neither proved adequate for Rene' 80.

A new constitutive model was proposed based on back stress and drag stress. The tensorial back stress was used to model directional effects; whereas, the scalar drag stress was used to model isotropic effects and cyclic hardening or softening. A flow equation and evolution equations for the state variables were developed in multiaxial form. Procedures were developed to generate the material parameters. The model predicted very well the monotonic tensile, cyclic, creep and stress relaxation behavior of Rene' 80 at 982 °C.

The model was then extended to 871 °C, 760 °C, and 538 °C. It was shown that strain rate dependent

iii

behavior at high temperatures, and strain rate independent behavior at the lower temperatures could be predicted very well. A large number of monotonic tensile, creep, stress relaxation and cyclic experiments were predicted.

The multiaxial capabilities of the model were verified extensively for combined tension/torsion experiments. The prediction of the model agreed very well for proportional, nonproportional and pure shear cyclic loading conditions at 982°C and 871°C. It was shown that the proposed back stress model predicts a phase angle between the inelastic strain rate and deviatoric stress vectors. Some possible extensions of the model in future research were identified.

ACKNOWLEDGEMENTS

TABLE OF CONTENTS

CHAPTER 1

INTRODUCTION

During the past fifteen years there have been significant advances in improving the fuel efficiency of gas turbine engines. An improvement in performance is usually associated with an increase in the operating temperatures of the engine components and/or a reduction in their weight. Development of high temperature superalloy materials has indeed been a major factor in accomplishing the conflicting goals of higher thrust and lower weight for engines.

One of the major tasks before turbine design engineers is the assurance of the structural durability of the various components designed. This is a challenging problem, especially in the case of components operating in a severe environment and complex loading conditions. For example, critical jet engine components such as turbine disks, blades and vanes are subjected to very high cyclic stresses and temperatures, which vary throughout the flight mission. Structural integrity and durability of these components must, however, be ensured. Analytical methods are extensively used in this process of life analysis of the engine components. Experimental verification using

1

component testing, which is very expensive, is performed for critical locations. To determine the life of a component, three types of analyses must be performed: (1) Structural analysis, (2) Thermal analysis and (3) Damage analysis. While all three are important, the primary focus in this report is on structural analysis methods.

There have been significant advances in the past in the areas of stress and thermal analysis techniques. Modern computers have dramatically improved our ability to perform stress analyses for complicated geometries. The Finite Element Method is the prime example. These methods have a high degree of accuracy if the stresses and temperatures are such that inelastic strains are negligibly small. However, they have not been as successful in analysing high temperature material behavior involving significant inelastic strains. The main reason for this is the deficiency in the mechanical constitutive equations that are used to model the material behavior. At high temperatures materials display a number of response characteristics, some of which are not observed at lower temperatures. Typical examples are strain rate dependence, creep, anelasticity, and cyclic hardening or softening. The classical plasticity and creep models that are

incorporated in most of the finite element codes used today are inadequate to model high temperature response of materials [1,2].

Development of more realistic constitutive models for high temperature superalloys has become necessary. Since the constitutive models are being evaluated for use in the gas turbine industry, several specific properties have been established that are necessary for high temperature superalloys. These models must: (1) have the ability to accurately predict the monotonic and cyclic response including strain and cyclic hardening or softening under multiaxial loading conditions; (2) be applicable over the temperature range occurring in gas turbines; (3) be practical for use in nonlinear finite element computer codes; and (4) be easily relatable to observed material response to determine the required material parameters.

Classical attempts at constitutive modeling are based on separating the strain into separate components to model the creep and plasticity. This approach, although computationally desirable, does not usually include an adequate method to model the coupling between creep and plasticity. More recently, several "unified" constitutive formulations have been proposed based on a single inelastic strain component to model

3

both creep and plasticity [14,17,19,24,25]. The models have shown encouraging results in modeling constitutive behavior at high temperatures. Some areas of difficulty have also become apparent [15,26].

In view of the many advantages, a research program has been carried out to investigate the existing models and develop a new unified constitutive equation. The research was primarily directed toward modeling the response of Rene´ 80 from 500°C to 1100°C. Support for the project was provided by NASA Lewis Research Center, Cleveland, Ohio. It is anticipated that the results will be incorporated into a finite element code, although this is not part of the present study. The work was directed toward three specific goals.

The first was to study the typical response of unified constitutive models. This work included a review of the literature, programming five models and evaluating their response using material data published in the literature. The two models that appeared most promising for high temperature superalloys were selected for further study. The material constants for each model were determined for Rene´ 80 at 982°C and the calculated response was compared to the experimental data. An evaluation of the models followed this exercise.

Secondly, a new unified constitutive model was developed using the above results. The model development was influenced by the observed deformation mechanisms present in Rene´ 80 between 500 °C and 1100 °C. The model is fully three dimensional, but the development was based on uniaxial response. Experimental and calculated results were compared for monotonic, creep and cyclic load histories at 538 °C, 760 °C, 871 °C, and 982 °C.

The third goal was the extension of the model to multiaxial loading histories. Even though the model is three dimensional, the multiaxial hardening aspects had to be considered. The response capabilities for proportional and nonproportional loading paths were compared to observed response.

CHAPTER 2

TYPICAL RESPONSE OF UNIFIED CONSTITUTIVE MODELS

Unified constitutive theories of material behavior have been under development for more than ten years. Although significant progress has been achieved, they have not yet fully developed to the extent that they can be used by design engineers. Several different unified models are available in the literature, and modifications are still in progress. In the mean time, classical theories of plasticity and creep are being widely used in inelastic analyses. In order to understand the special capabilities of the unified constitutive models and their advantages and disadvantages, it is helpful to review briefly the structure of the classical theories of plasticity and creep. The general structure of unified constitutive theories will be discussed next, noting the similarities and differences with the classical approach. This will be followed by a detailed investigation of the capabilities and limitations of a few of the unified constitutive models that have been used for high temperature superalloys.

2.1 Classical Theories of Plasticity and Creep

In the classical approach, the total strain (ϵ_{ij}) is considered to be decomposed into an elastic strain (ϵ_{ij}^e), a plastic strain (ϵ_{ij}^P), a creep strain (ϵ_{ij}^C), and a thermal strain (ϵ_{ij}^T); that is,

$$\epsilon_{ij} = \epsilon_{ij}^e + \epsilon_{ij}^P + \epsilon_{ij}^C + \epsilon_{ij}^T. \qquad (2.1)$$

The elastic strain is reversible upon removal of the applied load. For small strain it is described by Hooke's Law,

$$\epsilon_{ij}^e = (\frac{1+\gamma}{E})\ \sigma_{ij} - \frac{\gamma}{E}\ \sigma_{kk}\delta_{ij}, \qquad (2.2)$$

where E is the elastic modulus and γ is the Poisson ratio. Implied summation of the indices is always used in this report. The thermal strain arises due to thermal expansion of the material, $\epsilon_{ij}^T = \alpha\Delta T\ \delta_{ij}$, where ΔT is the temperature difference from a reference temperature and α is the thermal expansion coefficient. The plastic strain, ϵ_{ij}^P, cannot be recovered upon removal of the load. In the classical theory of plasticity, the plastic strain ϵ_{ij}^P is dependent on the history of loading but is considered time independent. Time dependency is introduced using the creep strain ϵ_{ij}^C, which also accounts for the stress relaxation and strain recovery properties of the material.

7

2.1.1 Mathematical Theories of Classical Plasticity

The classical theory of plasticity is fundamentally based upon the concept of a yield surface in the stress space. It is assumed that a yield function exists which delineates the elastic and plastic regime of material behavior. The yield function depends on the state of stress, temperature and previous stress history. For example, plastic strain is typically defined to occur if

$$f(\sigma_{ij}) \geq g(T,K) \qquad (2.3)$$

where g is a scalar function of temperature and strain hardening, the latter characterized by the parameter K. The yield surface $f(\sigma_{ij})$ is generally written as a function of the second invariant of the deviatoric stress tensor, J_2, since yield and plastic flow are independent of hydrostatic stress [3,4]. Two of the most widely used criteria were proposed by Von Mises, $f(\sigma_{ij}) = J_2$, and Tresca, $f = \sigma_1 - \sigma_3$, where σ_1 and σ_3 are the maximum and minimum principal stresses.

In addition to the yield surface the classical approach also requires the use of a plastic flow law. Some of the early work in plasticity theory was for the ideally plastic materials and for elastic perfectly plastic materials. However, most metals show consider-

able amount of work hardening. The concept of work hardening can be mathematically stated using the following inequalities proposed by Drucker, [5,6,7]:

(a) $d\sigma_{ij} \, d\epsilon_{ij} > 0$ upon loading (2.4)

(b) $d\sigma_{ij} \, d\epsilon_{ij}^P \geq 0$ for a cycle of loading (2.5)
     and unloading.

The first inequality requires the total work to be positive during the application of a stress increment, and the second states that the net plastic work performed over a stress application and removal cycle is positive or zero.

Two important results arise from these inequalities. First, Drucker showed that the initial yield surface and all subsequent yield surfaces must be convex. The second is that for a smooth yield surface the plastic strain increment vector must be normal to the yield surface; i.e.,

$$d\epsilon_{ij}^P = d\lambda \, \frac{\partial f}{\partial \sigma_{ij}} \qquad (2.6)$$

where the scalar function λ may depend on stress, temperature and the loading history.

Equation (2.6) is the Flow Rule, which relates the increment of plastic strain to an increment of stress. If the Von Mises yield function, $f(\sigma_{ij}) = J_2$, is used

in Equation (2.6), the Prandtl Reuss flow law results,

$$d\varepsilon_{ij}{}^P = d\lambda\, S_{ij}. \qquad (2.7)$$

Equation (2.6) enables the calculation of the plastic strain increments at any particular point during the loading history for any yield function $f(\sigma_{ij})$. However, it is still necessary to describe the work hardening.

A major part of the current mathematical theories of plasticity is the development of hardening rules. These rules describe how work hardening during plastic deformation affects subsequent yield surfaces and flow characteristics. The question of what is an appropriate hardening rule for many materials has never been answered completely. However, the isotropic and kinematic hardening rules have evolved as important contributions.

The isotropic hardening rule is based on the assumption that, during plastic deformation, the yield surface maintains its shape but the size increases. Usually the increase in size is controlled by a single scalar parameter that depends on the accumulated plastic strain or accumulated plastic work. Isotropic hardening is not always a good assumption since some materials develop anisotropic and Bauschinger effects that significantly change the size, shape and origin of the yield surface.

10

Kinematic hardening is based on the concept that during plastic deformation the yield surface does not change its size or shape, but translates in the stress space. Various versions of this rule have been proposed to describe how this translation occurs. Prager [8,9] proposed that the translation occurs in the direction of the normal to the yield surface. Ziegler [10] modified this rule for use with a yield surface with corners where the normal is not defined. Mroz [11] bounded the translation, size and shape with a limit surface.

In general, kinematic hardening or a combination of kinematic and isotropic hardening is a better assumption than the isotropic hardening alone in representing material behavior. However, in addition to expansion and translation, in multiaxial loading the yield surface may distort during plastic deformation [12,13]. Additional hardening may be present in the case of nonproportional loading histories. These enormously complicate the yield surface based plasticity theories.

2.1.2 Classical Approach to Creep

The creep strain, ε_{ij}^c, in Equation 2.1 has traditionally been calculated in a manner similar to the

plastic strain [55]. The creep strain at any time t is based on an empirical relation in the form

$$\epsilon_c = f(\sigma_c, t, T). \tag{2.8}$$

The creep test results are usually uniaxial and at constant stress σ_c and temperature T. In variable loading time hardening or strain hardening assumptions are frequently used. Time hardening is based on the assumption that creep rate depends on the time at a stress and temperature and independent of the current stress and thermal rates; i.e.,

$$\dot{\epsilon}_c = \frac{\partial f}{\partial \sigma_c} \dot{\sigma}_c + \frac{\partial f}{\partial T}\dot{T} + \frac{\partial f}{\partial t} \approx \frac{\partial f}{\partial t}. \tag{2.9}$$

The creep rate is defined to depend on strain rather than time in the strain hardening rule. Solving Equation 2.8 for time and combining with Equation 2.9 gives

$$\dot{\epsilon}_c = g(\sigma_c, T, \epsilon). \tag{2.10}$$

The total strain is estimated by integrating Equation 2.9 or 2.10 with stress and temperature as functions of time. This can only be a reasonable approximation for some very limited cases, yet it is used widely. A flow law similar to the Prandtl Reuss equation is assumed for multiaxial loading. The development is based on

purely phenomenological arguments and is similar to plasticity.

2.2 Unified State Variable Constitutive Theories

Recall that classical plasticity theory is rate independent and time dependence is introduced through empirically developed creep models. The two terms, creep and plasticity, are independent and there is no influence of plasticity on creep or creep on plasticity. Yet these effects are present in material response. It is very important that constitutive models have coupling between the creep and plasticity terms. This has proven extremely difficult using separate creep and plastic strain components. Thus, in the unified theories, the classical separation of strain into a time independent plastic strain and a time dependent creep strain is replaced by a total inelastic strain. In many recent theories the inelastic strain is assumed to occur even at stresses below the yield stress, is rate dependent and generally does not employ a yield surface. The total strain is written as the sum of a reversible elastic strain ε_{ij}^e, a nonreversible inelastic strain ε_{ij}^I and a thermal strain ε_{ij}^T; i.e.,

$$\varepsilon_{ij} = \varepsilon_{ij}^e + \varepsilon_{ij}^I + \varepsilon_{ij}^T \qquad (2.11)$$

13

A number of unified state variable constitutive models are available in the literature which have been developed for specific materials or classes of materials [14,15]. None of these models appear to have been fully developed to the extent that they can represent all aspects of material behavior; yet, there appears to be a significant improvement over the classical theory. There are also varying degrees of difficulty involved in the numerical implementation of these models. It appears helpful in the development of a new model to review these models individually and evaluate their capabilities and limitations in terms of accuracy of modeling material behavior, material parameter evaluation and numerical implementation. The specific material behaviors evaluated are strain rate sensitivity, creep, stress relaxation, cyclic hardening or softening and anelasticity. These properties are important in high temperature superalloys.

2.3 Response Characteristics of Some Unified Models

2.3.1 Walker Model

The viscoplasticity effects are modeled using two types of internal variables, an equilibrium stress,

Ω_{ij}, and a drag stress, K [14,16]. The equilibrium stress (back stress) is used to model kinematic hardening and Bauschinger effects in cyclic loading. The drag stress K models isotropic hardening and cyclic hardening or softening effects. The Walker model can be summarized as follows:

$$\dot{\epsilon}_{ij}^I = \left[\frac{X}{K}\right]^n \frac{\left[\frac{3}{2}S_{ij}-\Omega_{ij}\right]}{X} \qquad (2.12)$$

where $X = \sqrt{\frac{2}{3}\left[\frac{3}{2}S_{ij}-\Omega_{ij}\right]\left[\frac{3}{2}S_{ij}-\Omega_{ij}\right]}$

$$\dot{\Omega}_{ij} = (n_1+n_2)\dot{\epsilon}_{ij}^I + \epsilon_{ij}^I \frac{\partial^{n_1}}{\partial T}\dot{T} - (\Omega_{ij}-\Omega_{ij}^o - n_1\epsilon_{ij}^I)(\dot{G}-\frac{1}{n_2}\frac{\partial^{n_2}}{\partial T}\dot{T}) \qquad (2.13)$$

$$K = K_1 - K_2 e^{-n_7 R} \qquad (2.14)$$

$$\dot{G} = (n_3+n_4 e^{-n_5 R})\dot{R} + n_6(\frac{2}{3}\Omega_{ij}\Omega_{ij})^{\frac{m-1}{2}} \qquad (2.15)$$

$$\dot{R} = \sqrt{\frac{2}{3}\dot{\epsilon}_{ij}^I \dot{\epsilon}_{ij}^I} \qquad . \qquad (2.16)$$

$\dot{R}$ is an effective inelastic strain rate. n_i (i=1,7), K_i (i=1,2) and m are material parameters. The drag stress is a function of the accumulated inelastic strain and the back stress evolution equation has both static and dynamic recovery terms. A summary of the

15

equations in the uniaxial form and the constants for the Hastelloy-X are given in Appendix A.

In order to study the basic capabilities of this model, a computer program was developed for integrating equations (2.12-2.16). The material parameters were taken from Reference [14] for Hastelloy-X at 649°C. A number of uniaxial loading histories were imposed to study the strain rate sensitivity, creep, stress relaxation, and cyclic effects of the model. On monotonic loading the model showed sensitivity to the applied strain rate. Such strain rate sensitivity is a basic property of all the unified models. Another basic capability is creep and stress relaxation modeling. This stress relaxation was verified as shown in Figure 2.1. The response is similar to that seen in stress relaxation tests. Another major capability required of any model is the cyclic history dependence. A number of cycles were imposed at a constant strain rate but with increasing amplitude such that the stresses are elastic during the initial cycles, see Figure 2.2. The predicted hysteresis loops shown in Figure 2.3 are in qualitative agreement with normally observed material behavior. Notice that a model based on back stress has the capability of predicting the cyclic history dependence very well. The back stress response is also cyclic during the cyclic history of loading as shown in
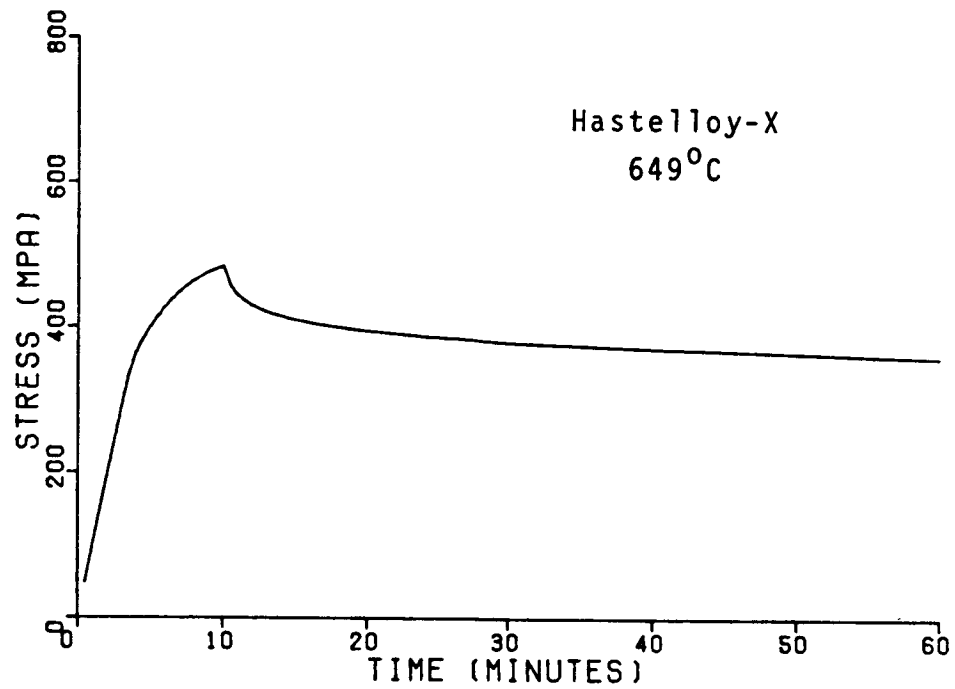
16

Figure 2.1   Stress Relaxation Using Walker Model
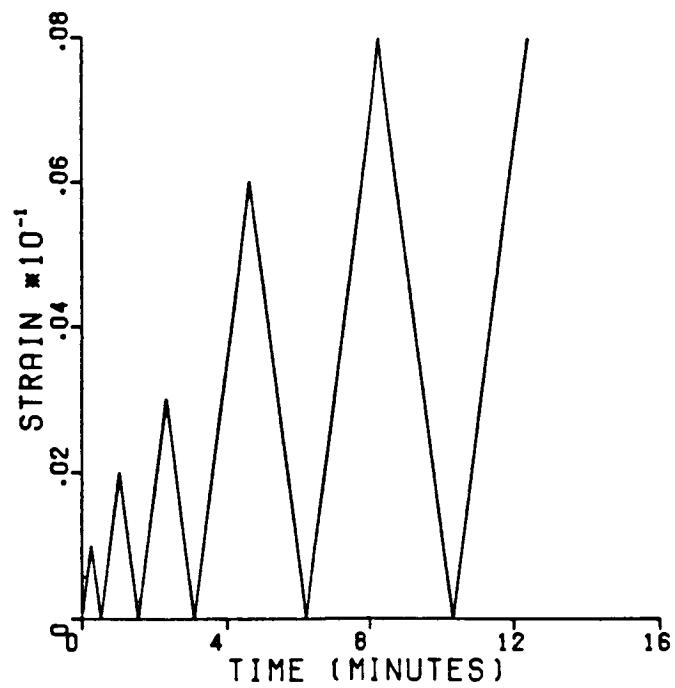
Figure 2.2   Strain History Imposed for Cyclic Capability Evaluation

Figure 2.4. The back stress is not near saturation; the flat portions in the response are during elastic loading and unloading where the inelastic strain rates are close to zero.

The material parameters from Reference [14] used in the previous calculations implied that the drag stress K remained constant since $n_7=0$ in Equation 2.14. To model cyclic hardening or softening behavior the drag stress K must be a variable. The cyclic softening modeling capability was qualitatively verified by using arbitrary values for K_2 and n_7 in Equation 2.14. It was possible to simulate cyclic softening by decreasing the drag stress as shown in Figure 2.5.

One of the major advantages of a back stress model is its capability to model anelastic recovery. It has been observed in materials at high temperature that, when a specimen is loaded into the inelastic regime and unloaded, there is a time dependent recovery of the residual inelastic strain [1]. Since the inelastic strain rate depends on the difference of the applied stress and back stress, Equation 2.12, anelastic strains can be modeled whenever this difference is negative. The constants K_2 and n_7 in Equation (2.14) were changed to verify the anelastic recovery of the Walker model. Figures 2.6 and 2.7 contain the results of this exercise where the strain is held at a low

Figure 2.3   Cyclic Hysteresis Loops Predicted Using
Walker Model
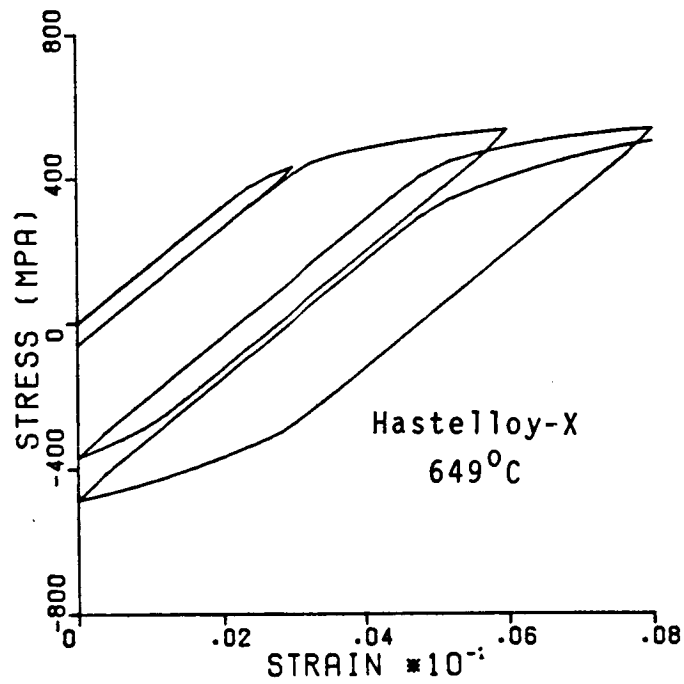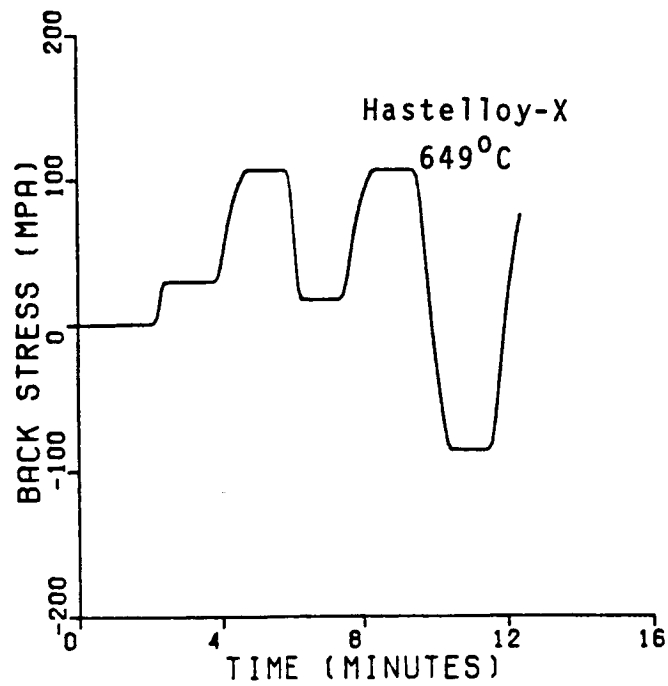

Figure 2.4   Back Stress Response of Walker Model for
Cyclic Loading

19
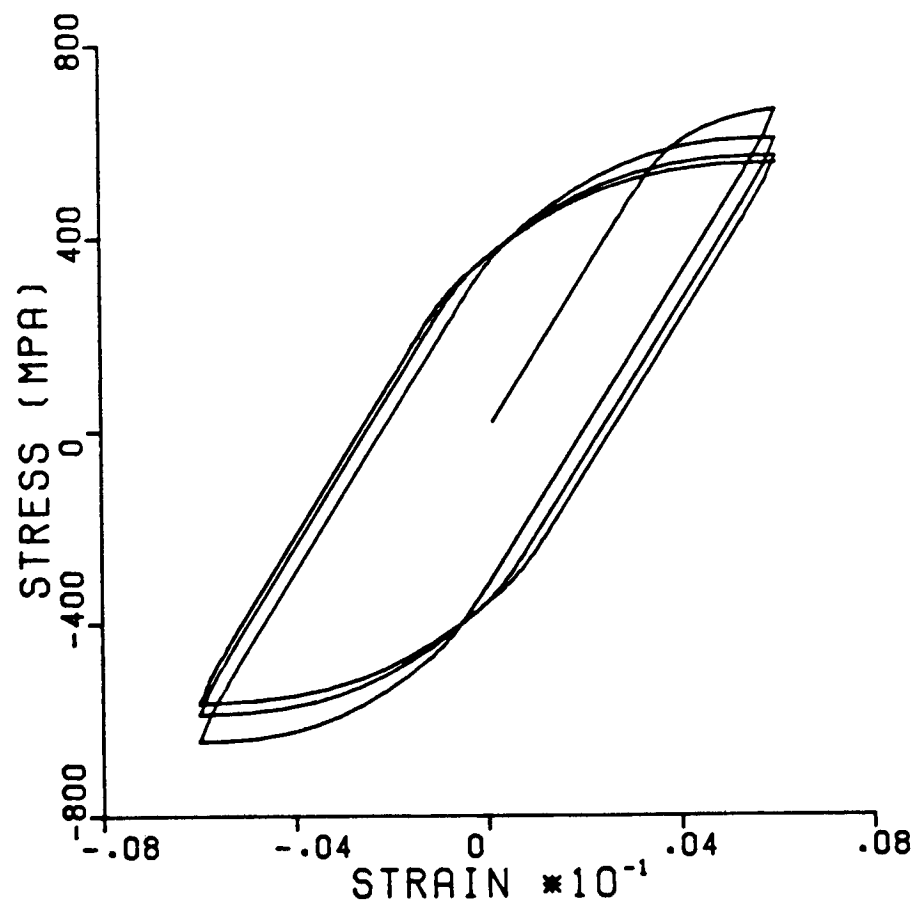
Figure 2.5   Cyclic Softening Prediction Capability of
Walker Model

20
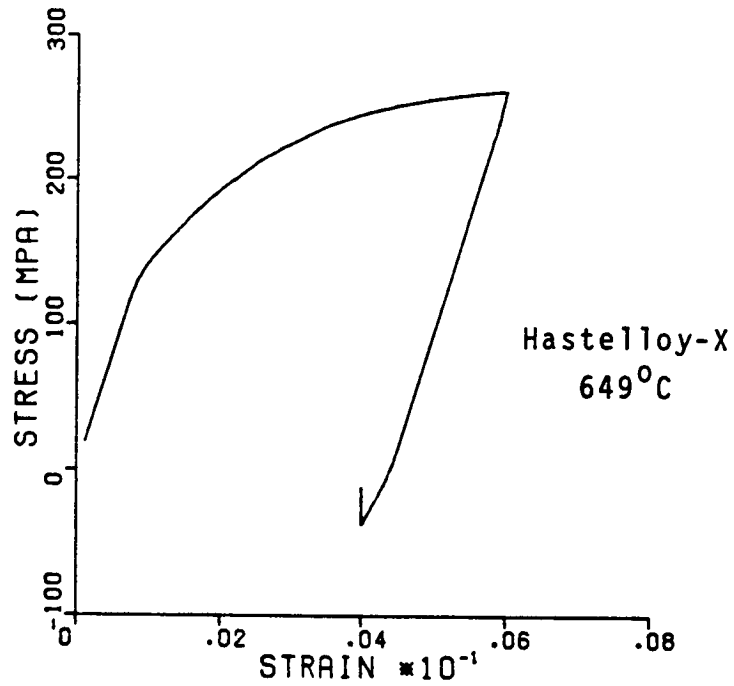
Figure 2.6   Loading History for Anelastic Modeling Capability
            Verification
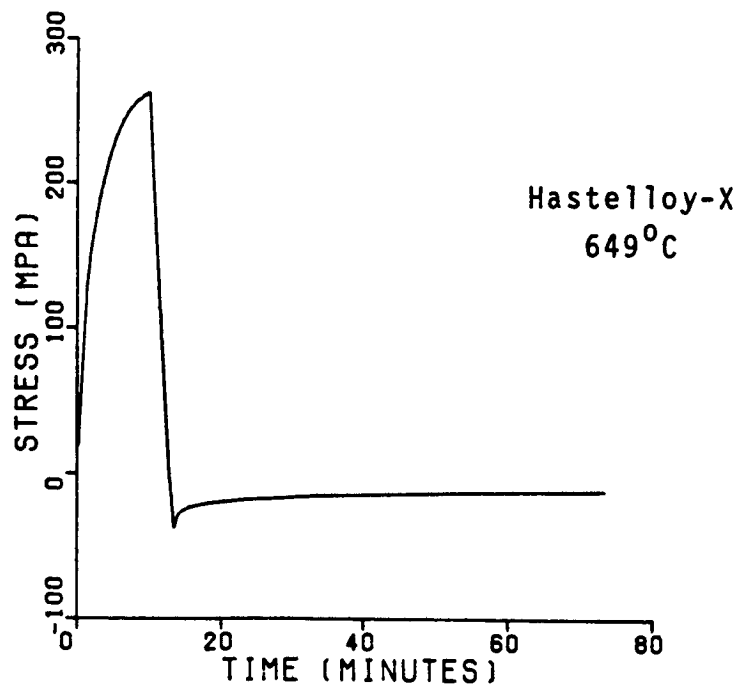
Figure 2.7   Walker Model Verification of Anelastic Modeling
            Capability

value of stress on the unloading branch. Time dependent recovery of the stress is observed in Figure 2.7.

2.3.2 Robinson Model

A unified constitutive model based on back stress and drag stress has been proposed by Robinson [17,18]. This model is different from the other models since different flow and evolution equations are used for loading and unloading. In this sense it bears close resemblance to classical plasticity in that it can also be derived from a plasticity potential. The model is considered as a unified theory since no distinction is made between creep and plastic strains. The model is summarized in the following equations and inequalities:

$$2\mu\dot{\varepsilon}_{ij}^{I} = \begin{cases} F^n \dfrac{\Sigma_{ij}}{\sqrt{J_2}} & ; \ F>0 \ \text{and} \ S_{ij}\Sigma_{ij}>0 \qquad (2.17) \\ 0 & ; \ F\leq0 \ \text{ or } \ S_{ij}\Sigma_{ij}\leq0 \qquad (2.18) \end{cases}$$

$$\dot{\alpha}_{ij} = \begin{cases} 2\mu h\dot{\varepsilon}_{ij}^{I} - r\dfrac{\alpha_{ij}}{\sqrt{I_2}} & ; \ G>G_0 \ \text{and} \ S_{ij}\alpha_{ij}>0 \qquad (2.19) \\ 2\mu\beta\dot{\varepsilon}_{ij}^{I} - r_0\dfrac{\alpha_{ij}}{\sqrt{I_2}} & ; \ G\leq G_0 \ \text{ or } \ S_{ij}\alpha_{ij}\leq0 \qquad (2.20) \end{cases}$$

where

$$F = (\frac{J_2}{K^2} - 1), \quad \Sigma_{ij} = (S_{ij} - \alpha_{ij}), \quad G = \sqrt{\frac{I_2}{K^2}} ,$$

$$I_2 = \tfrac{1}{2}\Sigma_{ij}\Sigma_{ij}, \quad J_2 = \tfrac{1}{2}\alpha_{ij}\alpha_{ij}, \quad h = \frac{H}{G^\beta}, \quad h_o = \frac{H}{G_o^\beta},$$

$$r = RG^{m-\beta} \quad \text{and} \quad r_o = RG_o^{m-\beta}.$$

The material parameters are μ, β, n, m, R, H and G_o.

The Robinson model has a back stress α_{ij} to model kinematic hardening characteristics. The isotropic variable K plays the role of a threshold stress below which the inelastic strain rate is zero. Isotropic hardening or softening can be modeled by varying K. Most of the applications appear to have been made with a constant value for K.

The Robinson model was programmed to explore its capabilities using the material parameters for 2¼ Cr -1 Mo steel at 538°C from Reference [18]. The model showed monotonic strain rate sensitivity, Figure 2.8, and appears to have some interesting creep response characteristics. Some materials display a delay in the creep response when stress is suddenly lowered during secondary creep as shown in Figure 2.9. It is seen that the Robinson model predicts creep at a lower rate after a brief delay which depends on the amount of stress drop, Figure 2.10. The response of the back stress, shown in Figure 2.11, gradually saturates to different limits.

23

The cyclic capability of the Robinson model was investigated by imposing constant strain rate strain histories with variable amplitude similar to that shown in Figure 2.2. The hysteresis response was similar to that shown in Figure 2.3.

In fully reversed cycling, the model tended to saturate after the first cycle as shown in Figure 2.12. This is perhaps due to an inadequate model for the drag stress, K. The model shows a fading memory of prior stress relaxation for large strain ranges. A comparison with and without a one minute tensile strain hold is shown in Figures 2.13 and 2.14. The tensile strain hold results in significant stress relaxation. However, after the first cycle, the effect of the stress relaxation appears to have been lost on the compression side of the loop. It was also noted that a one minute compressive strain hold also gave the same result at the end of the first cycle. These response characteristics are probably not realistic material behavior.

2.3.3 Bodner Model

Bodner and coworkers [19,20] have developed a unified theory which has a single scalar internal
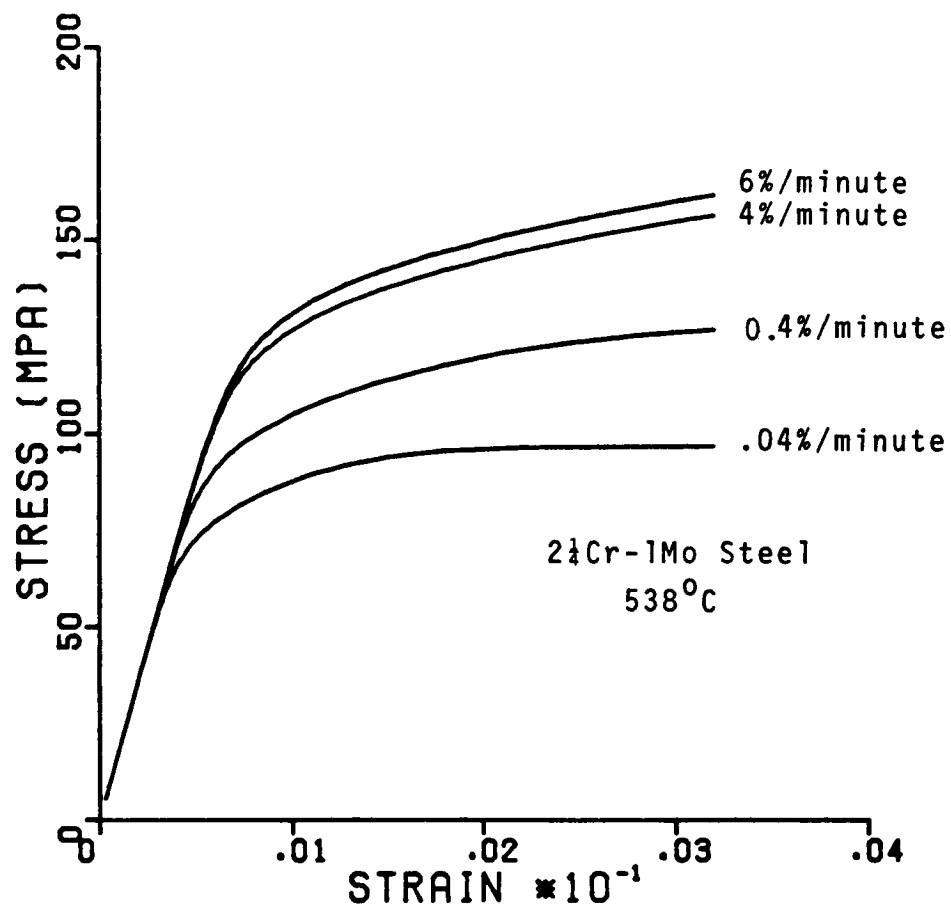
Figure 2.8 Strain Rate Sensitivity of Robinson Model
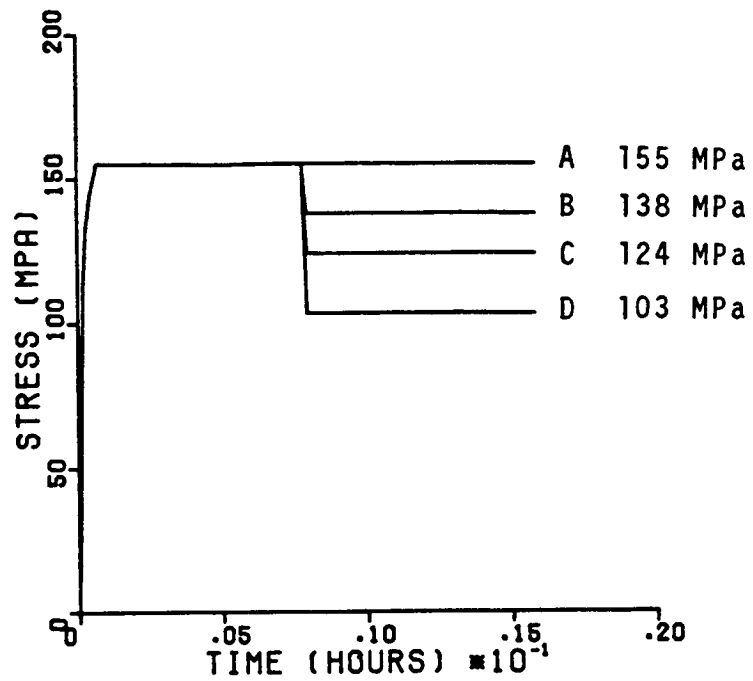
Figure 2.9   Creep Loading Conditions Imposed on Robinson Model
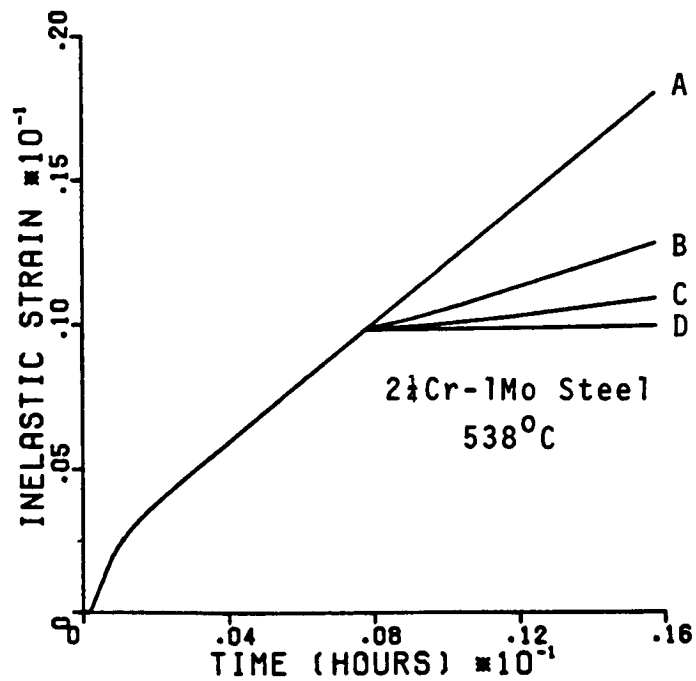
Figure 2.10   Creep Response of Robinson Model
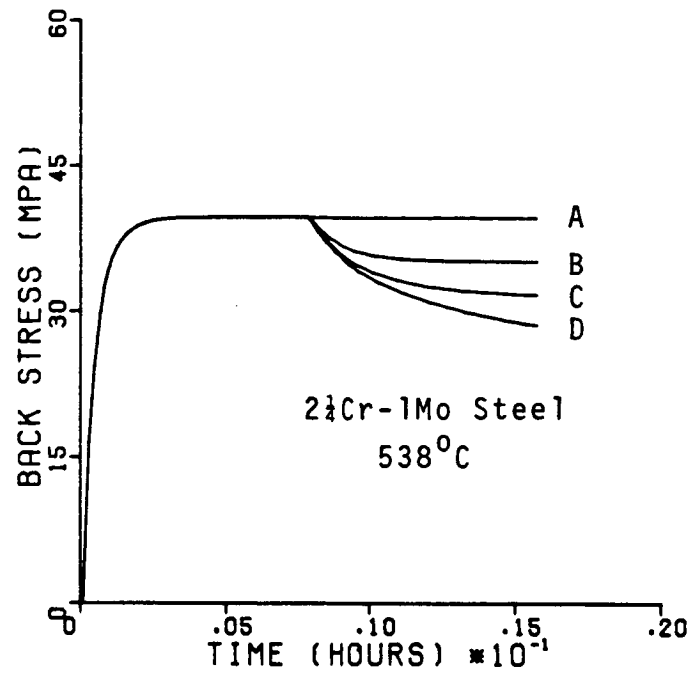
Figure 2.11 Back Stress Response of Robinson Model During
Creep
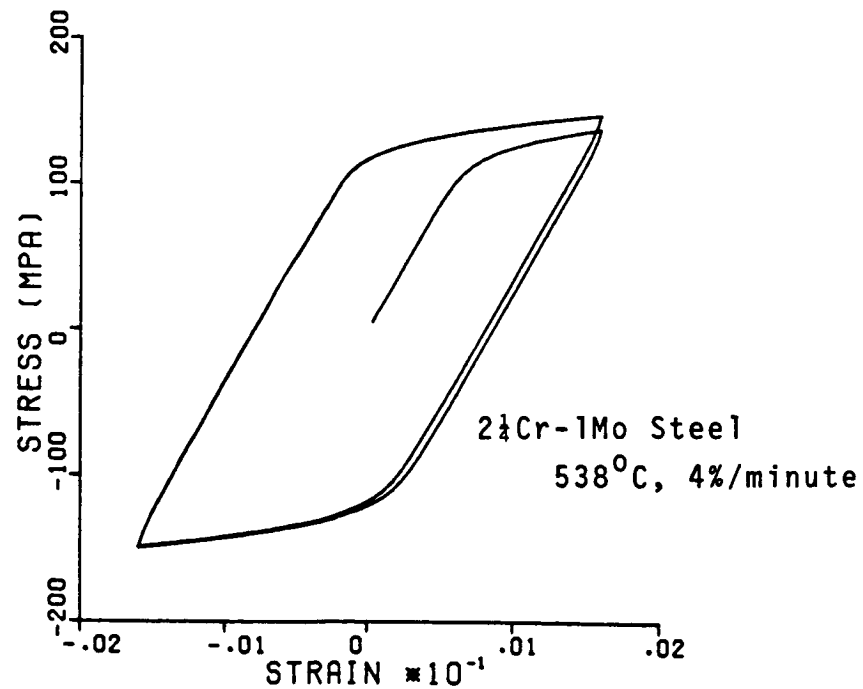
Figure 2.12 Cyclic Saturation of Robinson Model

variable. These equations are fairly simple and have been used for Rene´ 95, IN100, and IN718. The flow equation is similar to Prandtl Reuss flow law,

$$\dot{\varepsilon}_{ij}^{I} = \lambda S_{ij} \qquad (2.21)$$

where

$$\lambda^2 = \frac{D_2^P}{J_2} \qquad J_2 = \tfrac{1}{2} S_{ij} S_{ij}, \qquad (2.22)$$

and

$$D_2^P = D_o^2 \exp\left[-\frac{n+1}{2n}\left(\frac{Z^2}{3J_2}\right)^n\right]. \qquad (2.23)$$

The evolution equation for Z is given by

$$\dot{Z} = m(Z_1 - Z)\dot{W}^I - AZ_1\left(\frac{Z-Z_2}{Z_1}\right)^r \qquad (2.24)$$

where Z_1 is the maximum value of Z and Z_2 is the minimum recoverable value of Z. The internal variable Z has been interpreted as being a macroscopic representation of the resistance to inelastic flow. The evolution of Z depends on the inelastic work rate, $\dot{W}^I$, rather than $|\dot{\varepsilon}^I|$ as in the other models. In the absence of thermal recovery, A=0, Equation 2.24 can be integrated as

28
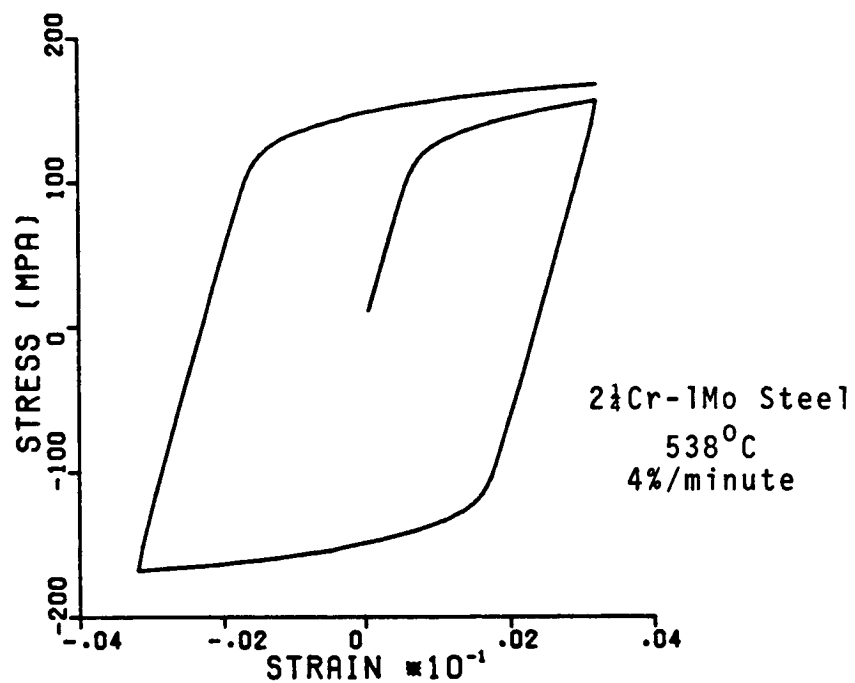
Figure 2.13   Cyclic Response of Robinson Model without Hold
Time
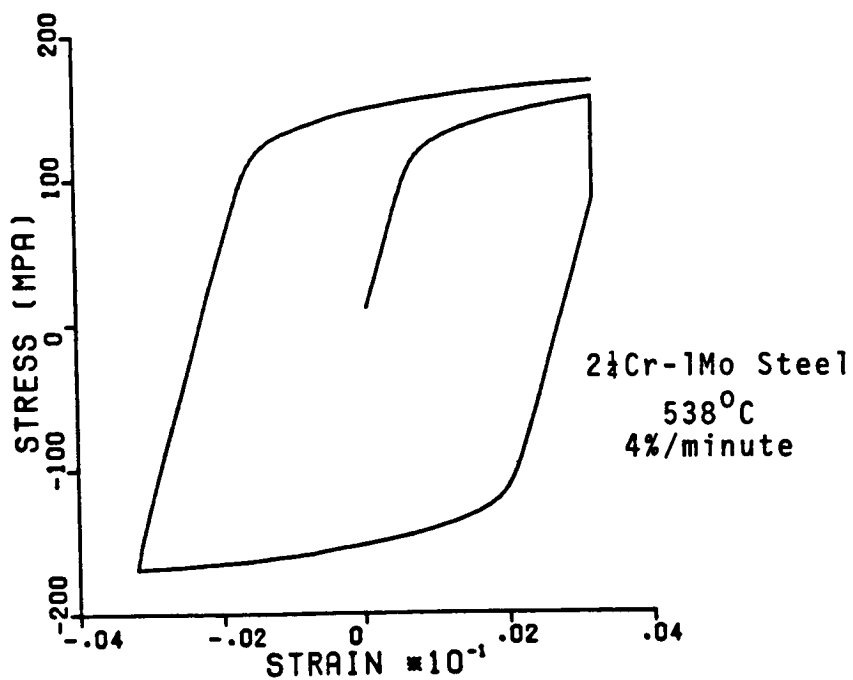
Figure 2.14   Cyclic Response of Robinson Model with One
Minute Tensile Hold

$$Z=Z_1+(Z_0-Z_1)e^{-mW^I} \qquad\qquad (2.25)$$

where W^I is the past accumulated inelastic work. Thus, in tensile tests the state variable Z is a monotonically increasing function of W^I and is used to model strain hardening.

This model is particularly simple and has only a few material parameters. Procedures have been established to systematically evaluate these parameters from test data [21]. Material parameters for Rene´ 95 at 649°c from Reference [20] were used to verify the strain rate sensitivity and creep response of this model. These are shown in Figures 2.15 and 2.16.

The Bodner model described above is for isotropic material response. It has been extended for anisotropic materials [22,23]. Bodner has recently modified the original model to incorporate a form of directional hardening. This will be discussed in more detail in Chapter 4.

2.3.4 Miller Model

A unified constitutive model based on a drag stress and rest stress (back stress) has been developed by Miller [24] for uniaxial loading. It has been
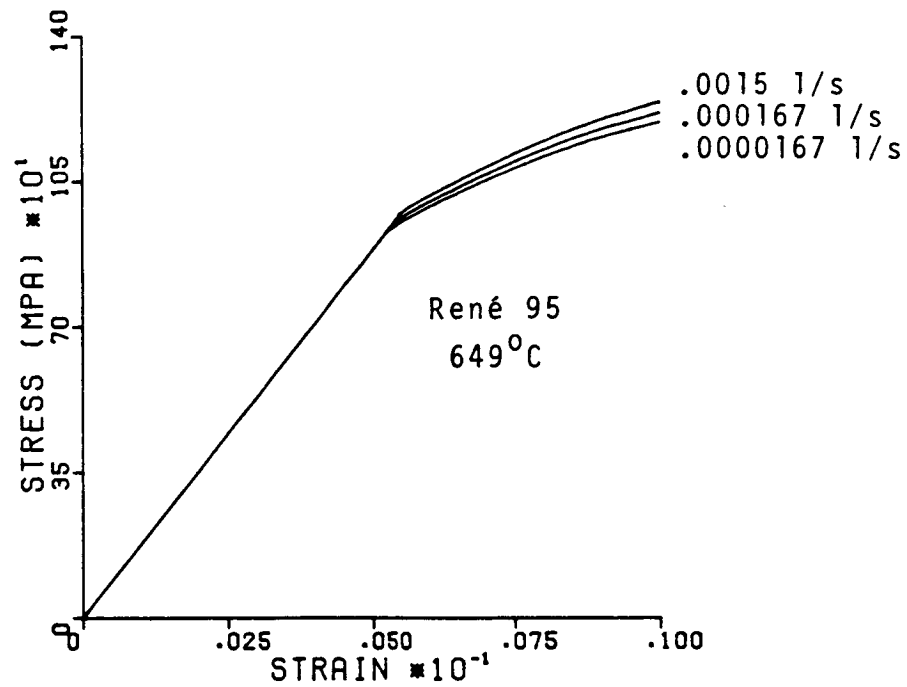
Figure 2.15   Strain Rate Sensitivity of Bodner Model
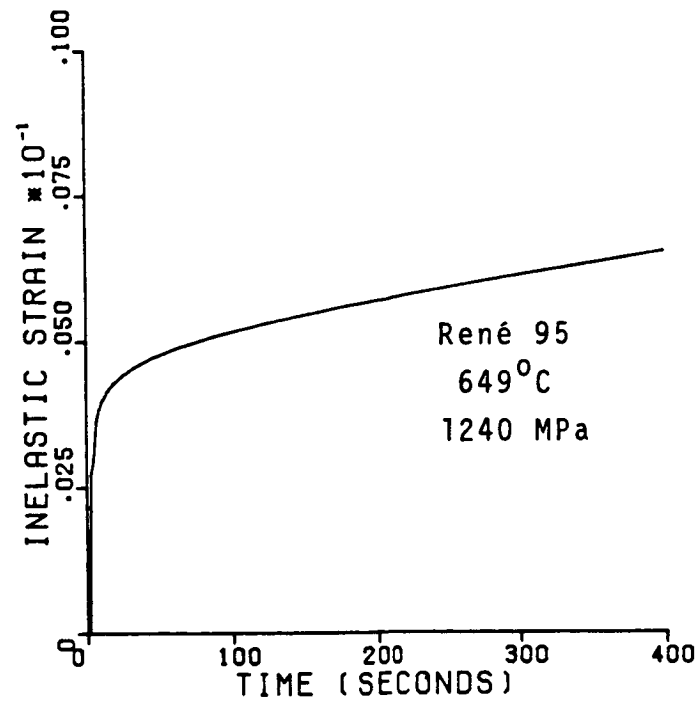
Figure 2.16   Creep Response of Bodner Model

observed for a number of materials that the steady state creep rate correlates with the applied stress in the form of the hyperbolic sine; i.e.,

$$\dot{\varepsilon}_{ss}^{C} = B'\{Sinh(A\sigma_{ss})\}^n \qquad (2.26)$$

where B' is a temperature dependent coefficient. Miller used this result to obtain a flow equation and static thermal recovery functions. Miller's model can be written for multiaxial loading in the following form [14]:

$$\dot{\varepsilon}_{ij}^{I} = B\theta'\left[Sinh\left\{\frac{X}{K}\right\}^{\frac{3}{2}}\right]^n \frac{\left[\frac{3}{2}S_{ij} - \Omega_{ij}\right]}{X}, \qquad (2.27)$$

where $X = \sqrt{\frac{2}{3}\left[\frac{3}{2}S_{ij} - \Omega_{ij}\right]\left[\frac{3}{2}S_{ij} - \Omega_{ij}\right]}$

$$\dot{\Omega}_{ij} = H_1\dot{\varepsilon}_{ij}^{I} - H_1 B\theta'\left[Sinh(A_1\alpha)\right]^n \frac{\Omega_{ij}}{\alpha}, \qquad (2.28)$$

$$\dot{K} = H_2\dot{K}\left[C_2 + \alpha - \frac{A_2}{A_1}K^3\right] - H_2 C_2 B\theta'\left[Sinh(A_2K^3)\right]^n \qquad (2.29)$$

where $\alpha = \sqrt{\frac{2}{3}\Omega_{ij}\Omega_{ij}} \qquad (2.30)$

$$\theta' = exp\left[-\frac{Q}{KT}\right] \quad for \ T \geq .6T_m \qquad (2.31)$$

32

$$\theta' = \exp\left[-\frac{Q}{.6KT_m}\left\{1+\ln\frac{.6T_m}{T}\right\}\right] \quad \text{for } T < .6T_m \quad (2.32)$$

$\dot{R}$ is an effective inelastic strain rate, defined previously.

A unique feature of this model is that only the material parameters θ' and K_0 (the initial value of K) are dependent on temperature. This could simplify the material parameter requirements for the model. The back stress equation contains only static thermal recovery terms; whereas, the drag stress equation has both static and dynamic recovery terms. The functional form for both the static recovery terms is similar to that used in the flow law.

This model has been exercised to evaluate various capabilities. It was found that numerical integration of the equations is far more difficult than for any other models considered in this study. The model requires very small time steps even fo simple loading cases. The numerical difficulties arise due to the highly nonlinear functional forms and the state variables tend to saturate very quickly. The calculated response of monotonic loading at different strain rates, shown in Figures 2.17-2.19, has trilinear behavior [14]. It is seen in Figures 2.18 and 2.19 that the state variables change from elastic to
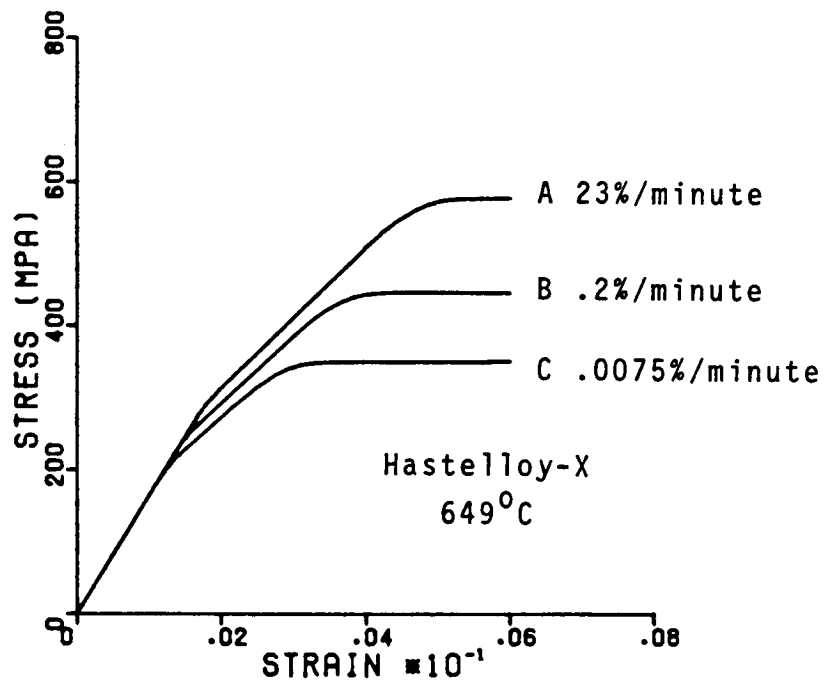
Figure 2.17   Strain Rate Sensitivity of Miller Model
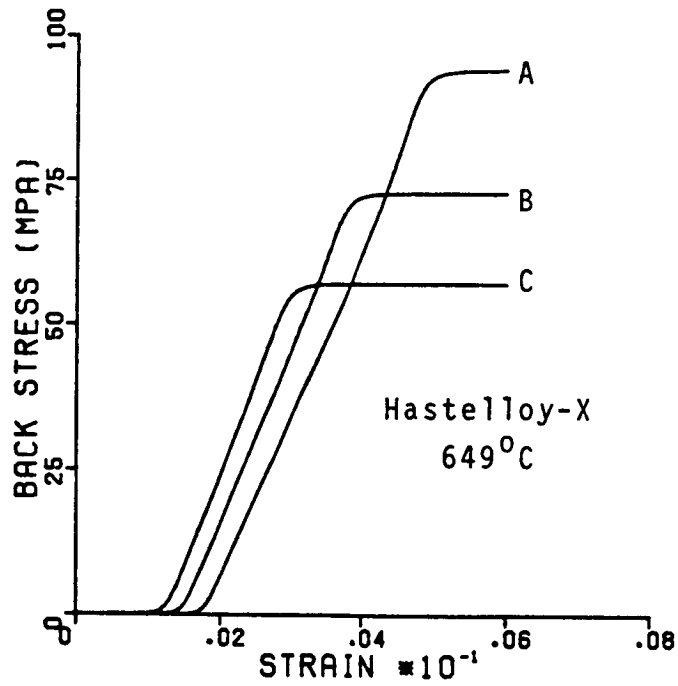
Figure 2.18   Back Stress Response of Miller Model
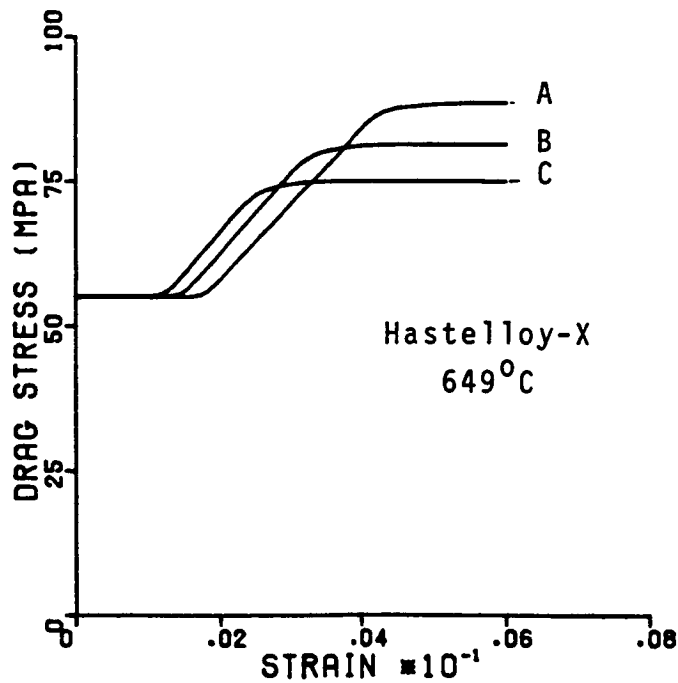
Figure 2.19   Drag Stress Response of Miller Model
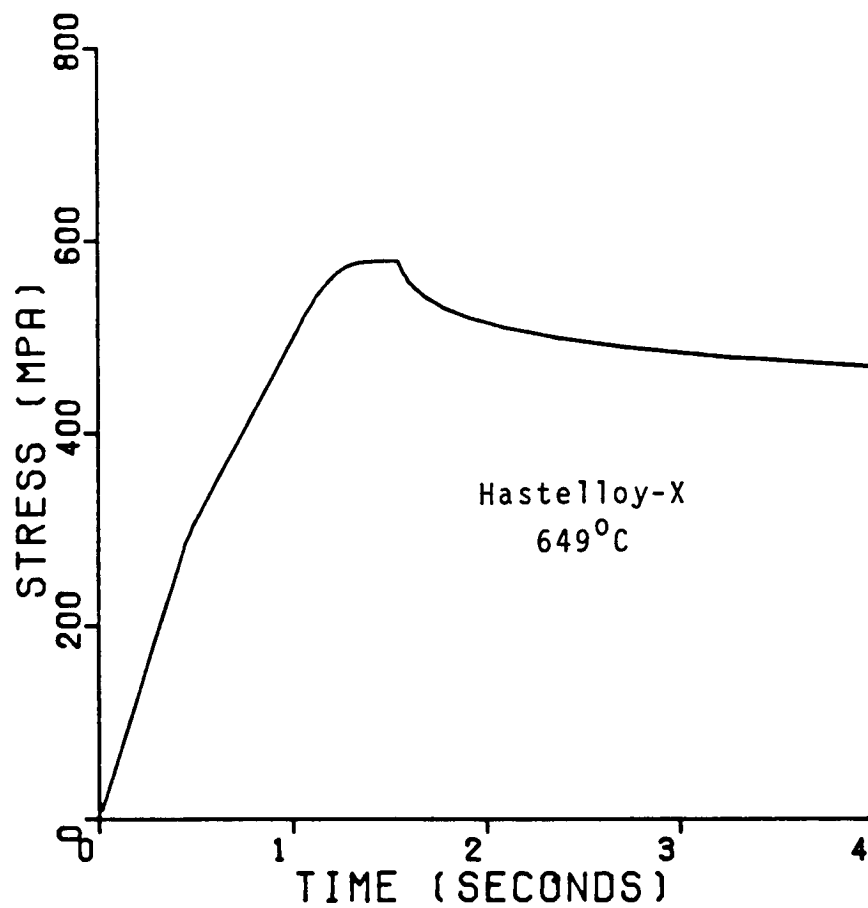
Figure 2.20   Stress Relaxation Prediction Using Miller Model

inelastic and to the saturated condition very rapidly in very distinct regions. The stress relaxation behavior predicted by this model is shown in Figure 2.20. The cyclic capabilities could not be fully evaluated. In general, it was possible to calculate the response for only one cycle due to the enormous number of time steps required. The hysteresis loops predicted by the model also showed a trilinear behavior similar to that in Figure 2.17. All the evaluations were done using material parameters for Hastelloy-X at 649°C from Reference [14].

2.3.5 Krieg, Swearengen and Rohde Model

This model also contains back stress and drag stress and has a power law type of flow equation. The back stress is identified with the effects of dislocation pileups at obstacles and the drag stress is considered as a mechanical strength variable. The equations for this model are written as follows [25]:

$$\dot{\underset{\sim}{\varepsilon}}_p = \dot{\varepsilon}_0 \left[\frac{|\underset{\sim}{\zeta}|}{R}\right]^m \frac{\underset{\sim}{\zeta}}{|\underset{\sim}{\zeta}|}, \qquad (2.33)$$

$$\underset{\sim}{\zeta} = \underset{\sim}{S} - \underset{\sim}{\alpha} \qquad (2.34)$$

$$\dot{\underset{\sim}{\alpha}} = A_\alpha \dot{\underset{\sim}{\epsilon}}_p - |\underset{\sim}{\alpha}| K_2 \left[\exp\left\{ \frac{K_3}{KT} |\underset{\sim}{\alpha}|^2 \right\} - 1 \right] \underset{\sim}{\alpha}, \text{ and} \qquad (2.35)$$

$$\dot{R} = A_R |\dot{\underset{\sim}{\epsilon}}_p| - K_1 \left[\frac{R - R_0}{T} \right]^n \exp\left(-\frac{u}{KT} \right). \qquad (2.36)$$

The model has only static recovery terms. The monotonic and creep behavior of the model have been discussed in detail for aluminum [25]. The model has not been extended to cyclic hardening or softening. The constants for aluminum reported in Reference [25] assume the drag stress to be constant.

This model was exercised for monotonic, creep and cyclic loading conditions. Two examples of response are shown in Figures 2.21 and 2.22. It can be seen that the state variables approach saturation rather abruptly, similar to the Miller model. This could be due to the value of the constants or perhaps the lack of dynamic recovery terms and the use of exponential form in static recovery. The model could not predict any anelastic recovery with the constants reported for aluminum.

2.4 Summary of Model Evaluation

The detailed evaluations performed on the five models discussed before were based on material

38
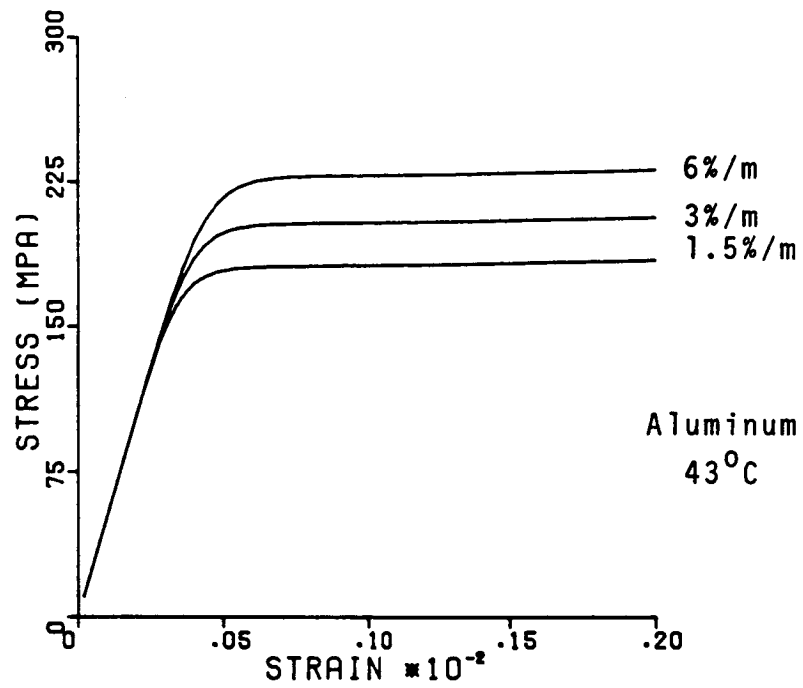
Figure 2.21   Strain Rate Sensitivity of Krieg Model
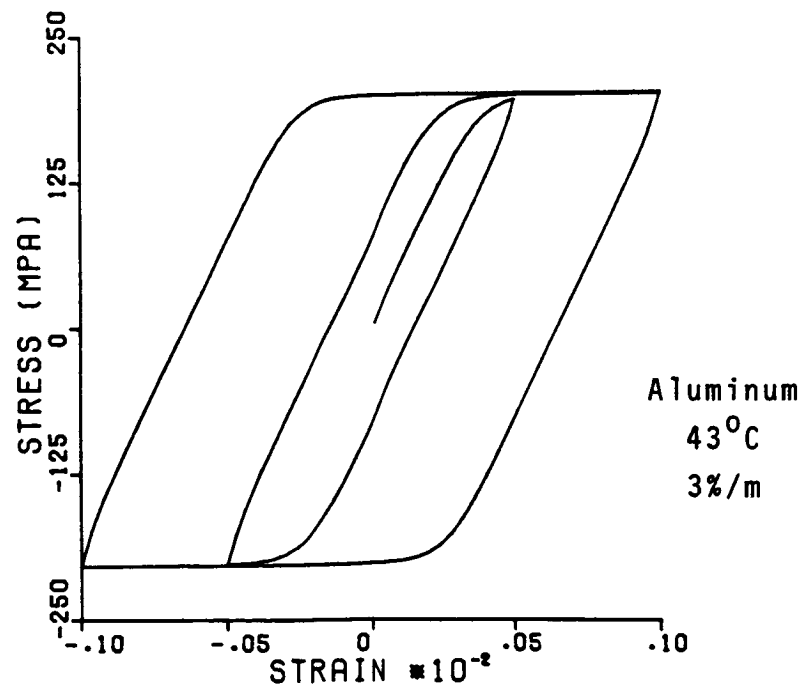
Figure 2.22   Cyclic Response for Krieg Model

constants for different materials and temperatures. They do not necessarily reflect the behavior of Rene´ 80, the material being investigated here. However, they have led to an understanding of the response characteristics of unified models in general. Some potential areas of difficulties in numerical implementation and material parameter evaluations for the models have also become apparent. These are briefly discussed below.

2.4.1 Strain Rate Sensitivity

All the models exhibited strain rate dependent tensile behavior. This is a basic requirement for models that are to represent high temperature material behavior. At low temperatures most materials do not show strain rate sensitivity. The capability of the unified models at low temperatures was not evaluated. The characteristic behavior of the internal variables is usually different for the various models. In the Walker, Robinson, and Bodner models, the state variables saturated to the same limit at high strain rates; whereas, for the Miller and Krieg models, the saturation values for the state variables are strain rate dependent.

40

2.4.2 Creep and Stress Relaxation

All the models examined appear to have the basic ability to predict primary and secondary creep. They also exhibit stress relaxation during a constant strain history. The basic feature of the models which provides these capabilities is the hardening recovery term in the evolution equations. Some models had both static and dynamic recovery terms. None of the unified models can predict tertiary creep. The Robinson model appears to have the ability to predict transients due to a stress drop during steady state creep. This is a desirable feature for practical applications.

2.4.3 Cyclic Behavior

Almost all the unified models available to date were developed based on monotonic and creep behavior; however, almost all the structural applications involve cyclic loads. It is extremely important that the models should adequately model cyclic behavior. The models examined had varying degrees of cyclic hardening or softening capabilities. Although the structure of the equations would permit modeling cyclic hardening or softening, none of the models appear to have been fully

41

developed in this regard. It appears that models based on a kinematic back stress and an isotropic drag stress can model cyclic behavior more realistically. In general, cyclic hardening or softening behavior is modeled using the variations of the drag stress.

2.4.4 Anelasticity

Anelastic recovery cannot be predicted by the classical Prandtl Reuss flow law. The Bodner model, which is an extension of this type of flow law, suffers the same drawback. The structure of the models based on back stress and drag stress enables the modeling of anelastic recovery. This capability was verified by using hypothetical material parameters in the Walker model.

2.4.5 Numerical Implementation

The computer programs used to make the evaluations employed a simple forward Euler integration scheme. This worked well for all the models. However, the time step size requirements for the Miller model were particularly small. Higher order integration schemes with automatic time incrementing would be beneficial

for this model. Even so, the Miller model appears least desirable from a numerical standpoint. This is due to the highly nonlinear functions used in the evolution equations. The Robinson model also has less desirable properties due to the inequalities. The functions used in the constitutive model change discontinuously across these inequalities. The Bodner model presented no major problems, although it required the use of small time steps. The Walker model also presented no major difficulties. In general, the back stress drag stress models require more storage.

2.4.6 Material Parameters

This perhaps is the biggest area of difficulty for the unified theories. The evaluation of material parameters varied significantly among the various models. There does not appear to be a general procedure to evaluate these parameters. The only exception is the Bodner model which has only one state variable. It is desirable to have a method of finding these constants from standard test data. Most of the models have been verified at only one temperature; thus, the temperature dependency of the material parameters is not clear.

CHAPTER 3

REVIEW OF THE EXPERIMENTAL PROGRAM

The main objective of the research program is the development and verification of constitutive equations for modeling high temperature material behavior. One of the most important requirements for accomplishing this objective is the establishment of an accurate data base for the material behavior under investigation. This data base must include a wide spectrum of loading histories and temperatures. In the past many constitutive equations have been formulated from a limited data base. The temperature range is limited and there is almost no multiaxial data at elevated temperatures. Differences in the chemistry, heat treatment and experimental techniques can cause considerable inconsistencies in the observed behavior. Recognizing this severe problem the National Aeronautics and Space Administration, Lewis Research Center, Cleveland, has sponsored a program which includes the development of a uniaxial and multiaxial data base for the two superalloys, Rene´ 80 [26] and B1900 [27] at several temperatures.

Rene´ 80 was experimentally evaluated by Van Stone [26,30] as part of a NASA contract to

General Electric Company, Aircraft Engine Business Group, Cincinnati, Ohio. This study was conducted in conjunction with the current research on constitutive modeling and is reported separately. However, the relevant aspects of the experimental study are included in this report because of their impact on the current research.

3.1 Description of the Program

The experimental program has several distinct objectives. These include the generation of mechanical response data that are relevant to gas turbine applications. The temperature, strain range and strain rates were selected to satisfy this need. The specimen designs used in the tests also conformed to this requirement. The program was designed to maximize the amount of data obtained from each test. Advantage is also taken of the recent developments in testing technology. Finally, computerized data reduction methods were developed which are specifically suited for constitutive equation development.

Three types of tests were performed; uniaxial, multiaxial (tension/torsion) and uniaxial tests on notched specimens. The uniaxial and multiaxial tests are for the development and verification of the

constitutive equations and are included the study. The structural verification study using the notch specimens will be reported separately [30]. The uniaxial tests were performed by Dr. R. H. Van Stone at General Electric Company, Evendale, Ohio. The tension/torsion tests were performed by Dr. R. Williams at General Electric Company, Schenectady, New York. The two categories of tests include model development and model verification. The results of the model development tests are used to generate the material parameters for the constitutive model. The results of the model verification tests are used for comparing the observed material behavior with that predicted by the constitutive model.

3.2 Material and Specimen

Rene´ 80 was chosen for investigation in this program. It is a nickel based superalloy that is widely used for high temperature components such as blades and vanes in gas turbine engines. The strength of this alloy is derived from gamma prime precipitates, $Ni_3(Al,Ti)$, and the solid solution of molybdenum and tungsten in the matrix gamma phase. The chemical composition of the material used in this program and nominal Rene´ 80 composition is given in Table 3.1.

46

Cylindrical specimen blanks were investment cast from remelt stock of Rene' 80 in two sizes. The smaller blanks (1.3 cm diameter x 10 cm) were used for tensile, creep and cyclic test specimens. The larger blanks (3.0 cm diameter x 15 cm) were used for tension/torsion testing. Both castings had approximately the same grain size ($\sim$ 0.6 cm). These specimen blanks were given the standard heat treatment for Rene' 80, shown in Table 3.2.

Specimens were later machined from these blanks. Figure 3.1 shows the thin wall tubular test specimens used for uniaxial experiments. A wall thickness of about .08 cm was chosen because it is typical of most blades and vanes used in engines. It has been reported [28] that there is a thin wall effect on at least some of the mechanical properties of Rene' 80. The grain size of Rene' 80 used in this study is much larger than the test specimen wall thickness. Although this may increase the risk of data scatter, thin wall specimens were specifically chosen to represent actual gas turbine components. Figure 3.2 shows the cylindrical hollow specimen used for the tension/torsion tests.

Table 3.1 Composition of Rene´ 80

Element	Specification	Certified Analysis
C	0.15-0.14	0.17
Mn	0.10 Max.	0.01
Si	0.10 Max.	0.02
S	0.0075 Max.	0.002
P	0.015 Max.	0.009
Cr	13.70-14.30	14.06
Ti	4.80-5.0	4.87
B	0.01-0.12	0.015
Al	2.8-3.2	3.05
W	3.70-4.30	4.00
Mg	3.70-4.30	4.06
W+Mo	7.70 Min.	8.06
Co	9.00-10.00	9.55
Zr	0.02-0.10	0.03
Fe	0.03 Max.	0.07
Cb	0.10 Max.	0.01
Ta	0.10 Max.	0.02
V	0.10 Max.	0.01
Cu	0.10 Max.	0.01
Hf	0.10 Max.	0.01
Mg	0.10 Max.	0.0032
Ni	Balance	Balance

Table 3.2 Heat Treatment of Rene' 80

(i)   1204°C (2200°F)/2 hours; cool to 1093°C (2000°F) within 10 minutes; cool to room temperature.

(ii)   1093°C (2000°F)/4 hours; cool to 649°C (1200°F) within 6 minutes; cool to room temperature.

(iii) 1052°C (1925°F)/8 hours; cool to 649°C (1200°F) within 30 minutes, cool to room temperature.

(iv)   843°C (1550°F)/16 hours; cool to room temperature.

101.6

50.8

15.7

9.5 9.5

4.76 (I.D.)

6.35 (O.D.)

(Dimensions in Millimeters)
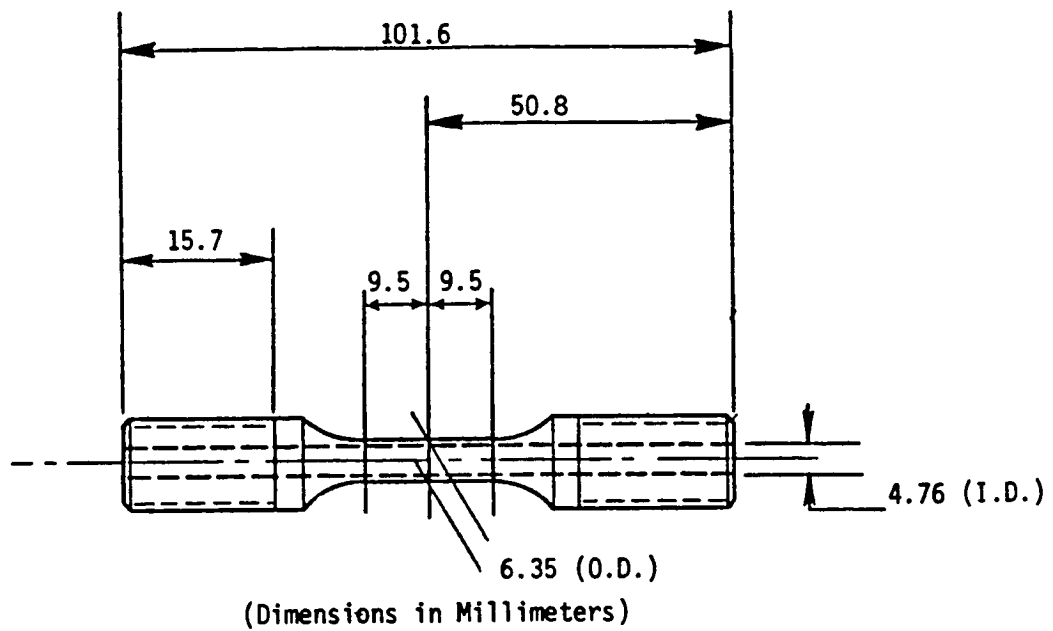
Figure 3.1 Test Specimen for Uniaxial Experiments

146

73

28.6 28.6

12.7 (O.D.)

10.8 (I.D.)

(Dimensions in Millimeters)
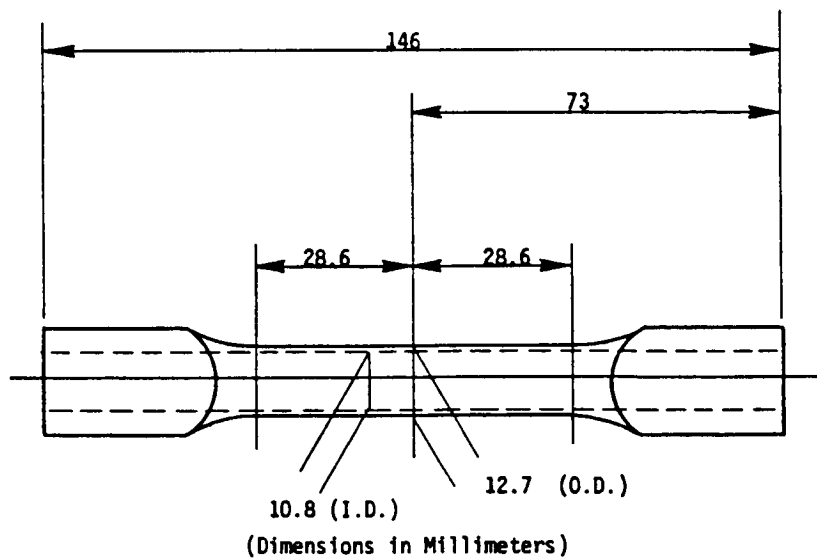
Figure 3.2 Test Specimen for Multiaxial Experiments

3.3 Description of the Uniaxial Testing Program

Three types of uniaxial tests were performed. They are monotonic tensile, constant load creep and cyclic tests. All tests were done on closed loop servocontrolled machines. The monotonic tensile tests were performed under strain rate control to obtain strain rate sensitivity data. Creep tests were performed under stress control conditions at different stress levels. The cyclic tests were also strain controlled and were performed at different strain rates, hold times and A_ϵ ratios (A_ϵ = alternating strain/mean strain). Variations were made in A_ϵ to study the effect of mean stress, which has been shown to have significant influence on low cycle fatigue life [29]. All the cyclic tests and tensile tests were performed under strain rate control. The cyclic tests were done in blocks of approximately twenty cycles with each block having a different strain amplitude. The same block strain range history (.0030, .0060, .0090, .0060, .0030, .0090, .0030) was used on all the uniaxial cyclic tests. The first three blocks had increasing strain amplitude and next two blocks had decreasing strain amplitude. The last two blocks had a sharply increasing and decreasing strain amplitudes to

study possible transient effects. An example of the imposed strain history is shown in Figure 3.3. Complete hysteresis loops were recorded at each point shown in this figure.

All of the above tests were performed at three primary temperatures of 982°C (1800°F), 871°C (1600°F) and 760°C (1400°F). A limited number of monotonic tensile and creep tests were also performed at 1093°C (2000°F), 649°C (1200°F) and 538°C (1000°F). The test matrix and specimen allocation for all uniaxial tests are shown in Table 3.3.

Most nickel base superalloys have a general change in response characteristics in the temperature range considered in this study. At the higher temperatures significant time and rate effects are observed. At the lower temperatures the rate sensitivity is essentially absent, but creep and relaxation response is present. The transition occurs at about 750°C to 800°C. At this temperature the ductility is minimal as shown in Figure 3.4. This type of behavior is expected to complicate both the testing and modeling.

3.3.1 Tests at 982°C (1800°F)

The monotonic tensile tests were performed at strain rates of .002 per minute, .02 per minute, .06
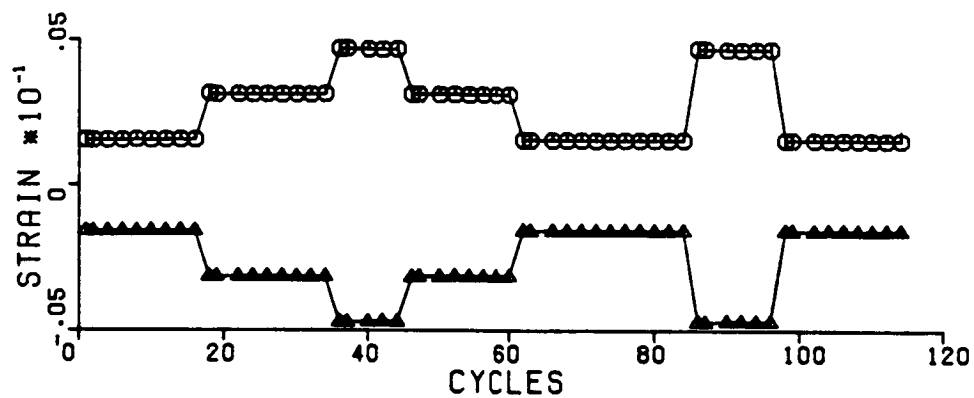
Figure 3.3 Typical Strain History Imposed for Cyclic Tests
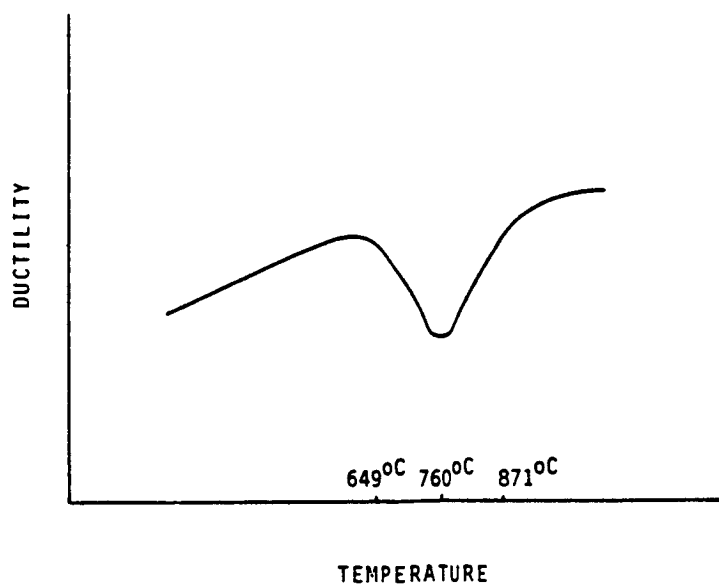
Figure 3.4 René 80 Ductility Variation with Temperature

TABLE 3.3 Specimen No. Allocation in the Uniaxial Tests

MONOTONIC TESTS

$\dot{\varepsilon}_M$ $^{-1}$			TEMPERATURE			
	538°C (1000°F)	649°C (1200°F)	760°C (1400°F)	871°C (1600°F)	982°C (1800°F)	1093°C (2000°F)
.2	G-06		K-06	U-81	S-06	
.2					J-205	
.06					N-05	
.02	L-81	V-06	C-05	R-81	J-05	
.002	T-05		D-81	P-05	A-06	

CYCLIC TESTS

A_ε	M $^{-1}$	Hold, Sec.	760°C (1400°F)	871°C (1600°F)	982°C (1800°F)
∞	.2	0	B-05	B-06	S-81
∞	.002	0	L-06	E-81	W-81
-1	.2	0	C-81	V-81	N-06
-1	.002	0		M-05	X-06
∞	.2	12 (Min)	R-06		I-81
∞	.2	120 (Min)	Y-06		F-06
+1	.2	0	U-05	T-06	
∞	.2	12 (Max)	H-06	D-05	
∞	.2	120 (Max)	K-05		

CREEP TESTS

Stress (MPa)/Spec. No.	760°C (1400°F)	871°C (1600°F)	982°C (1800°F)	1093°C (2000°F)
	684/V-05	493/M-06	300/F-81	114/0-06
	633/G-81	413/E-05	217/T-81	
	553/C-06	310/U-06	110/L-05	

per minute, and .2 per minute. One additional
monotonic tensile curve was obtained from a scheduled
cyclic test which accidentally failed due to initial
overload. The specimens were extended to strain values
of .016 to ensure saturation. At the end of each test
the strain was held constant to obtain stress
relaxation data. In general, terminal strains larger
than .016 resulted in specimen failure.

The creep tests were performed at 300 MPa, 217
MPa, and 110 MPa. These tests were done under load
control with an elastic strain rate of approximately
.02 per minute. These tests were stopped after an
inelastic strain accumulation of about .01 or after 150
hours.

It is observed [1] that, under typical aircraft
engine operating conditions, a negative mean strain
exists in turbine airfoils at higher temperatures.
The $A_\epsilon = -1$ tests at 982°C have negative mean strains.
Two tests were performed with 12 second and 120 second
hold times, at compressive peak strain. This is
frequently encountered in airfoils at high temperature.

3.3.2 Tests at 871°C (1600°F)

In general the ductility is lower at this
temperature. Thus, the monotonic tensile tests could

55

not be run to the high values of strain required for saturation. Three monotonic tensile tests were performed at strain rates of .2 M^{-1}, .02 M^{-1} and .002 M^{-1}. Three creep tests were performed at stress levels of 493 MPa, 413 MPa and 313 MPa. The cyclic test conditions were exactly the same as those at 982°C (1800°F).

3.3.3 Tests at 760°C (1400°F)

Most of these tests are the same as the tests at 871°C (1600°F). Creep tests were done at higher stress values to obtain measurable creep. Four additional cyclic tests included two with a tensile mean strain and two with tensile hold time. Since the ductility is very low at this temperature, the strain levels in the monotonic tests were expected to be low.

3.3.4 Tests at Other Temperatures

A limited number of tests were performed at other temperatures. Three monotonic tensile tests were performed at 538°C (1000°F) at strain rates of .2 M^{-1}, .02 M^{-1} and .002 M^{-1}. One strain rate controlled (.02 M^{-1}) monotonic tensile test was performed at 649°C (1200°F). A creep test at 114 MPa was performed at

1093°C (2000°F). No cyclic tests were done at these temperatures.

3.3.5 Results of the Uniaxial Experimental Program

The amount of data acquired during the experimental program is enormous and presentation of all the data for each test is not practical. Only typical examples are shown to discuss specific material phenomena. Additional data are presented in later chapters in comparison to predicted response.

The monotonic tests revealed the strain rate sensitivity of Rene 80 as a function of temperature. At 982°C (1800°F) there is a very large sensitivity to the applied strain rate, as shown in Figure 3.5; whereas, at 538°C (1000°F) there is no strain rate sensitivity, as shown in Figure 3.6. At 871°C (1600°F) there is some strain rate sensitivity but very little at 760°C (1400°F). The lack of monotonic strain rate sensitivity in the tensile tests at 760°C does not imply the absence of time dependent effects. As shown in Figure 3.7 there is a significant amount of creep. Similarly, there is a significant amount of stress relaxation at temperatures above 760°C. An example of stress relaxation is shown in Figure 3.8 for a 12 second compressive peak strain hold at 982°C (1800°F).
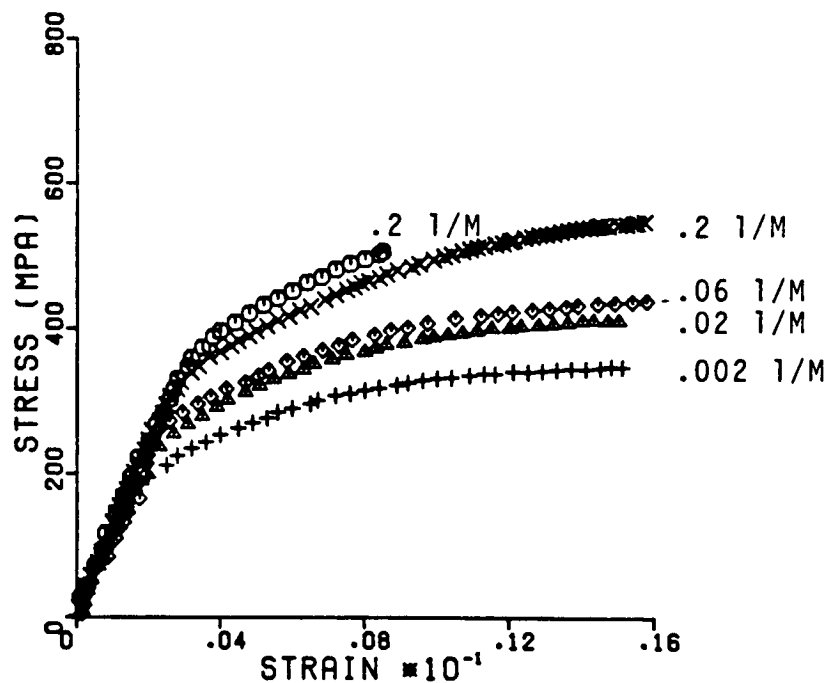
Figure 3.5   Strain Rate Dependent Tensile Behavior of René 80
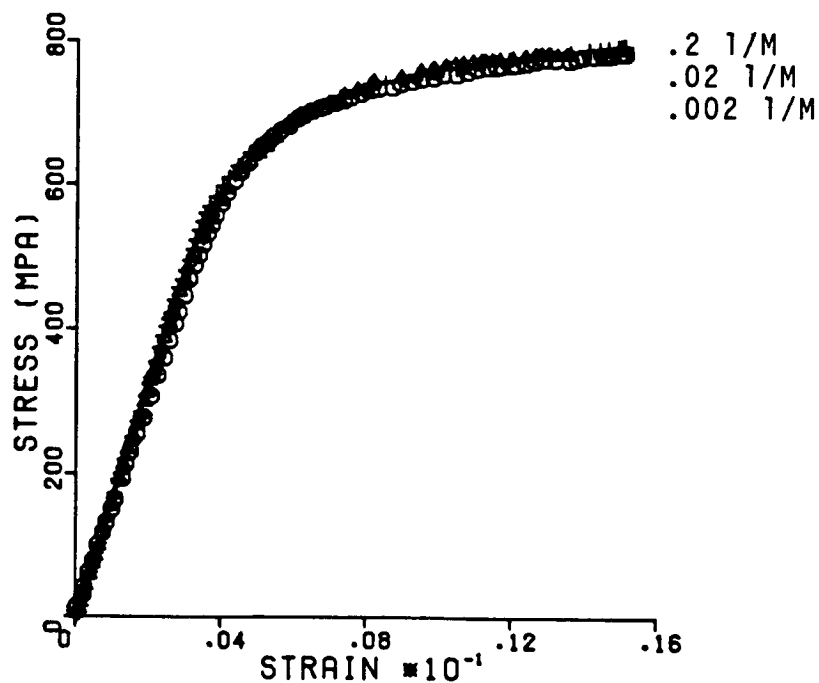at 982°C

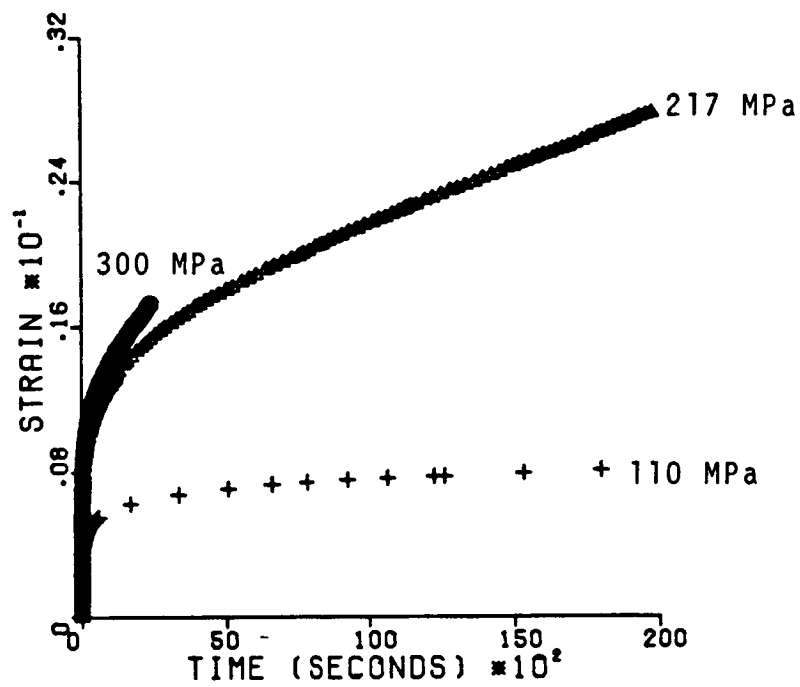Figure 3.6   Strain Rate Independent Tensile Behavior of
René 80 at 538°C

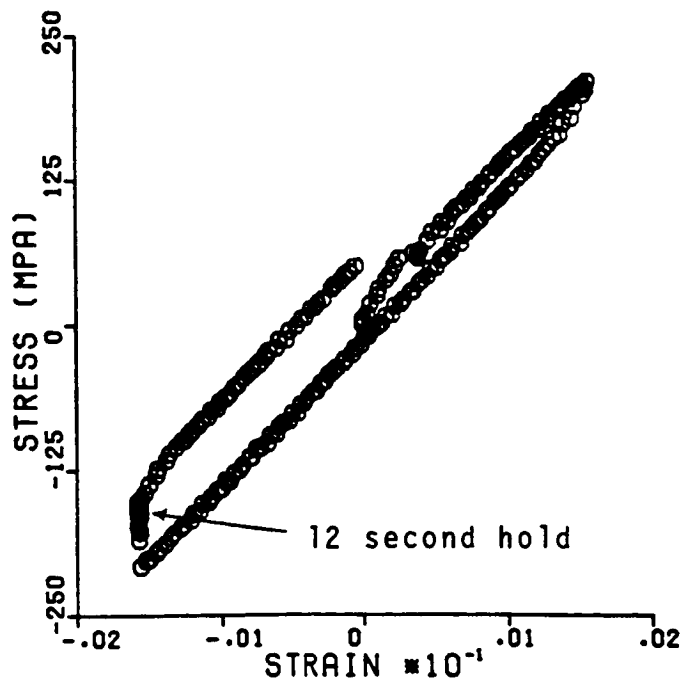Figure 3.7   Creep Response of René 80 at 982°C

Figure 3.8   Stress Relaxation of René 80 at 982°C

Rene´ 80 is generally cyclically stable at all temperatures except at the higher temperatures (982°C and 871°C) and higher strain rates, where some softening is observed for the first few cycles. Thus, cyclic softening behavior is a function of both temperature and strain rate. The cyclic stress strain behavior is compared with the monotonic stress strain curve in Figures 3.9, 3.10, and 3.11. The cyclic response is presented as half of the total stress and strain range for a number of cycles from the block history. At 982°C (1800°F), there is a considerable amount of cyclic softening at a strain rate of .2 per minute as shown in Figure 3.9. However, at the lowest strain rate of .002 per minute there is no softening (see Figure 3.10). Figure 3.11 shows the material is essentially cyclically stable at 760°C (1400°F). This result is not conclusive since the tensile test results are not ordered with respect to the strain rate. This scatter is probably associated with the lack of ductility at 760°C. The mean strain tests ($A_\epsilon = -1.0$) showed that there is a considerable amount of mean stress relaxation. An example is shown in Figure 3.12 for the first few cycles of mean strain test at 982°C (1800°F). This figure also shows the development of cyclic inelastic strain.
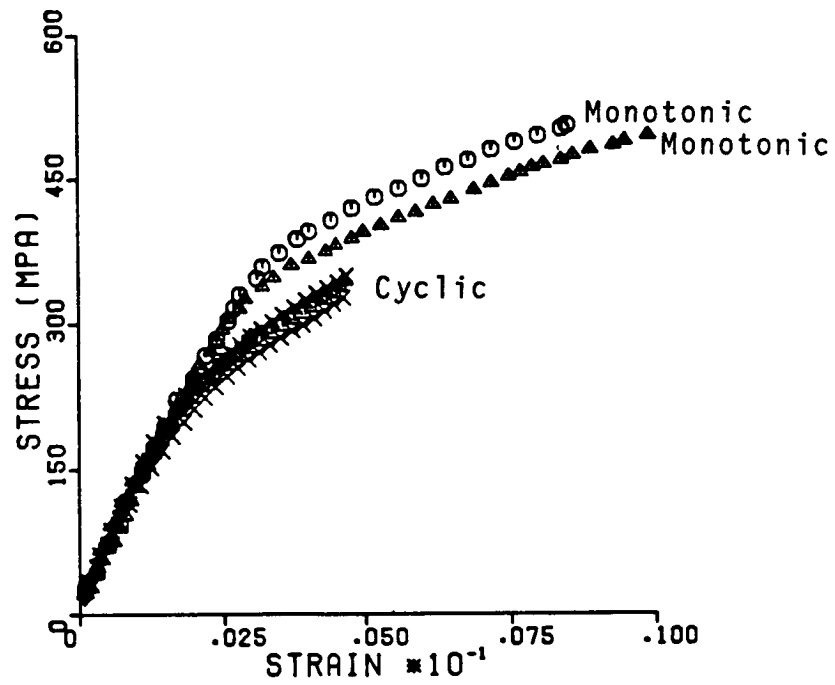
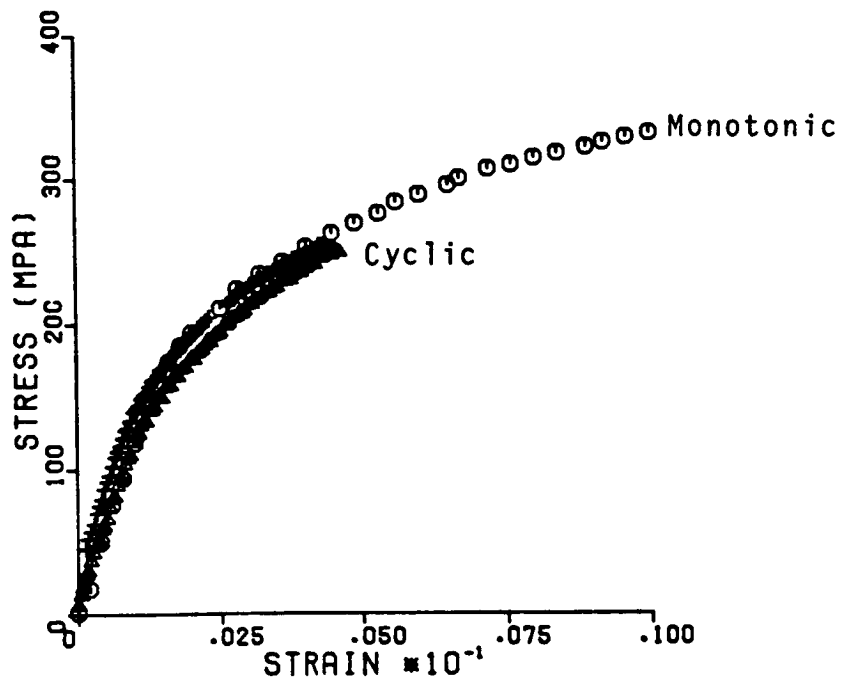Figure 3.9 Comparison of Monotonic and Cyclic Behavior of René 80 at 982°C, $.2M^{-1}$

Figure 3.10 Comparison of Monotonic and Cyclic Behavior of René 80 at 982°C, $.002M^{-1}$
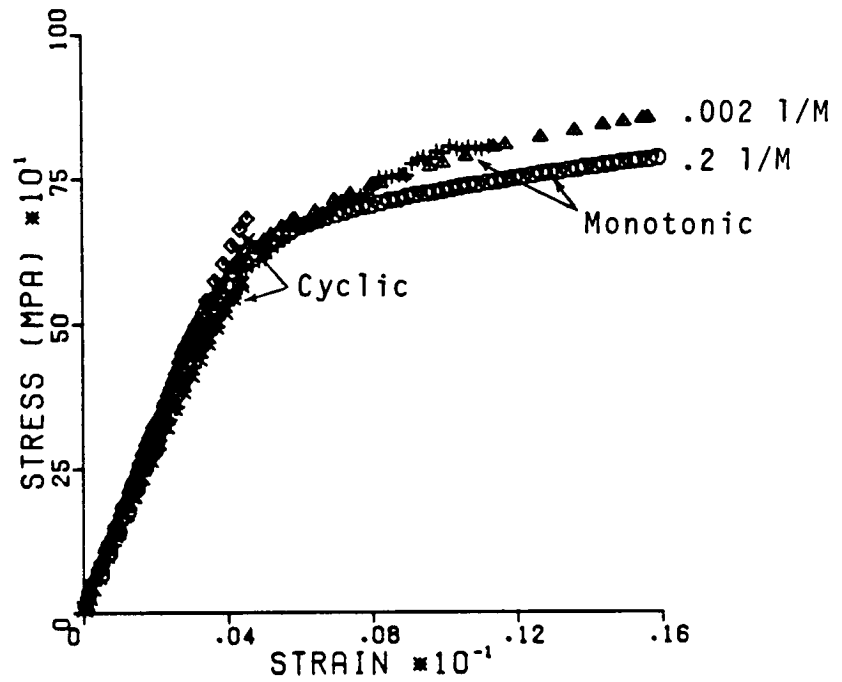
Figure 3.11   Comparison of Monotonic and Cyclic Behavior of
René 80 at 760°C
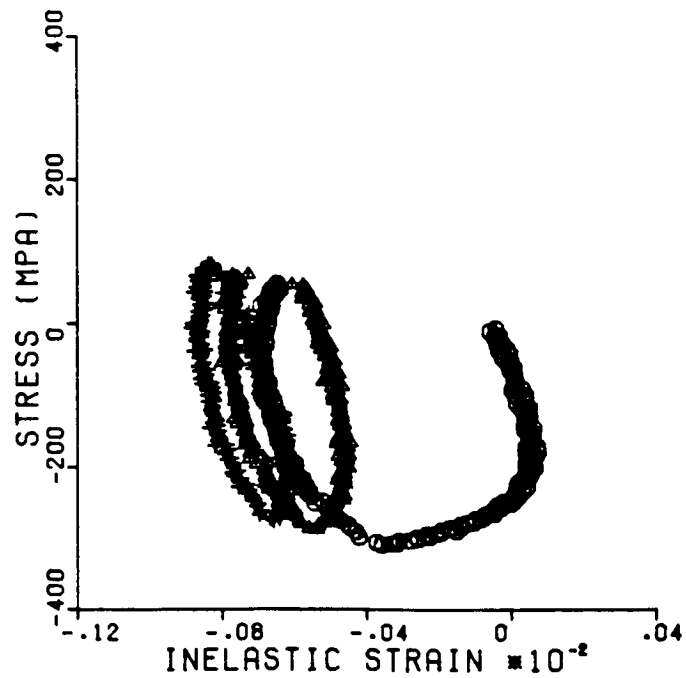
Figure 3.12   Cyclic Mean Stress Relaxation of René 80 at 982°C

3.4 Multiaxial Experiments

In structural components the state of stress and strain may not be uniaxial. Usually a complex three dimensional stress and strain state exists. In the past experimental investigations of three dimensional stress and strain states have been possible for elastic loading using photoelasticity techniques. Even in these studies the cyclic loading conditions which are of primary importance are not possible.

Room temperature biaxial tests have been conducted for a number of years in the experimental investigation of yield surfaces [13]. These usually involve a thin tubular specimen which is loaded simultaneously in tension and torsion or in tension and internal pressurization. Biaxial testing under cyclic loading conditions with independent control of the strain or load in each of the two directions has become possible only recently. Advances in extensometry and computer control have been responsible for sophisticated biaxial tests at high temperatures. These biaxial tests are usually in a tension/torsion mode.

The tension/torsion tests described below were performed by Dr. R. Williams at the Turbine Technology Laboratories of General Electric Company in Schenectady [30]. The axial/torsion extensometer used to measure

63

and control the tensile and shear strains simultaneously was developed by the Instron Corporation. The strain measurements were made using high temperature capacitive displacement gauges. The details of the extensometer are are given in References [26] and [30].

Multiaxial tests were performed at 982°C (1800°F) and 871°C (1600°F). Seven tests were performed at each temperature. Table 3.4 and Figure 3.13 give the details of the torsion and multiaxial tests. At each temperature two torsional cyclic tests were performed to determine the strain rate sensitivity. Strain rates of .002 per minute and .02 per minute were used. Two simple in phase axial/torsion tests were performed with $\epsilon_{xx} = C \cdot \gamma_{xy}$ for C being constant as shown in Figure 3.13a. Another in phase test was done with a 120 second hold at a peak strain point (see Table 3.4).

In analyzing multiaxial behavior, out of phase loading conditions are important. In an effort to harden the material in all possible planes, two types of out of phase tests were performed. These are shown in Figures 3.13b and 3.13c. In Figure 3.13b each block of cycles, such as A-A, is proportional. However, the sequence produces out of phase hardening effects since the maximum shear planes are different for each block. The out of phase test condition shown in Figure 3.13c

Table 3.4 Multiaxial Test Matrix

(For Temperatures of 982°C and 871°C)

Type of Test	Phase Relationship	$\dot{\varepsilon}$ (M⁻¹)	Figure
Torsion		.02,.002	
Tension/Torsion	In Phase (single)	.02,.002	13a
Tension/Torsion	In Phase (multiple)	Variable**	13b
Tension/Torsion	90° Out of Phase	.002	13c
Tension/Torsion 120 second hold*	In Phase	.02	13a

* The hold time is at maximum strain for the 871°C test and at minimum strain for the 982°C test.

** A constant cycle time of 360 seconds for all the cyclic blocks.

65

(a) In Phase, Proportional Loading
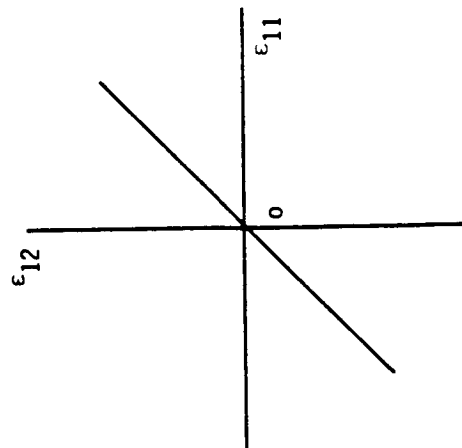
(b) Multiple In Phase, Nonproportional Loading

(c) 90 degree Out of Phase Nonproportional Loading
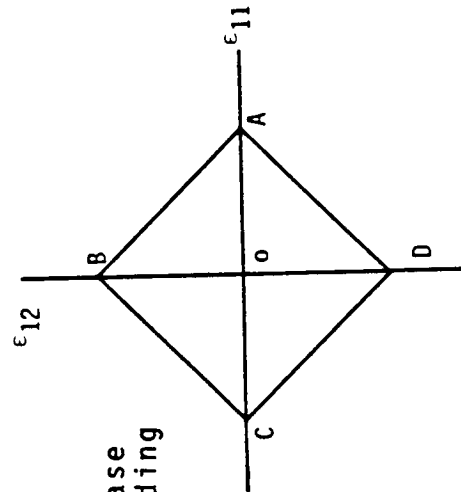
Figure 3.13 Loading Paths for Tension/Torsion Experiments

66

is continuous. The loading condition changes linearly from pure tension at point A to pure shear at point B. The peak strain values at points A and B were chosen such that the octahedral shear strains are the same at these two points. All the multiaxial tests except the multiple proportionality test (see Figure 3.13b) were performed in sequences of cyclic blocks with different strain ranges, similar to the uniaxial experiments.

3.4.1 Results of the Multiaxial Testing Program

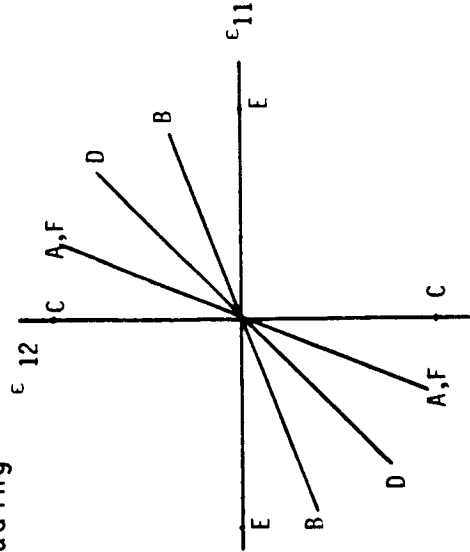Some examples of the experimental results from the torsional and multiaxial tests are given in Figures 3.14 to 3.16. Figure 3.14 shows six hysteresis loops (at the end of each block) from a torsion test at 982°C (1800°F). Three strain ranges of .0024, .0048, and .0072 were used and a strain rate of .002 M $^{-1}$ was maintained. The hysteresis loops coincide exactly for each strain range. This indicates the absence of any cyclic softening or hardening. It is also seen that the hysteresis loops are not symmetrical. The bias in the negative direction remains the same for all loops; therefore, it appears to depend on the initial loading. The bias was present in all pure torsion and in the in

phase tension torsion tests. Figure 3.16 is a typical example.

Only cyclic tests were performed in the torsion mode. Figure 3.15 compares the torsion test results from a number of hysteresis loops. The results are shown as half of the range quantities from the lower tip of the hysteresis loops. The coincidence of this result from various cycles confirms the lack of any cyclic softening or hardening. Recall that the same result was observed for the uniaxial tests at this strain rate (Figure 3.10). The lack of cyclic hardening or softening impies that the torsional cycle stress strain curve shown in Figure 3.15 can be considered as representing the initial torsional load up curve. The monotonic tensile loading response at the same temperature and strain rate is also shown in Figure 3.15 for comparison.

The cyclic hysteresis loops from the first and last block of a multiple in phase tension torsion test are compared in Figure 3.16. They are again coincident indicating the lack of any history effects due to changes in the proportionality factor during testing.
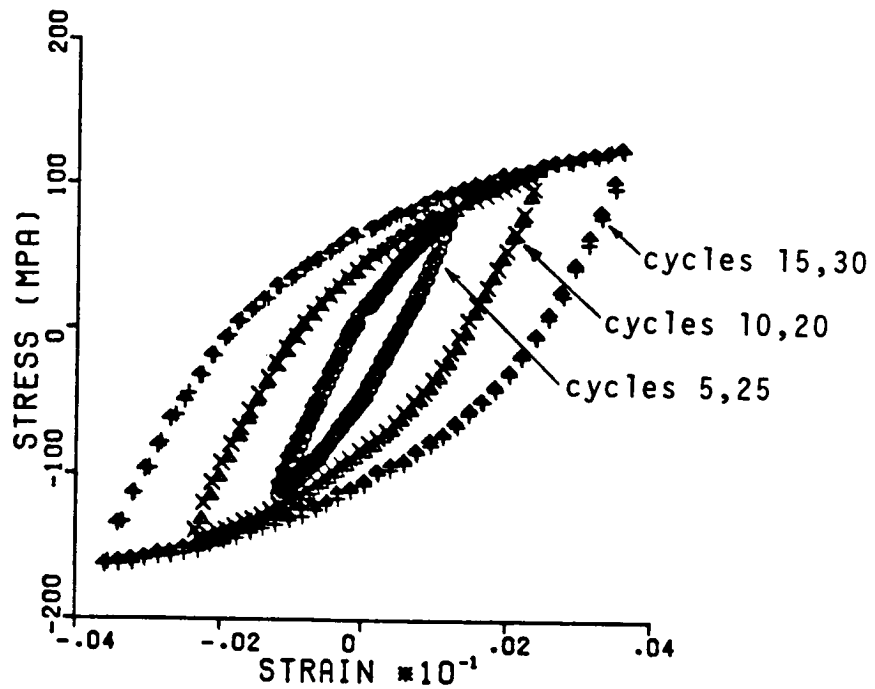
Figure 3.14   René 80 Pure Torsion Cyclic Hysteresis Loops
at 982°C, .002M^{-1}
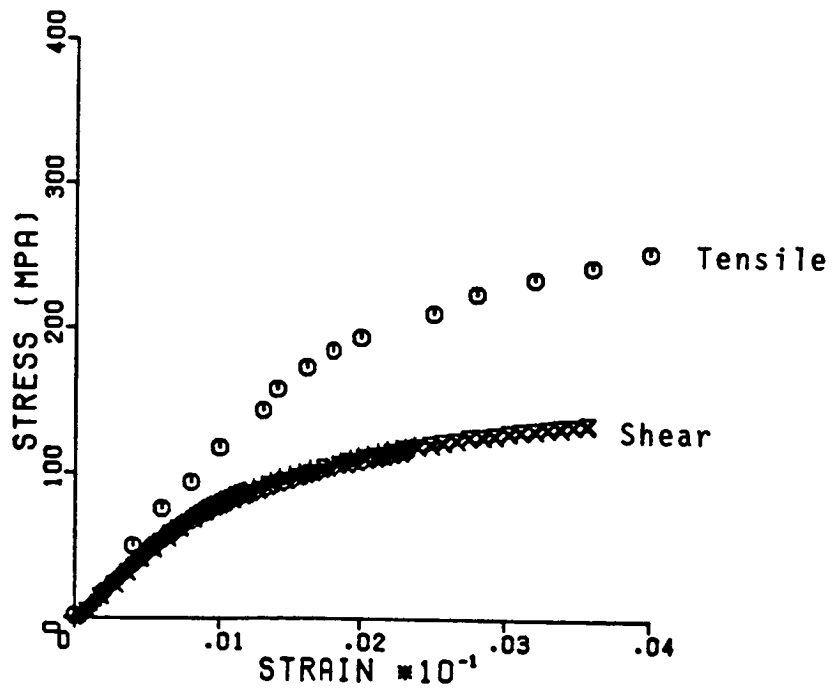
Figure 3.15   Comparison of Monotonic Tensile and Pure Shear
Response of René 80 at 982°C, .002M^{-1}
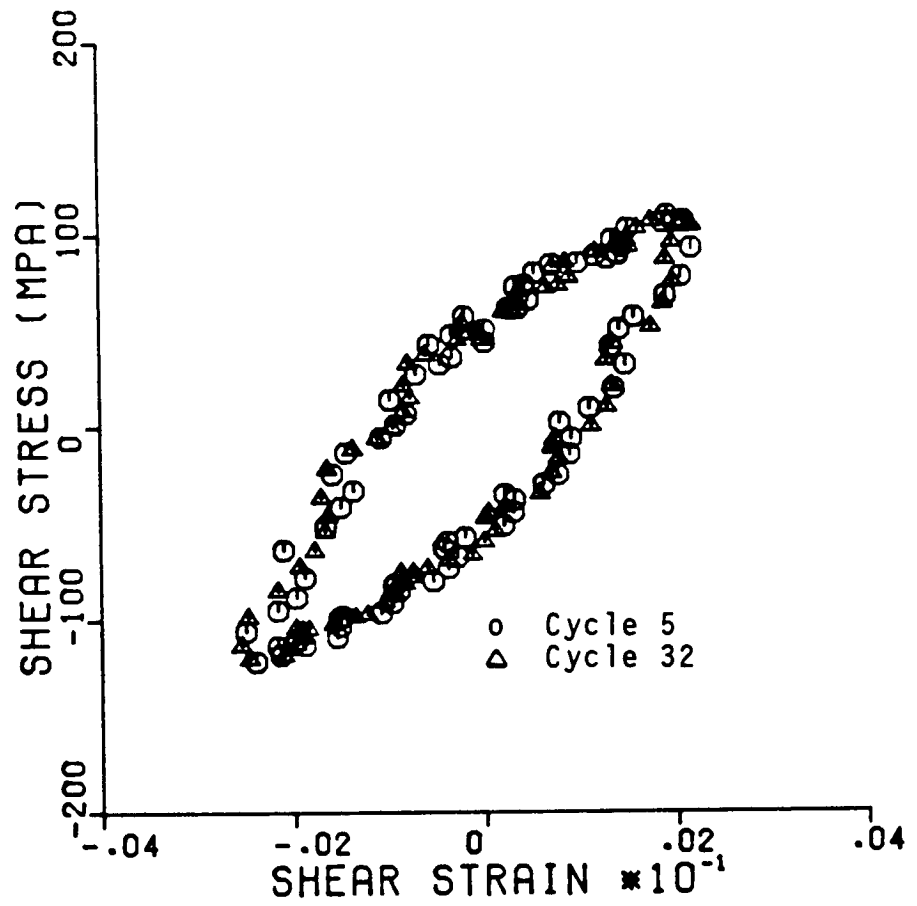
Figure 3.16   Comparison of René 80 Response at 982°C Before and After Nonproportional Loading

3.5 Data Processing

It is desirable to have stress, strain and time data at each instant during an entire test for the development of the constitutive parameters. This will aid in the modeling of both transient and steady state behavior. In uniaxial tensile tests the load-displacement curve was recorded on an X-Y plotter. This curve was later digitized to obtain approximately 100 data points. Since these tests were done at constant strain rate, time was calculated at each point. A similar procedure was used for the initial loading of creep tests. The displacement during creep was also continuously recorded on a strip chart. This displacement versus time plot for the entire test was later digitized.

An automated data acquisition system manufactured by Engineering Technical Services of Champaign, Illinois, was used for recording the cyclic test data. This system sampled and stored data at various points during a cycle. Voltage information related to load, displacement and time was stored in a buffer which was later transferred to tapes. Approximately 200 data points were taken for each cycle. Data was taken for the first three cycles at the beginning of each block

and subsequently for every other cycle. Loops were also recorded periodically on conventional X-Y plotters. These helped to verify the accuracy of the automated data acquisition system.

The load and displacement data were first converted to stresses and strains using the engineering definitions for these quantities. The elastic modulus for each test specimen was determined using the initial part of a stress strain curve. A significant variation in the values for the modulus was observed [26]. The inelastic strain was determined using the calculated modulus for each specimen.

The unified constitutive models usually predict the inelastic strain rate. To determine stress or inelastic strain rate from the test data, the stresses and inelastic strains were numerically differentiated with respect to time at each data point. A second order seven point sliding polynomial proved adequate for this purpose. Accumulated inelastic strain and inelastic work was also calculated. All the data for each specimen was stored on a computer file in a matrix of stress, strain, time, inelastic strain, stress rate, strain rate, inelastic strain rate, accumulated inelastic strain, accumulated inelastic work and cycle number. These computer files were later used for

generating the material parameters related to the constitutive models.

CHAPTER 4

PREDICTION OF RENE´ 80 RESPONSE USING UNIFIED MODELS

The response characteristics of some unified constitutive models were presented in Chapter 2 for a variety of loading conditions. This exercise demonstrated the general capabilities and limitations of the unified models. The study was essentially qualitative in nature due to the lack of a common experimental data base and appropriate material parameters. The materials and temperatures studied were Rene´ 95 and Hastelloy-X at 649°C, 2¼ CrMo Steel at 538°C and Aluminum at 43°C. It is desirable to reevaluate the ability of the unified models to analyze the response behavior of Rene´ 80 described in the previous chapter.

One outcome of the initial study is that the models could be categorized into two general types. The first type, typical of the Walker, Robinson, Krieg et.al. and Miller models, had a tensorial back stress and a scalar drag stress. The second type, like the Bodner model, has a single scalar state variable which is used to model the rate dependent strain hardening effects. In this chapter the merits of the two types of models are evaluated for their ability to predict

74

Rene' 80 response. This will require the evaluation of the material parameters for the models. A long standing difficulty in the application of unified constitutive models is the development of the material constants. This difficulty is alleviated to a certain extent by: (1) proposing a general procedure of material parameter evaluation that is applicable to most of the unified theories; and (2) evaluating parameters for a generic back stress drag stress model, rather than the four individual models, that contains the essential properties of this type of model.

4.1   Generic Back Stress Drag Stress Model

The various back stress drag stress models have different functional forms in their flow and evolution equations. There are also differences in the dynamic and static recovery terms. It appears that the functional forms in the different models were selected for modeling a specific material or class of materials. However, there are striking similarities in the general structure of the flow and evolution equations in the various back stress drag stress models. This has also been observed by Walker [14] and Lindholm [27]. The essential structure of the constitutive models can be characterized for uniaxial loading as:

75

$$\dot{\varepsilon}^I = F(\sigma, \Omega, Z, T) \tag{4.1}$$

$$\dot{\Omega} = f_1 \dot{\varepsilon}^I - f_2 \Omega |\dot{\varepsilon}^I| - R_1 \tag{4.2}$$

$$\dot{Z} = g_1 |\dot{\varepsilon}^I| - g_2 Z |\dot{\varepsilon}^I| - R_2 \tag{4.3}$$

where $\Omega(0)=0$ and $Z(0)=Z_0$ are the initial conditions. Equation 4.1 is the flow equation and Equations 4.2 and 4.3 are the evolution equations for the back stress, Ω, and the drag stress, Z, respectively. The first term in Equations 4.2 and 4.3 is for modeling hardening and the second term is for dynamic recovery of the state variables. The third term is a static thermal recovery term which is operative in long time predictions. There does not appear to be any consistency in the structure of the static thermal recovery terms R_1 and R_2. Further, the drag stress is frequently held constant, $\dot{Z}=0$, in many applications.

In order to keep the study of back stress drag stress approach as general as possible, it is proposed to retain the general framework of Equations 4.2 and 4.3. No specific functional forms for f_1, g_1, etc. will be assumed a priori. Experimental data will be examined in the framework of Equations 4.1, 4.2 and 4.3

and a choice of functional forms will be made on this basis. Such a model will be referred to as a "generic back stress drag stress model" in the following sections.

Stouffer and Bodner [21] have demonstrated a technique of obtaining a state variable history during any particular test by inverting the flow equation. Many of the back stress drag stress models proposed have a power law type of flow equation that is invertible. Thus, let us assume

$$\dot{\varepsilon}^I = D\left(\frac{|\sigma - \Omega|}{Z}\right)^n \frac{(\sigma - \Omega)}{|\sigma - \Omega|}. \tag{4.4}$$

Equations 4.2, 4.3, and 4.4 constitute the generic back stress drag stress model.

4.2 Determination of the Material Parameters

The long time static thermal recovery terms R_1 and R_2 in Equations 4.2 and 4.3 can be neglected for short duration tests such as monotonic tensile tests at high strain rates. When static thermal recovery effects are neglected the uniaxial scalar equation for the drag stress becomes

$$\dot{Z} = (g_1 - g_2 Z) |\dot{\epsilon}^I|. \tag{4.5}$$

This equation can be integrated to give

$$Z = Z_1 + (Z_0 - Z_1) e^{-g_2 \Sigma \epsilon^I} \tag{4.6}$$

where $\Sigma \epsilon^I$ is the accumulated inelastic strain from the beginning of the test and Z_0 and Z_1 are the initial and final values, respectively, of the drag stress . In most of the back stress drag stress models, the drag stress controlled the cyclic hardening or softening behavior, as described in Chapter 2. The stable condition is reached after cyclic hardening or softening when $\dot{Z} = 0$. Then Equation 4.5 reduces to the saturated value of the drag stress $Z_1 = g_1/g_2$. The initial condition is $Z(0) = Z_0$ and g_2 represents the rate of cyclic hardening or softening. The parameters Z_0, Z_1, and g_2 are assumed to be material constants at a particular temperature.

The accumulated inelastic strain is small for uniaxial tensile tests in comparison with the value from cyclic tests. Thus, the drag stress is almost constant and equal to the initial value in these tests. Further at about 2% strain the stress strain curves become flat; thus, at saturation $\dot{\sigma} = \dot{Z} = \dot{\Omega} = 0$ and $\dot{\epsilon}^I \approx \dot{\epsilon}$. If σ_0 and Ω_0 are the saturated values of the applied

78

stress and back stress respectively, Equation 4.4 for the tensile saturated condition becomes

$$\dot{\varepsilon}_0^I \simeq \dot{\varepsilon}_0 = D \left(\frac{\sigma_0 - \Omega_0}{Z_0} \right)^n .$$

(4.7)

If a number of monotonic tensile tests are performed to saturation at various constant strain rates the values of Ω_0, Z_0 and n can be determined. Equation 4.7 becomes

$$\ln \dot{\varepsilon}_0^I = n \ln(\sigma_0 - \Omega_0) - n \ln Z_0 + \ln D$$

(4.8)

which can be used in a nonlinear regression analysis to minimize the error between the left and right hand sides.

To determine the back stress history for the monotonic tensile tests, the flow equation was inverted to give

$$\Omega = \sigma - Z \{ \dot{\varepsilon}^I \}^{\frac{1}{n}} .$$

(4.9)

Since $Z \simeq Z_0$ and the stress, σ, and inelastic strain rate, $\dot{\varepsilon}^I$, are known at each point during the test the back stress, Ω, can be calculated throughout a test. This ability to determine the history of the state

79

variables during a test is the real advantage of the method. Once the back stress, Ω, is known during the test it is possible to estimate the back stress rate at each point in the history. The data (stress, strain, time) were collected at a large number of time points during all the tests. This made numerical differentiation of the back stress (or any other quantity) possible using a seven point sliding function technique. It was found that the function $\Omega = At^b$ gave the best estimate. The constants A and b were reevaluated at each time point. There is, however, one inherent difficulty. The inelastic strains and inelastic strain rates cannot be measured with confidence during the initial loading phase of the history. Thus, the back stress, Ω, and its rate, $\dot{\Omega}$, are known only from the yield point. A typical example of the calculated response for the back stress, Ω, and back stress rate, $\dot{\Omega}$, are shown in Figures 4.1 and 4.2. Notice that $\dot{\Omega}$ becomes very small near saturation.

Knowing the behavior of Ω and $\dot{\Omega}$ during tensile tests makes it possible to evaluate the material parameters in Equation 4.2. Neglecting the static recovery, R_1, Equation 4.2 can be written as follows:

$$\frac{\dot{\Omega}}{\dot{\epsilon}^I} = f_1 - f_2 \Omega. \tag{4.10}$$

Since Ω, $\dot{\varepsilon}^I$ and $\dot{\Omega}$ are known a plot of $(\dot{\Omega}/\dot{\varepsilon}^I)$ versus the back stress (Ω) can be constructed as shown in Figure 4.3. The data from the four monotonic tensile tests, varying in strain rate from .2 M^{-1} to .002 M^{-1}, tend to cluster around a straight line. Thus, f_1 and f_2 in Equation 4.10 can be treated as being material constants at 982 °C and can be determined.

At this point in the development the material parameters related to the flow equation (4.4) and the back stress evolution equation (4.2) have been determined. Recall that the calculation of the back stress, Ω, in a tensile test required the assumption that the drag stress is constant. This assumption can now be relaxed. The back stress, Ω, can be calculated by integrating Equation 4.2 with known values of f_1 and f_2. Equation 4.4 is inverted to obtain

$$Z = \frac{|\sigma - \Omega|}{|\dot{\varepsilon}^I|^{\frac{1}{n}}}. \tag{4.11}$$

Using Equation 4.11 the value of Z is calculated during a test using the measured values for stress, σ, and inelastic strain rate, $\dot{\varepsilon}^I$, and the integrated value for the back stress, Ω. The constants Z_1 and g_2 in the drag stress equation (4.6) can be evaluated using
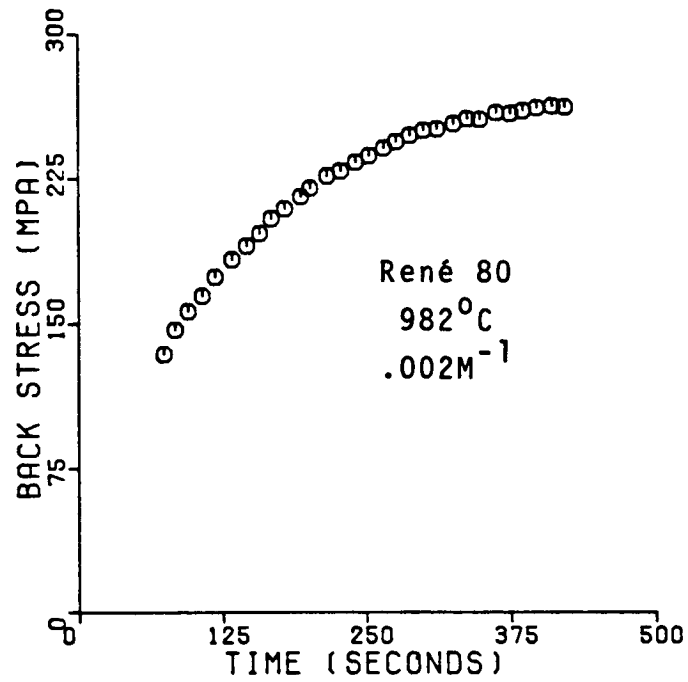
Figure 4.1   Back Stress Calculated from Experimental Data
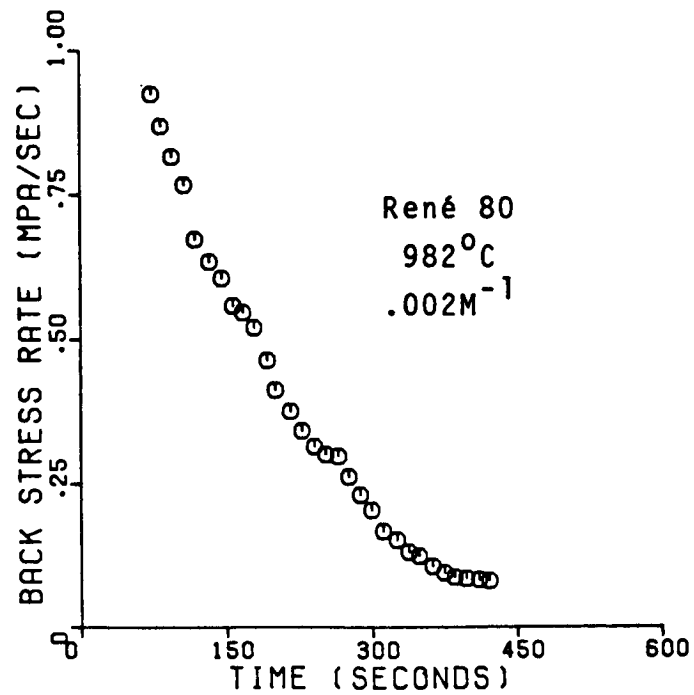

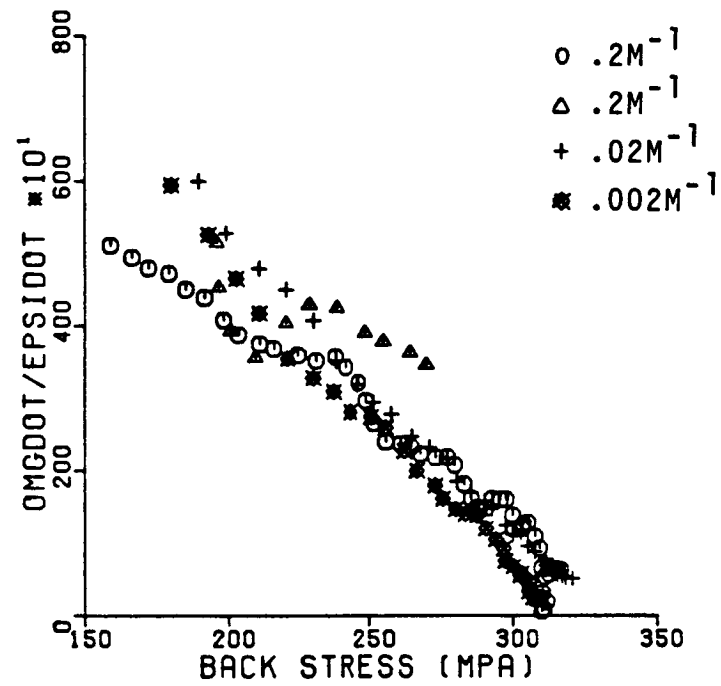Figure 4.2   Back Stress Rate Calculated from Experimental Data

Figure 4.3   Determination of Functional Forms of f_1, f_2

nonlinear regression of the data from monotonic and cyclic tests.

It is now possible to return to Equation 4.9 and calculate new values for the back stress, Ω, using the calculated variation of Z during a test. The process can be repeated until stable values are achieved. This procedure is shown in Figure 4.4 for the entire process of constant evaluation. The material parameters were evaluated using the computer code implementing the scheme described above. Five iterations were usually adequate. The scheme was applied separately for two tensile and two cyclic tests at strain rates of $.2M^{-1}$ and $.002M^{-1}$ as shown in Table 4.1.

4.3   The Generic Back Stress Drag Stress Model Results

The generic back stress drag stress model was used to calculate the tensile response for each test using the constants for that test as shown in Figure 4.5. Excellent agreement was obtained since the constants were determined separately for each test. These results verify that the constant evaluation procedure works very well. Cyclic calculations were made for the same strain rates using the constants from the monotonic $.2\ M^{-1}$ and $.002\ M^{-1}$ tests, respectively. The results are compared in Figure 4.6. The test results
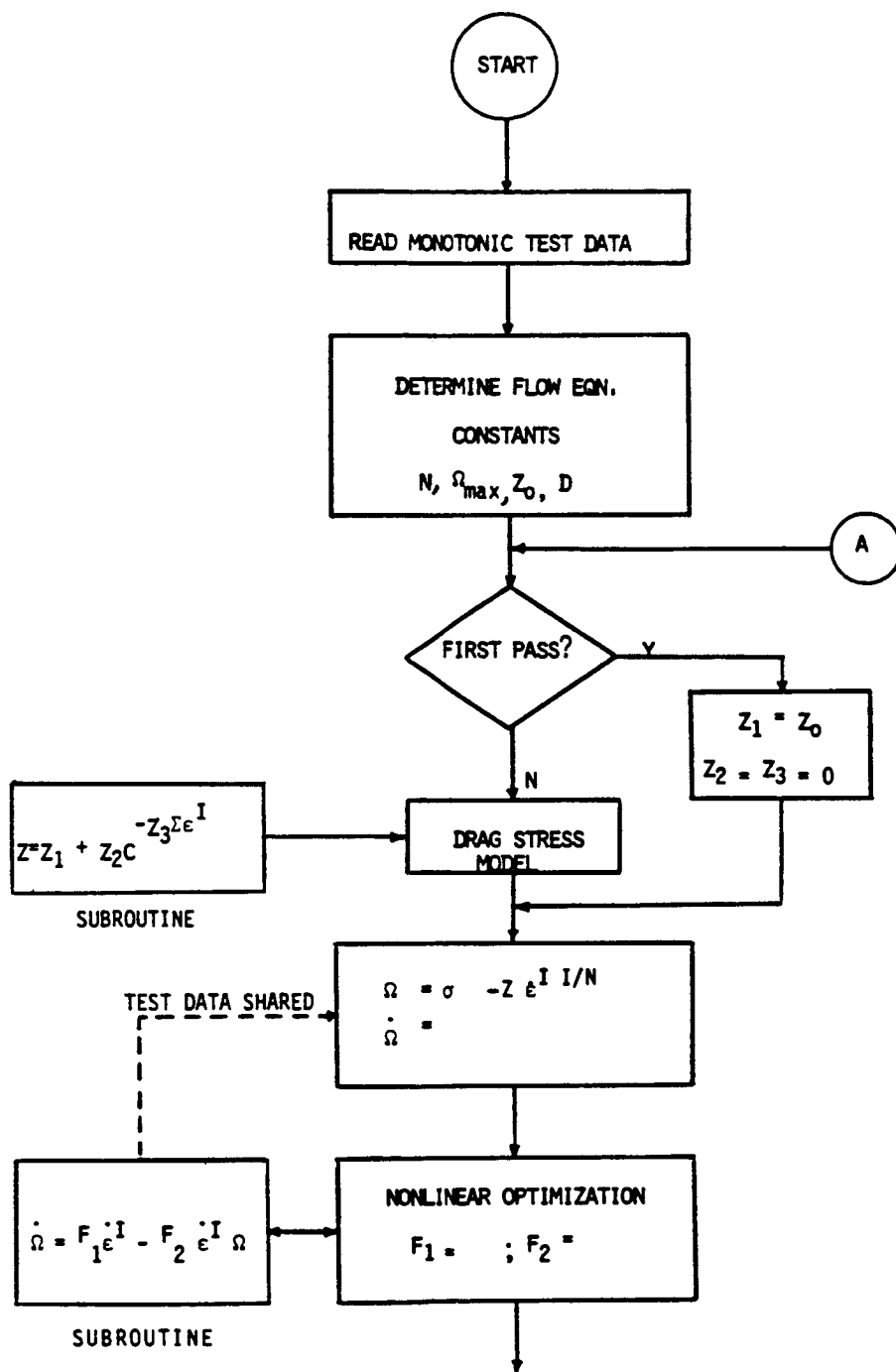
Figure 4.4   Schematic of Material Parameters Determination
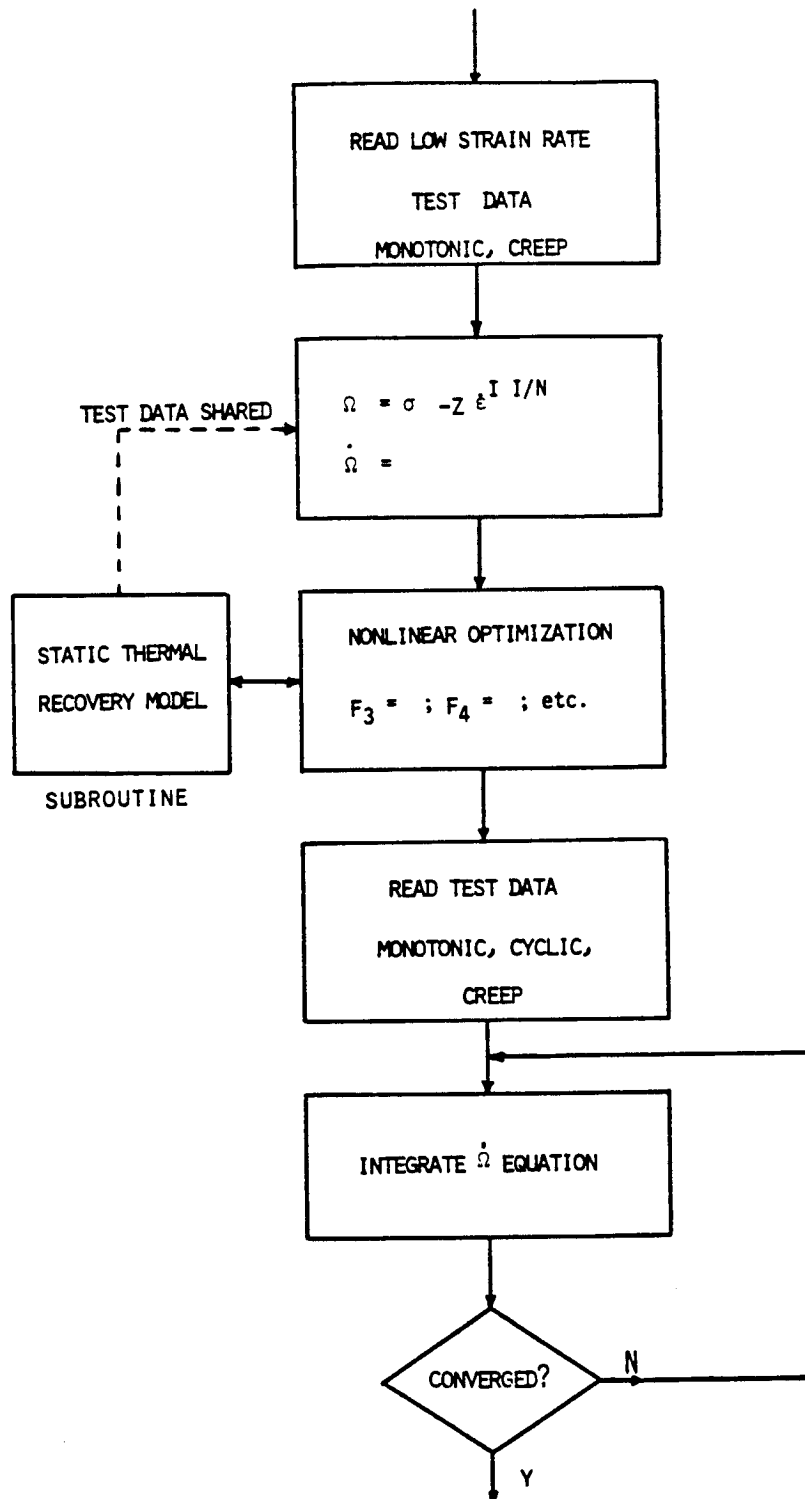Procedure (Part 1 of 3)

85

Figure 4.4   Schematic of Material Parameters Determination
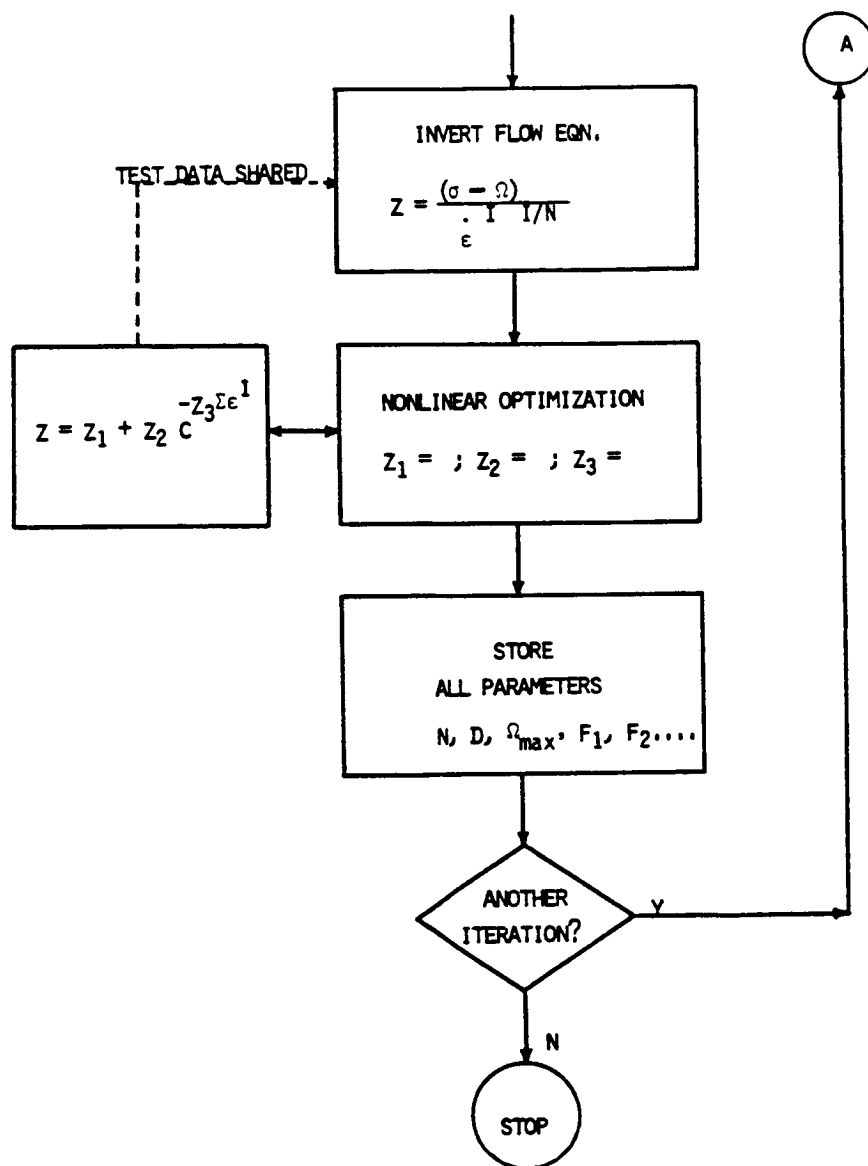Procedure (Part 2 of 3)

86

Figure 4.4 Schematic of Material Parameters Determination
Procedure (Part 3 of 3)

TABLE 4.1

MATERIAL CONSTANTS FOR RENE' 80, 982°C

(a) Generic Back Stress Drag Stress Model

Constant	Based on Monotonic Tests		Based on Cyclic Tests		Based on All Tests
	$.2M^{-1}$	$.002M^{-1}$	$.2M^{-1}$	$.002M^{-1}$	$.2M^{-1} \& .002M^{-1}$
$D_0(s^{-1})$	1.59	1.59	1.59	1.59	1.59
n	2.44	2.44	2.44	2.44	2.44
$f_1(MPa) \times 10^4$	5.6	7.75	19.8	4.1	6.02
f_2	140.2	234.5	845.6	242.8	173.0
$Z_0(MPa)$	955	2860	189	2287	1064
$Z_1(MPa)$	344	350	189	2287	107
g_2	93.2	212.3	0	0	44.4

(b) Bodner Model

$Z_0 = 8613 MPa$ $M = .6154 \ MPa^{-1}$ $n = .2853$

$Z_1 = 15141 MPa$ $A = .6793 \ s^{-1}$ $D_0 = 10^4 \ s^{-1}$

$Z_2 = 12058 MPa$ $r = 3.563$
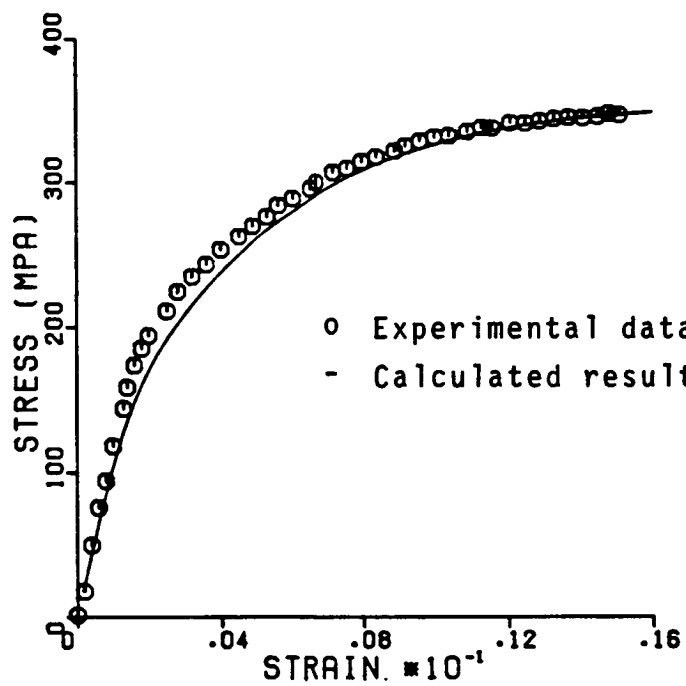
(a) .002M^{-1}, 982°C
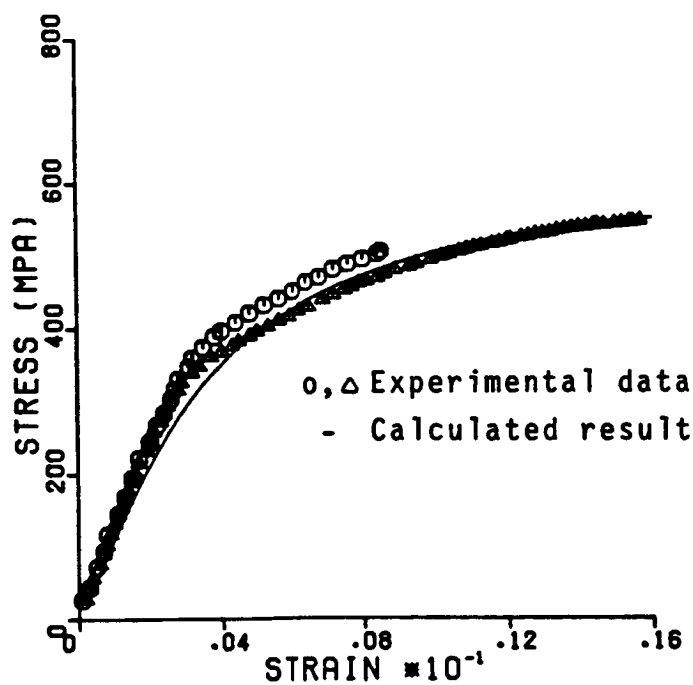
(b) .2M^{-1}, 982°C

Figure 4.5 Verification of Constant Evaluation Procedure

89

C-2

shown are at cyclic saturation; whereas, the calculations are for the first few cycles and the saturated cycle. The model displays cyclic softening behavior as in the tests. The qualitative properties of the model appear good, although the inelastic strains are considerably under predicted for the low rate test.

It is necessary to further investigate the cyclic capability of the generic back stress drag stress model. This was done using the same approach but with the constants based on the cyclic test data. The calculated results for each test at strain rates of .002 M^{-1} and .2 M^{-1} were excellent. The test data and calculations are shown in Figure 4.7 for $Z=Z_1=$constant since the results shown are for cyclic saturation. This further verified the cyclic capability of the model and the material constant evaluation procedure.

The previous calculations were limited in scope. Each strain rate and loading condition was treated separately. However, a constitutive model should apply for any kind of loading conditions and strain rates at each fixed particular temperature. Thus, it should be applicable for all the strain rate tests. The parameters for the generic back stress drag stress model were determined using the five monotonic tensile tests at 982°C. The material parameters, evaluated
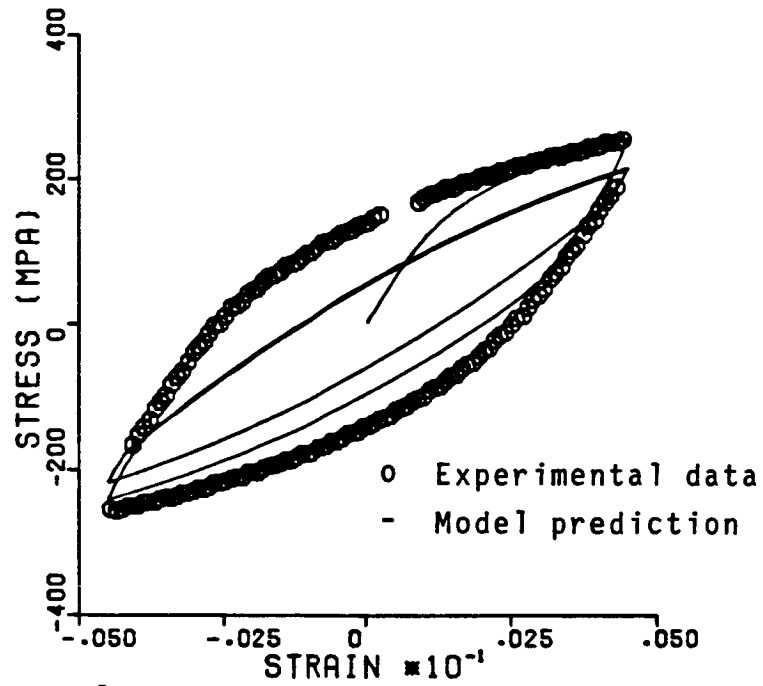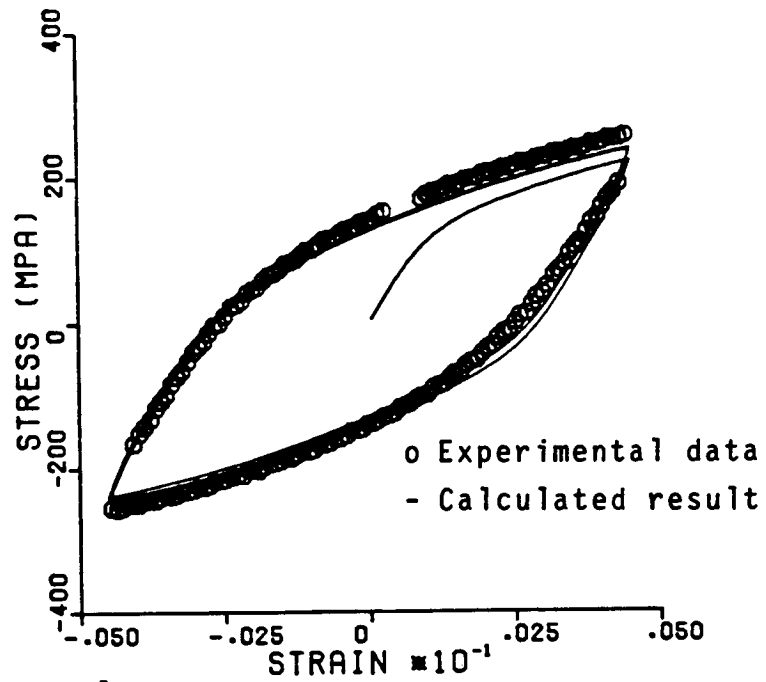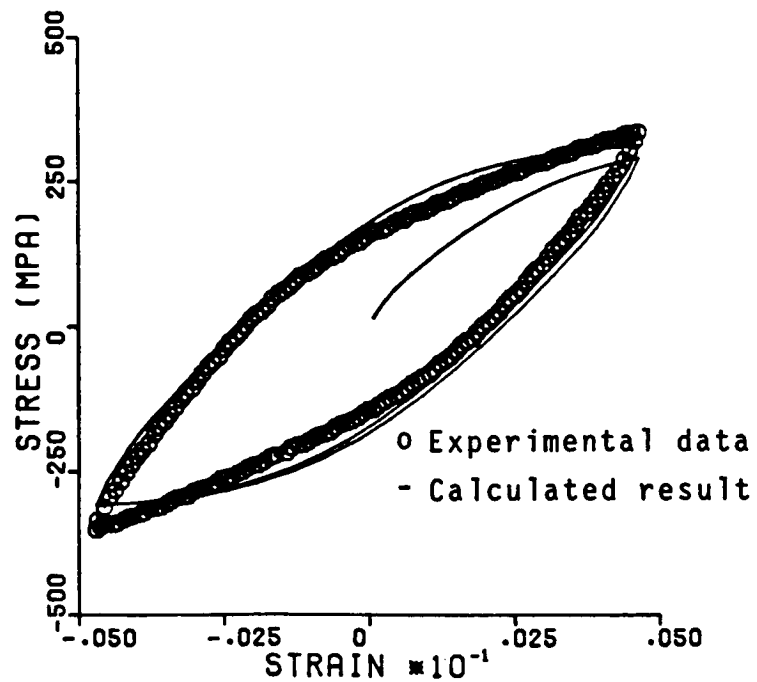
(a)   .002M^{-1}, 982°C
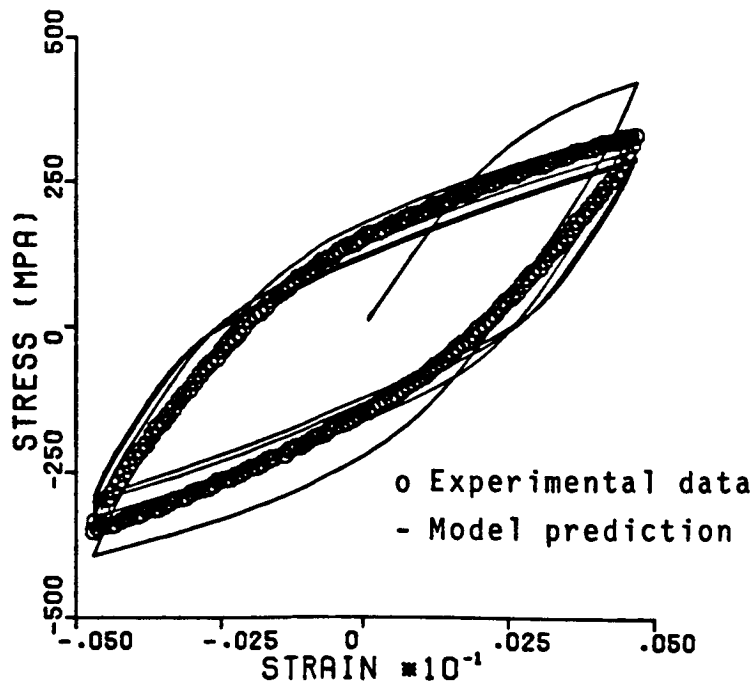
(b)   .2M^{-1}, 982°C

Figure 4.6 Cyclic Predictions of Generic Back Stress Drag
Stress Model Based on Monotonic Data

91

(a) .002M^{-1}, 982°C

(b) .2M^{-1}, 982°C

Figure 4.7   Cyclic Predictions of Generic Back Stress Drag
Stress Model Based on Cyclic Data

92

from these tests, were used to calculate the response for the tensile tests. Although the model was good for a particular strain rate (Figure 4.5), it is not good for the entire set of strain rates as shown in Figure 4.8. This is an inadequacy in the model. Notice in Table 4.1 that the material parameters related to the drag stress are significantly different among the various cases analyzed.

In summary, the generic back stress drag stress model appears to have the right tendencies for the cyclic behavior modeling. However, it has poor tendencies for modeling strain rate sensitivity in the monotonic tensile response.

4.4 Evaluation of the Bodner Model

The Bodner model was selected for study mainly based on its simplicity. It has only one state variable and fewer material parameters. The uniaxial form of the Bodner model as proposed in References [20-22] is

$$\dot{\varepsilon}^I = \frac{2}{\sqrt{3}} D_0 \exp\left\{ \frac{-n+1}{2n} \left(\frac{Z}{\sigma}\right)^{2n} \right\} \frac{\sigma}{|\sigma|} \qquad (4.12)$$

$$\dot{Z} = m(Z_1 - Z)\dot{W}^P - AZ_1 \left(\frac{Z-Z_2}{Z_1}\right)^r \qquad (4.13)$$
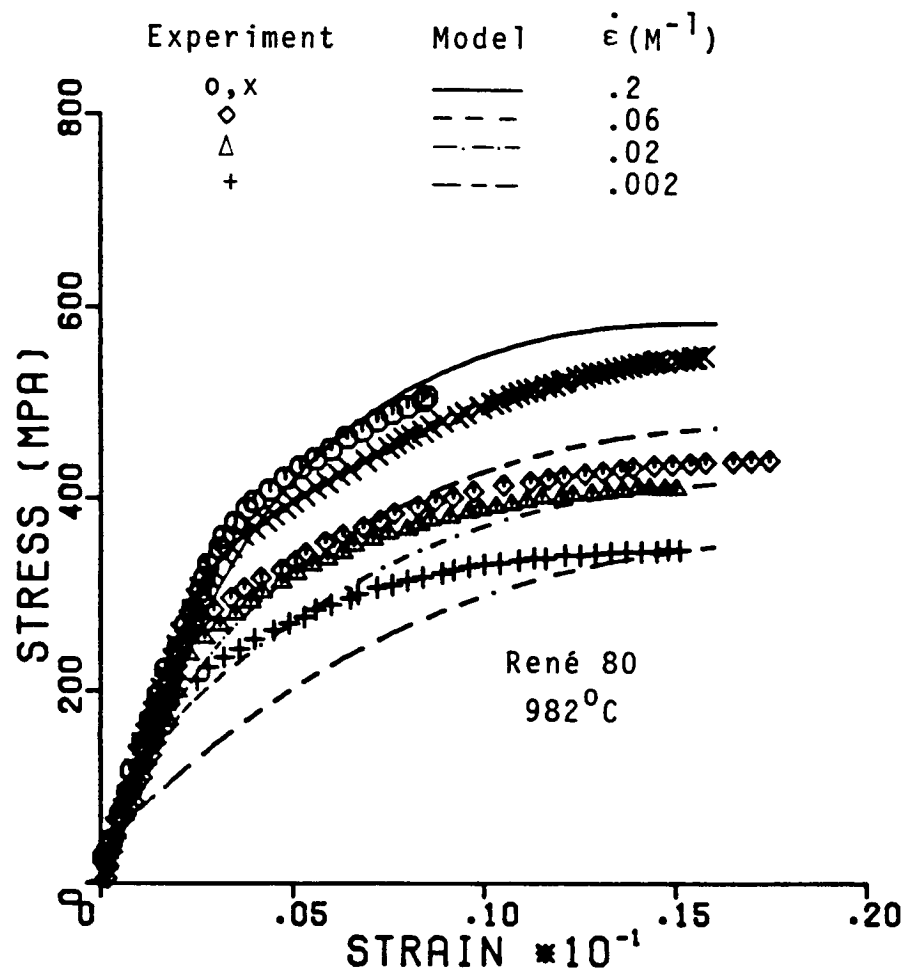
Figure 4.8   Monotonic Tensile Predictions Using Generic
              Back Stress Drag Stress Model

A method of evaluation of the material parameters for this model has been discussed in Reference [21]. The flow equation (4.12) can be inverted easily. Since σ and $\dot{\varepsilon}^I$ are known from experimental data, the history of Z can be calculated. This model fits very easily in the scheme of material parameter evaluation outlined in Section 4.2. The back stress is absent and the scalar state variable Z in the Bodner model is treated as the drag stress. The structure of the evolution equation (4.13) is similar to that for the uniaxial form of the back stress evolution equation (4.2). The major difference is that the inelastic work rate, $\dot{W}^P$, rather than the inelastic strain rate, $\dot{\varepsilon}^I$, is used to control hardening.

The computer code was modified and used to evaluate all the material parameters in Equations 4.12 and 4.13. The limiting strain rate, D_0, was chosen as 10^4 per second and m and Z_1 were determined from the high strain rate monotonic tensile tests. Since A, Z_2 and r characterize static thermal recovery, these parameters were found from the low strain rate tensile and creep tests using

$$AZ_1 \left(\frac{Z-Z_2}{Z_1} \right)^r = \dot{Z} - m(Z_1-Z)\dot{W}^P .$$ (4.14)
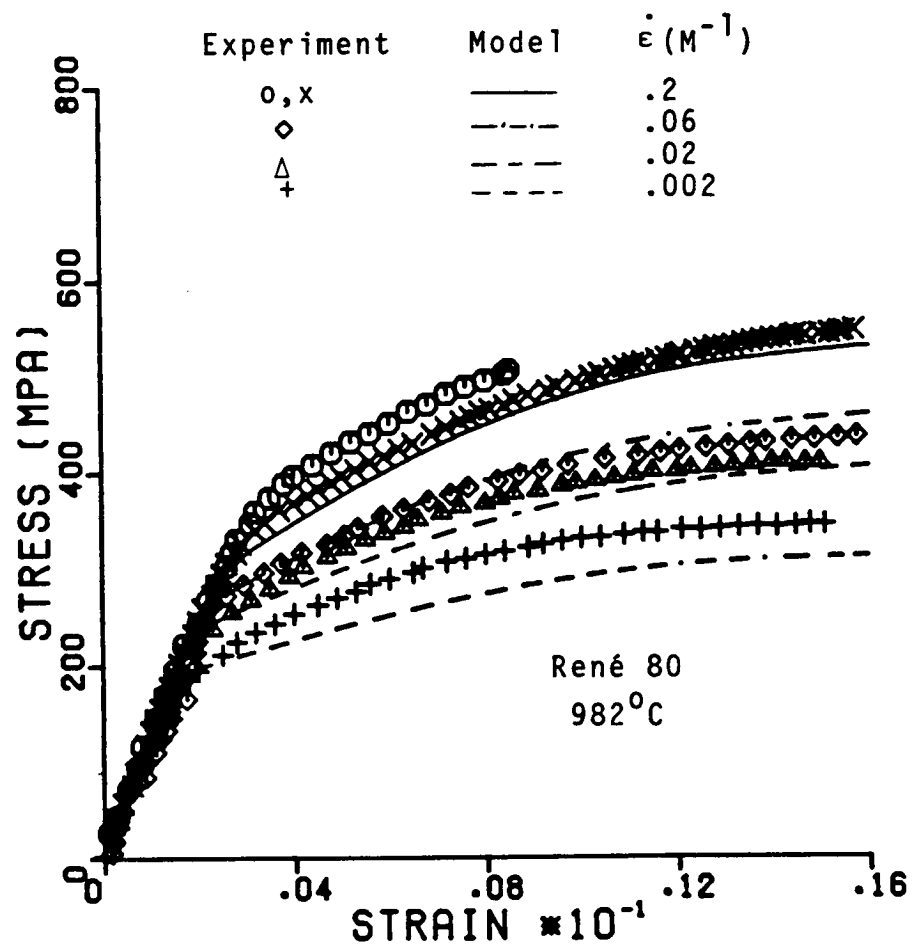
Figure 4.9   Monotonic Tensile Predictions Using Bodner Model

Since only one state variable is involved in the model the iteration procedure was not necessary for material parameter evaluation.

Using the material parameters evaluated as described above (see Table 4.1), the monotonic and cyclic capabilities of the model were evaluated. Figure 4.9 shows the experimental and calculated results for uniaxial tensile tests of Rene' 80 at 982°C (1800°F). The results are significantly better than those shown in Figure 4.8. The model seems to be able to span the strain rate range of .002 M^{-1} to .2 M^{-1} very well and the shape of the calculated curves match the experimental results relatively well.

The cyclic capabilities of the model were checked for strain rates of .002 M^{-1} and .2 M^{-1}. The experimental and calculated results using the Bodner model are shown in Figure 4.10. The model appears to be poor in predicting the cyclic response, especially at the high strain rate. The predicted cyclic hardening follows from the strain hardening in the tensile test; whereas, Rene' 80 is observed to cyclically soften at 982°C. This appears to be a problem in the Bodner model as proposed in References [19,20] since only one scalar state variable is used to predict both strain hardening and cyclic hardening or softening.

During the course of this investigation Bodner [27] has modified his model. The revised model has both an isotropic and directional state variable

$$Z = Z^I + Z^D \qquad\qquad (4.15)$$

where Z^D depends on a tensorial internal variable β_{ij}. Evolution equations are propsed for Z^I and β_{ij} in a form similar to Equation 4.13. The use of the kinematic variable β_{ij} is intended to replace the use of a kinematic back stress. A limited evaluation of this was made using some material parameters approximated from earlier results.

The addition of the kinematic variable β_{ij} appears to improve the cyclic capability of the model as shown in Figure 4.11, for the saturated cyclic case when $Z^I = Z_1$ (a constant). A new prediction program was developed using both Z^I and Z^D for the results shown in Figure 4.11. It was observed that for the fully reversed cyclic loading conditions the variation of the state variable Z was not continuous as shown in Figure 4.12. The state variable Z shows distinct discontinuities at points where the stress, σ, changes its sign. Jumps in the value of Z appear to be an artifact of the model itself and not due to physical changes in the material microstructure or deformation mode.
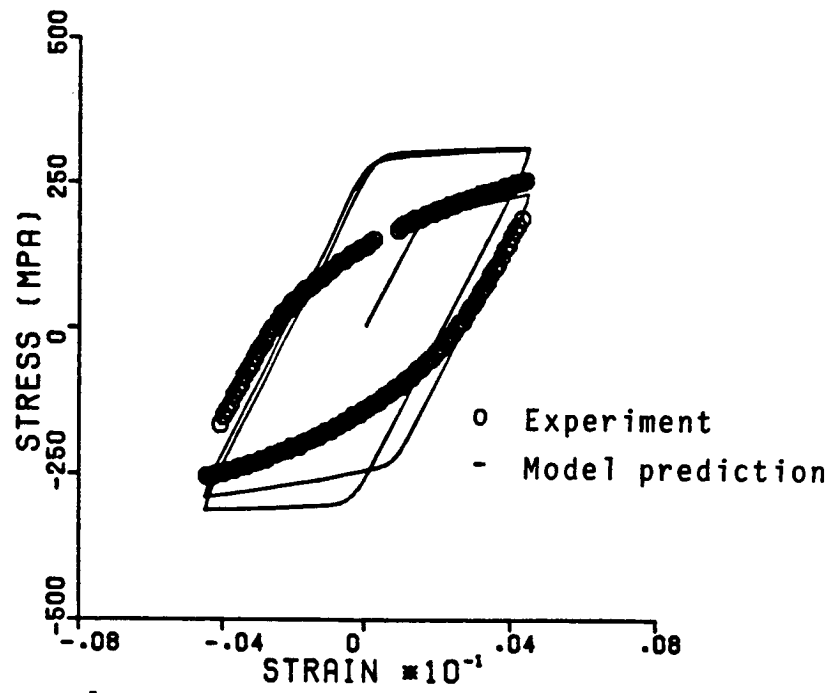
(a) .002M^{-1}, 982°C
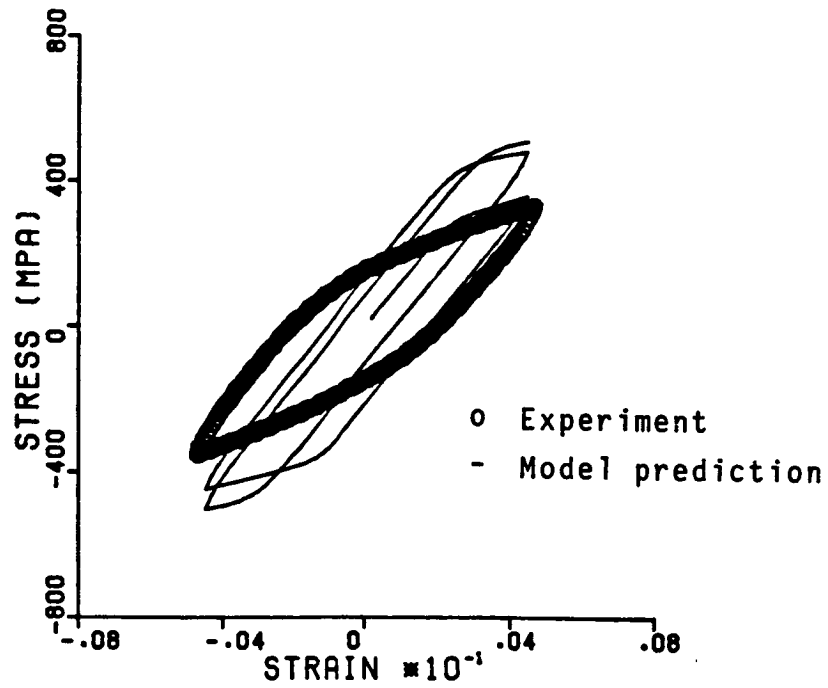
(b) .2M^{-1}, 982°C

Figure 4.10 Cyclic Predictions Using Bodner Model
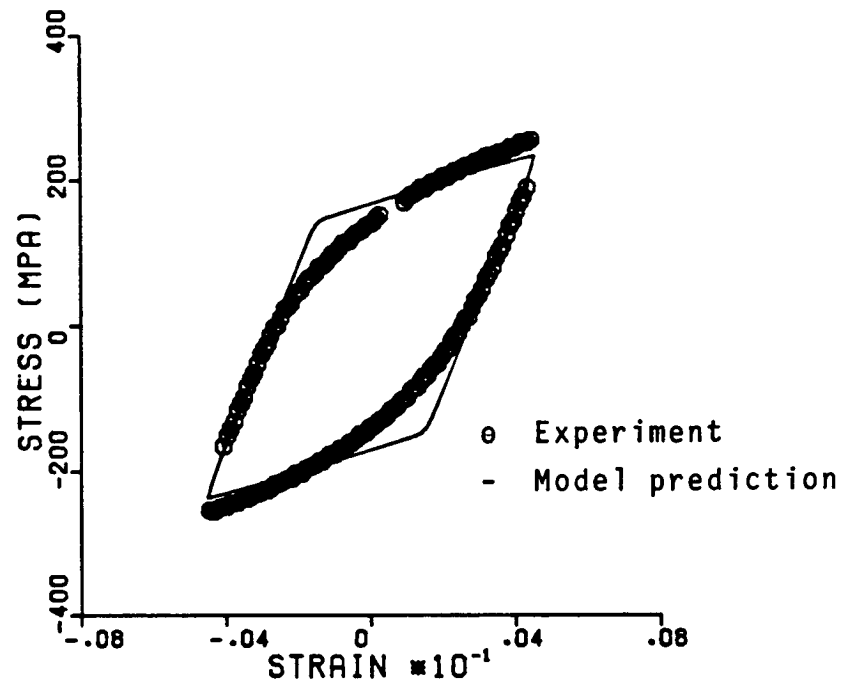
(a) .002M^{-1}, 982°C
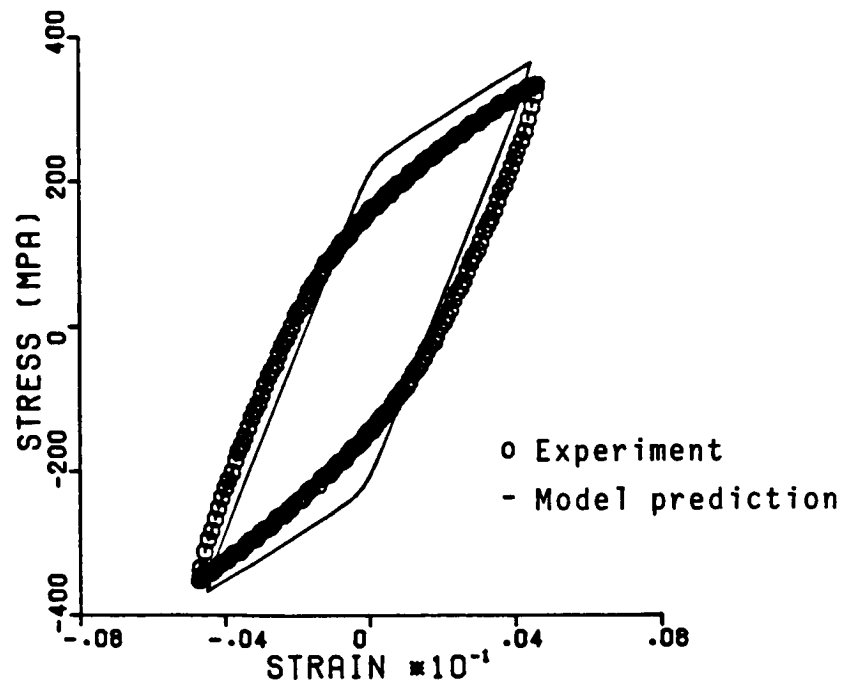
(b) .2M^{-1}, 982°C

Figure 4.11   Cyclic Predictions Using New Bodner Model

100
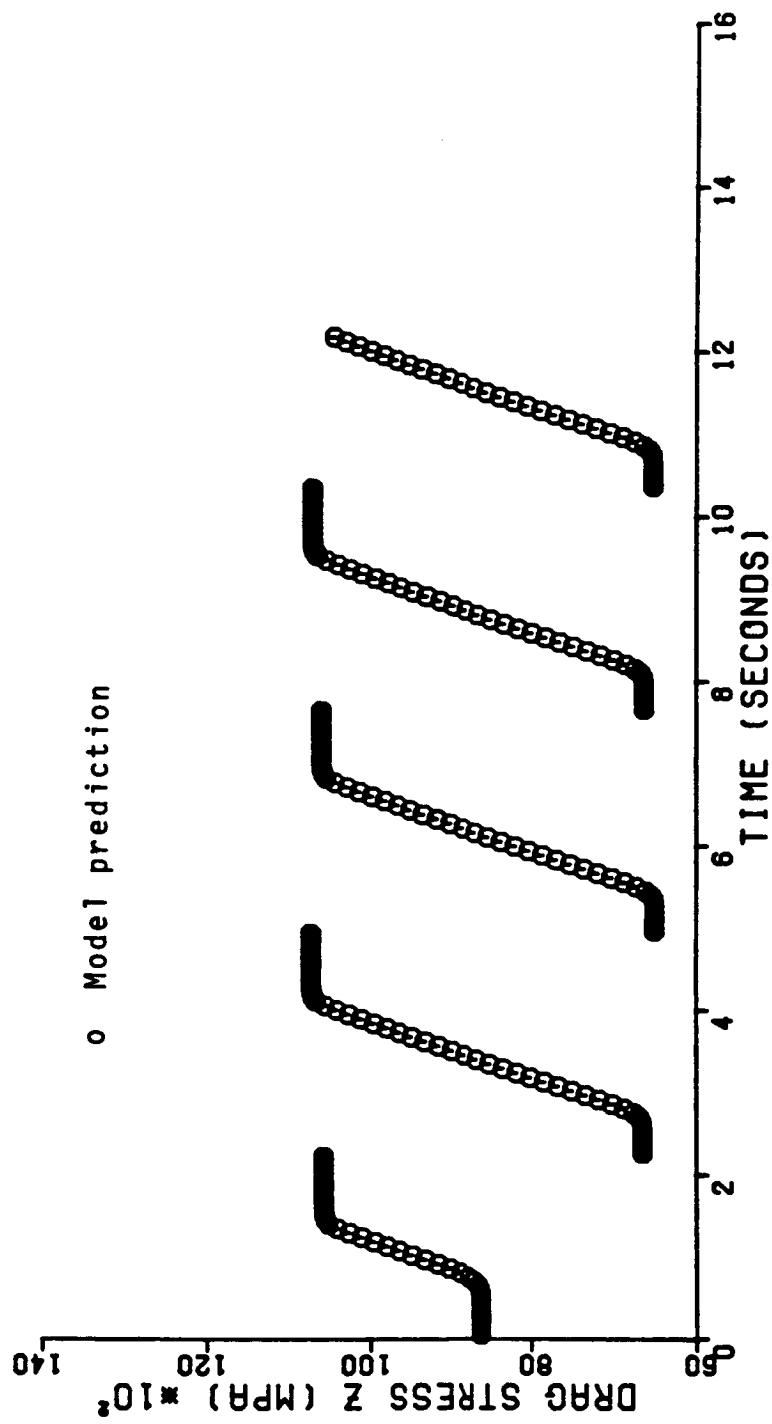
Figure 4.12 Variation of the State Variable (Z) in the New Bodner Model

4.5 Summary of the Evaluations

The previous study was to evaluate in detail the uniaxial capabilities of two types of unified models for the behavior of Rene´ 80 at 982°C. The generic back stress drag stress model appears to have good characteristics for representing cyclic hardening and softening behavior. However, it performed poorly for the monotonic tensile loading tests over the range of strain rates from .002 M^{-1} to .2 M^{-1}. The Bodner model had much better monotonic tensile capabilities, but the cyclic behavior was not adequate. It appeared unable to represent strain hardening in the monotonic tests and softening in the cyclic tests. Thus, it appears that neither of these two models will be completely adequate for representing Rene´ 80 behavior for a wide range of operating conditions.

CHAPTER 5

FORMULATION OF A NEW UNIFIED CONSTITUTIVE MODEL

The experimental results for Rene´ 80 at 982 °C in the previous chapter showed that the generic back stress drag stress model and the Bodner model are not totally adequate for characterizing this material. Each model had some desirable characteristics for specific types of loading conditions. It is necessary that the constitutive equation predicts both monotonic and cyclic behavior. The model should have the correct strain rate behavior at both high and low temperatures. In addition, the equations must be applicable for both proportional and nonproportional multiaxial loading conditions.

This chapter contains a description of the development of a new constitutive model. The development is based on uniaxial isothermal response of Rene´ 80. The primary emphasis is on predicting both the monotonic and cyclic behavior. The isothermal model is extended to other temperatures in Chapter 6. The equations are developed in multiaxial form, and the multiaxial response is presented in Chapter 7.

5.1 Physical Basis for Back Stress and Drag Stress

It is well established that inelastic deformation is the result of a number of microscopic processes and mechanisms. These include twinning, gliding of dislocations, climbing of dislocations, diffusional transportation of atoms and vacancies and grain boundary sliding [32-37]. These processes are in general dependent upon the material, strain rate, stress and temperature. It is also seen that in the higher temperature regimes the inelastic flow is primarily due to dislocation glide and climb with very little twinning [32]. The yield and ultimate strengths of a particular material depend heavily on its ability to immobilize dislocations by pinning and restrict dislocation multiplication. Restriction of dislocation motion can arise from several sources in the undeformed microstructure such as lattice resistance, solid solution atoms and discrete obstacles such as precipitates and grain boundaries. High temperature superalloys, such as Rene' 80, derive much of their strength from the gamma prime precipitates. During loading a network of dislocation walls are formed which develop into cells and subgrains within the material [31,38]. These dislocation networks also act as barriers to further dislocation motion.

104

5.1.1 Back Stress

When a dislocation moving in a slip plane encounters an obstacle such as a precipitate, its further movement is restricted by pinning. The pinned dislocation either cross slips or bows around the obstacle changing the local stress state. The pinned dislocations act to impede further dislocation motion and dislocation pileups develop. The dislocation pileups produce a net "back stress" which, in effect, opposes further inelastic deformation. The existence of a back stress has been experimentally established [39]. It may be viewed as a "threshold" stress which must be overcome either mechanically or thermally to produce further inelastic slip. Thermal activation can aid in further inelastic deformation by dislocation climb and cross slip. These mechanisms are generally associated with recovery.

The back stress which develops due to dislocation pileups is directional in nature. It reacts differently to changes in the direction of loading. For example, when the loading direction is reversed the dislocation pileup at an obstacle can be decomposed without the necessity of overcoming the obstacle itself. This results in inelastic deformation in the reverse direction at a lower stress, which is the well

105

known Bauschinger effect. Thus, the directional nature of the back stress is frequently modeled as "kinematic strain hardening". For constitutive modeling, it is then assumed that the back stress is a tensor valued quantity that can be modeled as a kinematic variable.

Several other phenomena in high temperature material behavior have been attributed to the existence of a back stress. It is known that when a material is loaded into the inelastic regime and unloaded, there is a time dependent recovery of the inelastic strain. This anelastic recovery has been observed in Rene˄ 80 as reported in Reference [1]. The initial inelastic loading creates dislocation pileups and a back stress opposing the applied stress. When the applied stress is removed, the back stress creates an inelastic flow in the reverse direction which decays with time. Similar effects have been observed in stress relaxation at various points in a hysteresis loop. It has been shown experimentally that negative stress relaxation can exist at a positive stress on the unloading branch of a cycle [40]. This occurs when the applied stress instantaneously falls below the back stress, resulting in a negative inelastic flow even for a positive applied load. Similarly, lateral softening effects have been observed in some materials when the direction of loading is shifted instead of reversed. This is

106

also attributed to the presence of a directional back stress which must be directional in nature [41].

5.1.2 Drag Stress

It has been observed experimentally that there are several microscopic effects that are isotropic in nature. These effects arise mainly from two sources; (1) the mutual interaction of dislocations and (2) physical changes in the obstacle structure itself. These effects change the inelastic strain rate (drag) and are associated with cyclic hardening or softening.

Dislocations move within a grain or subgrain until they are stopped at a barrier or interact with one another during their motion in a slip plane. There are numerous dislocations, i.e., dislocation forests, which propagate in an active slip plane. The intersection of a dislocation with the forest dislocations results in the formation of jogs in the dislocation lines. These jogs can impede the further motion of screw dislocations. The dislocation interaction process is a short range effect occurring over distances less than 5 to 10 interatomic distances; whereas, the strain hardening effect from dislocation pileups is a longer range effect [42].

107

Another isotropic effect is related to the physical changes in the obstacle structures as inelastic deformation progresses. Such changes occur over longer periods of time typical of creep or cyclic loading conditions. In many superalloys the smaller gamma prime precipitates can gradually dissolve and the larger particles coarsen [38]. Such instability effects usually occur at prolonged high temperature exposure. The strengths of the precipitates themselves can also change in time, making shearing easier. It has been observed in a number of materials that during cyclic softening the small dislocation cells produced during initial prestraining grow to larger cells. The cell size usually depends on the applied stress and inelastic strain range [43-46]. The cyclic deformation structure that develops is not reversible and it does not seem possible to explain the cyclic softening phenomenon solely based on variations of the subgrain size. For example, Moteff has shown that similar dislocation subgrains form during large strain monotonic and low cycle fatigue tests for a cyclically hardening material such as AISI 304 stainless steel [47].

Both of these effects, the mechanical strength variations of the precipitates and the evolution of dislocation subgrains, certainly influence the cyclic

inelastic behavior of the material. Moreover, this influence is isotropic in nature and should be modeled by a scalar variable. Thus, the drag stress is frequently introduced to model the cyclic behavior of the material.

5.2 Development of Flow Equation

Detailed analysis of individual crystallographic slip systems and development of equations representing individual dislocation movements and their interactions is perhaps possible for very simple material systems. However, for complex polycrystalline superalloys this approach is impractical. Thus, many investigators rely solely on phenomenological observations to propose a constitutive model. In this work both approaches are undertaken; that is, to propose a phenomenological model based on the observed deformation mechanisms.

It has been shown by Gilman [48], from dislocation velocity measurements [49] on pure crystals, that the inelastic strain rate has an exponential dependence on the ratio of the drag stress and the applied stress. This concept has been used by Bodner for the development of a constitutive model. However, precipitation hardened superalloys develop a complex dislocation substructure upon inelastic loading [31,38]

109

which tends to oppose further inelastic straining. The applied stress, S_{ij}, must overcome the back stress, Ω_{ij}, in order to produce further inelastic strains. Thus, $(S_{ij}-\Omega_{ij})$ is an effective stress that is required to produce inelastic flow. The exponential form of the flow equation proposed by Bodner is extended to incorporate the effective stress, $(S_{ij}-\Omega_{ij})$. The back stress, Ω_{ij}, depends on orientation, and both the back stress and drag stress depend on the history of loading.

In addition, the flow rule should be consistent with observed material behavior. The Prandtl Reuss equation and the Bodner equation are written as

$$\dot{\varepsilon}_{ij}^{I} = \lambda S_{ij}, \tag{5.1}$$

where λ is a scalar material function. Equation 5.1 requires that the direction of the inelastic strain rate vector, $\dot{\varepsilon}_{ij}^{I}$, is coincident with the applied deviatoric stress vector, S_{ij}. However, recent biaxial experiments on different materials have shown that this is not necessarily true [27,50] for high temperature superalloys. The angle between the two vectors varies as a function of loading in a nonproportional multiaxial test. The use of the back stress in the

110

model permits the two vectors to have different directions. Thus, the flow rule in Equation 5.1 is revised to include a back stress,

$$\dot{\epsilon}_{ij}^{I} = \lambda(S_{ij} - \Omega_{ij}),$$

(5.2)

where $(S_{ij} - \Omega_{ij})$ is an effective driving stress producing inelastic straining. Both S_{ij} and Ω_{ij} are deviatoric quantities so that Equation 5.2 satisfies the inelastic incompressibility condition. The scalar parameter λ can be found from the kinetic relation using a procedure suggested by Bodner [21]. Squaring Equation 5.2 and summing gives

$$\frac{1}{2}\dot{\epsilon}_{ij}^{I}\dot{\epsilon}_{ij}^{I} = \lambda^{2} \frac{1}{2}(S_{ij} - \Omega_{ij})(S_{ij} - \Omega_{ij}).$$

(5.3)

Using $\quad D_{2}^{I} = \frac{1}{2}\dot{\epsilon}_{ij}^{I}\dot{\epsilon}_{ij}^{I} \quad$ and

$$K_{2} = \frac{1}{2}(S_{ij} - \Omega_{ij})(S_{ij} - \Omega_{ij}),$$

the second invariants of the inelastic strain rate tensor and effective deviatoric stress tensor, respectively, the flow equation (5.2) can be written as

111

$$\dot{\varepsilon}_{ij}^I = \sqrt{D_2^I} \frac{(S_{ij} - \Omega_{ij})}{\sqrt{K_2}}. \tag{5.4}$$

The form of $\sqrt{D_2^I}$ must be chosen such that it depends on the back stress, Ω_{ij}, and drag stress, Z, in addition to the applied stress for an isothermal environment. Using the structure of the Bodner flow law, one can assume

$$\sqrt{D_2^I} = D \exp\left[-\frac{A}{2}\left(\frac{Z^2}{3K_2}\right)^n\right]. \tag{5.5}$$

In Equation 5.5 D, A, and n are temperature dependent material parameters. This equation has the form suggested by the microdynamical considerations discussed earlier. The exponent n is taken similar to the Bodner model. Both A and n control the strain rate sensitivity of the material. The parameter D can be interpreted as a limiting value for the inelastic strain rate at a particular temperature. Substituting Equation 5.5 in Equation 5.4, the general multiaxial flow equation is written as

$$\dot{\varepsilon}_{ij}^I = D \exp\left[-\frac{A}{2}\left(\frac{Z^2}{3K_2}\right)^n\right]\frac{(S_{ij} - \Omega_{ij})}{\sqrt{K_2}}. \tag{5.6}$$

112

A large number of the experiments in the area of constitutive modeling are performed in the uniaxial loading condition. Uniaxial tests are very useful in the determination of the material parameters as well as in evaluating the response of the model for complicated histories of loading. The multiaxial form of the flow equation can be simplified for the uniaxial case. Tensor quantities are written with subscripts "ij". The same symbol is used without the subscripts to denote its uniaxial value. Uniaxial loading conditions are defined as

$$\sigma_{ij} = \begin{bmatrix} \sigma & 0 & 0 \\ 0 & 0 & 0 \\ 0 & 0 & 0 \end{bmatrix}, \quad S_{ij} = \begin{bmatrix} \frac{2}{3}\sigma & 0 & 0 \\ 0 & -\frac{1}{3}\sigma & 0 \\ 0 & 0 & -\frac{1}{3}\sigma \end{bmatrix},$$

$$\dot{\varepsilon}_{ij}^I = \begin{bmatrix} \dot{\varepsilon}^I & 0 & 0 \\ 0 & -\frac{1}{2}\dot{\varepsilon}^I & 0 \\ 0 & 0 & -\frac{1}{2}\dot{\varepsilon}^I \end{bmatrix} \text{ and } \Omega_{ij} = \begin{bmatrix} \frac{2}{3}\Omega & 0 & 0 \\ 0 & -\frac{1}{3}\Omega & 0 \\ 0 & 0 & -\frac{1}{3}\Omega \end{bmatrix} \quad (5.7)$$

The parameter K_2 becomes

$$K_2 = \frac{1}{2}(S_{ij} - \Omega_{ij})(S_{ij} - \Omega_{ij}) = \frac{1}{3}(\sigma - \Omega)^2 \quad (5.8)$$

and an effective inelastic strain is defined as

113

$$\dot{\varepsilon}_e^I = \sqrt{\frac{2}{3}\dot{\varepsilon}_{ij}^I \dot{\varepsilon}_{ij}^I} \qquad (5.9)$$

for later use in the evolution equations. In uniaxial loading, $\dot{\varepsilon}_e^I = |\dot{\varepsilon}^I|$.

Using these and Equations 5.6 and 5.7, the uniaxial flow equation becomes

$$\dot{\varepsilon}^I = \frac{2}{\sqrt{3}}D \, \exp\left[-\frac{A}{2}\left(\frac{Z}{|\sigma-\Omega|}\right)^{2n}\right] \frac{(\sigma-\Omega)}{|\sigma-\Omega|}. \qquad (5.10)$$

5.3 Development of the Evolution Equations

The flow equation can be used to determine the inelastic strain rate when the applied stress, back stress, and drag stress are known. The back stress, Ω_{ij}, and drag stress, Z, are internal state variables which cannot be directly measured in an experiment. They depend on the entire thermomechanical history of loading; and, hence, their representations are sought in the form of rate or evolution equations. It is generally assumed that the rate of change of these quantities at any instant in time depends upon the current state of stress, inelastic strain rate, temperature and the internal variables; i.e.,

$$\dot{\Omega}_{ij} = F_1(\sigma_{ij}, \, \dot{\varepsilon}_{ij}^I, \, \Omega_{ij}, \, Z, \, T) \qquad (5.11)$$

114

and

$$\dot{Z}=F_2(\sigma_{ij},\ \dot{\varepsilon}_{ij}^I,\ \Omega_{ij},\ Z,\ T). \qquad (5.12)$$

Representations for F_1 and F_2 usually embody the observed mechanical behavior such as strain hardening, dynamic recovery, static thermal recovery and cyclic hardening or softening. The state variables Ω_{ij} and Z can be interpreted as macroscopic representations of the microscopic behavior of the material.

## 5.3.1 Uniaxial Back Stress Evolution Equation

The evolution equation for the generic back stress drag stress model discussed in Chapter 4 appeared to have the right characteristics. Recall that the evolution equation had the following uniaxial form:

$$\dot{\Omega}=f_1\dot{\varepsilon}^I-f_2\Omega|\dot{\varepsilon}^I|-R_1 \ . \qquad (4.2)$$

The first term in the above equation is used to characterize strain hardening, the second dynamic recovery and the function R_1 models static thermal recovery. The value of the back stress in an

undeformed material state is taken as zero; i.e., $\Omega(0)=0$. Furthermore, from Equation 4.2, at time zero $\dot{\varepsilon}^I \approx 0$ and R_1 is negligible so that $\dot{\Omega}(0)=0$. It was also shown in Chapter 4 that f_1 and f_2 are constants for René 80.

It was shown that it is possible to estimate the back stress and back stress rate by inverting the flow equation (5.10) for a particular loading history. This was done for tensile loading of René 80 at 982°C for four strain rates. Figure 5.1a shows the back stress rate from the experimental data and Equation 4.2. Both the test data and model are in reasonable agreement for large strain and $\dot{\Omega}$ approaches zero as saturation occurs at the end of the test. The prediction for Ω in the "elastic" region, where the inelastic strains cannot be accurately measured, cannot be confirmed; i.e., the test data does not show that $\dot{\Omega}(0)=0$. The back stress and the applied stress during "elastic" loading are shown in Figure 5.1b for the highest strain rate test. The dotted line is the back stress calculated using Equation 4.2. The difference $(\sigma-\Omega)$, which is the stress producing the inelastic strain rate, becomes very large early in the elastic range and produces the peaks in the curves shown in Figure 5.1a. This response appears to be unrealistic. This problem in the elastic region has been observed by other

116
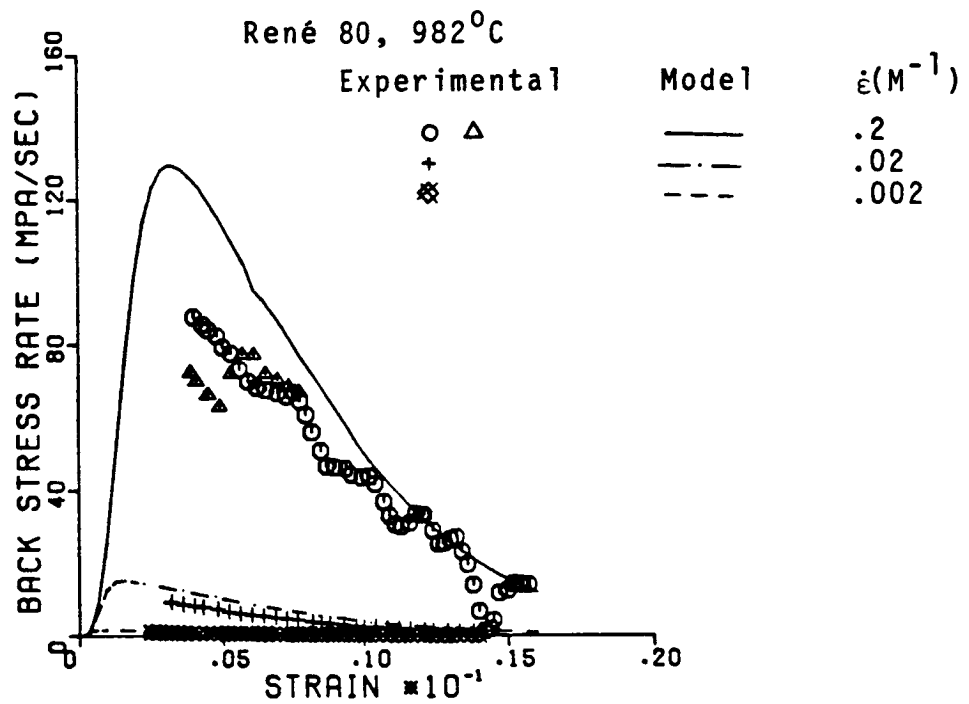
(a) Monotonic Tensile Tests
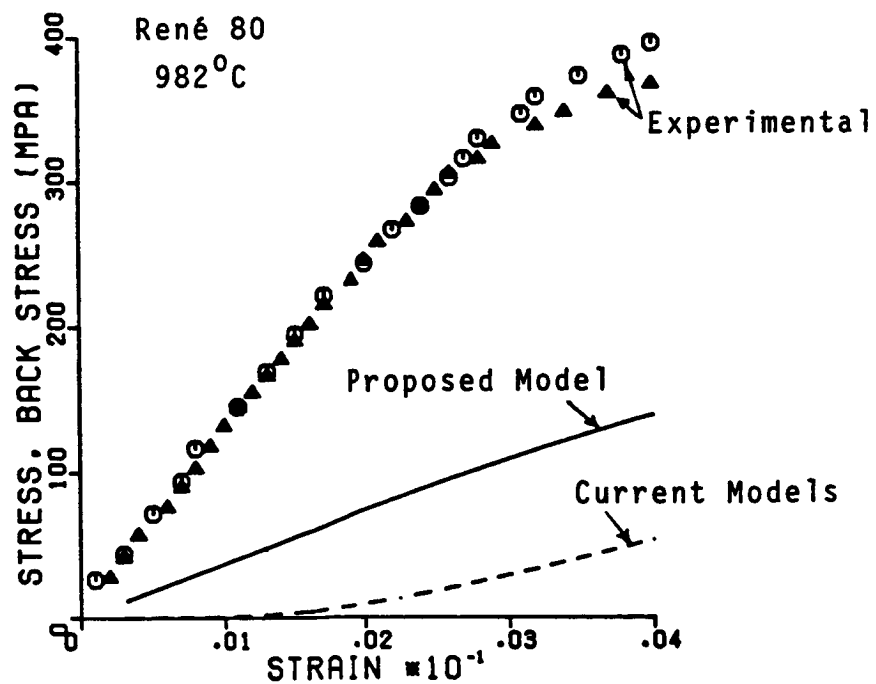
(b) Elastic Region

Figure 5.1 Back Stress Rate Variation in a Typical Back Stress Model

investigators [15] from other considerations. Thus, let us assume the stress and the back stress are proportional in the elastic region. This is shown by the solid line in Figure 5.1b. This idea can be easily incorporated in Equation 4.2 using a term that is proportional to the stress rate.

To begin, first note that the constants f_1 and f_2 in Equation 4.2 are related to the maximum value of the back stress, Ω_{max}, at saturation; i.e.,

$$\frac{f_1}{f_2} = \Omega_{max}. \tag{5.13}$$

Using Equation 5.13 and adding a stress rate term, the back stress evolution equation for uniaxial loading can be rewritten as

$$\dot{\Omega} = \frac{3}{2} f_1 \dot{\epsilon}^I - \frac{3}{2} f_1 \frac{\Omega}{\Omega_{max}} |\dot{\epsilon}^I| + \frac{G}{E}\dot{\sigma} - R_1, \tag{5.14}$$

where the factor 3/2 is used for later convenience.

The physical significance of the stress rate term in Equation 5.14 can be determined during "elastic" loading or unloading when $\dot{\epsilon}^I$ can be neglected. In this case,

$$\dot{\Omega} \approx \frac{G}{E}\dot{\sigma},\qquad\qquad\qquad (5.15)$$

where G is the initial slope of the back stress versus total strain curve. Thus, $G\sigma/E$ is a reversible component of the total back stress that is recovered instantaneously upon unloading. The total back stress, Ω, can be viewed as having elastic and inelastic components; i.e.,

$$\Omega = \frac{G}{E}\sigma + \Omega^I.\qquad\qquad\qquad (5.16)$$

The back stress evolution equation (5.14) can now be refined as

$$\dot{\Omega}^I = \frac{3}{2}f_1\dot{\varepsilon}^I - \frac{3}{2}f_1\frac{\Omega}{\Omega_{max}}|\dot{\varepsilon}^I| - R_1.\qquad (5.17)$$

The results of using Equation 5.14 are significantly better than those from Equation 4.2. A comparison of the calculated behavior with experimental data is shown in Figure 5.2a. Figure 5.2b contains a comparison of the response of the total back stress Ω and the inelastic component Ω^I during uniaxial tensile loading at different strain rates. It is clear that the "elastic" component of the back stress dominates in the

119
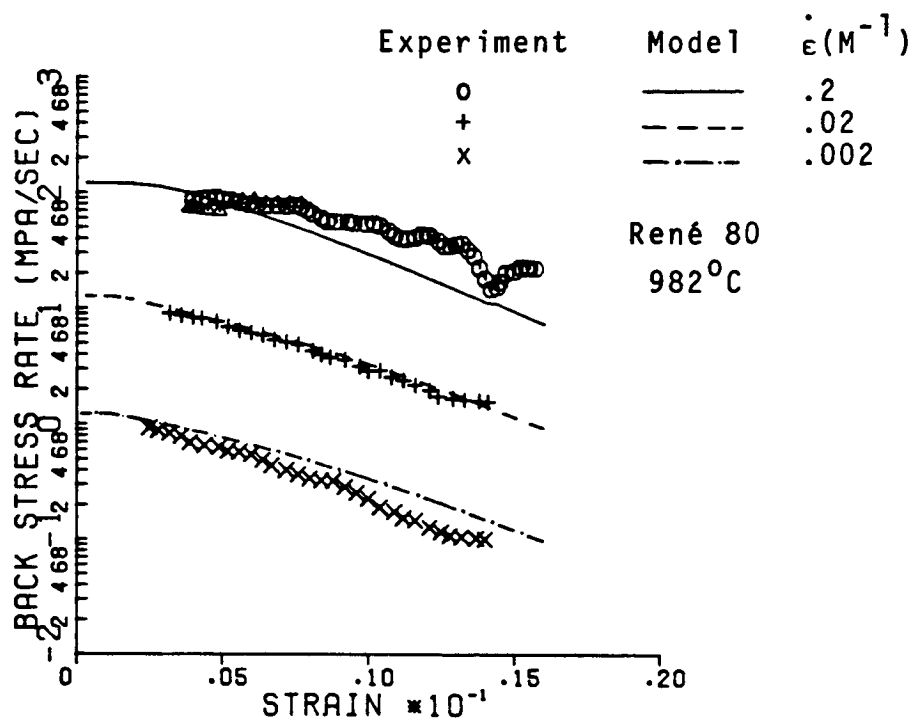
(a)   Monotonic Tensile Tests
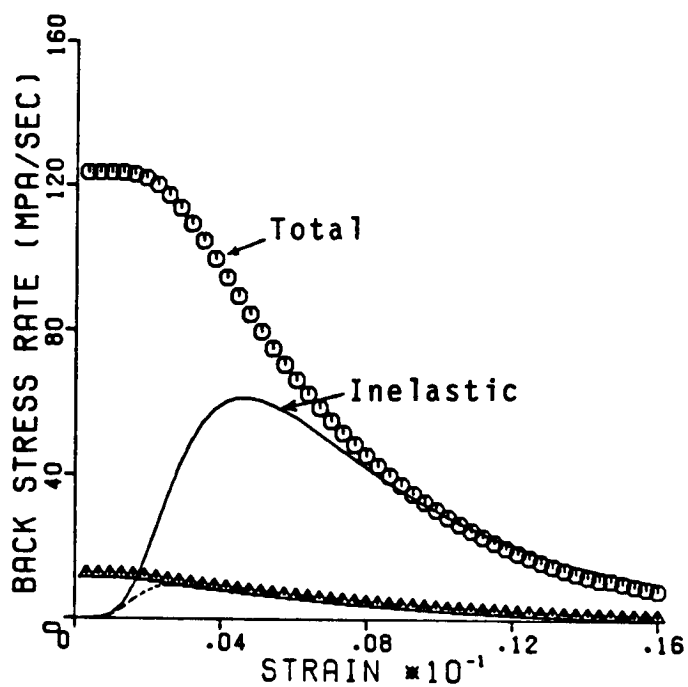
(b)   Comparison of Total and Inelastic Components

Figure 5.2   Back Stress Rate Variation in the Proposed Model

early part of loading; whereas, the inelastic component dominates as inelastic strains become significant.

5.3.2 Multiaxial Form of the Back Stress Evolution Equation

Equation 5.14 described the evolution of the back stress for uniaxial loading conditions. However, multiaxial loading conditions are present in most structural applications. Thus, it is necessary to develop a general multiaxial back stress evolution equation which reduces to Equation 5.14 for the uniaxial loading.

A general representation can be obtained by considering the material parameters in Equations 5.16 and 5.17 as fourth order tensors; i.e., assume

$$\Omega_{ij} = E_{ijkl} S_{kl} + \Omega_{ij}^I \tag{5.18}$$

and

$$\dot{\Omega}_{ij}^I = f_{ijkl} \dot{\epsilon}_{kl}^I - g_{ijkl} \Omega_{kl} |\dot{\epsilon}^I| - R_{ij}. \tag{5.19}$$

Since the material being investigated is isotropic, it is reasonable to assume that the material parameters f_{ijkl}, etc are isotropic tensors. The fourth order

isotropic tensor f_{ijkl}, for example, can be written as [51]

$$f_{ijkl}= a\delta_{ij}\delta_{kl}+b(\delta_{ik}\delta_{jl}+\delta_{il}\delta_{jk})+c(\delta_{ik}\delta_{jl}-\delta_{il}\delta_{jk}).\qquad(5.20)$$

Since the inelastic strain rate tensor, $\dot{\varepsilon}_{ij}^{I}$, is symmetric the back stress tensor, Ω_{ij}, is also symmetric; thus, the last term in Equation 5.20 can be eliminated. Expanding the first term of Equation 5.20 yields

$$f_{ijkl}\dot{\varepsilon}_{kl}^{I}=\left[a\delta_{ij}\delta_{kl}+b(\delta_{ik}\delta_{jl}+\delta_{il}\delta_{jk})\right]\dot{\varepsilon}_{kl}^{I}\qquad(5.21)$$

and

$$f_{ijkl}\dot{\varepsilon}_{kl}^{I}=a\dot{\varepsilon}_{kk}^{I}\delta_{ij}+2b\dot{\varepsilon}_{ij}^{I}.\qquad(5.22)$$

Since $\dot{\varepsilon}_{kk}^{I}=0$ due to incompressibility, the first term in Equation 5.19 reduces to

$$f_{ijkl}\dot{\varepsilon}_{kl}^{I}=f_1\dot{\varepsilon}_{ij}^{I},\qquad(5.23)$$

where f_1 is a scalar parameter. Using the same reasoning, it can be shown that E_{ijkl} and g_{ijkl} reduce to G/E and $3f_1/2\Omega_{max}$, respectively. Thus, it is seen

that for isotropic response the material parameters in Equations 5.18 and 5.19 are scalar. Hence, the multiaxial form of the back stress evolution equation can be summarized as

$$\Omega_{ij} = \frac{G}{E} S_{ij} + \Omega_{ij}^I \tag{5.24}$$

and

$$\dot{\Omega}_{ij}^I = f_1 \dot{\epsilon}_{ij}^I - \frac{3}{2} f_1 \frac{\Omega_{ij}}{\Omega_{max}} \dot{\epsilon}_e^I - R_{ij}, \tag{5.25}$$

where $\dot{\epsilon}_e^I$ is given by Equation 5.9 and f_1, G and Ω_{max} are the scalar parameters determined from the uniaxial experiments.

5.3.3 The Drag Stress Evolution Equation

The drag stress is a scalar quantity introduced to represent isotropic hardening or softening effects. Physically it is interpreted as being a macroscopic representation of the resistance offered by the microstructural precipitates and grain boundaries to dislocation motion.

Rene′ 80 at 982°C can cyclically soften. As shown in Figure 3.9 this softening is seen to be strain rate

dependent with significant softening at high strain rates and no softening at low strain rates. In most models cyclic hardening or softening is taken as being dependent on the accumulated inelastic strain. Measures of cyclic softening based on accumulated inelastic strains are not adequate; because, for the same value of accumulated strain the predicted response to high and low strain rates would be the same. However, a measure based on accumulated inelastic work would produce different response for the high and low strain rates.

A representation for the drag stress is proposed which is identical to the Bodner Equation; i.e.,

$$\dot{Z} = m(Z_1 - Z)\dot{W}^I - R_2, \qquad (4.13)$$

with the initial condition $Z(0) = Z_0$. But the physical interpretation and the role of the drag stress are different from the Bodner model. In the above equation, the drag stress models cyclic softening with $Z_0 > Z_1$; whereas, Bodner used Equation 4.13 to model strain hardening in the tensile response with $Z_1 > Z_0$. The value of Z_1 in Equation 4.13 is the saturated value of the drag stress Z and the rate of cyclic softening is determined by the parameter m. In the experiments

performed on Rene´ 80, there was no time dependent recovery of the cyclically softened state; hence, the recovery term R_2 is omitted. In this case, Equation 4.13 can be integrated to give

$$Z = Z_1 + (Z_0 - Z_1) e^{-mW^I} \ . \tag{5.26}$$

Since $Z_1 \leq Z_0$, Equation 5.26 represents Z as a monotonically decreasing function of the accumulated inelastic work, W^I. This happens after a sufficient number of cycles in a cyclic test.

5.4   Evaluation of the Material Parameters

The material parameters in the model can be determined from uniaxial test data using a procedure similar to that outlined in Chapter 4 for the generic back stress drag stress model. Recall, two assumptions were made as part of this analysis. First, the back stress is saturated at the end of tensile tests, $\Omega = \Omega_{max}$. Second, the drag stress variation is small for the tensile tests, $Z \simeq Z_0$. The flow equation (5.10) can be inverted to give

$$\left(\frac{Z_0}{\sigma_s - \Omega_{max}} \right)^{2n} = -\left[\frac{2}{A} \ln \frac{\sqrt{3} \dot{\varepsilon}^I_s}{2D} \right] \tag{5.27}$$

125

where the subscript s in the above equation indicates saturation. The constant A is related to the strain rate sensitivity at lower temperatures. At 982°C, A is taken as unity. The scaling factor D is taken as one per second. Z_0, Ω_{max} and n are then determined from a number of monotonic tensile tests at different strain rates.

The history of the back stress for a particular uniaxial loading history can be calculated using

$$\Omega = \sigma - Z \left[-\frac{2}{A} \ln \frac{\sqrt{3} \ \dot{\epsilon}^I}{2D} \right]^{-\frac{1}{2n}} \tag{5.28}$$

For tensile tests $Z \simeq Z_0$ is used initially, consistent with the second assumption made earlier. The initial slope of the back stress versus strain curve, G, in Equation 5.16 is then determined. Using Equation 5.28 the back stress rate, $\dot{\Omega}$, is calculated numerically. The constant f_1 in Equation 5.17 is then determined.

The material parameters in the drag stress evolution equation are determined in a slightly different manner. The flow equation is first inverted as

$$Z = (\sigma - \Omega) \left[-\frac{2}{A} \ln \frac{\sqrt{3} \dot{\epsilon}^I}{2D} \right]^{-\frac{1}{2n}} . \tag{5.29}$$

126

Notice from Equation 5.26 that when the accumulated
inelastic work W^I is large, such as in a cyclic test,
$Z=Z_1$. The back stress history is first calculated for
a saturated cyclic hysteresis loop using Equation 5.28.
Since the starting value for Ω for the saturated cycle
is not known, an iterative procedure is necessary. The
average value of Z_1 is then determined using Equation
5.29 and two saturated cyclic hysteresis loops at high
and low strain rates. The remaining parameter, m, is
determined using Equation 5.26 and performing nonlinear
regression of monotonic and cyclic test data. The
various parameters are listed in Table 6.1.

5.5 Static Thermal Recovery

Almost all the unified constitutive models have
static thermal recovery terms added in the evolution
equations. This can be done in the model proposed,
using R_1 and R_2 in Equations 4.13 and 5.17. These
static thermal recovery terms purportedly model
thermally activated processes, such as dislocation
climb and cross slip, and are active only for long
duration tests, such as creep and stress relaxation.
The origin of such an approach can be traced to Orowan
and Bailey [52,53].

In general, functional forms for the static thermal recovery term R_1 in the back stress equation (5.17) can be determined, based on the creep tests and low strain rate tensile tests. However, in the proposed model, the predictions are very good for creep and stress relaxation tests at 982°C without the use of R_1. Thus, it is concluded that the necessary recovery effects, at least at 982°C, are already included in the dynamic recovery term in Equation 5.17.

The drag stress variation models cyclic softening or hardening and is physically related to the mechanical changes occurring to the precipitates. These changes are irreversible and cannot be recovered. Thus, it is not expected that a recovery term R_2 in Equation 4.13 should be necessary.

5.6 Application to Cyclic Load Histories

The constitutive equations (5.6), (5.24), (5.25), and (4.13) have been programmed to calculate the material behavior for different load histories. The program performs numerical integration of these equations using a forward Euler scheme. One of the difficulties involved in using unified constitutive models is that they require a large number of time steps for many loading histories, with each time step

involving a number of iterations. This makes predictions difficult when a large number of cycles are involved. Many tests in the experimental program described in Chapter 3 are under cyclic conditions. Recall, these tests were performed in cyclic blocks, involving a series of strain ranges, as shown in Figure 3.3. To predict the response of the model during such a test would involve integrating the constitutive equations cycle-by-cycle for the entire test. This approach was abandoned as being too expensive.

Instead a new scheme is proposed which limits the actual integration to only those cycles where significant transient behavior is expected. In the beginning of each cyclic block integration is performed for a few cycles until the back stress hysteresis loop stabilizes. The inelastic work from the latest cycle is then extrapolated to the final cycle of that particular block. The drag stress at the beginning of the last cycle is calculated using the extrapolated value of the inelastic work and Equation 5.26. Complete integration is then performed for this final cycle of the current block and continues to the next block until the transients again stabilize. The same process is then repeated for the entire test sequence. This scheme is illustrated in Figures 5.3, 5.4, and 5.5. Figure 5.3 shows the strain history imposed. Two
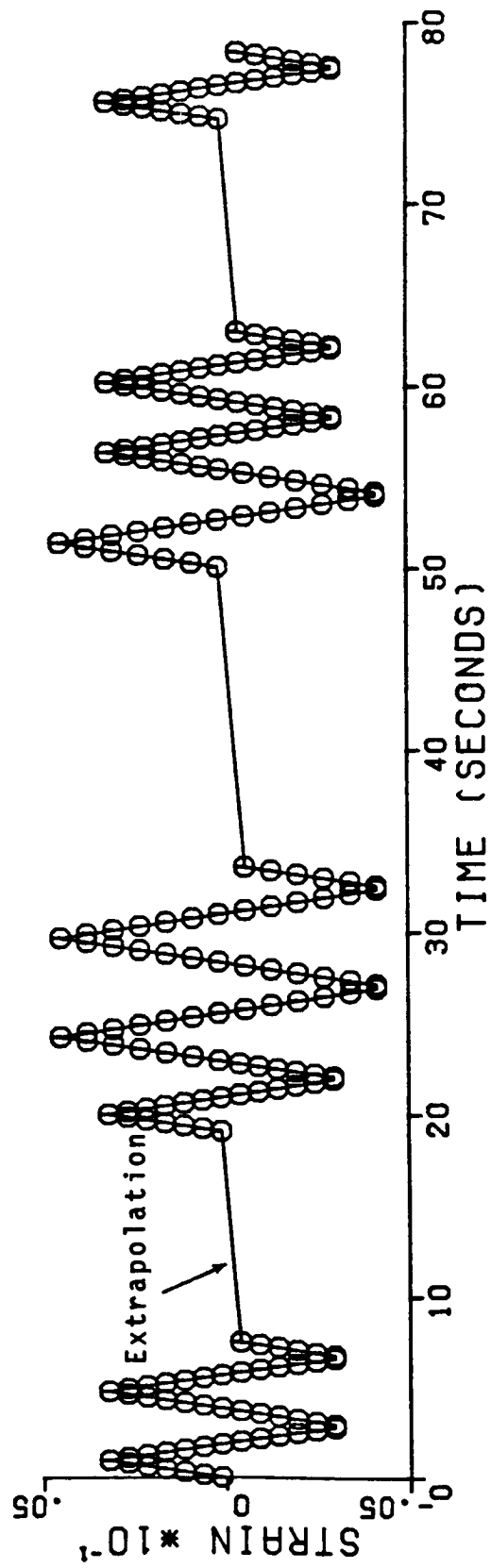
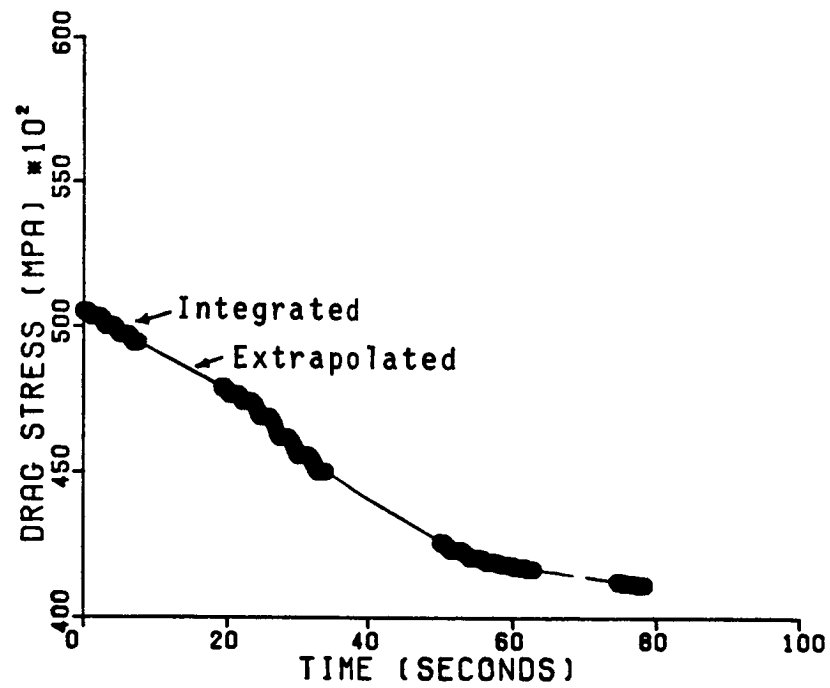Figure 5.3   Integration Scheme for Complex Cyclic Loading Histories

Figure 5.4   Drag Stress Extrapolations in the Cyclic Integration Scheme
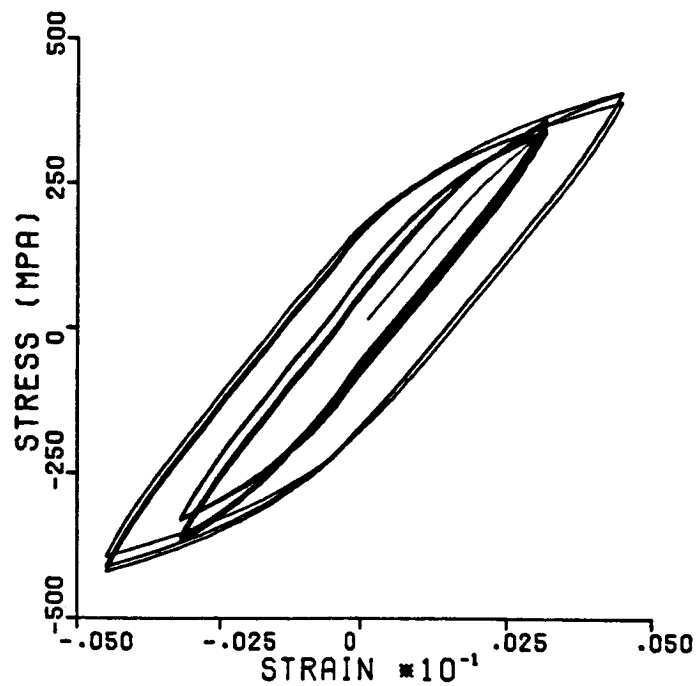

Figure 5.5   Typical Hysteresis Loops Using the Cyclic Integration Scheme
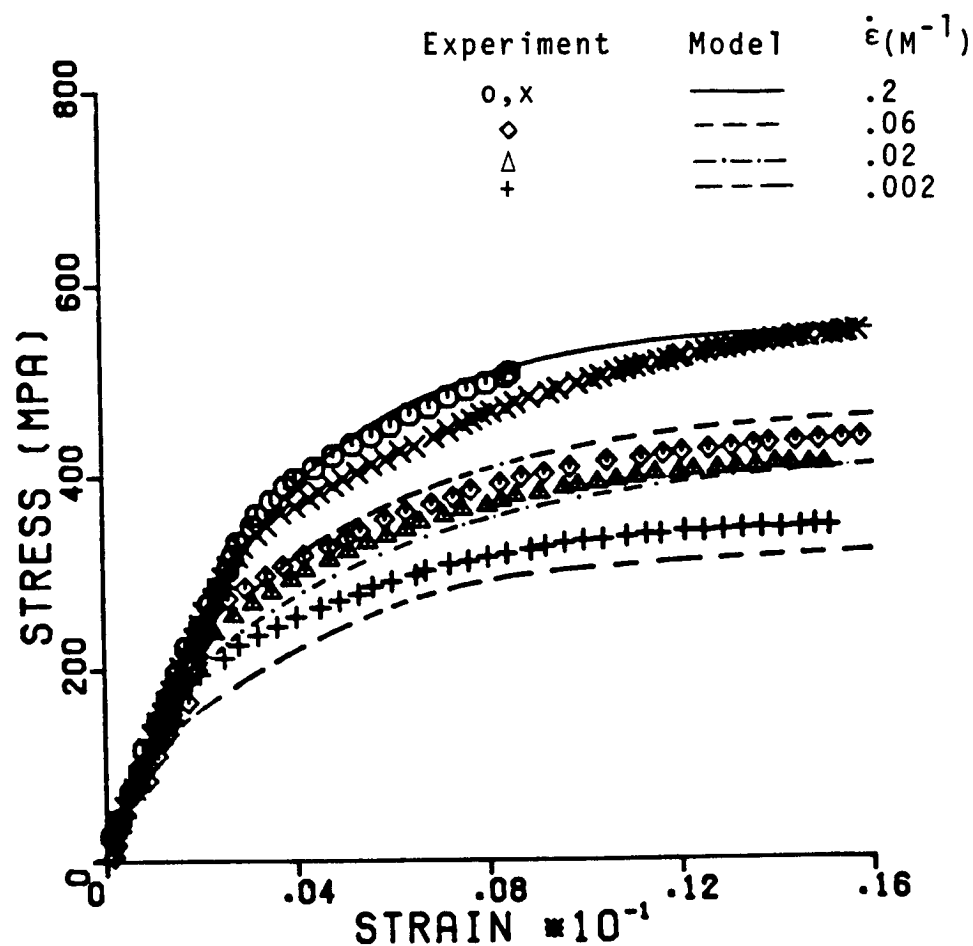
131

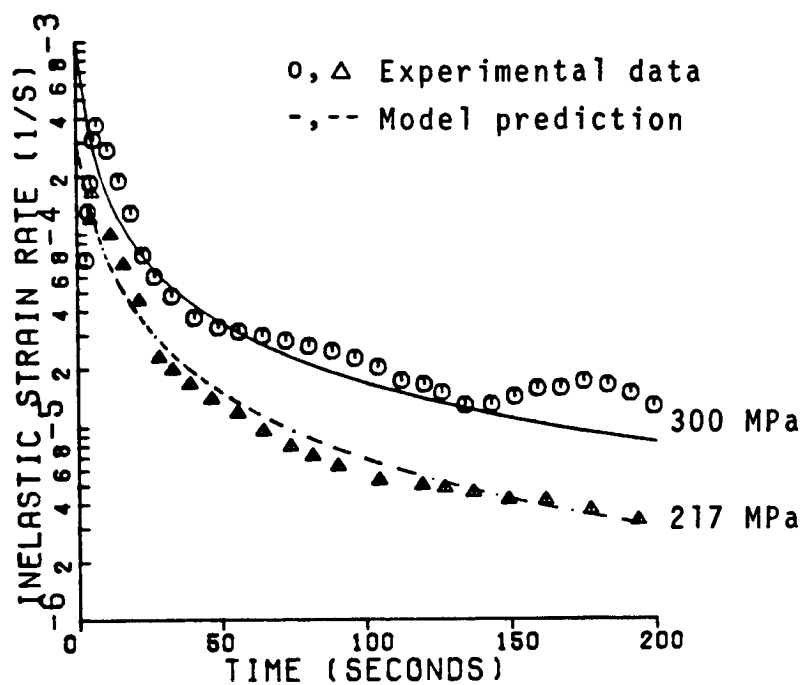Figure 5.6   Predicted and Experimental Monotonic Tensile
Response of René 80 at 982°C

transient loops are taken in each block. Figure 5.4
shows the behavior of the drag stress using the
extrapolation scheme. Figure 5.5 shows the nested
hysteresis loops calculated for the three cyclic
blocks.

This scheme was used for making model predictions
for all the uniaxial and multiaxial tests.
Conceptually, this scheme can be made more
sophisticated, based on some well chosen criteria for
extrapolating the state variables. This can provide a
powerful tool for analyzing long time load histories
with minimal amount of computation.

5.7 Analysis of Rene' 80 Behavior at 982°C

In this section, some typical examples are given
comparing the predictions of the proposed unified model
to Rene' 80 experimental results at 982°C. The material
parameters used for the predictions are given in Table
6.1.

The tensile test results and model predictions are
shown in Figure 5.6. The model is seen to represent
the strain rate sensitivity very well. The saturated
values of the stresses and the shapes of the stress
strain curves are reasonably well predicted. Recall

(a) Inelastic Strain Rate
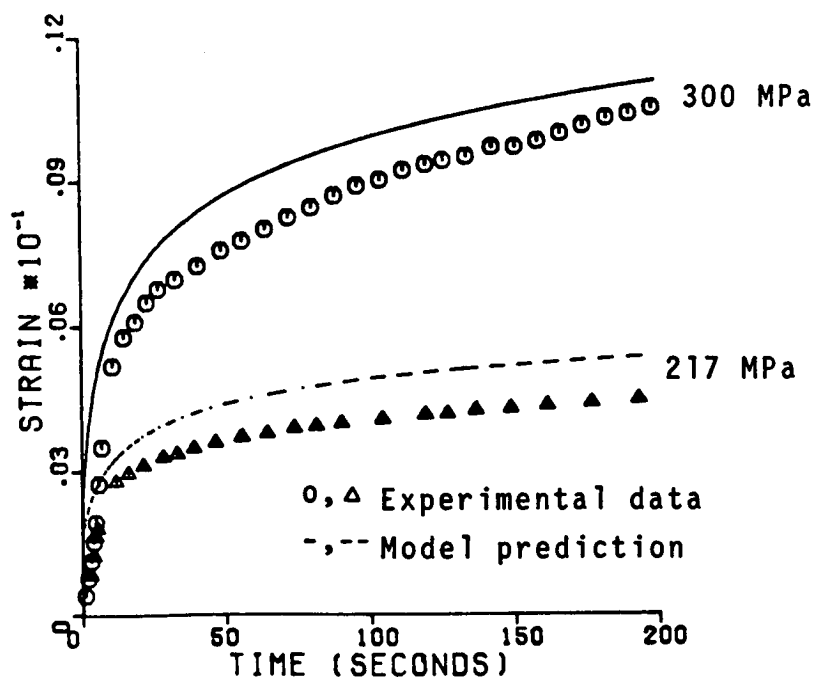
(b) Total Strain

Figure 5.7 Predicted and Experimental Creep Response of
René 80 at 982°C

134

that some of these results were used in calculating the material parameters for the model.

Figure 5.7 shows the results of the creep analysis at two different stress levels. The agreement between the model and test data is very good. The creep data was not included in the analyses for material constant evaluation.

The cyclic analyses are shown in Figures 5.8-5.12. Figures 5.8 and 5.9 are the cyclic saturated loops at the high $(.2 \ M^{-1})$ and low $(.002 \ M^{-1})$ strain rates, respectively. These two loops had been used in evaluating Z_1 and m in Equation 4.13. The predictions were made using the extrapolation scheme presented in the previous section. The correlation between the model and the test data appears good.

The rest of the cyclic test results shown are pure predictions. That is, none of these data were used in constant evaluation and the predictions are based on the extrapolation scheme. Figure 5.10 shows a cyclic test with a compressive mean strain. Notice that the mean stress relaxes as cycling progresses. The model also predicts exactly the same transient behavior. The first two cycles are shown in Figure 5.10a. A saturated cycle (cycle number 78) is shown in Figure 5.10b. The agreement between the model and test data is excellent. This is a low strain rate $(.002 \ M^{-1})$
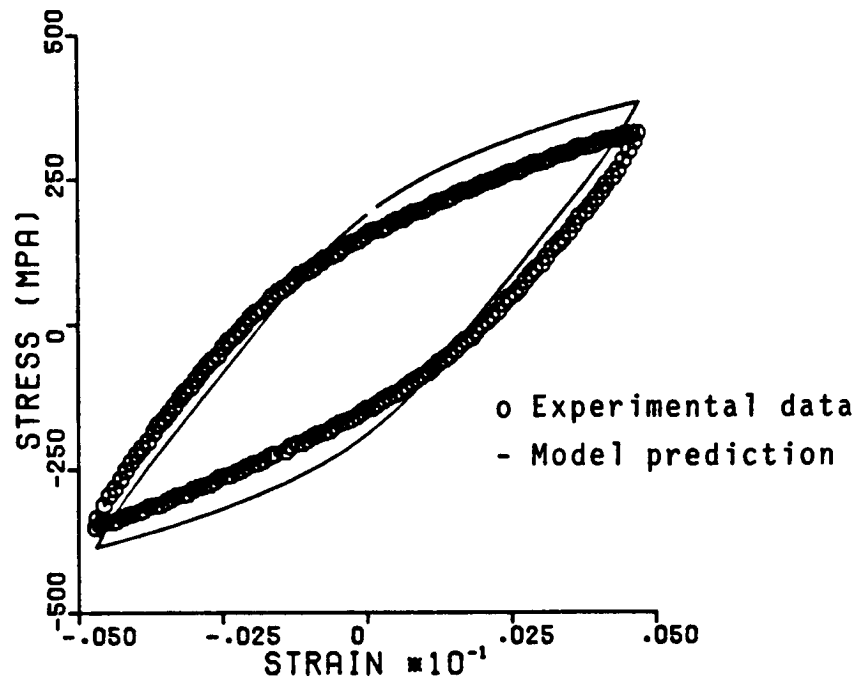
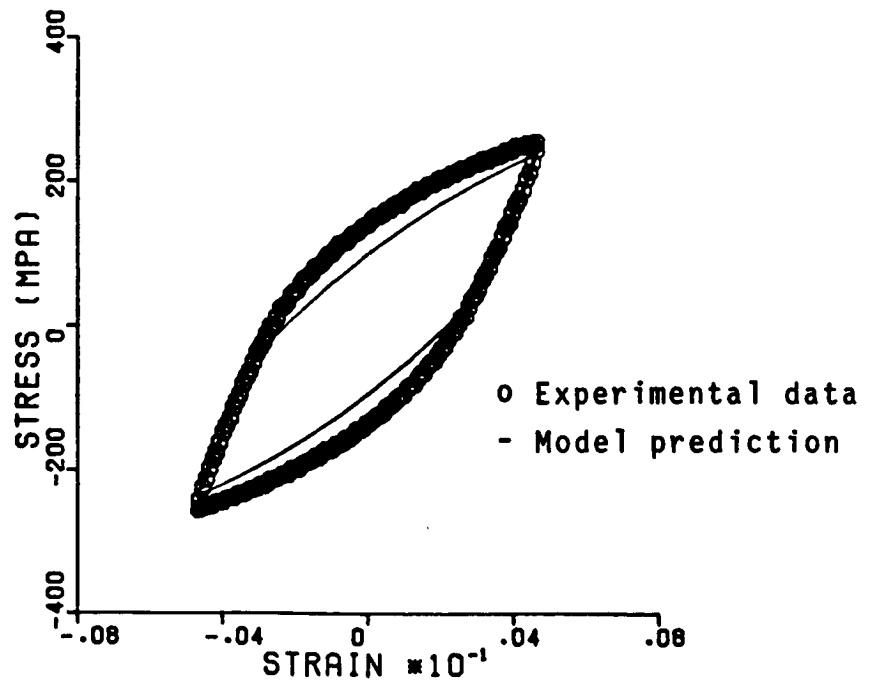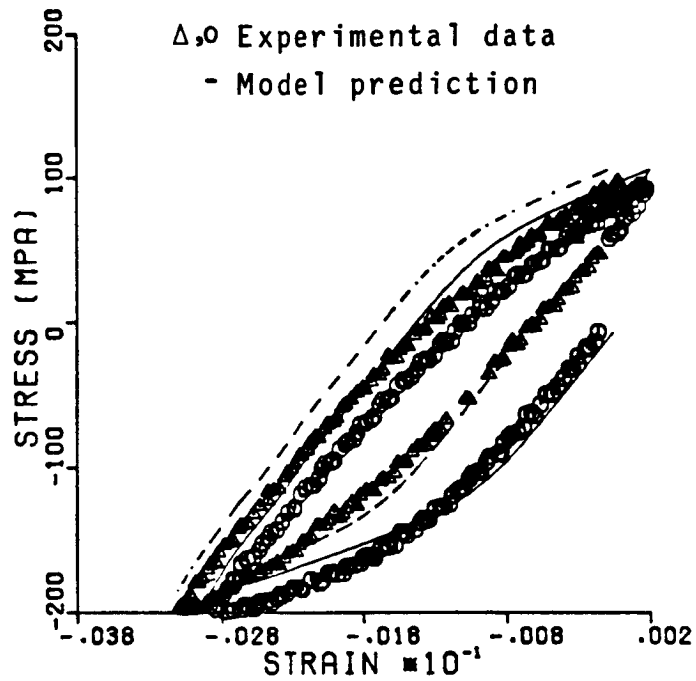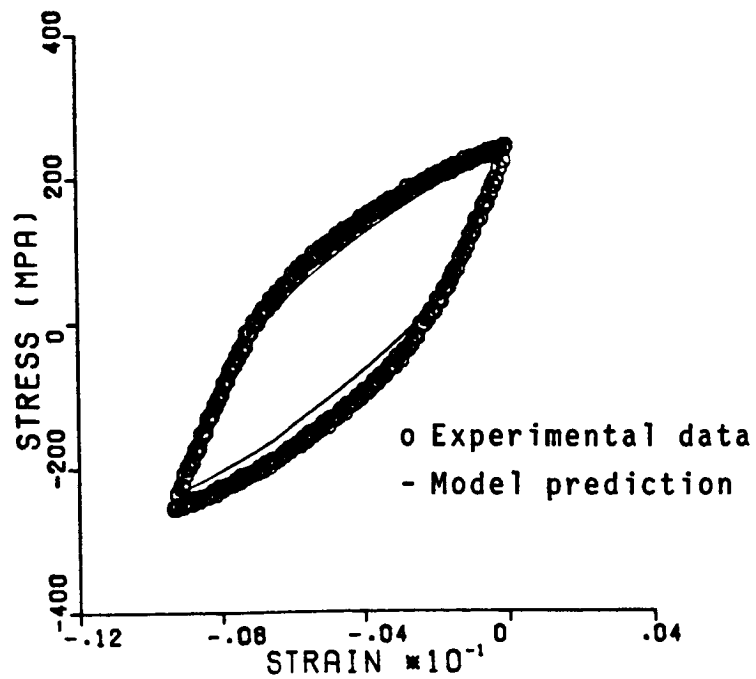Figure 5.8   Predicted and Experimental Saturated Cyclic Loop, 982°C, .2M⁻¹

Figure 5.9   Predicted and Experimental Saturated Cyclic Loop, 982°C, .002M⁻¹

136
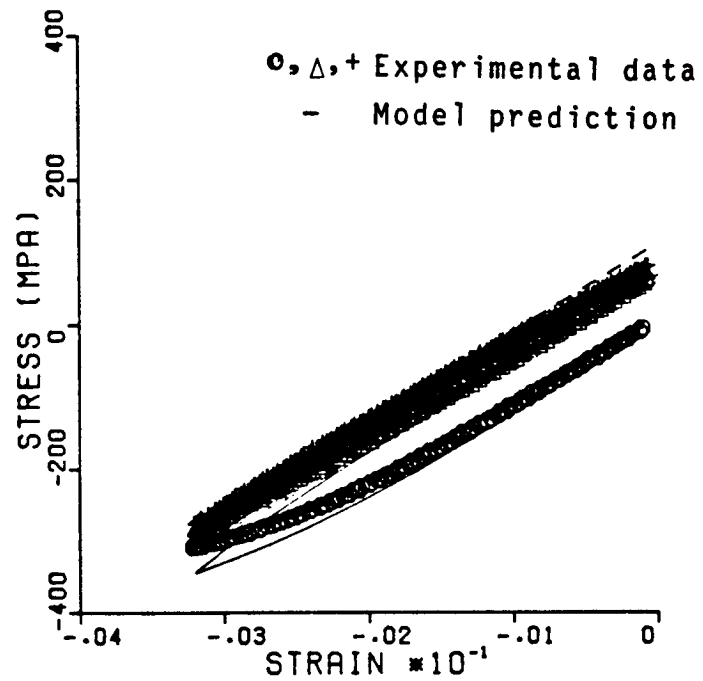
(a) First Two Cycles
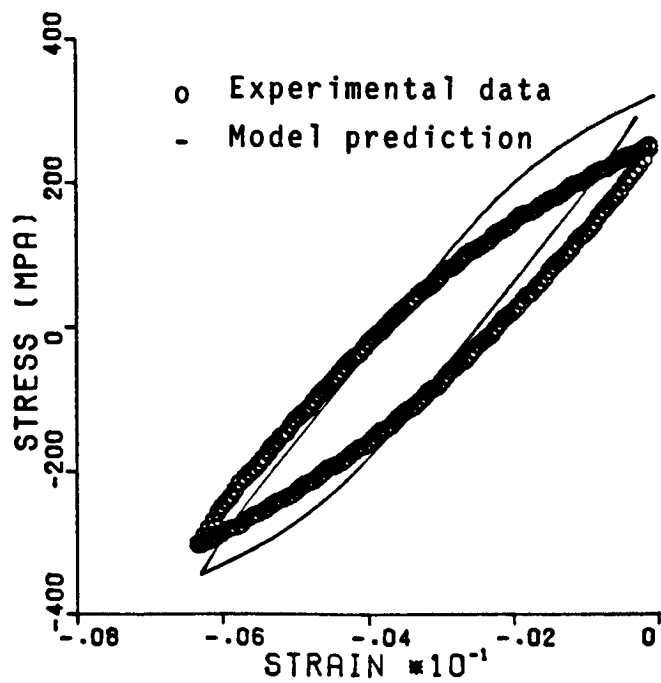

(b) Cycle No. 78

Figure 5.10 Predicted and Experimental Cyclic Behavior, 982°C, .002M^{-1}, A$_\epsilon$= -1
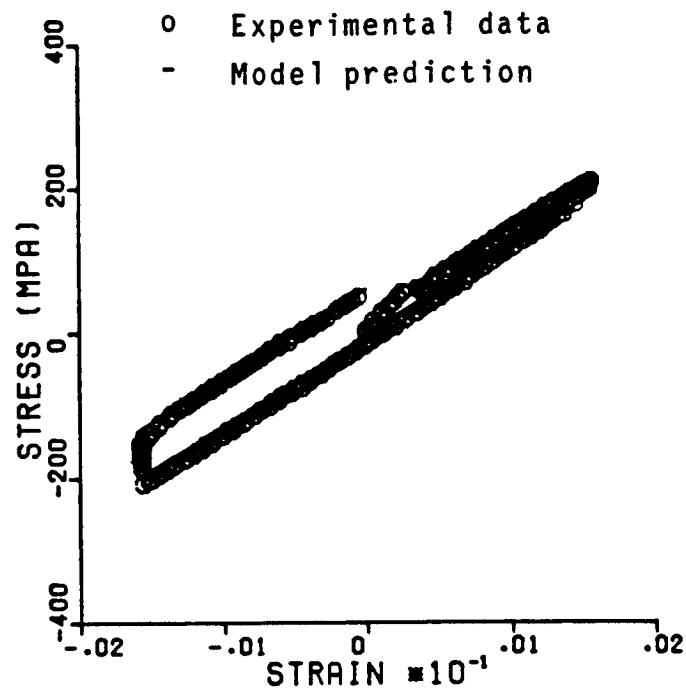
(a) First Four Cycles
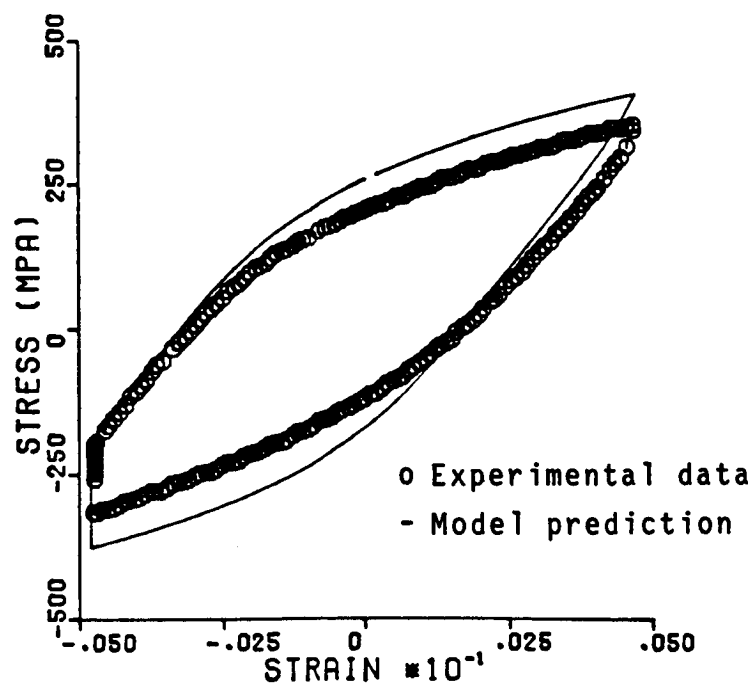

(b) Cycle No. 58

Figure 5.11 Predicted and Experimental Cyclic Behavior,
982°C, .2M^{-1}

138

(a) First Cycle

(b) Cycle No. 30

Figure 5.12 Predicted and Experimental Cyclic Behavior, 982°C, 12 Second Hold Time

test. The results are not as good for a similar test at high strain rate (.2 M^{-1}), as shown in Figure 5.11.

Figure 5.12 shows the results for a 12 second compressive strain hold cyclic test. The amount of stress relaxation predicted by the model is in good agreement with the test data. The hysteresis loop is also predicted very well.

In summary, the model is seen to be capable of representing well the rate dependent Rene' 80 behavior at 982°C under monotonic, cyclic, and creep loading conditions. In particular, the mean stress transient behavior is predicted very well. This is expected to enhance the low cycle fatigue life analyses. The creep and cyclic stress relaxation predictions are very encouraging.

CHAPTER 6

<u>NONISOTHERMAL LOADING CONDITIONS</u>

The constitutive modeling discussed in the previous chapters was directed toward identifying the physical basis of the model and developing the mathematical structure. Procedures were also developed to evaluate the various material parameters. Further, the capabilities of the model were verified for monotonic, cyclic and creep loading histories for Rene´ 80 at 982°C. In actual service, however, blades and vanes are subjected to a variety of temperatures.

Extending the model to other temperatures is challenging because the low temperature behavior of Rene´ 80 is significantly different from its high temperature behavior. Recall, the major differences are in strain rate sensitivity (Figures 3.5 and 3.6), cyclic softening (Figures 3.9 and 3.11) and ductility (Figure 3.4). The objective of this phase of the research is to extend the new model to various other temperatures. It will be shown that this can be done essentially within the same mathematical framework of the model developed in Chapter 5. The isothermal form for the constitutive model is summarized below for convenience:

$$\dot{\varepsilon}_{ij}^I = D \exp\left\{-\left[\frac{A}{2}\left(\frac{Z^2}{3K_2}\right)^{2n}\right]\right\}\frac{(S_{ij}-\Omega_{ij})}{\sqrt{K_2}}, \tag{5.6}$$

$$\Omega_{ij} = \frac{G}{E}S_{ij} + \Omega_{ij}^I, \tag{5.24}$$

$$\dot{\Omega}_{ij}^I = f_1\dot{\varepsilon}_{ij}^I - f_1\frac{\Omega_{ij}}{X}\dot{\varepsilon}_e^I - R_{ij}, \tag{5.25}$$

$$\dot{Z} = m(Z_1-Z)\dot{W}^I - R_2, \tag{4.13}$$

where, $K_2 = \frac{1}{2}(S_{ij}-\Omega_{ij})(S_{ij}-\Omega_{ij})$, $\dot{\varepsilon}_e^I = \sqrt{\frac{2}{3}\dot{\varepsilon}_{ij}^I\dot{\varepsilon}_{ij}^I}$ and,

$X = \frac{2}{3}\Omega_{max}^*$.

In nonisothermal loading conditions, it is expected that the model parameters are temperature dependent; i.e., $D(T)$, $A(T)$, $n(T)$, etc. In addition, the saturated values for the back stress, Ω_{max}, and the drag stress, Z, are also dependent on the temperature. The temperature dependence can be estimated from experimental data at various constant temperatures if temperature rate effects are neglected. In addition to 982°C (1800°F), experimental data for Rene' 80 is available at 871°C (1600°F) and 760°C (1400°F).

---

* The formulation for the steady state value, X, of the back stress is modified, as shown later in this chapter.

A limited amount of data is also available at 1093°C (2000°F), 649°C (1200°F) and 538°C (1000°F). Methods for evaluating the material parameters were discussed in detail in Chapters 4 and 5. In general, the same procedures were used at the other temperatures. However, at 760°C (1400°F) and below there are some differences which will be discussed later in this chapter.

6.1 Tensile Response at Various Temperatures

As discussed in Chapters 4 and 5, most of the material parameters in the constitutive model can be evaluated from the experimentally measured tensile response of the material. A number of monotonic tensile tests have been performed for Rene´ 80 at various temperatures and strain rates as shown in Table 3.3. The results of these tests clearly show the differences in the material behavior at the various temperatures.

The major result of the monotonic tensile tests is that the strain rate sensitivity of Rene´ 80 is seen to be strongly dependent upon the temperature. As shown in Figures 3.5 and 3.6, at high temperature (982°C) the strain rate sensitivity is high; whereas, at low temperature (538°C) there is no strain rate

sensitivity. It was seen that at 871°C, Rene´ 80 behavior is strain rate dependent, although to a smaller extent than at 982°C. The results at 760°C are mixed. There is more scatter in data at this temperature and no strain rate sensitivity is evident. Other investigators have also reported considerable scatter in experimental results of Rene´ 80 at 760°C [31]. Recall, the ductility of Rene´ 80 is strongly dependent on temperature, as shown in Figure 3.4. The ductility is poor at 871°C and 760°C and the tensile tests at these temperatures failed at low values of strain before saturation was reached. The saturated values of tensile stress at 871°C and 760°C were determined by extrapolation.

The saturated value of stress in the tensile tests is plotted as a function of temperature in Figure 6.1 for three strain rates, .2 M^{-1}, .02 M^{-1}, and .002 M^{-1}. The saturated values of stress are ordered with respect to the strain rate at all temperatures except 760°C. The saturated tensile stress increases with decreasing temperature, reaching a plateau at 760°C and below. The reduction in strain rate sensitivity at lower temperatures is also evident in Figure 6.1.

6.2 Evaluation of Material Parameters at Low Temperatures

A systematic method of evaluating the various material parameters in unified models was outlined in Chapter 4. This procedure was later used for Rene´ 80 at 982°C, as discussed in Chapter 5. At 871°C Rene´ 80 behavior is generally similar to that at 982°C and the same material parameter evaluation procedure was used. The saturated value for the back stress, Ω_{max}, the initial value of the drag stress, Z_0, and the exponent n in the flow equation (5.10) were determined from the saturated condition of the three monotonic tensile tests. The scaling parameter D was chosen to be ten per second. Then the history of the back stress, Ω, was calculated for the entire tensile test by inverting the flow equation (5.10) and assuming $Z \approx Z_0 = $constant. The various parameters in the back stress evolution equation were then calculated exactly the same way as for 982°C. The drag stress equation parameters were also calculated exactly the same way, using two saturated cyclic hysteresis loops.

However, at 760°C and lower, the lack of strain rate sensitivity, ductility and consequent data scatter, required some modifications in the constant evaluation scheme. First, the saturated value of the back stress, Ω_{max}, cannot be evaluated using the

same technique. The values of Ω_{max} at 982°C and 871°C are plotted in Figure 6.1. It is seen that the effective stress (σ-Ω) increases at lower temperatures; i.e., a larger value of the effective stress (σ-Ω) is required in order to produce the same inelastic strain rate. It is assumed that this trend continues at temperatures lower than 871°C. Thus, the Ω_{max} versus temperature curve is extrapolated up to 760°C. Since the saturated value of the stress reaches a plateau at 760°C, it is reasonable to expect that the saturated back stress, Ω_{max}, shows a similar behavior. This has been confirmed using experimental data from the three tensile tests at 538°C. Thus, an approximate curve is constructed for the variation of Ω_{max} with temperature. This is also shown in Figure 6.1. The values of Ω_{max} at 760°C and below are taken from this curve.

The uniaxial form of the flow equation (5.10) at the saturated condition in a tensile test can be written as

$$\ln\left(\frac{2D}{\sqrt{3}\ \dot{\varepsilon}_s^I}\right) = \frac{A}{2}\left(\frac{Z_o}{\sigma_s - \Omega_{max}}\right)^{2n}. \tag{6.1}$$

In the above equation, the subscript s indicates saturation. Notice that $\dot{\varepsilon}_s^I \approx \dot{\varepsilon}$, the applied strain

rate, which ranged from .002 M^{-1} to .2 M^{-1}. At 760°C, σ_S is essentially strain rate independent and Ω_{max} is found from Figure 6.1. The initial value of the drag stress, Z_0, is considered temperature independent and known. Then, the parameters D, A, and n are determined such that predicted values of σ_S using Equation 6.1 for strain rates from .002 M^{-1} to .2 M^{-1} are within the scatter of experimental results. Once these flow equation material parameters are known, the back stress evolution equation parameters f_1 and G/E can be determined, using the same procedure as for 982°C and 871°C. The various material parameters at 760°C are listed in Table 6.1. Their variation with temperature is shown in Figures 6.2-6.5. The average elastic modulus from the uniaxial tests at several temperatures is shown in Figure 6.6.

6.3 Calculated Tensile Response

The monotonic tensile response of Rene' 80 has been calculated at 871°C, 760°C, and 538°C using the material parameters shown in Table 6.1. The calculations are for three strain rates, .2 M^{-1}, .02 M^{-1} and .002 M^{-1}. The results are compared with experimental data in Figures 6.7, 6.8, and 6.9.
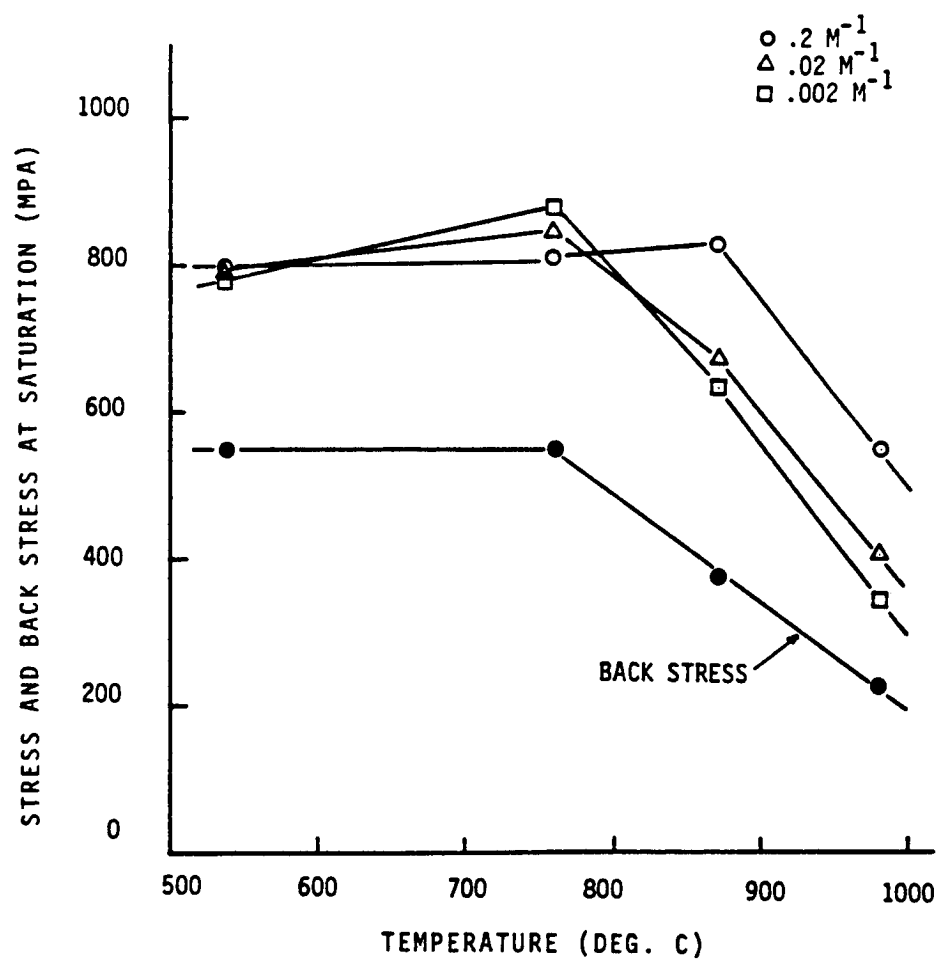
147

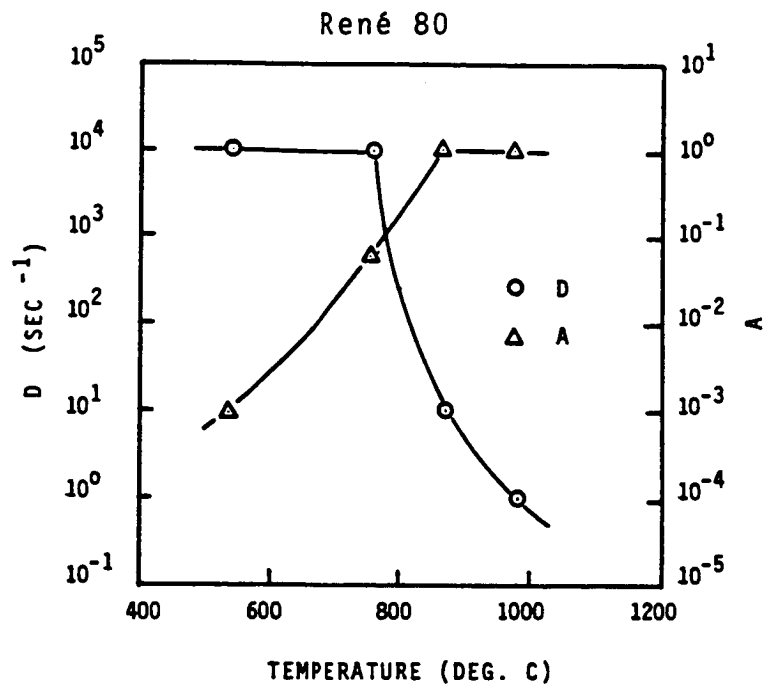Figure 6.1 Variation of Saturated Stress with Temperature
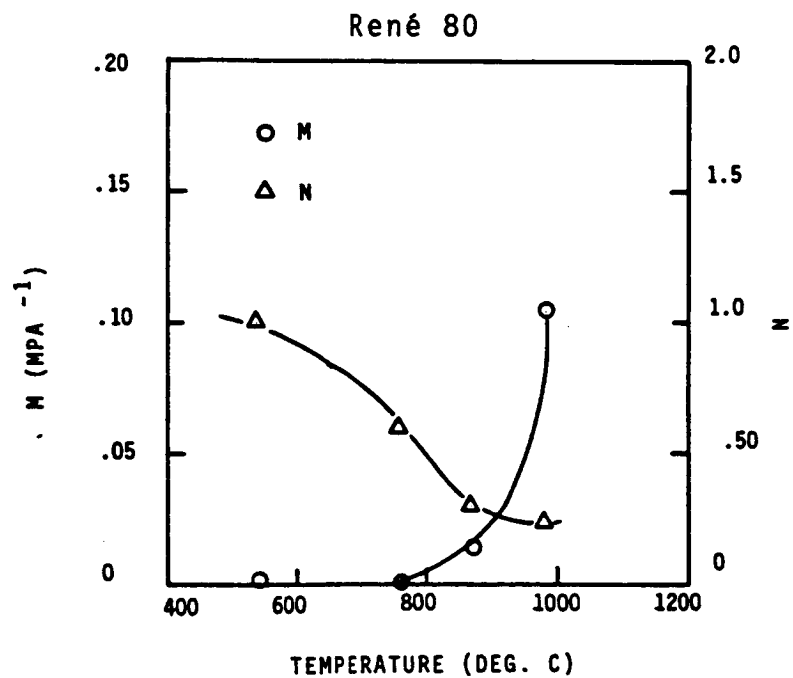
Figure 6.2   Variation of D and A with Temperature

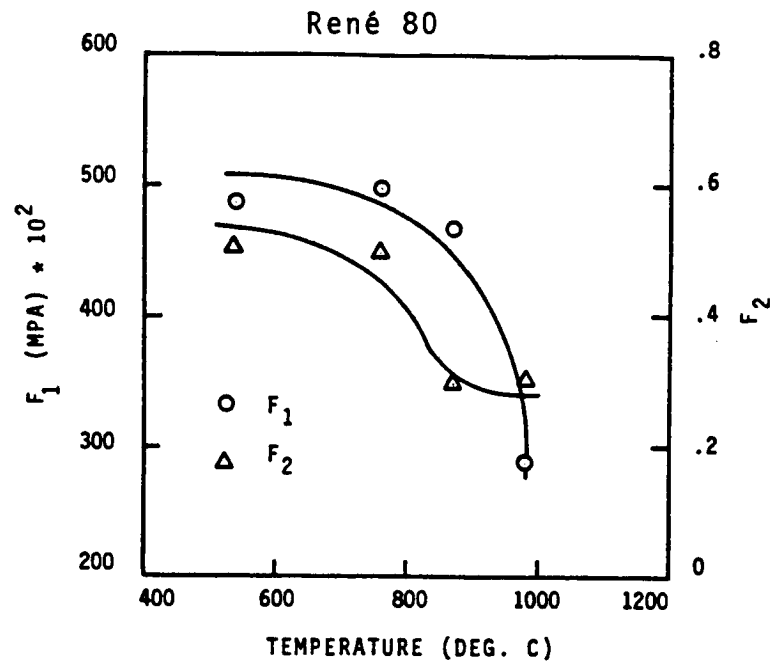Figure 6.3   Variation of M and N with Temperature

Figure 6.4 Variation of f_1 and f_2 with Temperature
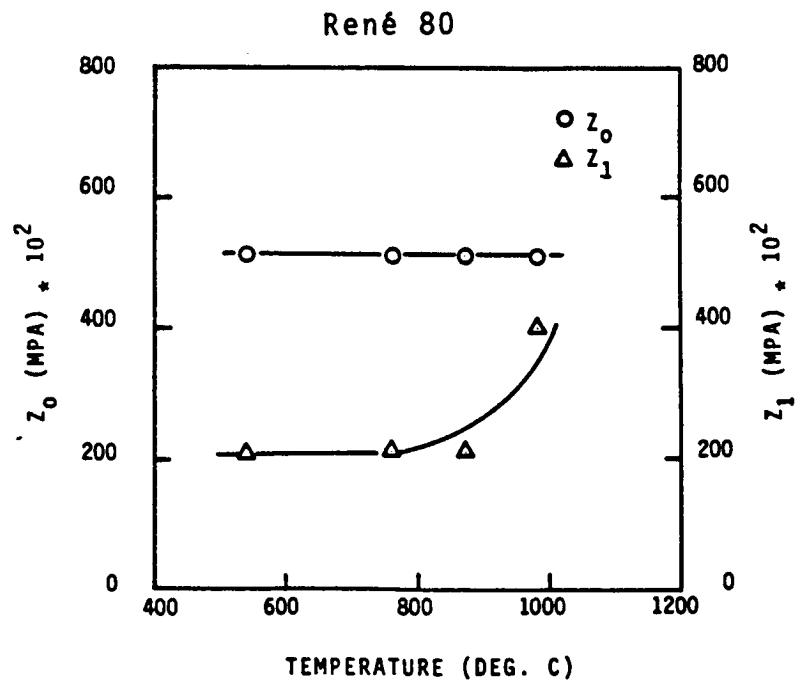

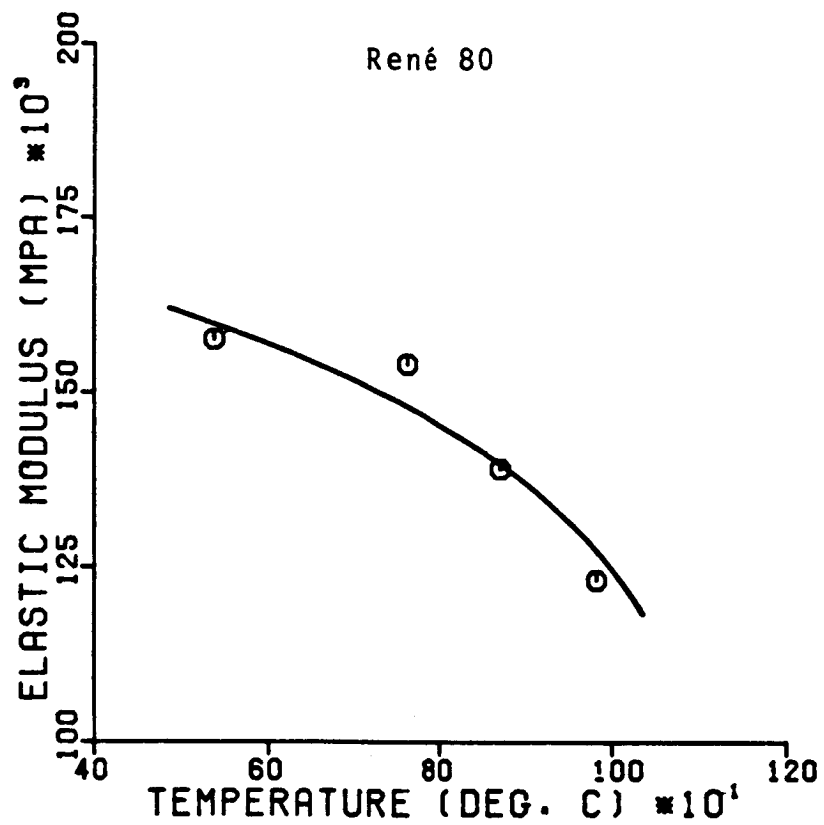Figure 6.5 Variation of Z_0 and Z_1 with Temperature

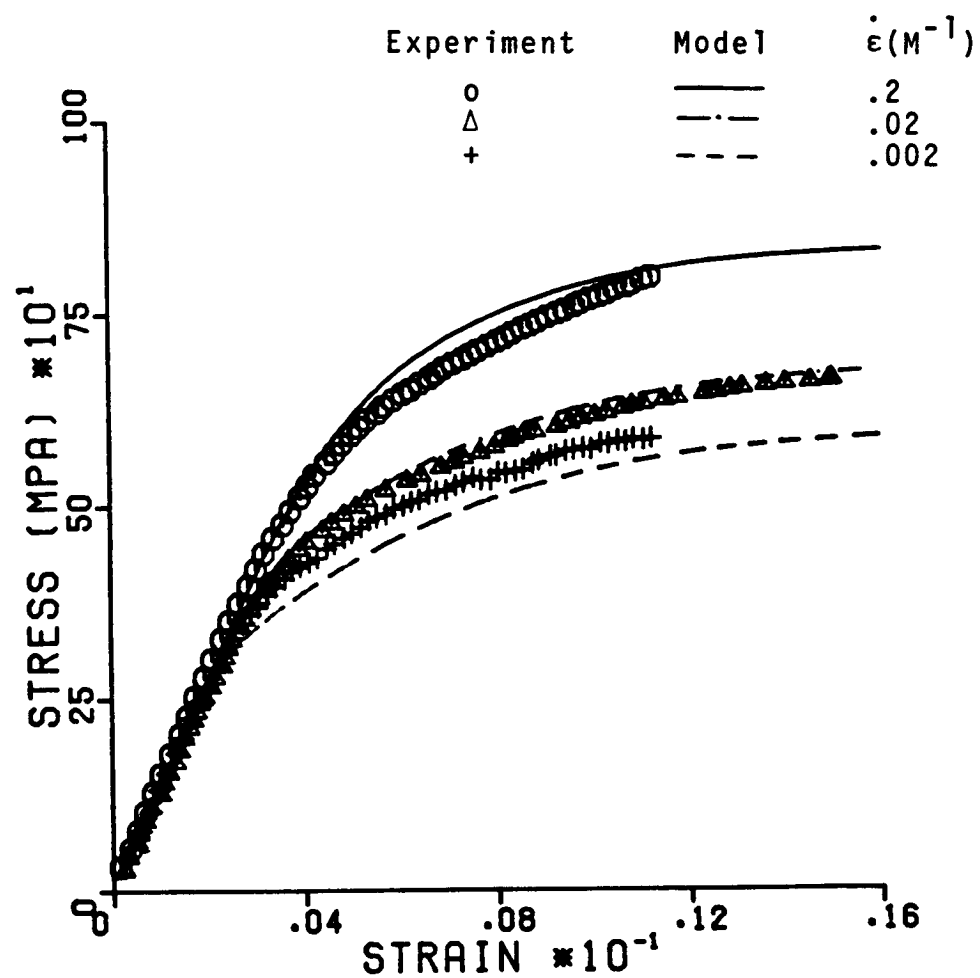Figure 6.6   Variation of Elastic Modulus with Temperature

Figure 6.7   Predicted and Experimental Tensile Response at 871°C
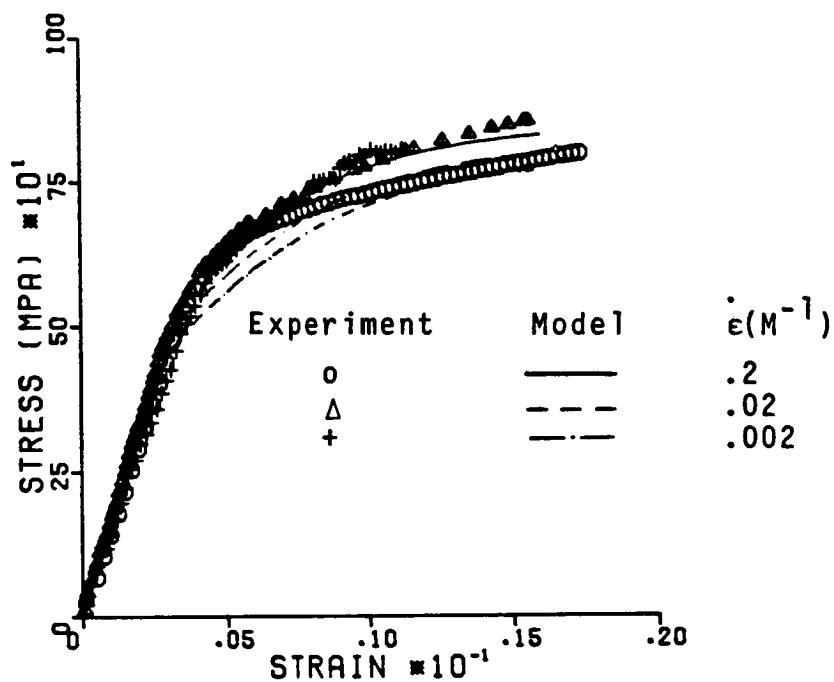
Figure 6.8   Predicted and Experimental Tensile Response at
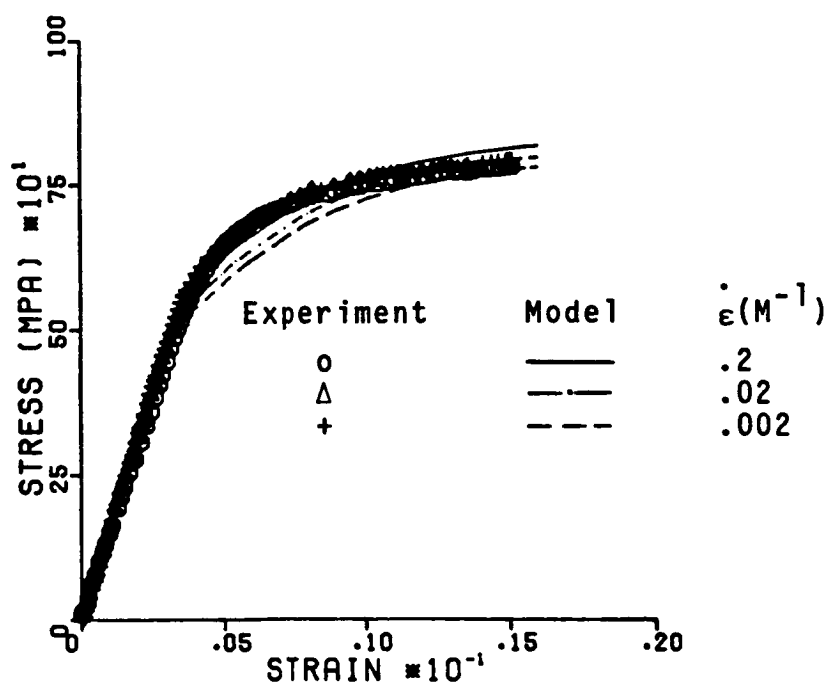   760°C

Figure 6.9   Predicted and Experimental Tensile Response at
             538°C

At 871°C, the strain rate dependent behavior of Rene´ 80 is modeled very well, as evidenced by the very good agreement between the calculated response and the test data. This is to be expected, since the material parameters were based on these data. However, the applicability of the model at 871°C is verified. Figures 6.8 and 6.9 show similar results at 760°C and 538°C. The agreement between the model and test data is again good. Notice the large difference in the strain rate sensitivity at 871°C and 538°C. The model predicts a small amount of strain rate sensitivity at 760°C. The results are, however, in close agreement with test data. This is a very significant result because it demonstrates that the unified constitutive equations developed here can model strain rate independent behavior at high temperatures. This essentially verifies the temperature capabilities of the model and constitutes a major step in nonisothermal modeling.

One monotonic tensile test was performed at 649°C (1200°F) at a strain rate of .02 M^{-1}. The tensile response of this test was calculated based on interpolated values of the various material parameters. The results are shown in Figure 6.10. The agreement between the model and the test results is excellent.
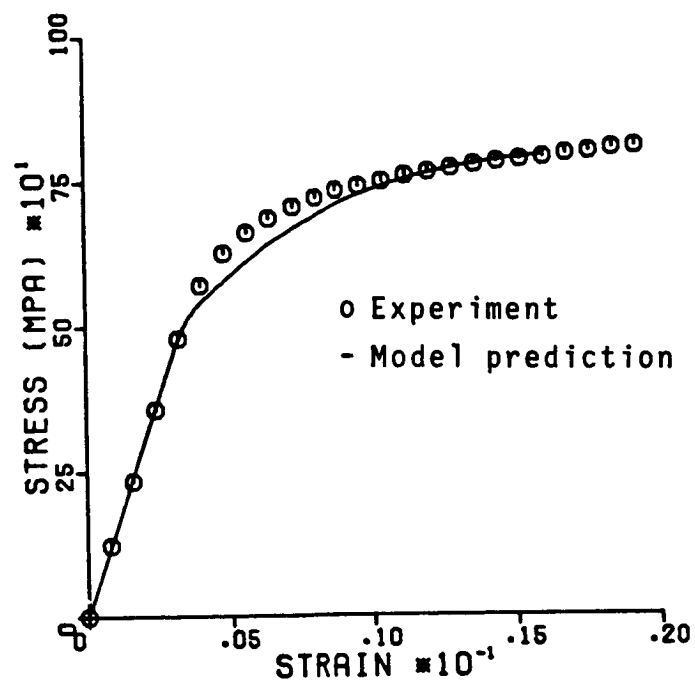
154

Figure 6.10   Predicted and Experimental Tensile Response at 649°C

This verifies that interpolation of the material parameters is possible at the intermediate temperatures. This indicates that the thermomechanical cyclic predictive capability of the model may be good.

6.4   The Cyclic Response of Rene´ 80

Gas turbine engine components can experience cyclic loads during service.   Thus, constitutive modeling of cyclic material behavior is very important. A large number of cyclic tests have been performed on Rene´ 80 at 982°C, 871°C and 760°C.   In Chapter 5, the cyclic response of the proposed constitutive model at 982°C was found to be in very good agreement with experimental data for a wide variety of cyclic tests. This section describes similar results for 871°C and 760°C.

At 871°C, cyclic softening behavior in the first few cycles was observed, similar to 982°C.   The softening is isotropic in nature and is modeled using the drag stress (Equation 4.13) which decreases as a function of the accumulated inelastic work.   The material parameters related to the cyclic softening model were determined using cyclically saturated hysteresis loops, as described previously, and are recorded in Table 6.1.   At 871°C, the rate of cyclic

softening is much less than at 982 °C and it is not certain from the test data that cyclic saturation had been reached for all the tests.

6.4.1 Cyclic Predictions at 871 °C

Cyclic behavior predictions have been made for the various cyclic tests at 871 °C using the cyclic integration scheme described in Section 5.6. Figure 6.11 shows the results for a fully reversed, high strain rate (.2 M^{-1}) cyclic test. Loops are shown for cycles 64 and 116. The latter is near the end of the test and is considered as the saturated hysteresis loop for material parameter evaluation.

The model appears to predict the cyclic behavior very well at this strain rate. The saturated hysteresis loop for a similar test at a low strain rate (.002 M^{-1}) is shown in Figure 6.12. The model predicts less softening, and there is some difference in the elastic modulus. Notice that the test data shows a slight tension-compression asymmetry. The stress relaxation during a 120 second tensile strain hold is shown in Figure 6.13 for cycle 50 in the test. Next, a compressive mean strain test (A_ϵ=-1) was run to induce mean stress transient behavior. The first four cycles of a test at a strain rate of .002 M^{-1} are shown in
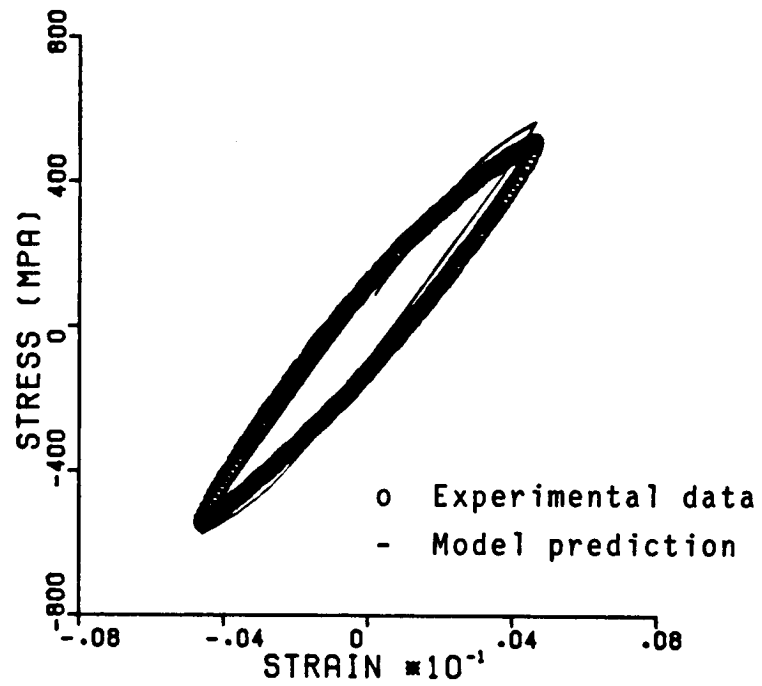
(a) Cycle No. 64
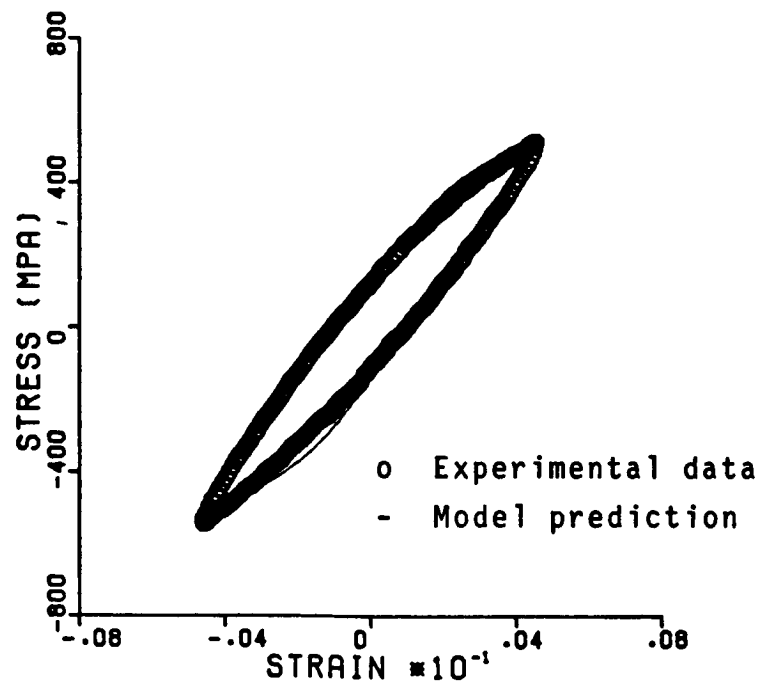
(b) Cycle No. 116

Figure 6.11 Predicted and Experimental Cyclic Response at
871°C, .2M⁻¹

158

Figure 6.12   Predicted and Experimental Cyclic Response at
871°C, .002M^{-1} (Cycle No. 46)
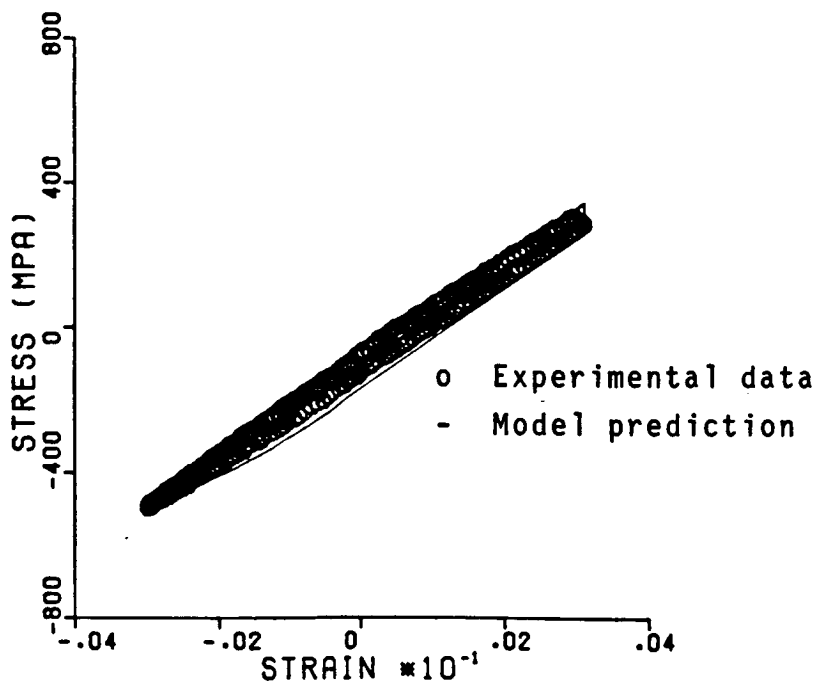
Figure 6.13   Predicted and Experimental Cyclic Response at
871°C, 120 Second Hold Time   (Cycle No. 50)

o, Δ , +   Experimental data
—   Model prediction

(a)   Cycles 1, 2, 3

o   Experimental data
-   Model prediction
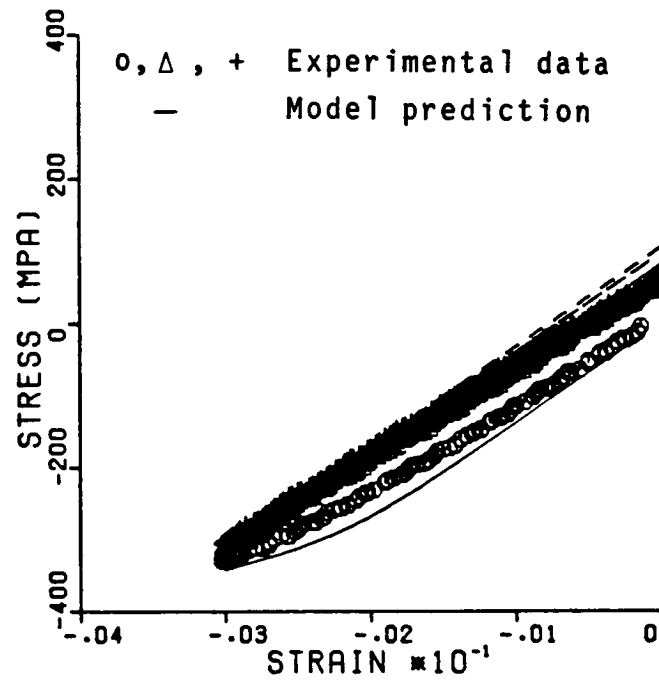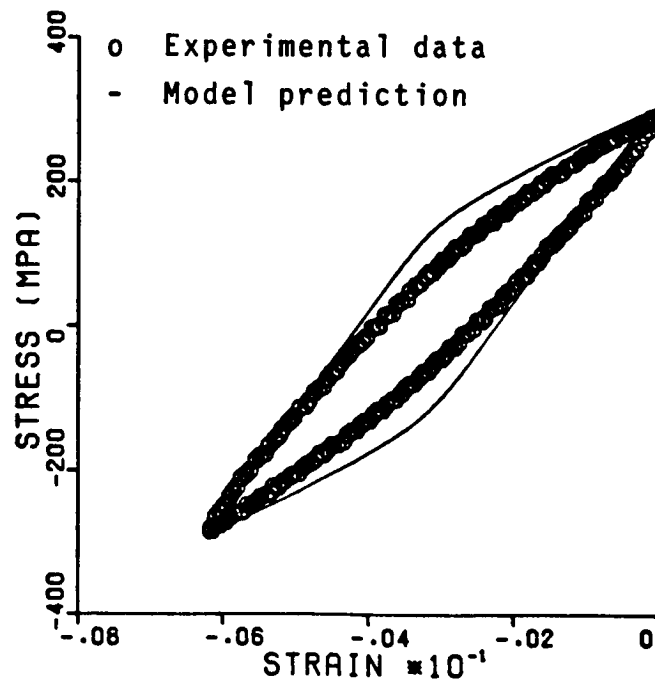
(b)   Cycle No. 64

Figure 6.14   Predicted and Experimental Cyclic Response at
871°C, A_ϵ= -1

Figure 6.14a. The compressive mean stress is seen to relax to a stable value after a few cycles. Figure 6.14b shows the steady state hysteresis loop for cycle 64. The predictions appear good especially considering that this result is after a number of transients due to changes in the strain range.

6.4.2 Cyclic Predictions at 760°C

In general, all the cyclic tests at 760°C showed very little inelasticity even for the largest strain ranges. Since there is no cyclic softening at this temperature, the cyclic predictions were made using a constant drag stress ($Z=Z_0$). Figure 6.15 shows cycle 114 of a fully reversed, high strain rate ($.2$ M^{-1}) test. The model predicts a larger inelastic strain range; however, the experimental result ($\Delta\epsilon^I \approx .0005$) is near the resolution of the extensometer. The tensile peak stress is predicted well but not the compressive peak. Notice that there is a tension-compression asymmetry in the experimental results. Figure 6.16 shows cycle 54 of a fully reversed cyclic test at .002 M^{-1}. Both the model and test data contain a larger inelastic strain range as compared to the high strain rate test. Again, the model overpredicts the inelastic

Figure 6.15   Predicted and Experimental Cyclic Response at
760°C, .2M^{-1} (Cycle No. 114)
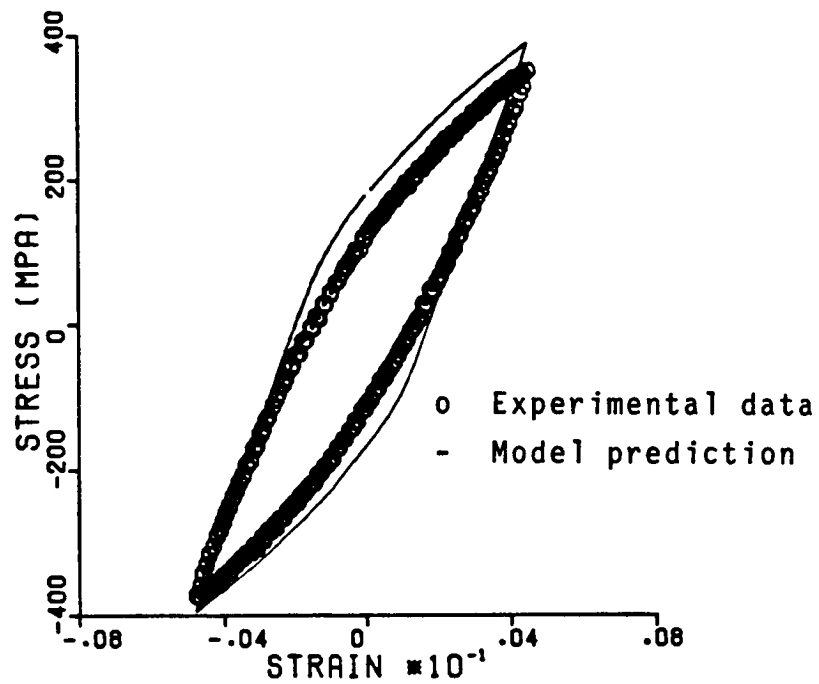

Figure 6.16   Predicted and Experimental Cyclic Response at
760°C, .002M^{-1} (Cycle No. 54)
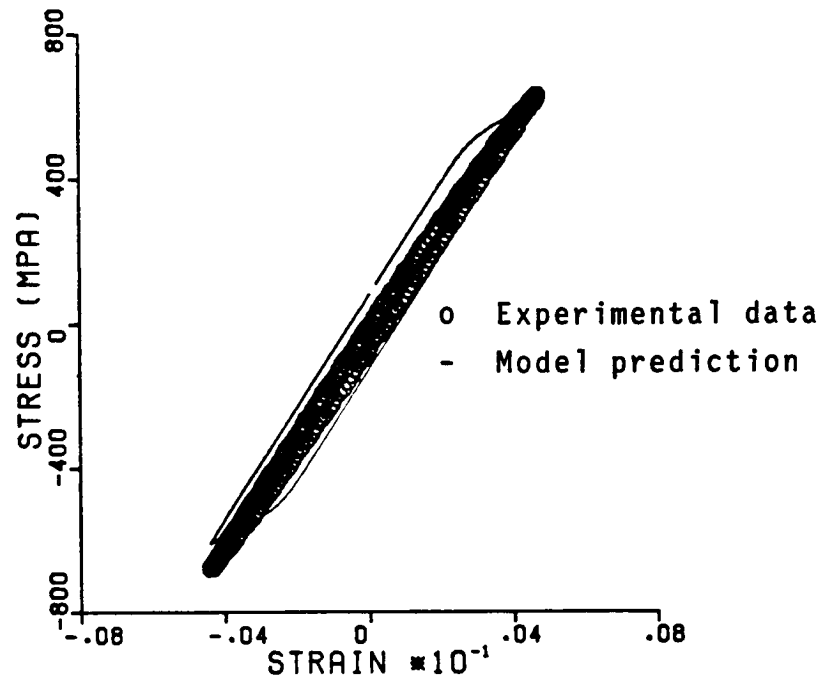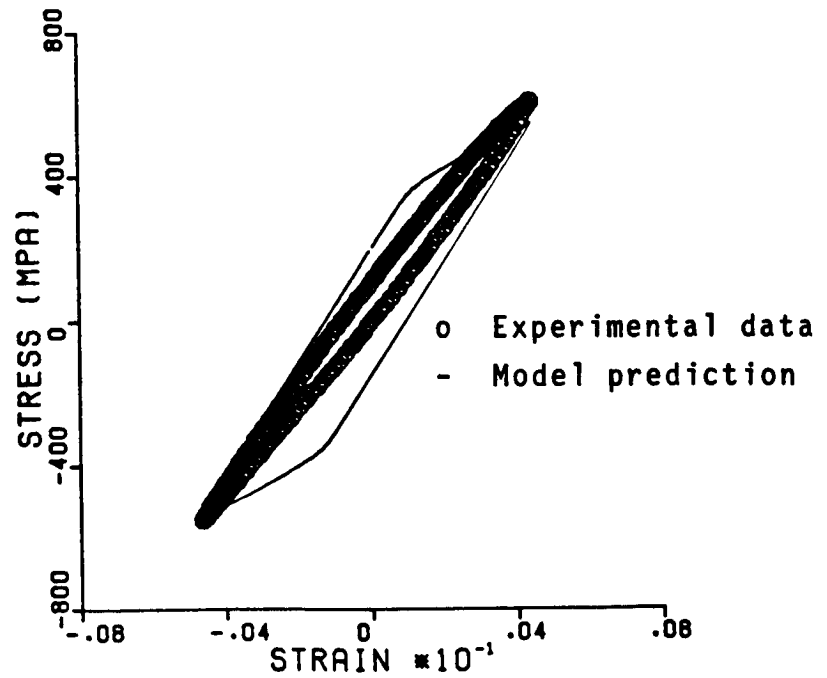
162

strain range, and there is also asymmetry in experimental results.

Figure 6.17a shows the various hysteresis loops predicted by the model for a cyclic test with a tensile mean strain (A_ϵ=+1) at .2 M^{-1}. Notice that the peak stresses decrease during cycling, and the mean stress decreases. The loops shown in this figure represent the entire history of 183 cycles. Notice also the influence of reversed inelastic flow on the subsequent cycles. The predicted results are compared with test data in Figures 6.17b, 6.17c and 6.17d for various cycles. Even though cycle 45 (Figure 6.17b) and cycle 85 (Figure 6.17d) have the same strain range, the stress ranges are very different due to the inelastic strain history and mean stress relaxation. Figure 6.17c shows the hysteresis loop for cycle 63 which has a higher strain range and, hence, shows a larger, but still very small, inelastic strain.

Figure 6.18 shows the results for a 120 second tensile strain hold cyclic test. It is significant to note that the test result shows some stress relaxation, even though the tensile behavior at 760°C is rate independent. Cycle 20 (Figure 6.18a) is almost elastic with a small amount of stress relaxation. Cycle 94 has a larger strain range and shows larger inelastic
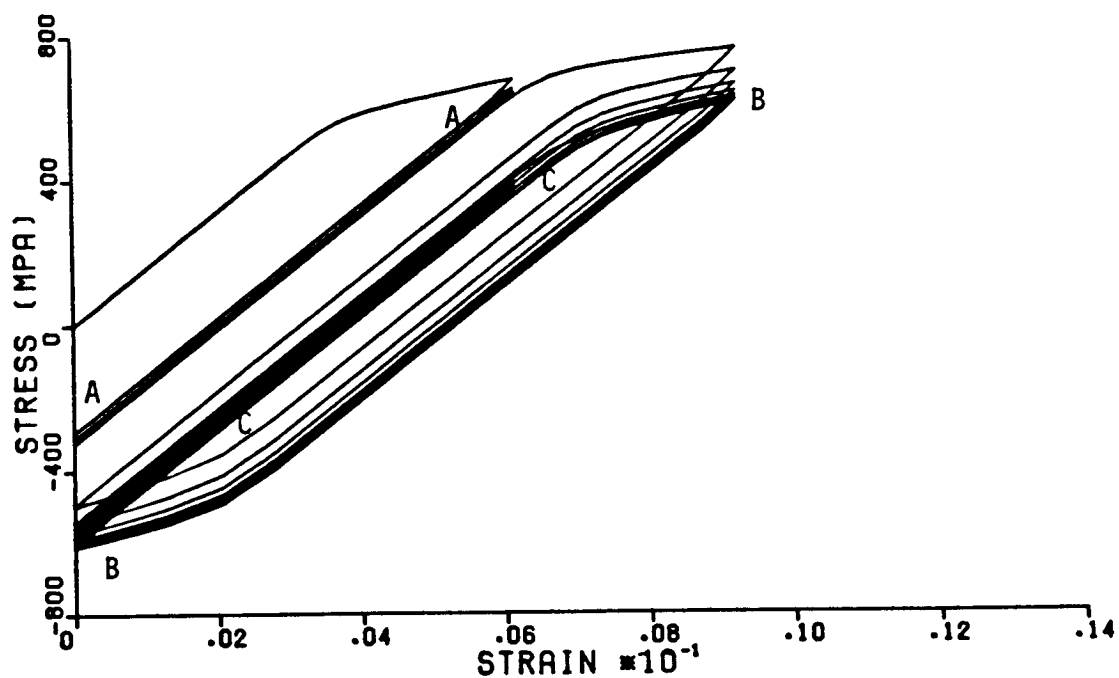
(a) Predicted Hysteresis Loops for the Entire Test

o Experimental data
- Model prediction
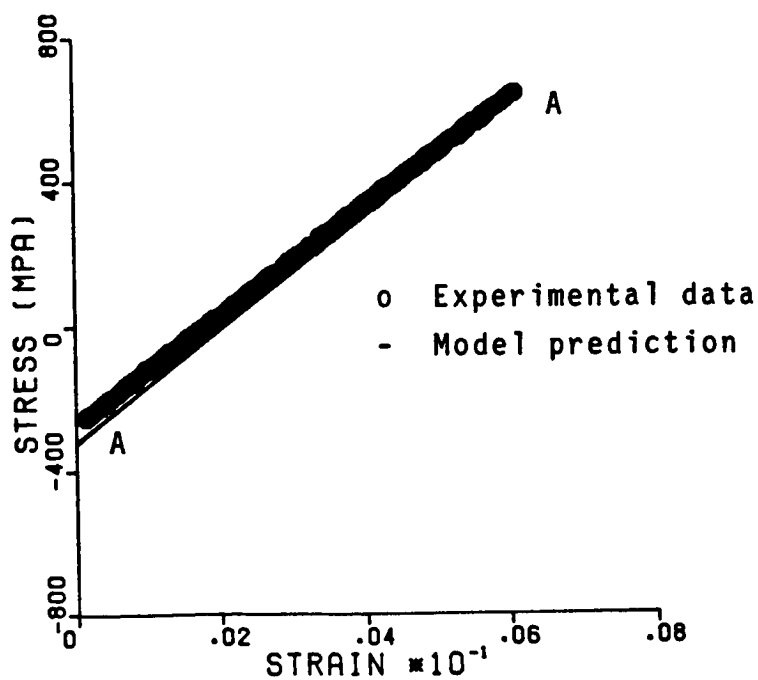
(b) Cycle No. 45

Figure 6.17 Predicted and Experimental Cyclic Behavior with Mean Stress at 760°C, $.2M^{-1}$

164
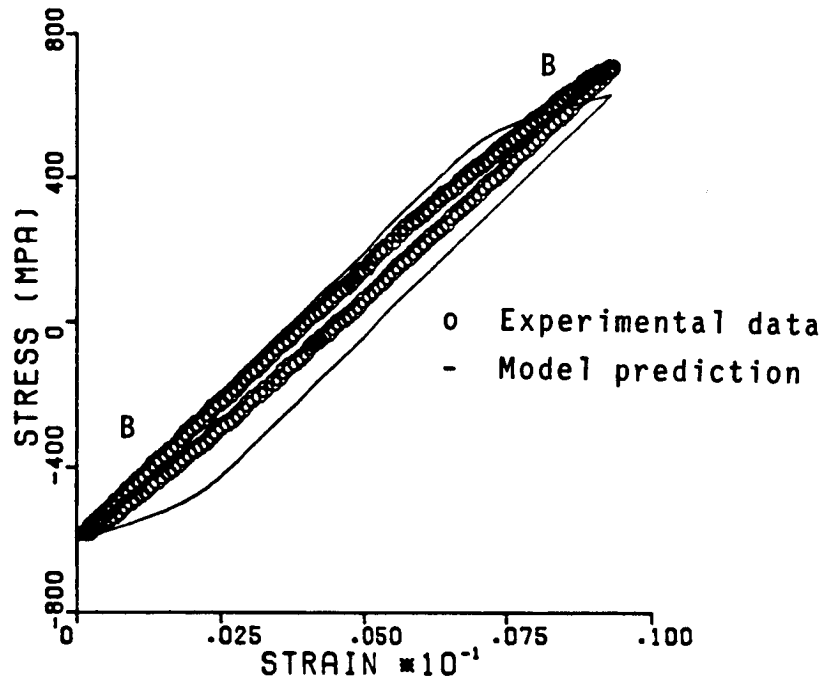
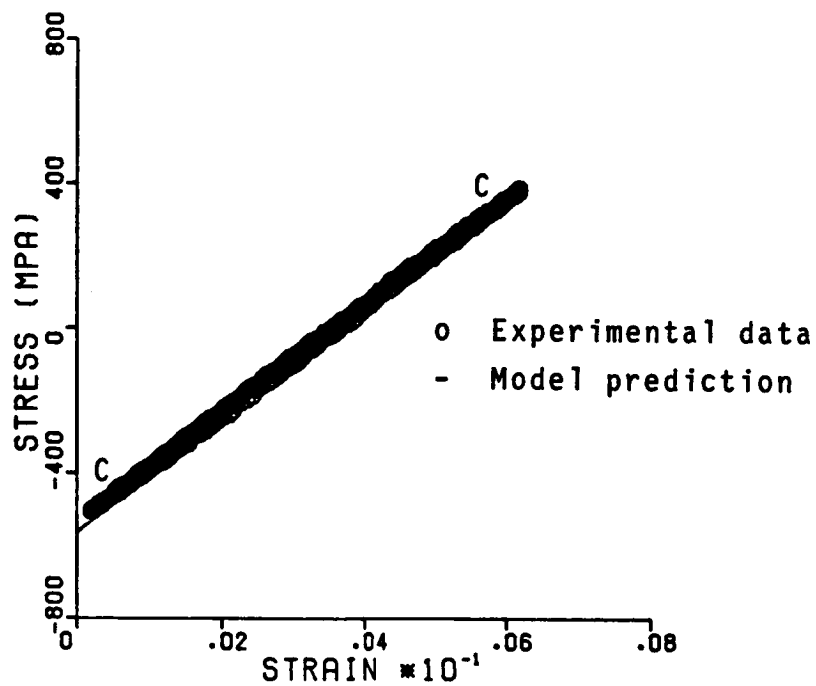(c) Cycle No. 63

(d) Cycle No. 85

Figure 6.17 (cont.) Predicted and Experimental Cyclic Behavior with Mean Stress at 760°C, .2M^{-1}

165
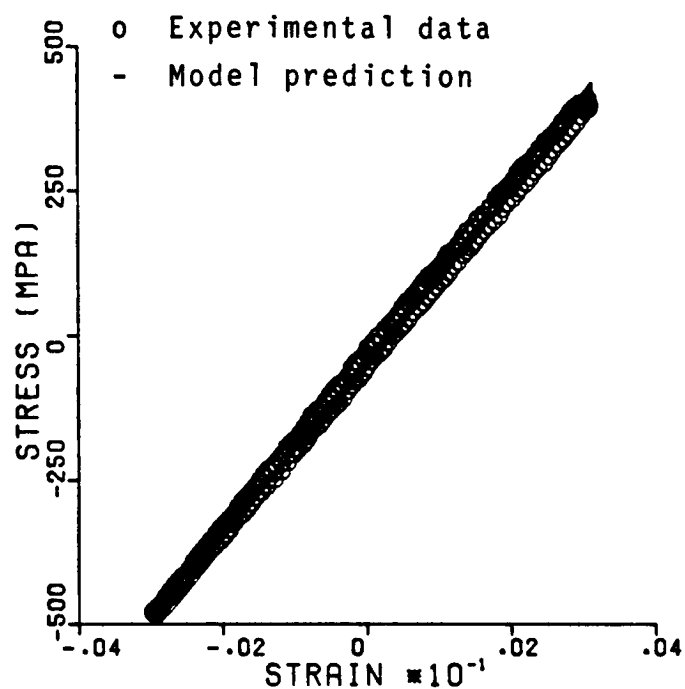
(a) Cycle No. 20
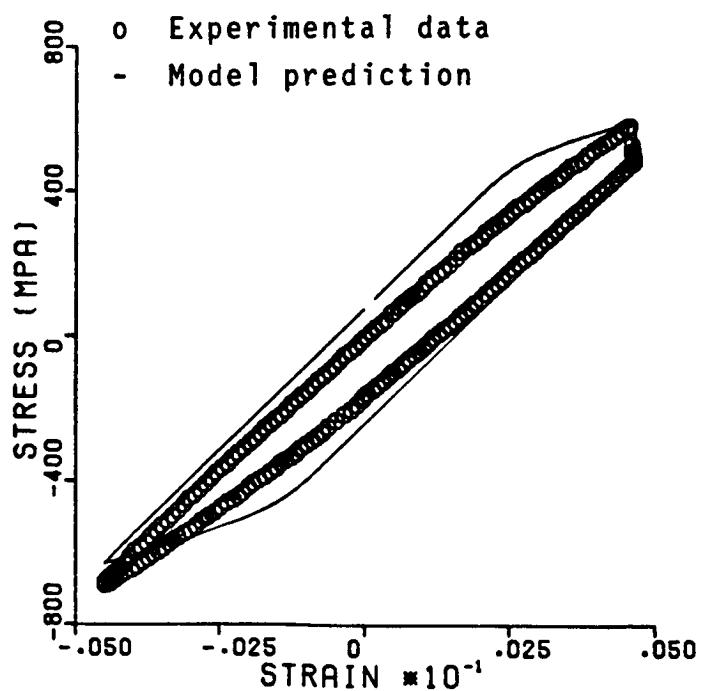
(b) Cycle No. 94

Figure 6.18   Predicted and Experimental Cyclic Behavior at
760°C, 120 Second Hold Time

166

strains and stress relaxation. The model appears to predict the amount of stress relaxation reasonably well. In general, there is a significant difference in the elastic moduli of the various test specimens. An average elastic modulus was used for all calculations.

6.5 Creep Response at 871°C and 760°C

Recall, Rene' 80 displayed strain rate independent tensile behavior at 760°C and below. However, as shown in Figure 6.18, stress relaxation was observed during a 120 second tensile strain hold. It has also been observed that at high values of stress, creep also occurs at 760°C. The unified model could predict reasonably well the time dependent response at 982°C and strain rate independent tensile behavior and short time stress relaxation at 760°C. The creep response is a long time behavior, and it was found that it could not be predicted well. This led to a further investigation of the monotonic and creep response results.

The saturated values of the stress and strain rates in the tensile and creep tests are shown in Figure 6.19. At 982°C, the monotonic and creep results are consistent; however, this is not the case at 871°C and 760°C. At 871°C, strain rate sensivity is present
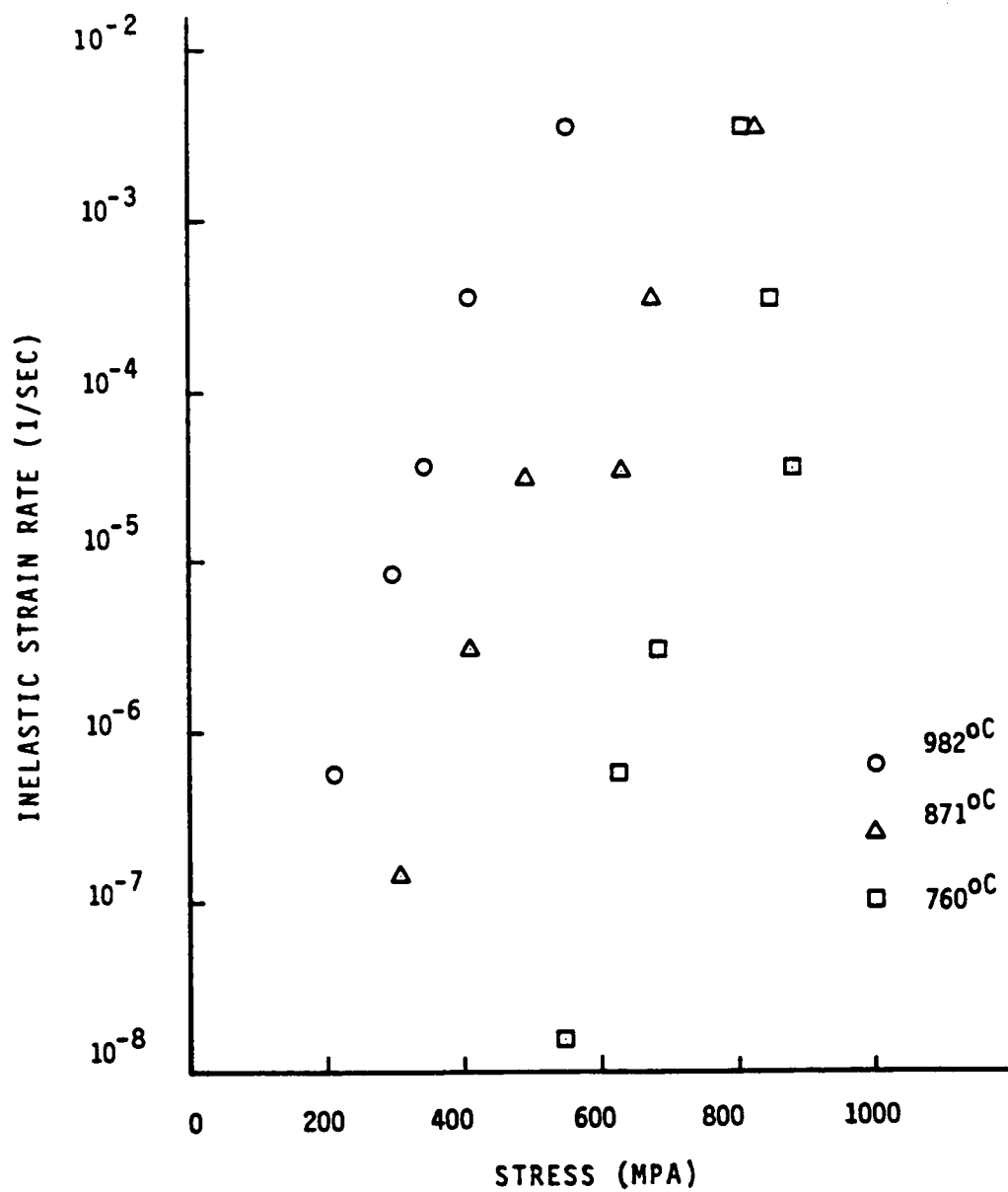
Figure 6.19   Inelastic Strain Rate Versus Saturated Stress
for René 80

168

in both the short time (tensile) response and the long time (creep) response. However, there is a distinct discontinuity in the curve between short time and long time results. At 760°C, there is no rate dependence in the tensile data, but creep is present.

Static thermal recovery effects in the long time response of materials have traditionally been modeled using terms like R_{ij} in Equation 5.25. A number of attempts at this showed that such static recovery terms in the proposed model are not effective in modeling creep behavior. An examination of the evolution equation (5.17) for the back stress shows that it approaches a steady state value, Ω_S, during creep and this value is not the same as Ω_{max}, determined in the high rate tensile tests. Thus, for long time creep response, the steady state back stress decreases as shown in Figure 6.20 for creep at 760°C. Physically, this could correspond to dislocation pileups decreasing through a dislocation climb process over long periods of time.

The back stress recovery can then be modeled as

$$\dot{\Omega}_S = -A\left(\frac{\sigma}{\sigma_0}\right)^n(\Omega_S - \Omega_{sat}), \tag{6.2}$$

where $\Omega_S(0) = \Omega_{max}$. In Equation 6.2, Ω_S is the steady
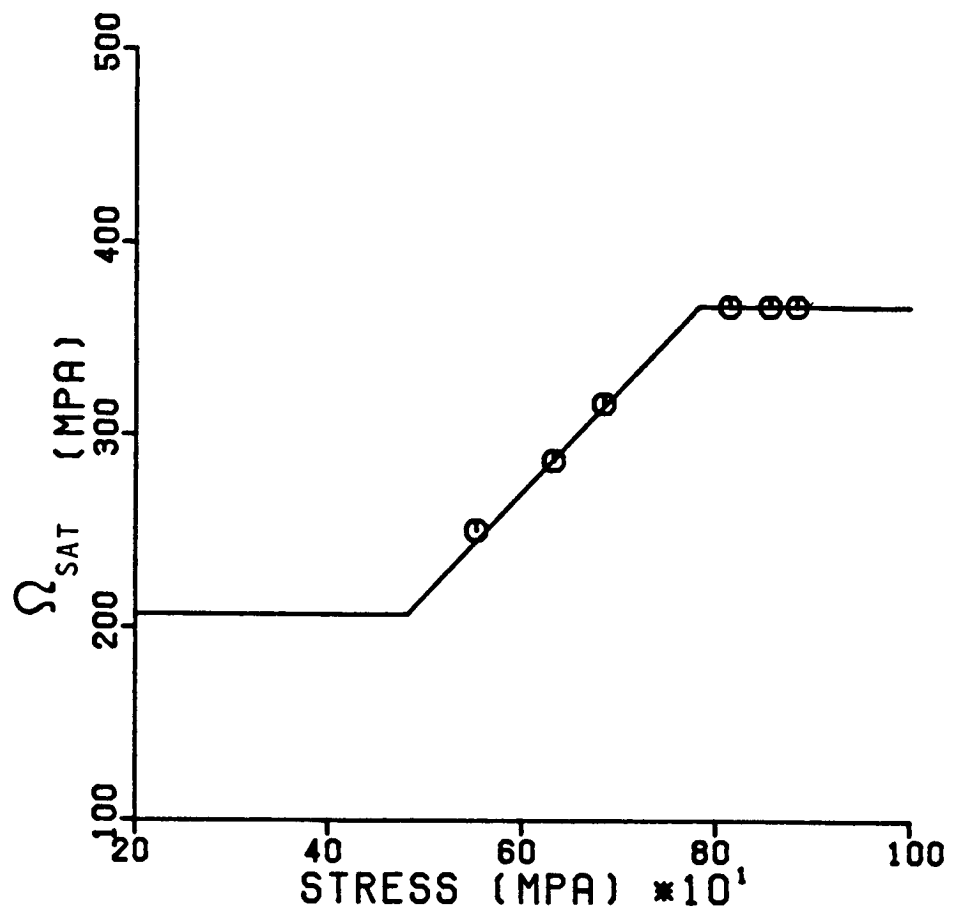
Figure 6.20   Variation of Saturated Back Stress with Applied
Stress   (René 80, 760°C)

state value of the back stress; Ω_{sat} is the saturated value of the back stress observed in uniaxial monotonic and creep tests. The value of Ω_{sat} is expressed as a function of the effective stress, as shown in Figure 6.20. A lower bound is imposed on the minimum value of Ω_{sat} to represent the minimum value of the back stress. Modeling long time recovery effects using the saturated value of back stress has been suggested by other investigators also [54].

The results of using the back stress recovery equation (6.2) appear to give good results for Rene' 80 at 760°C and 871°C. Figure 6.21 shows the results for the three creep tests at 760°C. Both the high stress and low stress creep results appear good; whereas, the intermediate stress case is not predicted quite as well. Similar results are shown in Figure 6.22 for the three creep tests at 871°C. It was found that the creep predictions at the lower temperatures are very sensitive to the saturated value of the back stress, Ω_s.

In summary, it is seen that the proposed constitutive model is applicable for a range of temperatures. It is able to model the strain rate sensivity difference at high and low temperatures. The monotonic, cyclic, and creep predictions are in good
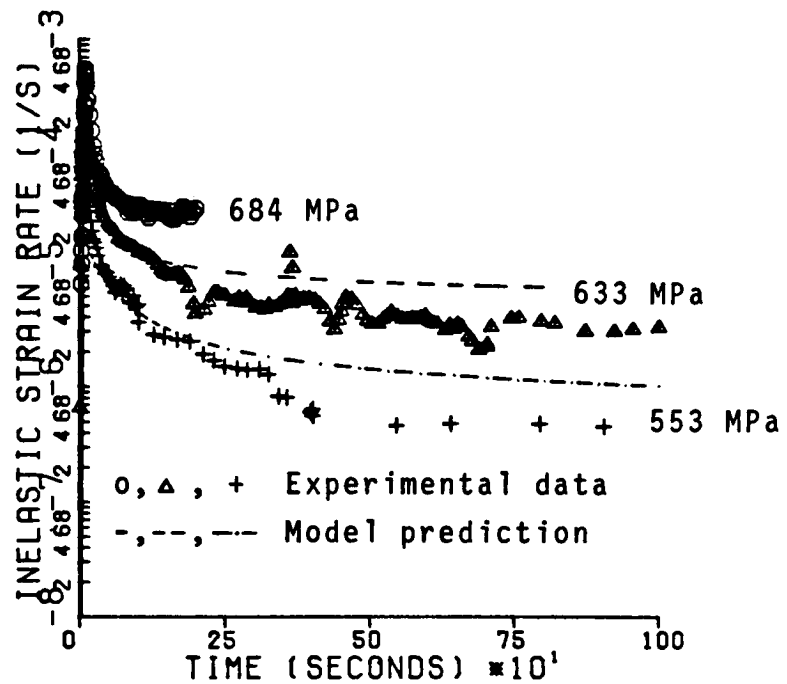
(a) Inelastic Strain Rate
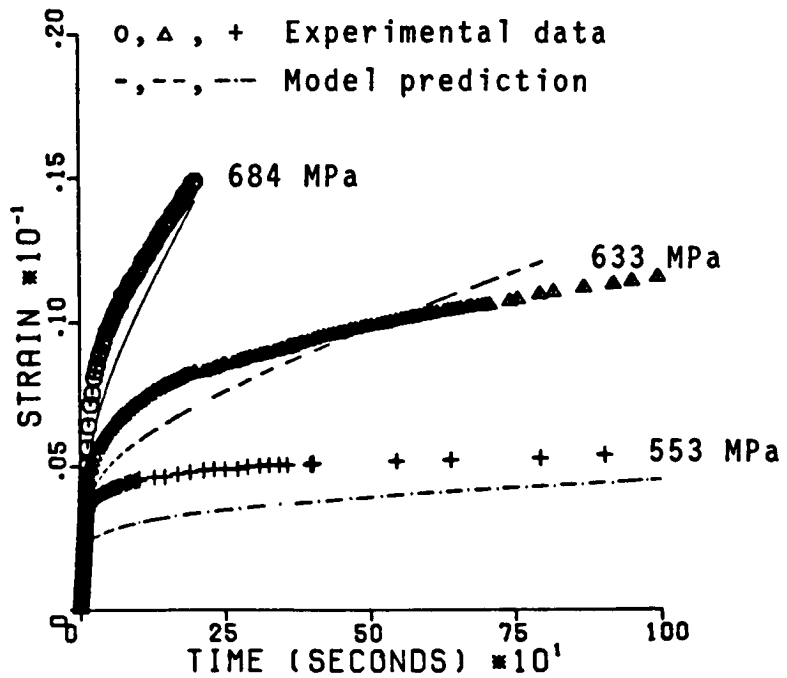
(b) Total Strain

Figure 6.21   Predicted and Experimental Creep Response at 760°C

172
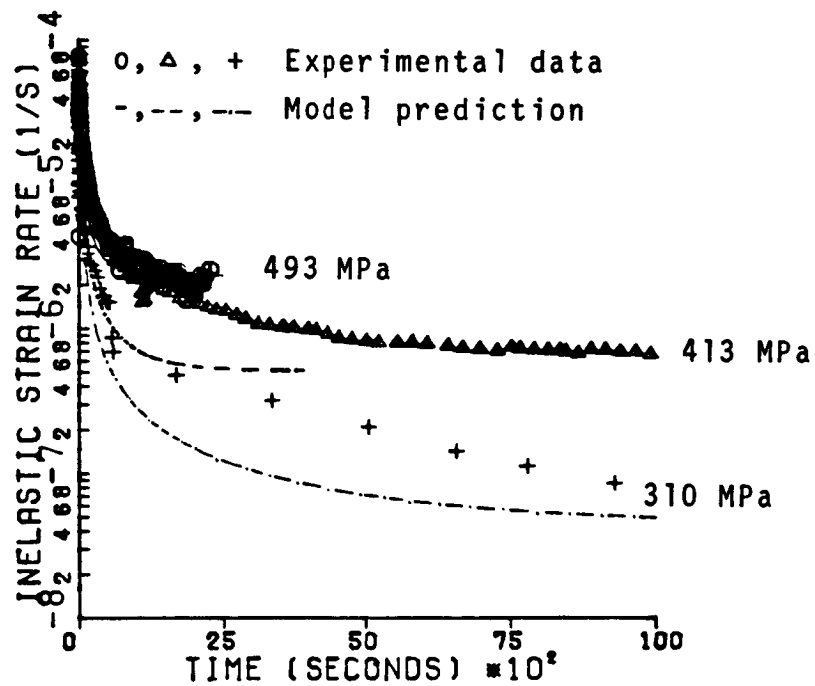
(a) Inelastic Strain Rate
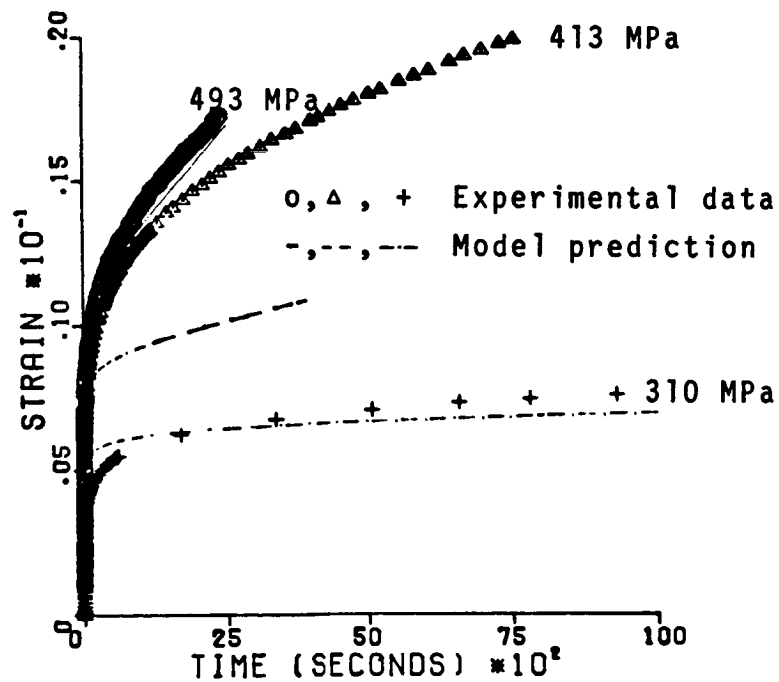
(b) Total Strain

Figure 6.22 Predicted and Experimental Creep Response at 871°C

173

agreement with experimental data at 982°C, 871°C and 760°C. A new form of recovery model is proposed which predicts low temperature creep behavior relatively well.

TABLE 6.1

MATERIAL CONSTANTS FOR PROPOSED MODEL (RENE´ 80)

Constant	TEMPERATURE 982°C (1800°F)	871°C (1600°F)	760°C (1400°F)	538°C (1000°F)
n	.2418	.3005	.6	1.0
D sec^{-1}	1.0	10.0	10,000	10,000
A	1.0	1.0	.0609	.000916
f_1 MPa	2.88×10^4	4.65×10^4	4.97×10^4	4.86×10^4
f_2	.3005	.2926	.4944	.5058
f_3	.4772	.4566	.5018	0
f_4 MPa	10.3	-29.5	-28.3	0
f_5 sec^{-1}	4.526×10^{-4}	2.126×10^{-3}	7.625×10^{-7}	0
r	8.458	3.0609	13.7	0
x_1 MPa	91.8	91.8	229.6	367.4
x_2 MPa	188.4	256	367.4	367.4
Ω_{max} MPa	283	384	551	551
m MPa^{-1}	.103	.0126	0	0
Z_o MPa	5.1×10^4	5.1×10^4	5.1×10^4	5.1×10^4
Z_1 MPa	4.0×10^4	2.1×10^4	2.1×10^4	2.1×10^4

CHAPTER 7

MODELING MULTIAXIAL RESPONSE CHARACTERISTICS

Almost all the constitutive models that have been developed to date are based on uniaxial experimental results. This is due to a lack of an adequate multiaxial behavior experimental data base. The typical approach has been to extend the uniaxial model to multiaxial cases based on equivalent stresses and strains [55] and the assumption of plastic incompressibility. However, such approaches can lead to significant errors for some types of materials and multiaxial loading conditions [56].

In the model proposed here the material functions in the evolution equation for the back stress were considered as fourth order tensors. This form of the equation is more general than the uniaxial form. For the case of an incompressible isotropic material the constitutive parameters reduced to scalar functions that can be determined from the uniaxial response. The resulting multiaxial constitutive equations (4.13, 5.6, 5.24, and 5.25) are fairly simple. Recall, the uniaxial response of the model was verified for a number of experiments at several temperatures. In this chapter the multiaxial capabilities of the model will

be described in detail. The multiaxial loading
conditions and the associated material phenomena are
briefly discussed first.

7.1 Multiaxial Material Behavior

The multiaxial material response poses major
challenges both experimentally and theoretically. Most
of the multiaxiality studies to date have been
concerned with the analysis of low cycle fatigue life
[57-61] and the development of appropriate failure
criteria.   The multiaxiality effects on fatigue life
arise mainly due their impact on the cyclic inelastic
behavior.   Multiaxial predictions are also important
for the dimensional stability of structures such as
blades and vanes.   Thus, it is important that
constitutive equations be able to model the cyclic
inelastic response under multiaxial loading conditions.

There are two basic types of multiaxial loading
conditions: proportional and nonproportional.   Under
conditions of strain control, proportional loading is
defined by

$$\epsilon_{ij}(t) = F(t) \cdot C_{ij}, \tag{7.1}$$

where C_{ij} is independent of time and $F(t)$ is a scalar

function of time. Equation 7.1 implies that all the components of the strain tensor ϵ_{ij} vary proportionately in time at all locations in a structure. Proportionality can also be defined for the stress tensor, σ_{ij} [57]. In general, these two definitions are not equivalent when inelastic strains are involved. In some high temperature applications such as blades and vanes of gas turbines, approximately proportional loading conditions prevail. However, in most applications loading conditions are usually nonproportional.

The effects of the proportionality or nonproportionality of the multiaxial loading are most significant in the cyclic behavior of the material. Usually it is assumed that materials which cyclically harden or soften attain a unique final state. Based on this assumption the cyclic transient behavior is neglected and only the stable behavior is modeled, using a cyclic stress strain curve [62-64]. These approaches were proposed based mostly on uniaxial experiments. However, it has been experimentally shown that, under multiaxial loading conditions, the assumption of a unique cyclically stable state is valid only for proportional loading [65-67]. For nonproportional loading conditions, a number of cyclically

hardening materials are found to attain cyclically stable states which are harder than that attained under proportional loading conditions [56,60,65,68,69]. However, there is very little experimental data available under nonproportional multiaxial loading conditions for cyclically softening materials. It has been suggested that cyclically softening metals may soften less or even harden under nonproportional loading [70].

The additional hardening observed for nonproportional loading conditions has generally been attributed to the differences observed in the deformation mechanisms. For proportional strain cycling, Equation 7.1, the principal directions of the applied strain are constant. In this case it is expected that slip and dislocation interactions are limited to a few, favorably oriented planes in each grain during the entire loading cycle. However, for nonproportional loading the principal directions and the maximum shear planes are not constant. For example, in 90 degree out of phase tension/torsion cycles, the maximum shear plane continuously sweeps through all the planes. Similarly, dislocation interaction also occurs on all the planes under nonproportional cycling conditions. This increased level of dislocation interactions is largely responsible for the additional hardening. In addition,

deformation induced material transformations have also been reported for some materials [71]. These general implications of observed differences in material behavior for proportional and nonproportional loading cycles have not been established for Rene' 80.

Constitutive modeling must be guided by experimental results for both proportional and nonproportional multiaxial loading cycles. The following sections describe the modeling of Rene' 80 at 982°C and 871°C at two strain rates, .02 M^{-1} and .002 M^{-1}. Pure torsion results are also included for comparisons with proportional and nonproportional tension/torsion results. The constitutive model developed in Chapter 5 is used to predict the response. The predictions are based on Equations (4.13, 5.6, 5.24, and 5.25) with no additional terms for nonproportional loading. The material parameters used are those shown in Table 6.1.

7.2 Pure Cyclic Shear Response

The proposed constitutive model was developed in fully three dimensional form. The material parameters in the model were evaluated based on uniaxial experiments as discussed previously. Another verification of the constitutive model can be obtained

by predicting the experimental results from pure torsion tests. For pure shear loading

$$\varepsilon_{ij} = \begin{bmatrix} 0 & \varepsilon_{12} & 0 \\ \varepsilon_{12} & 0 & 0 \\ 0 & 0 & 0 \end{bmatrix}, \qquad S_{ij} = \begin{bmatrix} 0 & \tau & 0 \\ \tau & 0 & 0 \\ 0 & 0 & 0 \end{bmatrix},$$

$$\dot{\varepsilon}_{ij}^{I} = \begin{bmatrix} 0 & \dot{\varepsilon}_{12}^{I} & 0 \\ \dot{\varepsilon}_{12}^{I} & 0 & 0 \\ 0 & 0 & 0 \end{bmatrix}, \qquad \Omega_{ij} = \begin{bmatrix} 0 & \Omega_{12} & 0 \\ \Omega_{12} & 0 & 0 \\ 0 & 0 & 0 \end{bmatrix} \qquad (7.2)$$

and

$$K_2 = (\tau - \Omega_{12})^2 \quad \text{and} \quad \dot{\varepsilon}_e^{I} = \frac{2}{\sqrt{3}} \dot{\varepsilon}_{12}^{I} \ .$$

The tensorial shear strain, ε_{12}, (half of the engineering shear strain γ) is used throughout this study. Using Equation 7.2 the constitutive equations (4.13, 5.6, 5.24, and 5.25) for pure torsion become

$$\dot{\varepsilon}_{12}^{I} = D \ \exp\left[-\frac{A}{2} \left\{ \frac{Z}{\sqrt{3}(\tau - \Omega_{12})} \right\}^{2n} \right] \frac{(\tau - \Omega_{12})}{|\tau - \Omega_{12}|} \qquad (7.3)$$

$$\Omega_{12} = \frac{G}{E}\tau + \Omega_{12}^{I} \qquad (7.4)$$

$$\dot{\Omega}_{12}^{I} = f_1 \dot{\varepsilon}_{12}^{I} - \sqrt{3} f_1 \frac{\Omega_{12}}{\Omega_{max}} \dot{\varepsilon}_{12}^{I} \qquad (7.5)$$

181

$$\overset{\bullet}{Z} = 2m(Z_1 - Z)\tau \overset{\bullet}{\epsilon}_{12}^{I} \tag{7.6}$$

Equation 7.5 predicts that for monotonically increasing torsional load, saturation occurs when $\Omega_{12} = \frac{1}{\sqrt{3}}\Omega_{max}$, where Ω_{max} is the saturated value of the back stress determined from uniaxial tensile tests. This has been verified in the computer program used to make the analytical predictions, using the same equivalent strain rate for tensile and torsional loading.

Pure cyclic torsion tests were performed using cyclic block sequences with variable strain ranges, similar to the uniaxial cyclic tests shown in Figure 3.3. Two strain rates, .02 M^{-1} and .002 M^{-1}, and two temperatures, 982°C and 871°C, were used. In all the torsion tests the cyclic hysteresis loops show a small bias in the negative loading direction. This asymmetry in the stress strain behavior remained almost constant throughout the test. It is possible that this may be related to the starting conditions in a test (the data is not clear). It has also been noticed that a small amount of axial stress develops for the pure torsion tests. The exact cause of this axial stress and whether it has any relationship to the asymmetry in the hysteresis loops cannot be conclusively determined from

the existing data. A possible way of modeling the asymmetric torsional behavior will be shown later in this section.

Figures 7.1 and 7.2 show comparisons of the predicted and experimental behavior in cyclic torsion at 982°C at .02 M^{-1} and .002 M^{-1}. The agreement between the model and the test data is very good. Recall that all the material parameters had been determined from only the uniaxial tests. The cyclic integration scheme outlined in Chapter 5 was used to avoid cycle-by-cycle calculations. Notice the bias in the test data; whereas, the model predicts symmetric behavior.

The bias can be modeled in the back stress evolution equation (5.25) by introducing an initial value for the back stress, α_{ij}^0; i.e.,

$$\dot{\Omega}_{ij}^I = f_1 \dot{\epsilon}_{ij}^I - \frac{3f_1}{2\Omega_{max}}(\Omega_{ij}-\alpha_{ij}^0)\dot{\epsilon}_e^I - R_{ij}.$$

(7.7)

Since the bias in stress remains approximately constant α_{ij}^0 may be taken as a constant tensor. Its value can be determined for torsion cases using Equation 7.3 which may be rewritten as

o Experimental data
- Model prediction

(a)   Cycle No. 16

o Experimental data
- Model prediction
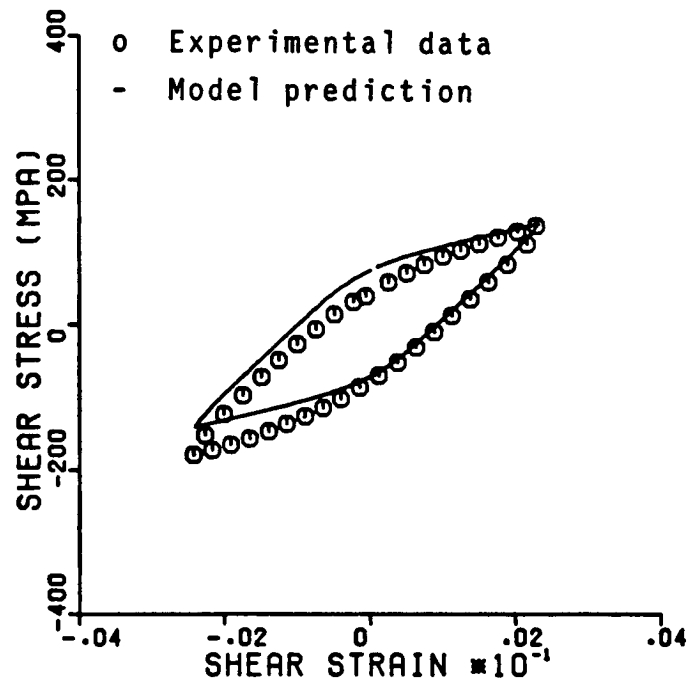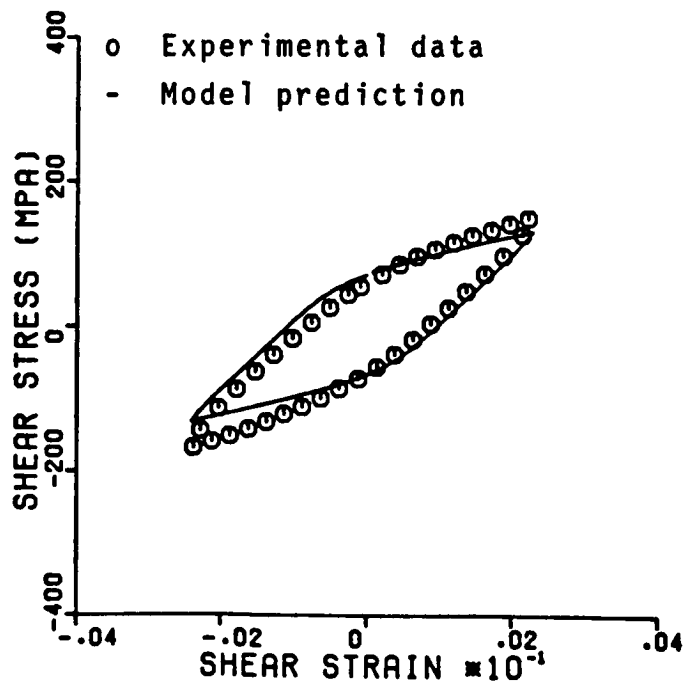
(b)   Cycle No. 37

Figure 7.1   Predicted and Experimental Cyclic Shear Response
at 982°C, .02M^{-1}
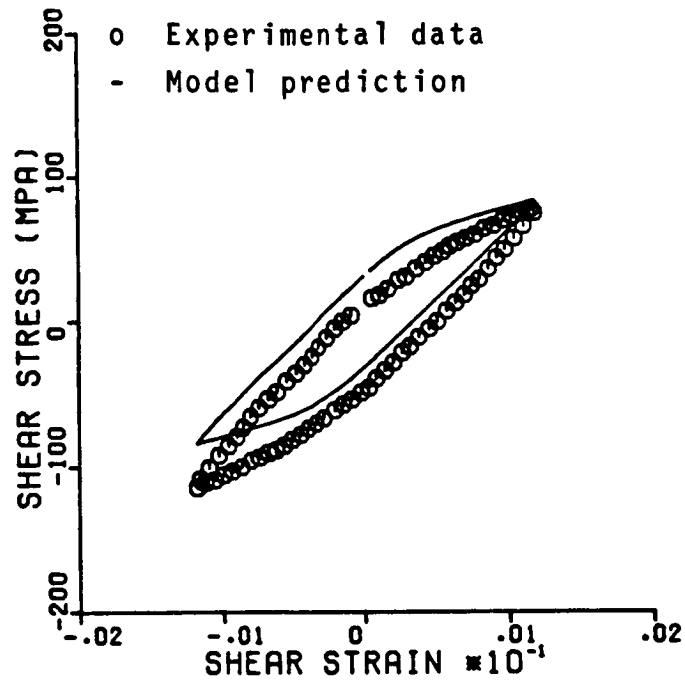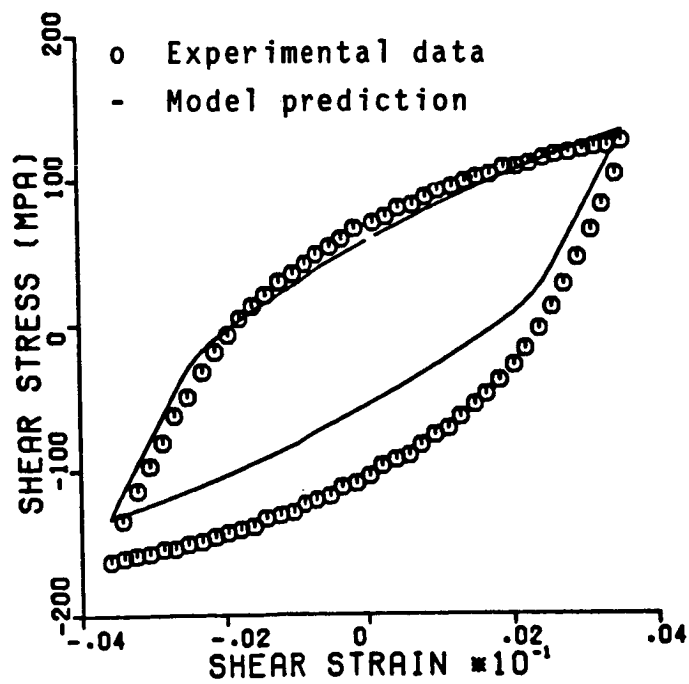
184

(a)   Cycle No. 5

(b)   Cycle No. 34

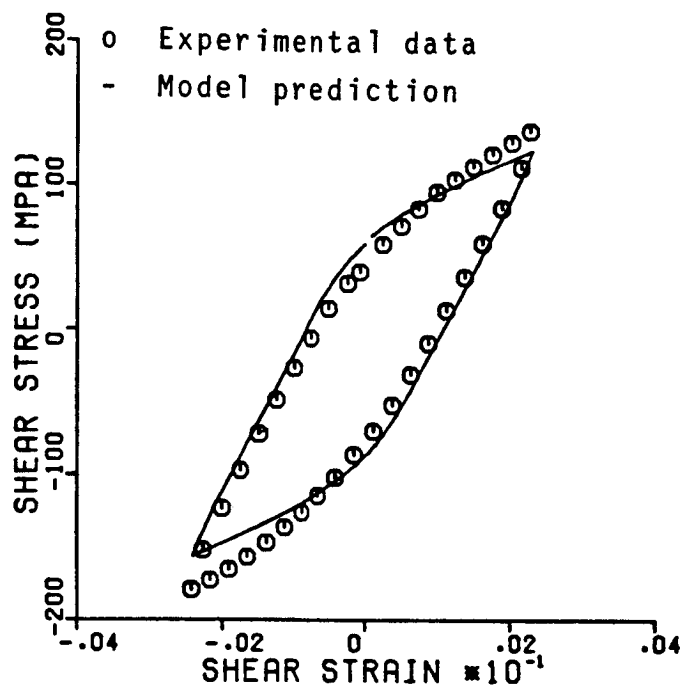Figure 7.2   Predicted and Experimental Cyclic Shear Response
at 982°C, .002M^{-1}

185

$$(\tau - \Omega_{12}) = \frac{Z}{\sqrt{3}} - \frac{2}{A}\ln\left(\frac{|\dot{\epsilon}_{12}^I|}{D}\right)^{\frac{-1}{2n}} \tag{7.8}$$

Since ϵ_{12}^I is found to be symmetric, the asymmetry in τ arises due to an asymmetry in Ω_{12}. The value of α_{ij}^0 can be found from the magnitude of the difference in the values of τ at the positive and negative peak points. For Rene´ 80 at 982 °C,

$$\alpha_{ij}^0 = \begin{bmatrix} 0 & -2.5 & -2.5 \\ -2.5 & 0 & -2.5 \\ -2.5 & -2.5 & 0 \end{bmatrix}$$

The model predictions using Equation 7.7 are shown in Figure 7.3. Notice that both the hysteresis loops are asymmetrical. This demonstrates that the proposed model can be easily adapted to include asymmetric behavior. However, implementation will be made only after the exact causes of the asymmetric behavior are understood.

Figures 7.4 and 7.5 show the results for pure torsion analyses and tests at 871°C at strain rates of .002 M^{-1} and .02 M^{-1} respectively. For a large number of cycles (Figure 7.5b) the model predicts more softening than is seen in the test data. Considering the various factors involved in the analysis, such as uniaxial test based material parameters, extrapolated cyclic integrations, variable cyclic block strain

C-2
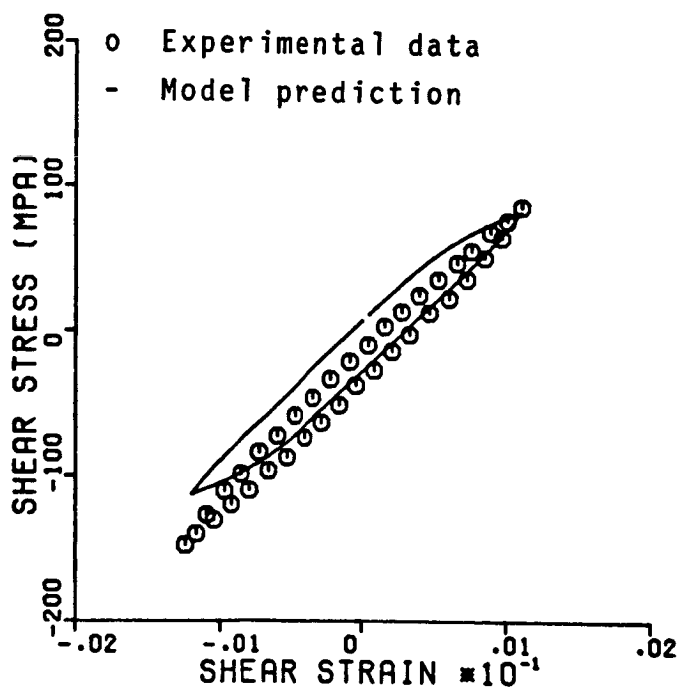
(a)   Cycle No. 16

(b)   Cycle No. 62

Figure 7.3   Predicted and Experimental Cyclic Shear Response
(Nonsymmetric) at 982°C, .02M^{-1}

187

o Experimental data

− Model prediction

(a) Cycle No. 31

o Experimental data

− Model prediction
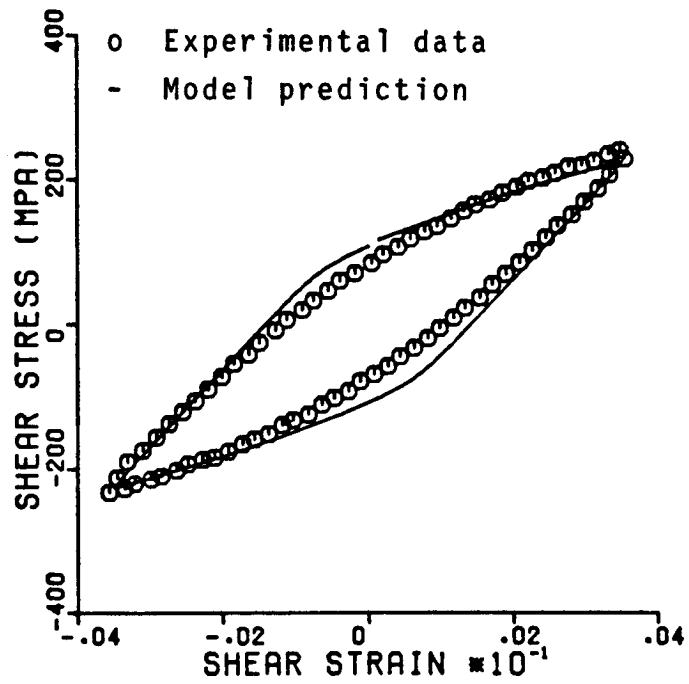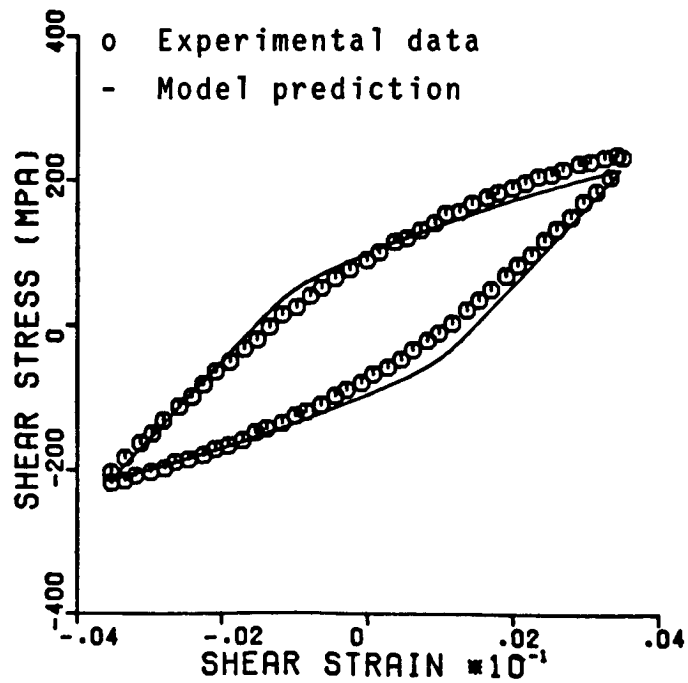
(b) Cycle No. 54

Figure 7.4   Predicted and Experimental Cyclic Shear Response
at $871^{\circ}C$, $.002M^{-1}$

188
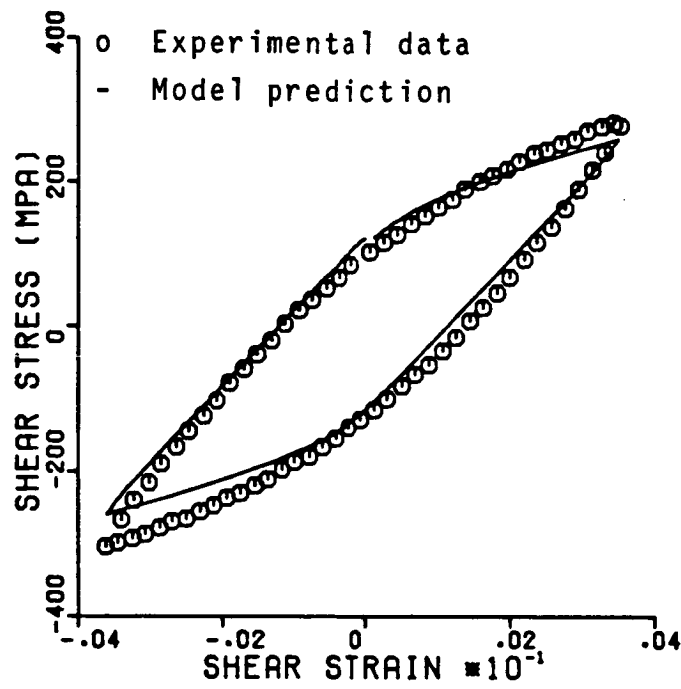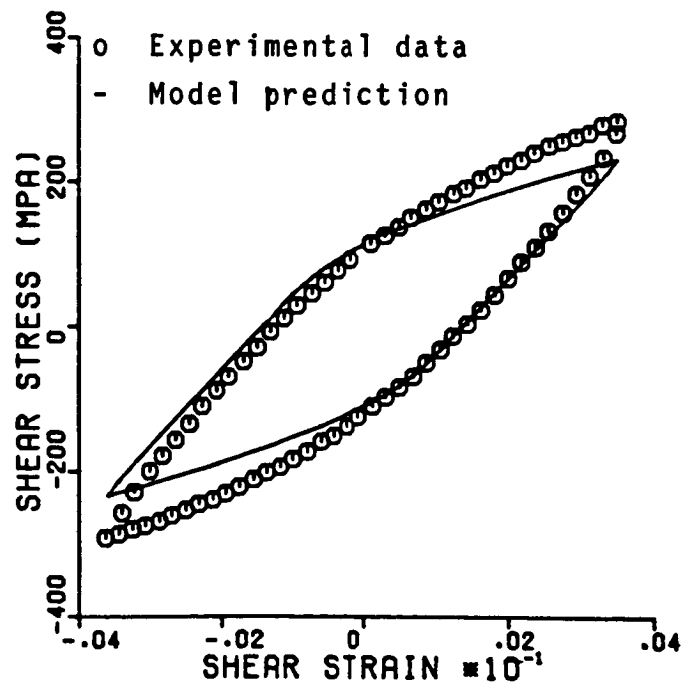
(a) Cycle No. 46

(b) Cycle No. 104

Figure 7.5 Predicted and Experimental Cyclic Shear Response at 871°C, .02M^{-1}

ranges, etc, the results for all the torsion analyses are remarkably good.

7.3 Proportional Cyclic Loading

The in phase tension/torsion loading condition, shown in Figure 3.13a, is a proportional multiaxial loading case since $\epsilon_{12}=C\epsilon_{11}$ where C is a constant throughout the test. This is different from the cases considered so far because this involves simultaneous loading in two modes, tension and torsion, at two different constant strain rates. These tests were also performed in cyclic blocks with different strain ranges. The response predicted by the model was calculated as before but with independent control of axial and shear strains.

Figures 7.6-7.8 show the comparisons of the model predictions with experimental data for an in phase tension/torsion cyclic test at 982°C at a shear strain rate of .002 M^{-1}. Both the axial response and shear response are shown at three points in the cyclic history. Clearly, there is very good agreement between the response predicted by the model and the experimental results. Notice the negative bias in the experimental data. Part of this bias is due to a small asymmetry in the strain control limits.
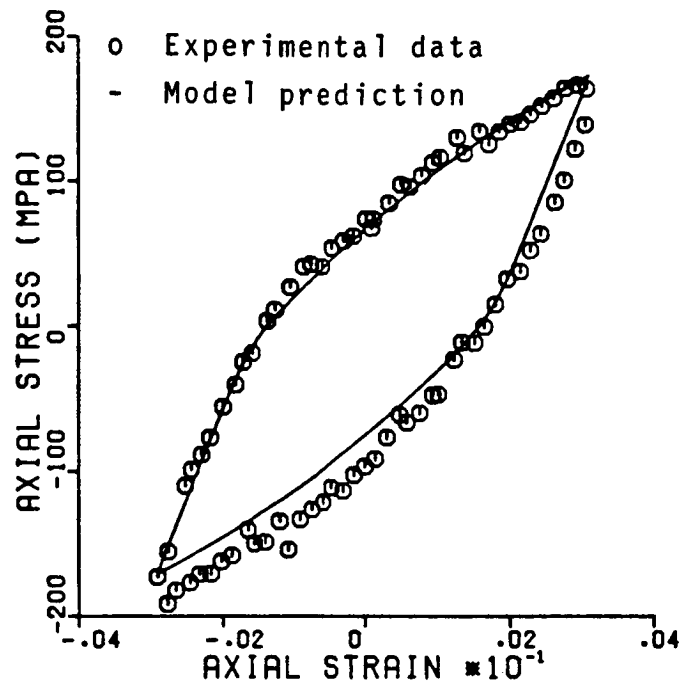
(a) Axial Response
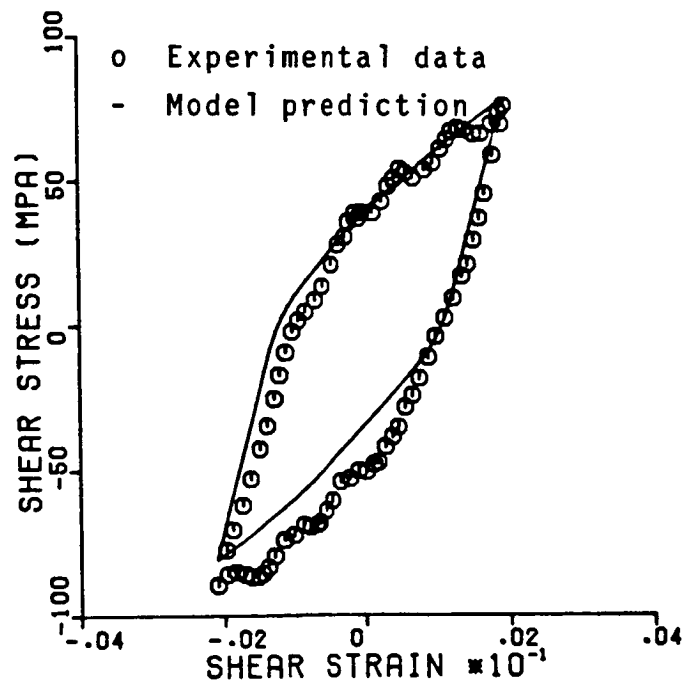
(b) Shear Response

Figure 7.6   Predicted and Experimental Cyclic Response --
In Phase Tension/Torsion, 982°C, Cycle No. 18

191

(a) Axial Response

(b) Shear Response

Figure 7.7   Predicted and Experimental Cyclic Response --
In Phase Tension/Torsion, 982°C, Cycle No. 23

192

(a)   Axial Response

(b)   Shear Response

Figure 7.8   Predicted and Experimental Cyclic Response--
In Phase Tension/Torsion, 982°C, Cycle No. 39

Figures 7.9-7.11 show the results for a similar in phase tension/torsion test at 871°C. In this case also the model predictions are in agreement with the experimental results. Towards the end of the experiment (Figure 7.11) the model appears to overpredict cyclic softening. However, most of the discrepancies appear related to the negative bias of the experimentally determined stress response. Based on the results in this section, it is concluded that the multiaxial modeling capability of the proposed model for proportional loading histories is good.

7.4 Multiaxial Nonproportional Loading Cyclic Response

The proportional loading conditions discussed in the previous section are encountered in certain high temperature applications and represent an important class of problems. However, the most general case of multiaxial loading is nonproportional, which may involve additional hardening or softening as discussed previously. Two types of nonproportional loading histories have been investigated to study the capabilities of the proposed model: multiple in phase tension/torsion loading and sinusoidal 90 degree out of phase loading.
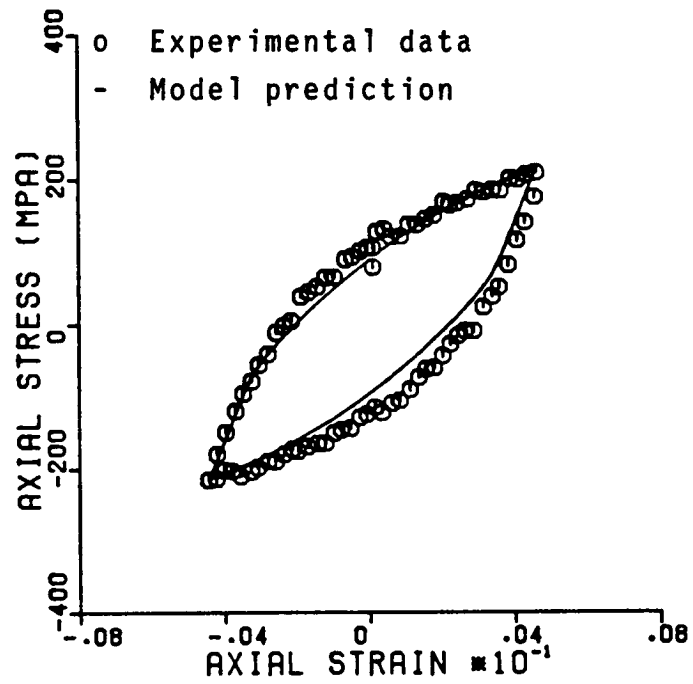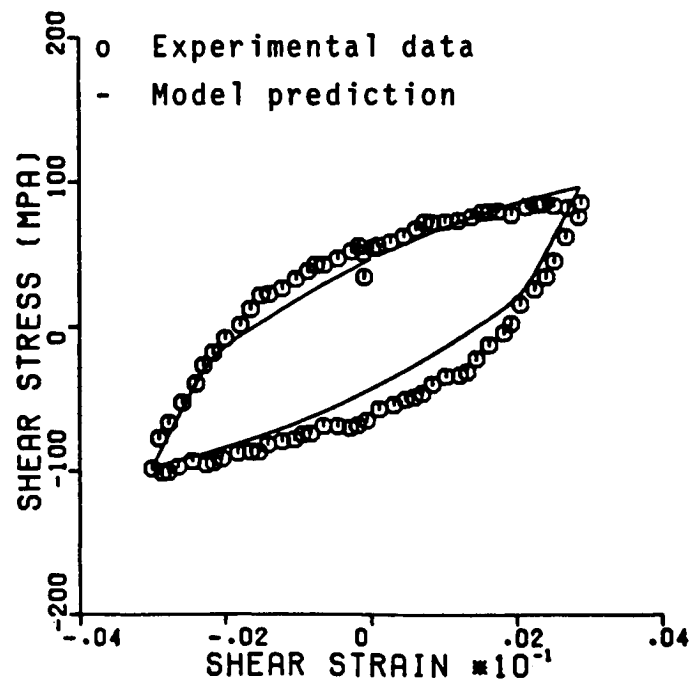
194

(a) Axial Response

(b) Shear Response

Figure 7.9   Predicted and Experimental Cyclic Response --
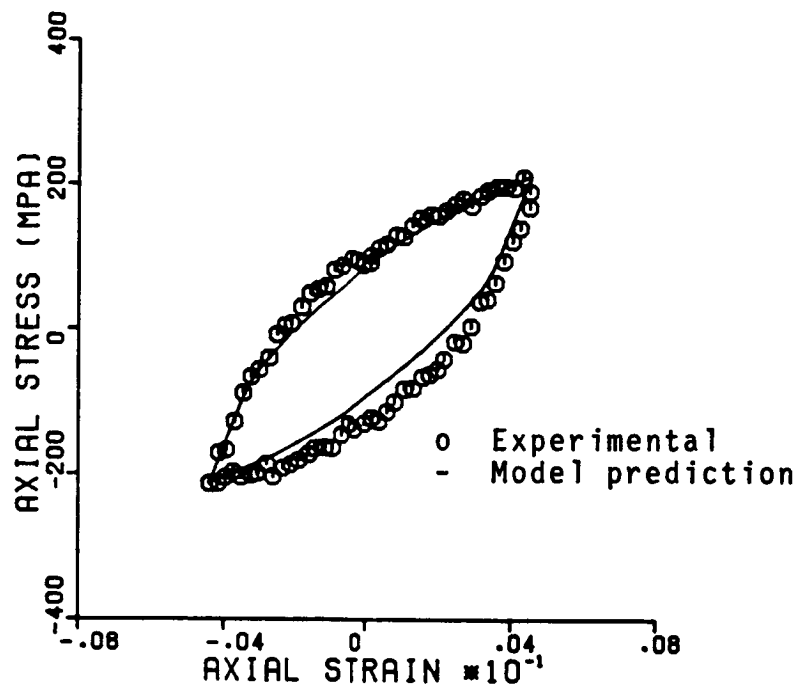In Phase Tension/Torsion, 871°C, Cycle No. 26

195
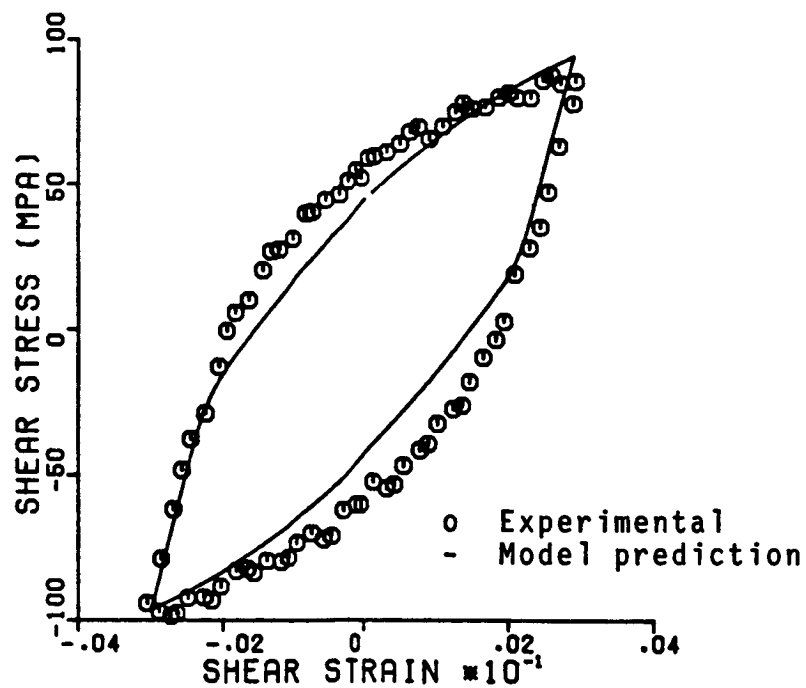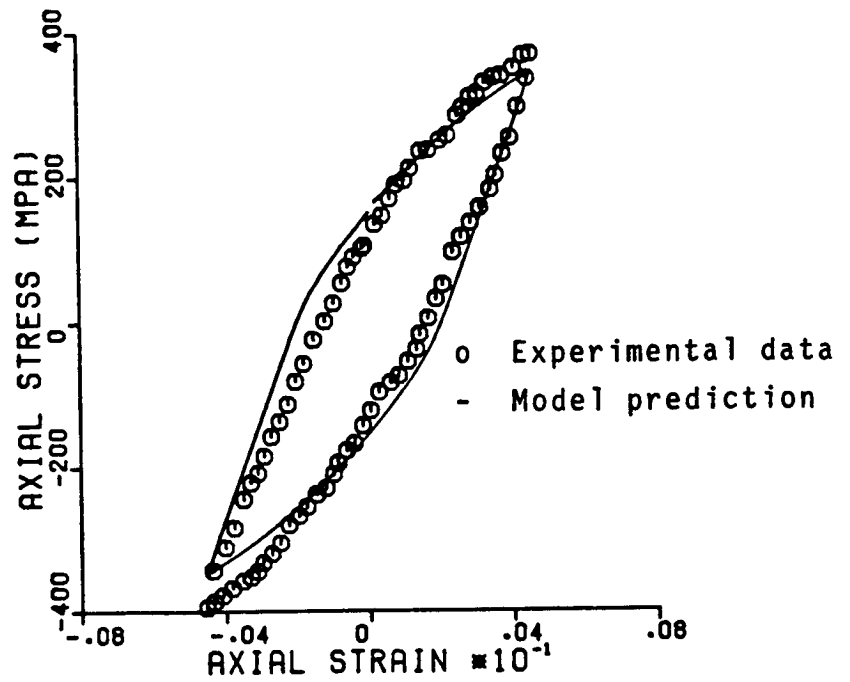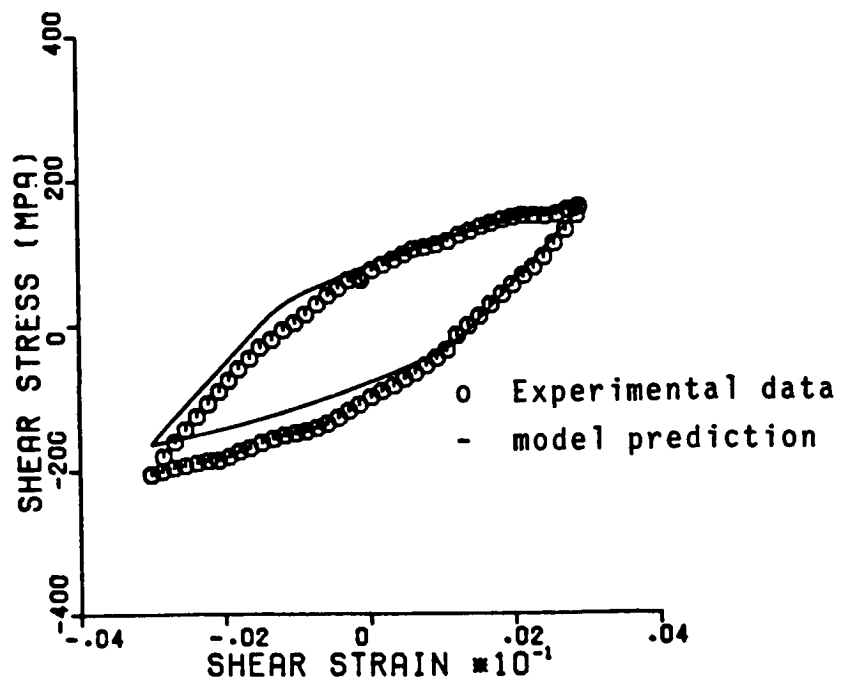
(a) Axial Response

(b) Shear Response

Figure 7.10   Predicted and Experimental Cyclic Response --
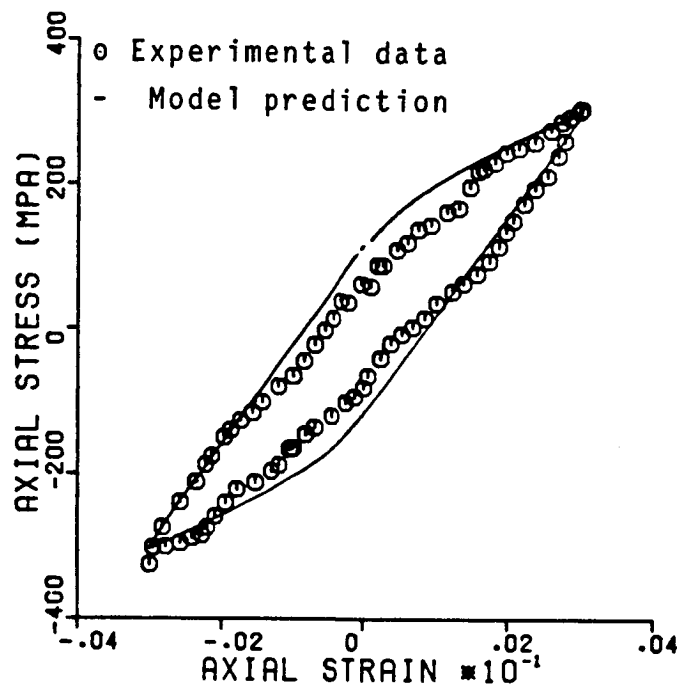In Phase Tension/Torsion, 871°C, Cycle No. 34

196
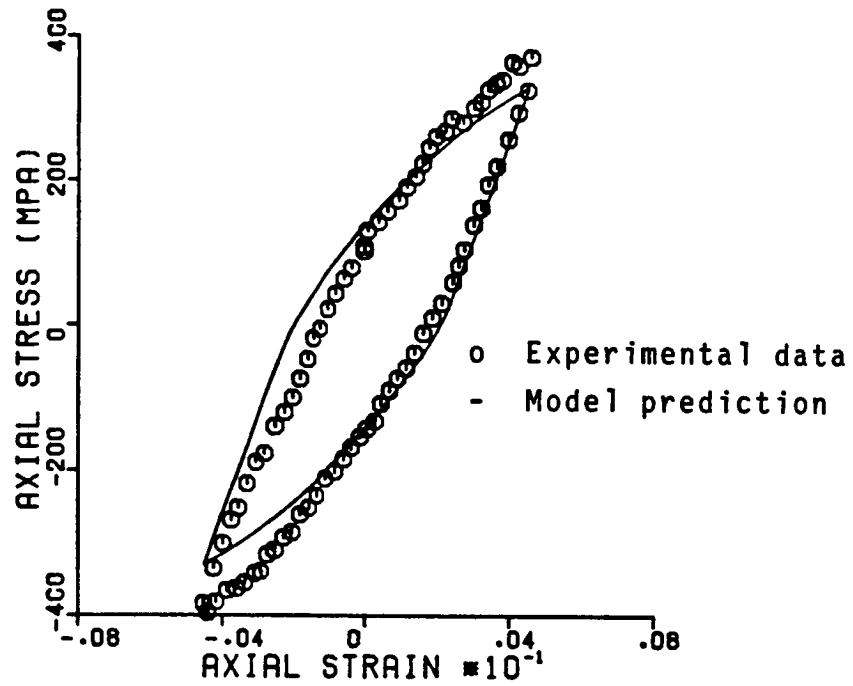
(a) Axial Response
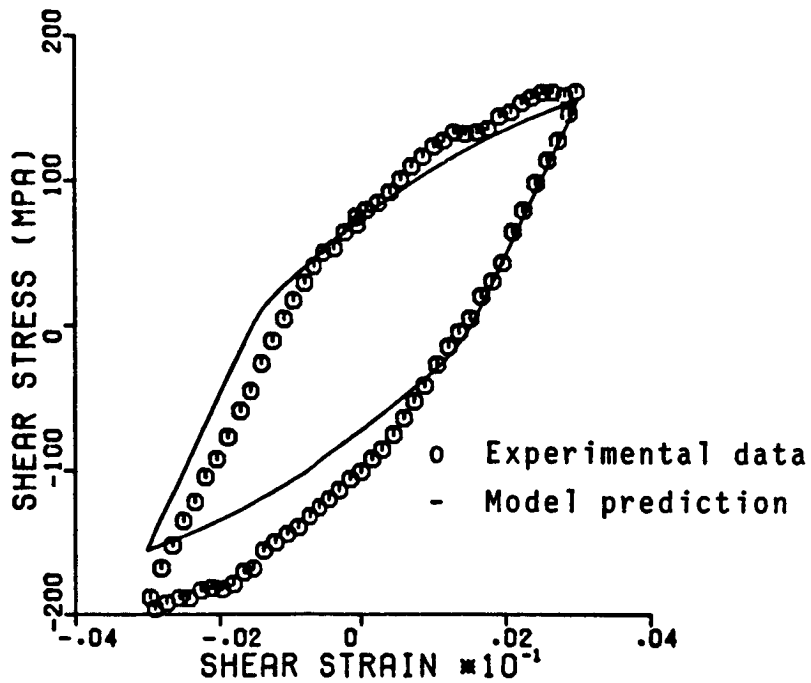
(b) Shear Response

Figure 7.11   Predicted and Experimental Cyclic Response --
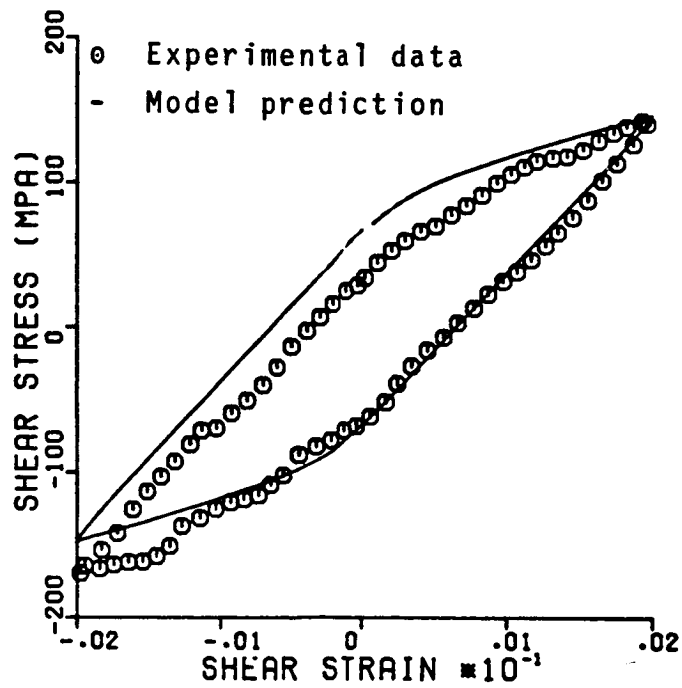In Phase Tension/Torsion, 871°C, Cycle No. 49

7.4.1 Multiple In Phase Tension/Torsion Cyclic Loading

This test involves a series of in phase tension/torsion cycles as shown in Figure 3.13b. Each segment of the test, such as AA, is proportional individually and the planes of maximum shear strain remain fixed. Most of the microscopic deformation related phenomena are thus limited to only a few planes. After stabilization in each segment the proportionality factor between the axial and shear strains is changed, such as path BB, and the maximum shear strain planes are different for the new path. Thus, a sequence of variable proportional loading paths can be used to construct a nonproportional loading history. Such a history has been shown to produce the additional hardening phenomenon observed in other materials [66,70].

Multiple in phase nonproportional loading history tests have been performed on Rene' 80 at 982°C (Figure 3.13b), including pure shear (path CC) and pure axial (path EE) cycles. In this test each path had a different strain rate since the cyclic period was fixed at 360 seconds throughout the entire test. The strain ranges for the various paths are such that the octahedral shear strain is approximately constant at the peak points of each cycle.

198

Figures 7.12-7.15 show the predicted and measured cyclic response at the end of each segment of the history. Figure 7.12, which shows the results of the first and last segments of the test, summarizes the objective of this test. The strain paths AA, the first segment, and FF, the last segment, are identical. However, the specimen is subjected to a nonproportional loading history between these two segments. Figure 7.12a shows that the experimental stress strain response in shear for the paths AA and FF are exactly the same, indicating that there are no additional effects due to nonproportional loading of Rene´ 80 at 982°C. The model prediction is in good agreement with the test data. The axial response experimental data shows some scatter; however, paths AA and FF are close to being pure torsion, and the axial stress and strain measurements are subject to substantial error.

Figures 7.13 and 7.14 show the results for strain paths BB and DD. There appears to be some scatter in the measured response, which is probably related to the biaxial extensometer. The asymmetry of the measured hysteresis loops is again evident. Figure 7.15 shows the response for segment CC, which is pure torsion, and Figure 7.16 shows the response for the segment EE, which is uniaxial.

199
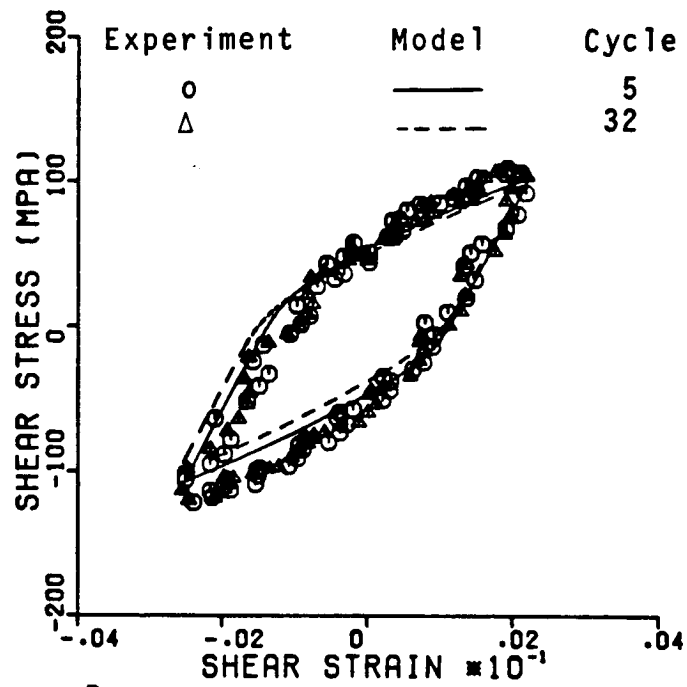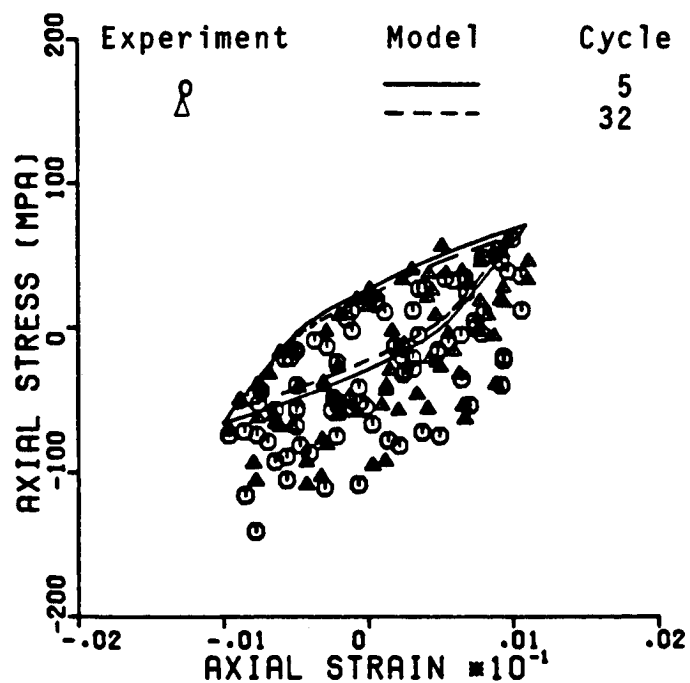
(a) Shear Response

(b) Axial Response

Figure 7.12   Predicted and Experimental Response --
             Multiple In Phase, Nonproportional Loading,
             982°C, Cycles 5 and 32

o Experimental data

– Model prediction

(a) Shear Response

o Experimental data

– Model prediction
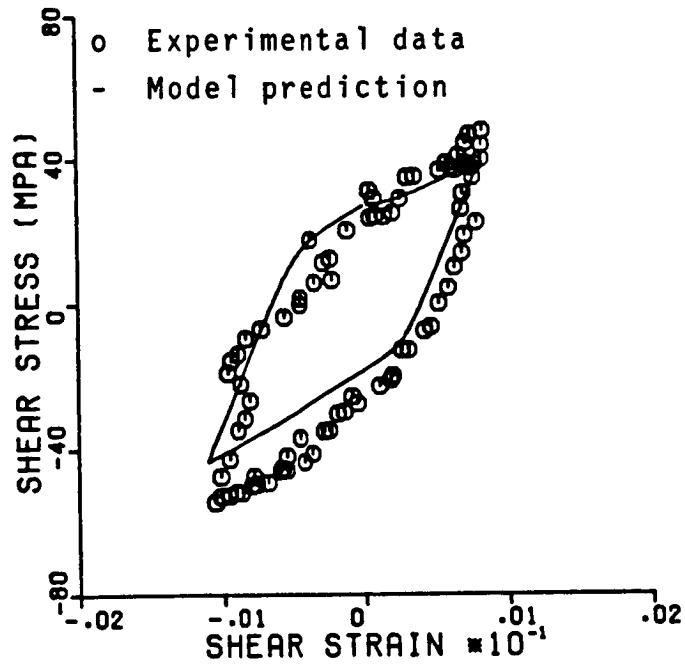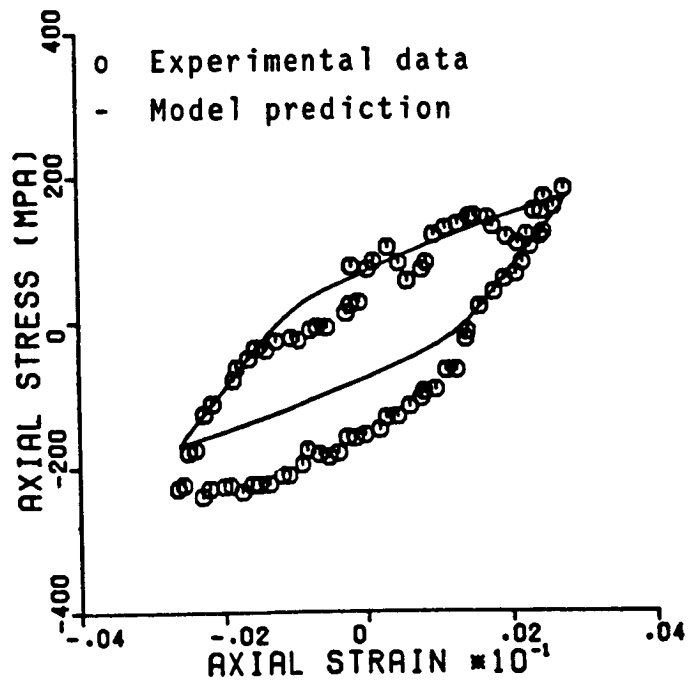
(b) Axial Response

Figure 7.13   Predicted and Experimental Response --
Multiple In Phase, Nonproportional Loading,
982°C, Cycle No. 10

201
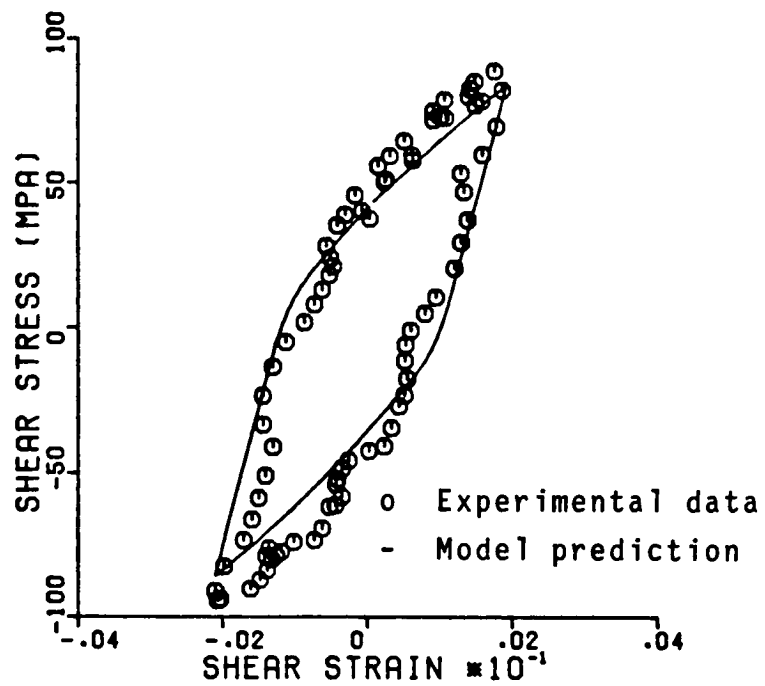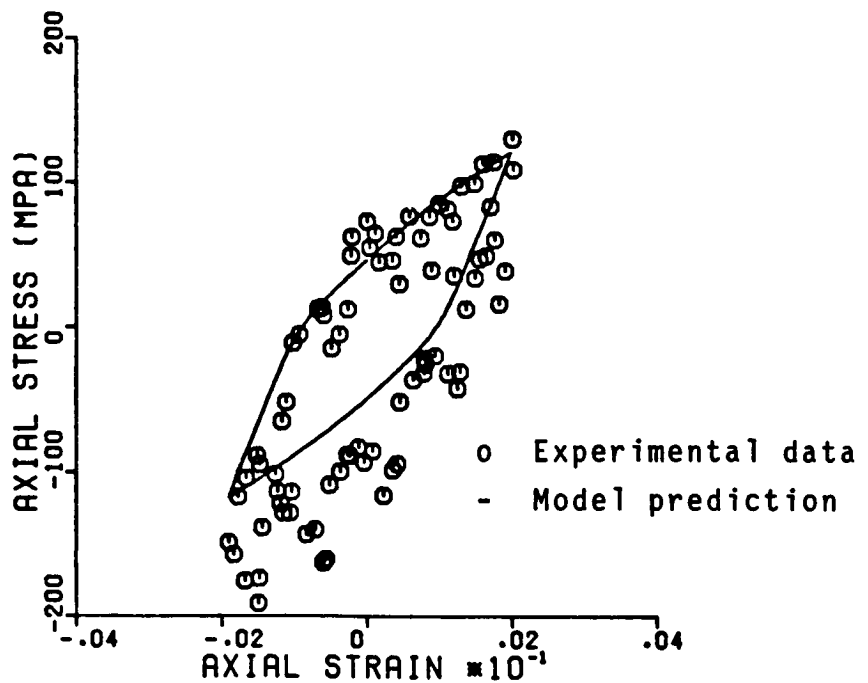
(a) Shear Response

(b) Axial Response

Figure 7.14   Predicted and Experimental Response --
Multiple In Phase, Nonproportional Loading,
982°C, Cycle No. 23

202
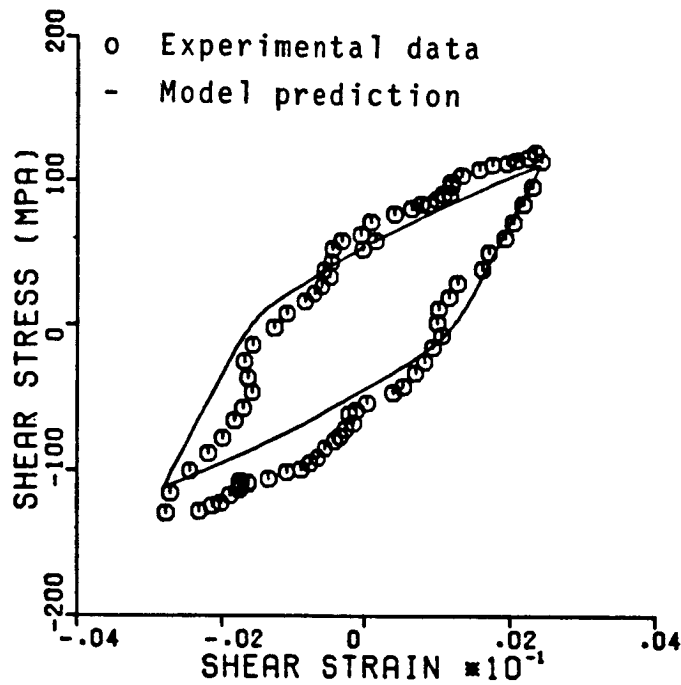
Figure 7.15   Pure Shear Response in the Nonproportional
History (Cycle No. 27)
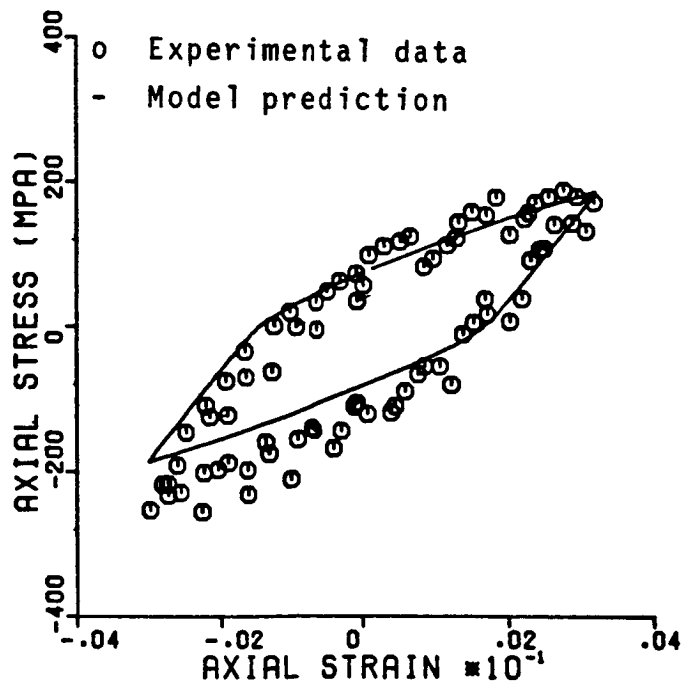
Figure 7.16   Pure Axial Response in the Nonproportional
History (Cycle No. 17)

The results shown in Figures 7.12-7.16 are encouraging for two reasons. First, Rene´ 80 does not appear to exhibit additional hardening or softening for nonproportional loading at high temperatures. This has been experimentally verified at 982°C (Figure 7.12) as well as at 871°C. The second important consequence of these results is that the multiaxial capability of the model appears good for this material. The test described in this section is perhaps the most complicated one in this program, since it involves both nonproportionality and variable strain rates.

7.4.2 Out of Phase Tension/Torsion Cyclic Loading

A typical nonproportional cyclic loading condition that is used in tension/torsion experiments can be represented by

$$\epsilon_{11} = a_1 \sin \omega t \tag{7.9}$$

and

$$\epsilon_{12} = a_2 \sin(\omega t - \phi). \tag{7.10}$$

Sinusoidal wave forms are used for the axial strain ϵ_{11}

204

and shear strain ε_{12} with amplitudes of a_1 and a_2, respectively. ω is the frequency of the cycle, and ϕ is the phase angle between the axial and torsional strains. When $\phi = 0$ the loading is exactly in phase and proportional, and when $\phi = \pi/2$ the loading is exactly out of phase. A value of ϕ other than zero corresponds to nonproportional loading. In the nonproportional loading represented by Equations 7.9 and 7.10, the principal strain directions and the maximum shear strain directions continuously sweep through all the material planes. Thus, hardening or softening is distributed throughout all the material planes which could result in additional hardening, as has been reported for some materials [72,73]. The angle between the inelastic strain rate vector and the deviatoric stress vector also varies continuously, as shown in Reference [72].

The response of Rene' 80 at 982°C for 90 degree ($\phi = \pi/2$) out of phase sinusoidal tension/torsion strain cycles has been analyzed using the new constitutive model, and the results are shown in Figures 7.17 and 7.18. The axial and shear strain amplitudes in Equations 7.9 and 7.10 were chosen such that the octahedral shear strain remained constant throughout the cycle. Note in Figure 7.17 that the stress

205

response tends to stabilize inside an ellipse. Recall that Rene 80 cyclically softens at 982°C under high strain rates. For cyclically hardening materials the stress response tends to stabilize on the outside of an ellipse as shown in References [72,73].

It is significant to note that the proposed constitutive model predicts a phase angle between the inelastic strain rate vector and the deviatoric stress vector. This is shown in Figure 7.18. This phase angle, θ, is calculated as

$$\theta = \cos^{-1} \frac{\dot{\varepsilon}^I \cdot \underset{\sim}{S}}{|\dot{\varepsilon}^I||\underset{\sim}{S}|}. \qquad (7.11)$$

It is observed that θ varies during a cycle. Its response stabilizes after a transient period, as seen in Figure 7.18. The phase angle, θ, has been experimentally measured for Hastelloy-X at room temperature and is shown in Figure 7.19 [27]. The variation of θ shown in Figure 7.18 is in qualitative agreement with the measured results for Hastelloy-X.

The axial and shear hysteresis loops for the 90 degree out of phase cyclic loading condition are shown in Figure 7.20. Notice the cyclic softening that is evident in these hysteresis loops. The general shapes

206

of the axial and shear hysteresis loops are in good
qualitative agreement with those reported for other
materials [73].
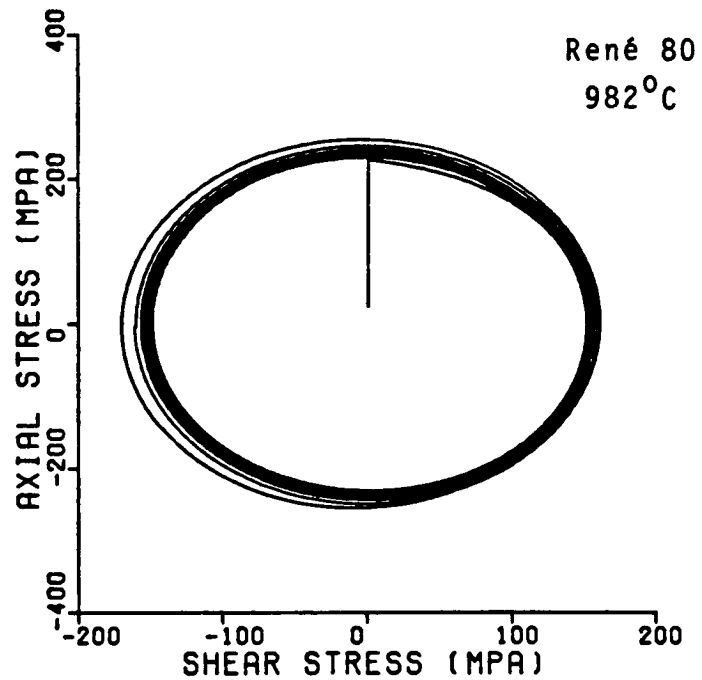
Figure 7.17   Predicted Stress Response in 90° Out of Phase
Tension/Torsion
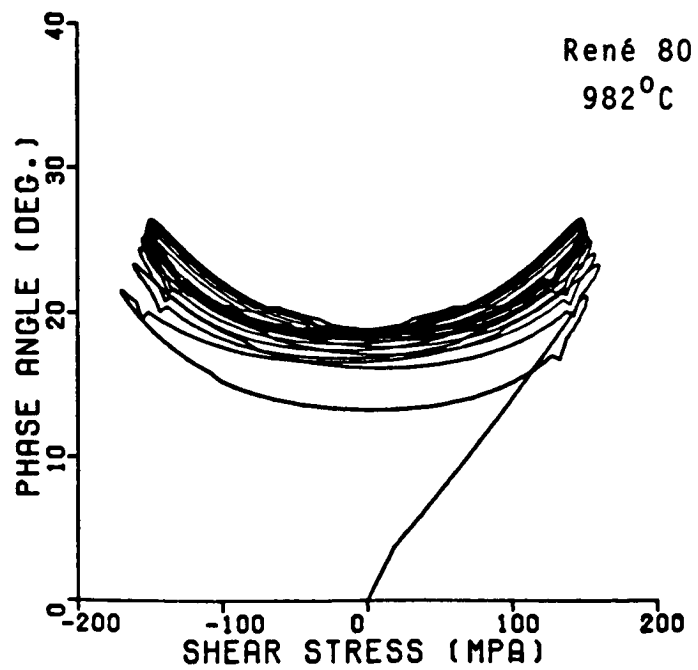
Figure 7.18   Predicted Phase Angle Between Inelastic Strain
Rate Vector and Deviatoric Stress Vector
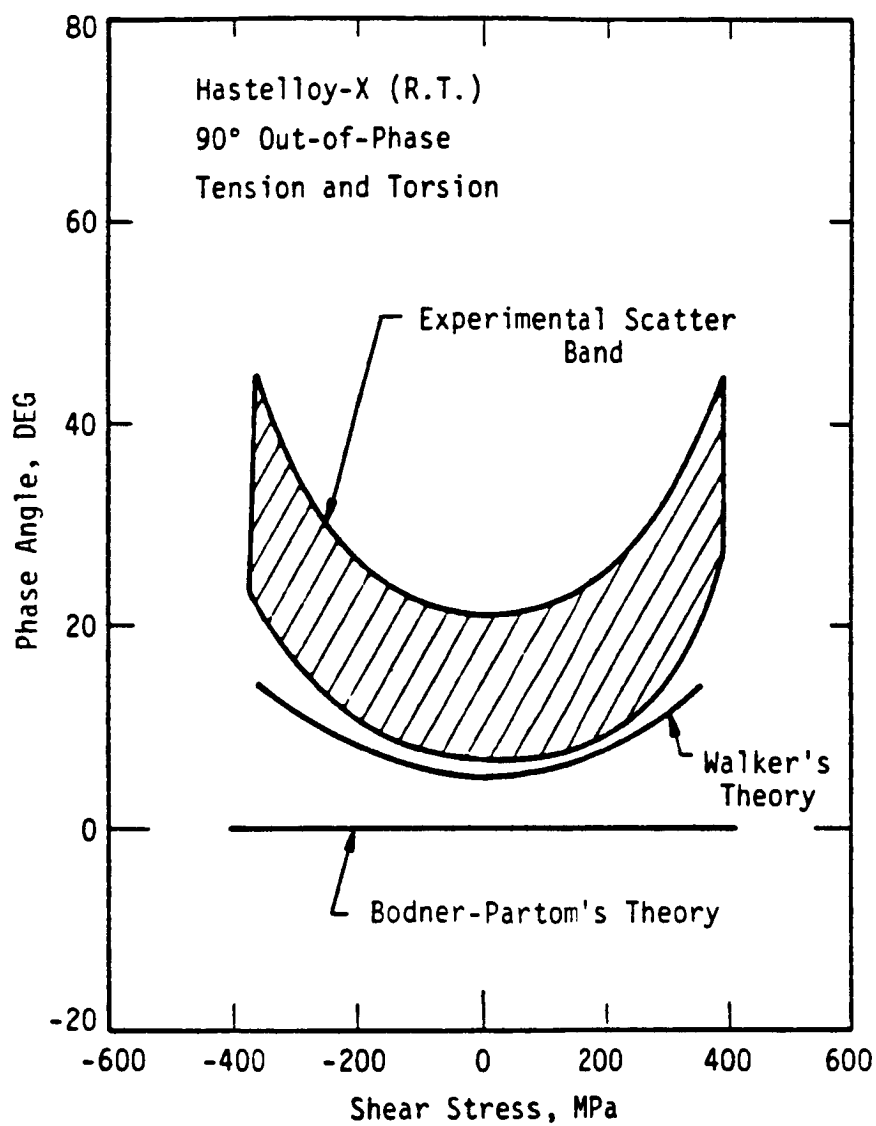
Figure 7.19   Phase Angle Between Inelastic Strain Rate
and Deviatoric Stress Vectors for Hastelloy-X
(From References [27] and [72])
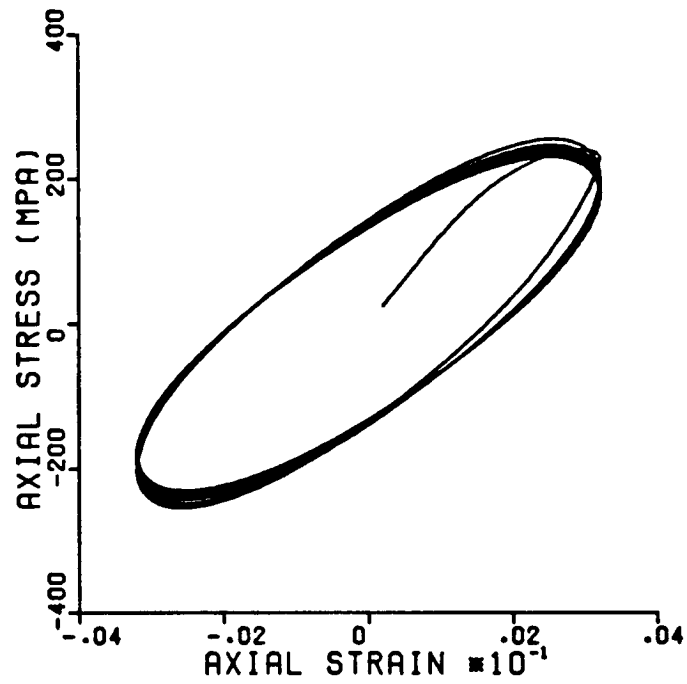
(a) Axial Response
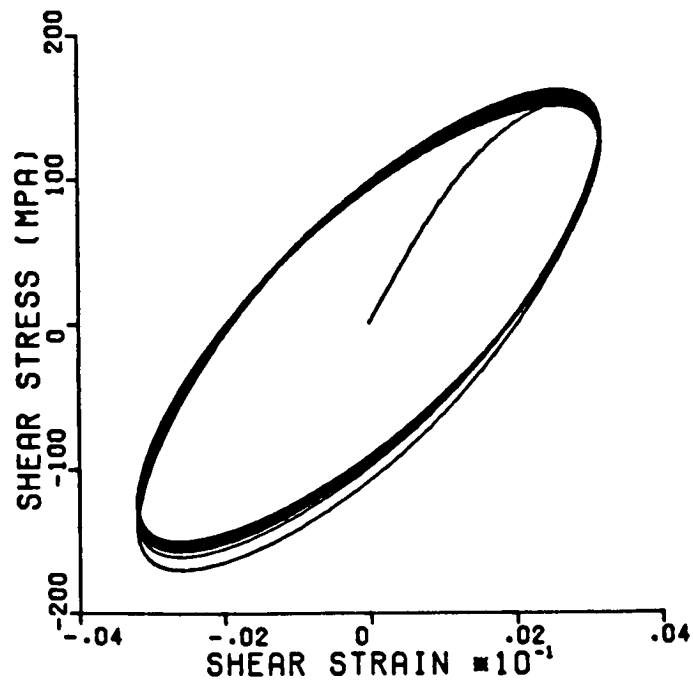
(b) Shear Response

Figure 7.20   Predicted Cyclic Hysteresis Loops for 90° Out
of Phase Tension/Torsion Sinusoidal Cycles

210

CHAPTER 8

DISCUSSION AND SUMMARY

The objective of this research program was to develop a set of constitutive equations which can model a wide variety of nonlinear material behavior phenomena observed in high temperature superalloys. The various aspects of the material behavior and model development were discussed in detail in the previous chapters. This chapter briefly summarizes the key elements of the constitutive model, its capabilities and limitations. Suggestions are made to further extend the capabilities of the model. Some aspects related to the implementation of the model in finite element codes are briefly discussed.

8.1 A Review of Important Results

Metallurgists have long recognized the existence of internal stresses in inelastically deformed high temperature metals. There is ample evidence of this in some types of observed macroscopic behavior as well as in microscopic observations of the associated dislocation network. There is clear physical evidence of a back stress which is directional in nature and

produces anelastic effects, Bauschinger effects, negative stress relaxation and non-coaxiality of inelastic strain rate and deviatoric stress vectors. There are also a number of isotropic effects related to dislocation behavior and strengthening mechanisms in a solid. The proposed constitutive model is physically based and incorporates both a back stress, Ω_{ij}, and a drag stress, Z.

The structure of the constitutive equations was developed on the basis of observed material behavior for Rene′ 80 at 982°C. The experimental data base for Rene′ 80 is extensive and the problem of the material parameter evaluation from experimental results has been addressed and demonstrated at several temperatures. Throughout the entire research, special emphasis has been placed on modeling and verification of the cyclic inelastic behavior of the materials that is encountered in gas turbine engine components. The strain rate sensitivity, creep and stress relaxation of Rene′ 80 are predicted well at 982°C (Figures 5.6, 5.7, and 5.12). The cyclic softening and mean stress relaxation behavior are also predicted well (Figures 5.8-5.11).

The model was then extended to 871°C, 760°C and 538°C. The material displayed some strain rate sensitivity at 871°C but none at the lower temperatures.

The material parameters were evaluated at the various temperatures and it was shown that the model can also be used in the strain rate independent regime. The capability of the model at other temperatures was verified by predicting Rene´ 80 behavior at 649°C. It was shown that in modeling creep behavior the recovery formulation generally used in unified constitutive models did not produce satisfactory results for Rene´ 80. A new form of recovery based on the saturated value for the back stress was shown to produce much better results (Figures 6.21 and 6.22). The major result of this phase of the research is that the unified constitutive model can represent strain rate dependent behavior at high temperatures and strain rate independent behavior at low temperatures. The monotonic tensile, creep and cyclic behavior of Rene´ 80 predicted by the model compared very well with experimental data at several temperatures.

In general, it is not sufficient to model only the uniaxial material behavior. Loading conditions in real world structures are usually multiaxial. The new constitutive model was developed in three-dimensional form. The multiaxial capabilities of the model were verified using a series of tension/torsion experiments. Proportional and nonproportional conditions of

multiaxial loading were explored and pure torsion response was also analyzed. In all cases the predictions of the model were in very good agreement with the experimental response at the two temperatures tested, 982°C and 871°C. These results, detailed in Chapter 7, are very significant because all of the material parameters in the constitutive model were determined from uniaxial experiments. It was further demonstrated that the model predicts the direction of the inelastic strain rate vector, which is not coincident with the deviatoric stress vector. The cyclic variation of the phase angle between the two vectors predicted by the model appears to have the right trend. Cyclic softening and saturation under biaxial conditions was also demonstrated (Figures 7.17 and 7.18). Thus, the multiaxial capabilities of the new model appear to be very good.

8.2 Potential Extensions

There are a few aspects of the new constitutive model which may be further improved upon, based on some additional experiments. The current cyclic softening modeling capability is reasonably good. The material parameters related to cyclic softening or hardening can

be determined more accurately if simpler cyclic tests with constant strain range are used. Next, the stress response in the torsion and multiaxial experiments is not symmetric, even for symmetric strain control conditions. The exact source of this asymmetric behavior is not clear. It may be due to the large grain size of Rene⁻ 80 in the thin wall test specimens. The development of a small axial stress during pure torsion testing may also be related to this result. Additional experiments are necessary to establish the exact cause of the asymmetric cyclic behavior. The constitutive model predicts symmetric stress response for symmetric strain control; however, a proposed way to incorporate asymmetric cyclic behavior in tension/torsion prediction was demonstrated (Figure 7.3). Incorporation of this method in the model is delayed until the asymmetric behavior is fully understood.

Another characteristic of the model which warrants further investigation is the sensitivity during creep. The steady state creep rate is very sensitive to the value of the steady state back stress. This is more evident at lower temperature creep. It appears that the same characteristics of the model which enabled strain rate independent behavior at low temperature

give rise to the back stress sensitivity during steady state creep. Methods to improve this should be explored.

8.3 Modeling Thermomechanical Response

The constitutive model was developed on the basis of isothermal tests at 982°C, 871°C, 760°C and 538°C. A form of temperature dependency was introduced through the variations in the material parameters. The predictions at each of these isothermal temperatures are quite adequate; however, it is not clear that the theory will accurately model the response in a thermal cycle [1,74]. The model is isothermally based and does not include the thermal history effects and complex thermomechanical interactions. There is only a parametric dependence on temperature in the current model. For accurate modeling of TMF behavior, perhaps both temperature and temperature rate should be included. It is expected that the drag stress equation will be affected drastically, since cyclic hardening or softening behavior is dependent on temperature. The inelastic strain rate appears to depend on temperature in the form of an Arrhenius relationship. This is evident from the variation of the parameter D in the

flow equation. Thus, it appears that the flow equation
may be written as

$$\dot{\varepsilon}_{ij}^{I} = D_0 e^{\frac{-H}{kT}} \exp\left[-\frac{A}{2}\left(\frac{Z^2}{3K_2}\right)^n\right] \frac{(S_{ij} - \Omega_{ij})}{\sqrt{K_2}},$$
(8.1)

where H is an activation energy for inelastic flow, K
is the Boltzmann constant, and D_0 is a constant.
Further investigation of such temperature dependencies
in the flow and evolution equations may be
advantageous. It is also necessary to study the
differences in the physical mechanisms of deformation
between isothermal and nonisothermal histories. For
example, it is known that in Rene´ 80 the slip
deformation character is distinctly dependent upon
temperature [75]. At 650°C the deformation mode is
planar slip; whereas, at 982°C wavy slip is observed.
In a TMF cycle there will be complex interactions
between these deformation modes, and the resulting
nonisothermal material response may be different from
the isothermal response. The TMF model should be able
to model these transitions in microscopic mechanisms of
deformation.

8.4 Finite Element Modeling

Structural analyses of almost all the critical gas turbine engine components are performed today using finite element models. The constitutive equations for material behavior must, therefore, be implemented in the FEM codes. This is being done as reported in [26] and [30]. It will then be possible to analyze the material response in complex geometries, such as notches and holes.

The unified theories are, in general, a set of coupled nonlinear differential equations which are usually numerically stiff to integrate. These may require the development of special numerical techniques to make the solutions more efficient, as discussed by several authors [76-79]. All the model predictions made in this report were using a simple Euler forward integration scheme. Automatic time step selection schemes were incorporated but did not result in any substantial gain in efficiency. The uniaxial and tension/torsion analyses performed in this study are much simpler than FEM analyses at a notch root using a large number of elements. It has been suggested that simple integration schemes such as the Euler method are not suitable for analyzing nonproportional loading [79]. This was found not to be true in this study.

218

The numerical stiffness and the efficiency of numerical integration of the unified theories appear to be strongly dependent on the specific functional forms and the material parameters. Table 8.1 contains the computer processing time required for simple monotonic tensile loading cases at three strain rates. Results are shown for two unified models, the isotropic Bodner model using only one state variable and the model developed in Chapter 5 which has two state variables. It was found that the new model uses less computer time and that lower strain rate and lower temperature analyses have less efficiency. Based on the earlier attempts to model static thermal recovery it has become clear that the efficiency of numerical integration appears to be significantly dependent upon the nature of the static thermal recovery terms. The preliminary results shown in Table 5.1 appear to confirm this observation.

The new model has been implemented in a two dimensional finite element code. Solution times using this code are comparable to those shown in Table 8.1; however, the new model is found to require additional storage space due to the presence of the back stress tensor. The monotonic and cyclic predictions using the FEM code are in agreement with the predictions made in

this report. Further numerical work may become
necessary to make the use of the new model more
efficient in analyzing complicated geometries.

8.5   Extension of the Model to Other Materials

All the work in this report is based on the
experimentally observed behavior of Rene´ 80, a typical
high temperature superalloy used for blades and vanes
in gas turbine engines. The model has been demonstrated
to work well for this material; however, the model
should be further tested by applying it to other
materials. There are considerable differences in the
microscopic and macroscopic behavior of the various
high temperature superalloys. The strain rate
sensitivity, temperature dependence and cyclic hardening
and softening behavior may be significantly different
from Rene´ 80. In fact, there could be some materials
for which the inelastic strain rate vector and the
deviatoric stress vector may be codirectional, in which
case the flow equation (5.6) will be inapplicable.

Perhaps the most significant difference in the
behavior of materials is under nonproportional cyclic
loading conditions. It was seen that Rene´ 80 did not
exhibit any additional hardening or softening for

TABLE 8.1

Computer Processing Time * (seconds)

Model	Temp.	$\dot{\varepsilon}$ (per minute)		
		.2	.02	.002
New	982°C	1.75	2.36	4.77
New	871°C	1.78	2.35	4.18
New	760°C	6.67	7.22	23.20
Bodner	982°C	2.94	2.92	10.48

* Monotonic tensile loading

nonproportional loads. This is not the general case. Additional hardening may require some modifications in the drag stress equation. It is also necessary to develop some suitable measures of nonproportionality. Some preliminary work has been done in this area, but a full development is possible only after appropriate experiments are performed on other materials.

UNIAXIAL FORM OF SOME UNIFIED CONSTITUTIVE MODELS

The subroutines used for the detailed evaluation of the various constitutive models reported in Chapter 2 used the general three dimensional form of the models, as reported in the cited references. However, for the purpose of evaluating the various material parameters of the models from test data, it is useful to reduce the general equations to uniaxial, isothermal form. Such uniaxial forms are listed here for the five theories examined in Chapter 2.

In these equations, the following notations are used (uniaxial):

$$\dot{\varepsilon}^I = \text{Inelastic Strain Rate}$$

$$\sigma = \text{Applied Stress}$$

$$\Omega = \text{Back Stress}$$

$$Z = \text{Drag Stress}$$

$$R \int |\dot{\varepsilon}^I| \, dt$$

1. Walker Model

$$\dot{\varepsilon}^I = \frac{|\sigma - \Omega|}{Z}^n \frac{(\sigma - \Omega)}{|\sigma - \Omega|}$$

$$\dot{\Omega} = (n_1 + n_2)\dot{\varepsilon}^I - (\Omega - \Omega_0 - n_1\varepsilon^I)\left[\left(n_3 + n_4 e^{-n_5|R|}\right)|\dot{\varepsilon}| + n_6|\Omega|^{m-1}\right]$$

$$Z = Z_1 - Z_2 e^{-n_7 |R|}$$

The following constants were used for Hastelloy-X at 649°C:

Z_1 = 95631 PSI n_1 = 0 n_5 = 0

Z_2 = 0* n_2 = 1.5E7 PSI n_6 = 0

n^{-1} = 0.079 n_3 = 781 n_7 = 0*

m = 1.16 n_4 = 0 Ω_0 = -2000 PSI

* Z_2 = -60,000 PSI and n_7 = 100 were used for checking the cyclic softening capability.

2. Krieg, Swearengen and Rohde's Model

$$\dot{\varepsilon}^I = C_1 \frac{|\sigma - \Omega|^{C_2}}{Z} \frac{\sigma - \Omega}{|\sigma - \Omega|}$$

$$\dot{\Omega} = C_3 \dot{\varepsilon}^I - C_4 \Omega^2 \left[e^{C_5 \Omega^2} - 1 \right] \frac{\Omega}{|\Omega|}$$

$$\dot{Z} = C_6 |\dot{\varepsilon}^I| - C_7 (Z - Z_0)^n$$

The following constants were used for Aluminum at 43°C:

C_1 = 6.0 x 10^{-13} 1/sec C_6 = 0

C_2 = 6.05 C_7 = 0

C_3 = 424 MPa Z_0 = 0

C_4 = 7.8016 x 10^{-15} MPa^{-2} n = 1.0

C_5 = 1.15875 x 10^{-3} MPa^{-2}

3. Miller Model

$$\dot{\epsilon}^I = \left\{ \beta\theta' \; \text{Sinh}\left[\frac{|\sigma-\Omega|}{Z}\right]^{1.5} \right\}^n \; \frac{(\sigma-\Omega)}{|\sigma-\Omega|}$$

$$\dot{\Omega} = H_1\dot{\epsilon}^I - H_1\beta\theta' \left[\text{Sinh}\,(A_1|\Omega|)\right]^n \; \frac{\Omega}{|\Omega|}$$

$$\dot{Z} = H_2|\dot{\epsilon}^I|\left(C_2+ |\Omega| - \frac{A_2}{A_1} Z^3\right) - H_2C_2\beta\theta' \left[\text{Sinh}\,(A_2Z^3)\right]^n$$

$$\theta' = e^{-Q/kT} \quad \text{for } T\geq 0.6Tm$$

$$= e^{-\left\{\frac{Q}{0.6kTm} \left(1 + \ln\frac{0.6Tm}{T}\right)\right\}} \quad \text{for } T\leq 0.6Tm$$

The following constants were used for Hastelloy-X at 649°C:

Z_0 = 8000 psi	C_2 = 50,000 psi
n = 1.598	A_2 = 5.9425E-12 psi^{-3}
β = 1.0293 E14 1/sec	Q = 104600 Cal./Mole
H_1 = 1.0E7 psi	T_m = 1588 °K
A_1 = 9.305E-4 psi	k = 1.9859
H_2 = 100	

4. Robinson Model

$$\dot{\varepsilon}^I = \frac{1}{2\mu} F^{\frac{n-1}{2}} \left(\frac{2}{3}\sigma - \Omega\right) \quad F>0, \ \sigma\Omega>0 \text{ and } \sigma\left(\frac{2}{3}\sigma-\Omega\right)>0$$

<div align="center">or</div>

$$F>0 \text{ and } \sigma\Omega<0$$

$$= 0 \quad F \leq 0$$
$$\text{or } F \geq 0, \ \sigma\Omega>0 \text{ and } \sigma\left(\frac{2}{3}\sigma-\Omega\right)\leq 0$$

$$\dot{\Omega} = \frac{2\mu H}{\sqrt{\frac{3}{4}\left|\frac{\Omega}{K}\right|}^{\beta}} \dot{\varepsilon}^I - R\left[\sqrt{\frac{3}{4}}\left|\frac{\Omega}{K}\right|\right]^{n-\beta-1}\Omega \ ; \quad \begin{array}{l}|\Omega|>\Omega_0 \\ \sigma\Omega>0\end{array}$$

$$= \frac{2\mu H}{\sqrt{\frac{3}{4}\left|\frac{\Omega_0}{K}\right|}^{\beta}} \dot{\varepsilon}^I - R\left[\sqrt{\frac{3}{4}}\left|\frac{\Omega_0}{K}\right|\right]^{n-\beta-1}\Omega \ ; \quad \begin{array}{l}|\Omega|<\Omega_0 \\ \sigma\Omega<0\end{array}$$

The following constants were used for 2-1/4 Cr-Mo Steel at 538 °C:

$\mu = 3.61 \times 10^7$	$R = 9.0 \times 10^{-3}$ ksi/h
$n = 4$	$H = 1.37 \times 10^{-4}$ ksi/h
$m = 7.73$	$\Omega_0 = 0.14$ ksi
$\beta = 1.5$	$K = 0.82$ ksi

5. Bodner Model

$$\dot{\varepsilon}^I = \frac{2}{\sqrt{3}} \frac{\sigma}{|\sigma|} D_0 \exp\left[-\left[\frac{n+1}{2n}\left(\frac{Z}{\sigma}\right)^{2n}\right]\right]$$

$$\dot{Z} = m(Z_1 - Z)\,\dot{W}^p - AZ_1\left[\frac{(Z-Z_2)}{Z_1}\right]^r$$

The following constants were used for Rene´ 95 at 649°C:

$D_0 = 10^4$ sec^{-1} $A = 4 \times 10^{-4}$ sec^{-1}

$n = 3.2$ $r = 1.5$

$Z_1 = 319$ ksi $E = 2.57 \times 10^4$ ksi

$Z_0 = 232$ ksi $m = 2.758$

$Z_2 = 319$ ksi

REFERENCES

1. McKnight, R.L., Laflen, J.H., and Spamer, G.T. "Turbine Blade Tip Durability Analysis", NASA CR165268, February 1982.

2. Krempl, E. "Cyclic Creep--An Interpretive Literature Survey", WRC Bulletin No. 195, Welding Research Council, 1974.

3. Bridgman, P.W. "The Compressibility of Thirty Metals as a Function of Pressure and Temperature", Proceedings of the American Academy of Arts and Sciences, 58, p. 163, 1923.

4. Crossland, B. "The Effect of Fluid Pressure on the Shear Properties of Metals", Proceedings of the Institute of Mechanical Engineers, 169, p. 935, 1954.

5. Drucker, D.C. "A More Fundamental Approach to Plastic Stress Strain Relations", Proceedings of the First U.S. National Congress of Applied Mechanics, Chicago, p. 487, 1951.

6. Drucker, D.C. "Some Implications of Work-Hardening and Ideal Plasticity", Quarterly Journal of Applied Mathematics, 7, p. 411, 1952.

7. Drucker, D.C. "A Definition of Stable Inelastic Material", Journal of Applied Mechanics, 26, pp. 101-6, 1959.

8. Prager, W. "The Theory of Plasticity: A Survey of Recent Achievements", Proceedings of the Institute of Mechanical Engineers, 169, p.41, 1955.

9. Prager, W. "A New Method of Analyzing Stresses and Strains in Work-Hardening Plastic Solids", Journal of Applied Mechanics, 23, pp. 493-496, 1956.

10. Ziegler, H. "A Modification of Prager's Hardening Rule", Quarterly Journal of Applied Mathematics, 17, p. 55, 1959.

11. Mroz, Z. "On the Description of Anisotropic Work-Hardening", Journal of Mechanics and Physics of Solids, 15, p. 163, 1967.

12. Hecker, S.S. "Experimental Studies of Yield Phenomena in Biaxially Loaded Metals", in Constitutive Equations in Viscoplasticity-- Computational and Engineering Aspects, ASME AMD, 20, 1976.

13. Liu, K.C. and Greenstreet, W.L. "Experimental Studies to Examine Elastic-Plastic Behaviors of Metal Alloys Used in Nuclear Structures", in Constitutive Equations in Viscoplasticity --Computational and Engineering Aspects, ASME AMD, 20, 1976.

14. Walker, K.P. "Research and Development Program for Nonlinear Structural Modeling with Advanced Time-Temperature Dependent Constitutive Relation- ships", NASA CR165533, November 1981.

15. Eftis, J. and Jones, D.L. "Evaluation and Development of Constitutive Relations for Inelastic Behavior", Final Report, AFOSR-80-0096, AFOSR-81-0241.

16. Flugge, W. Viscoelasticity, Blaisdell Publishing, 1967.

17. Robinson, D.N. "A Unified Creep-Plasticity Model for Structural Metals at High Temperature", ORNL TM-5969, October 1978.

18. Robinson, D.N. and Swindeman, R.W. "Unified Creep-Plasticity Constitutive Equations for 2¼ Cr-1 Mo Steel at Elevated Temperature", ORNL TM-8444, October 1982.

19. Bodner, S.R. and Partom, Y. "Constitutive Equations for Elastic-Viscoplastic Strain- Hardening Materials", ASME Journal of Applied Mechanics, 42, p. 385, 1975.

20. Bodner, S.R. "Representation of Time Dependent Mechanical Behavior of Rene´ 95 by Constitutive Equations", AFML Report, AFML-TR-79-4116, August 1979.

21. Stouffer, D.C. and Bodner, S.R. "A Relationship Between Theory and Experiment for a State Variable Constitutive Equation", ASTM STP, 765, p. 239, 1982.

22. Stouffer, D.C. and Bodner, S.R. "A Constitutive Model for the Deformation Induced Anisotropic Plastic Flow of Metals", International Journal of Engineering Science, 17, p. 757, 1979.

23. Bodner, S.R. and Stouffer, D.C. "Comments on Anisotropic Plastic Flow and Incompressibility", International Journal of Engineering Science, 21, No. 3, p. 211, 1983.

24. Miller, A.K. "An Inelastic Constitutive Model for Monotonic, Cyclic, Creep Deformation: Part I--Equations Development and Analytical Procedures; Part II--Applications to Type 304 Stainless Steel", Trans. ASME Journal of Engineering Materials and Technology, 96, p. 97, 1976.

25. Krieg, R.D., Swearengen, J.C., and Rohde, R.W. "A Physically Based Internal Variable Model for Rate Dependent Plasticity", in Inelastic Behavior of Pressure Vessel and Piping Components, ASME/CSME, PVP-PB-028, p. 15, 1978.

26. Ramaswamy, V.G., Van Stone, R.H., Dame, L.T., and Laflen, J.H. "Constitutive Modeling for Isotropic Materials", Annual Report, NASA CR17485, March 1985.

27. Lindholm, U.S., Chan, K.S., Bodner, S.R., Weber, R.M., Walker, K.P., and Cassenti, B.N. "Constitutive Modeling for Isotropic Materials", NASA CR174718, May 1984.

28. Kaufman, M. "Examination of the Influence of Coatings on Thin Superalloy Sections--Volume 1", NASA CR134791, December 1974.

29. Cook, T.S. "Evaluation of Mean Stress Effects on Low Cycle Fatigue of Inconel 718", ASME Paper 84-PVP-27, 1984.

30. Ramaswamy, V.G., Van Stone, R.H., Dame, L.T., and Laflen, J.H. "Constitutive Modeling for Isotropic Materials", Final Report, NASA NAS3-23927.

31. Domas, P.A. "An Investigation of Notch Low Cycle Fatigue Life Behavior of Rene' 80 at High Temperature", Ph.D. Dissertation, University of Cincinnati, 1981.

32. Frost, H.J. and Ashby, M.F. Deformation Mechanism Maps, Pergamon Press, Oxford, 1982.

33. Argon, A.S. Physics of Strength and Plasticity, MIT Press, Cambridge, 1969.

34. Christian, J.W. in Physics of Strength and Plasticity, edited by A.S. Argon, MIT Press, Cambridge, 1969.

35. Nabarro, R.F.N. "Report of a Conference on the Strength of Solids", London Physical Society, p. 75, 1948.

36. Herring, C. "Diffusional Viscosity of Polycrystalline Solid", Journal of Applied Physics, 21, p. 437, 1950.

37. Raj, R. and Ashby, M.F. "On Grain Boundary Sliding and Diffusional Creep", Met. Trans., 2, p. 1113, 1971.

38. Antolovich, S.D., Liu, S., and Baur, R. "Low Cycle Fatigue Behavior of Rene ´ 80 at Elevated Temperature", Met. Trans., 12A, p. 473, 1981.

39. Edwards, E.H., Washburn, J., and Parker, E.R. "Some Observations on Work Hardening of Metals", Trans. AIME, 197, p. 1525, 1953.

40. Wilson, D.A. and Walker, K.P. "Constitutive Modeling of Engine Materials", AFWAL-TR-84-4073, pp. 2-17, 1984.

41. Edwards, E.H. and Washburn, J. "Strain Hardening of Latent Slip Systems in Zinc Single Crystals", Journal of Metals, 6, p. 1239, 1954.

42. Dieter, G.E. Mechanical Metallurgy, McGraw Hill, New York, 1961.

43. Grosskreutz, J.C. and Mughrabi, M. "Description of the Work-Hardened Structure at Low Temperature in Cyclic Deformation", in Constitutive Equations in Plasticity, A.S. Argon, ed., p. 251, 1975.

44. Feltner, C.E. and Laird, C. "Cyclic Stress-Strain Response of F.C.C. Metals and Alloys--II. Dislocation Structures and Mechanisms", ACTA Metallurgica, 15, No. 10, p. 1633, 1967.

45. Abdel-Raouf, H. and Plumtree, A. "The Influence of Deformation Rate on the Cyclic Behavior of Pure Iron", Met. Trans., 2, p. 1863, 1971.

46. Pratt, J.E. "Dislocation Substructure in Strain-Cycled Copper as Influenced by Temperature", ACTA Metallurgica, 15, p.319, 1967.

47. Moteff, J. "Deformation Induced Microstructural Changes in Metals", Proceedings of Workshop on a Continuum Mechanics Approach to Damage and Life Prediction, D.C. Stouffer, ed., General Butler State Park, Carrollton, Kentucky, May 1980.

48. Gilman, J.J. "Progress in the Microdynamical Theory of Plasticity", Proceedings of the Fifth U.S. National Congress of Applied Mechanics, Minneapolis, p. 385, 1966.

49. Vreeland, T.J. "Dislocation Velocity Measurements", Techniques of Metals Research, R.F. Bunshak, ed., 2, Part 1, p. 341, Wiley-Interscience, New York, 1968.

50. McDowell, D.L. "The Significance of Nonproportional Loading Tests for Characterization of Cyclic Response of Metals", Proceedings of Spring Meeting of SEM, Las Vegas, Nevada, p. 229, 1985.

51. Malvern, L.E. Introduction to the Mechanics of a Continuous Medium, Prentice-Hall, 1969.

52. Orowan, E. "The Creep of Metals", Journal of West Scotland Iron and Steel Institute, 54, p. 45, 1946.

53. Bailey, R.W. "Note on the Softening of Strain Hardening Metals and Its Relation to Creep", Journal of the Institute of Metals, 35, p. 27, 1926.

54. Rice, J.R. "Continuum Mechanics and Thermodynamics of Plasticity in Relation to Microscale Deformation Mechanisms", in Constitutive Equations in Plasticity, A.S. Argon, ed., p. 23, 1975.

55. Mendelson, A. Plasticity--Theory and Application, Macmillan Company, New York, 1968.

56. Krempl, E. "The Influence of State of Stress on Low-Cycle Fatigue of Structural Materials", ASTM STP549, 1974.

57. Laflen, J.H. and Cook, T.S. "Equivalent Damage--A Critical Assessment", NASA CR167874, 1982.

58. Brown, M.W. and Miller, K.J. "Two Decades of Progress in the Assessment of Multiaxial Low-Cycle Fatigue Life", ASTM STP770, p. 482, 1982.

59. Garud, Y.S. "Multiaxial Fatigue: A Survey of the State of the Art", Proceedings of the ASTM/SAE Workshop on Elasto-Plastic Materials Behavior and Component Fatigue Analysis, Minneapolis, April 1980.

60. Kanazawa, K., Miller, K.J., and Brown, M.W. "Low-Cycle Fatigue under Out-of-Phase Loading Conditions", Journal of Engineering Materials and Technology, 99, No. 3, p. 222, 1977.

61. Brown, M.W. and Miller, K.J. "High Temperatur Low Cycle Biaxial Fatigue of Two Steels", Fatigue of Engineering Materials and Structures, 1, No. 2, p. 217, 1979.

62. Landgraf, R.W., Morrow, J., and Endo, T. "Determination of the Cyclic Stress-Strain Curve", Journal of Materials, ASTM, 4, No. 1, p. 176, 1969.

63. Garud, Y.S. "A New Approach to the Evaluation of Fatigue under Multiaxial Loadings", Proceedings of the Symposium on Methods for Predicting Material Life in Fatigue, ASME, p. 247, 1979.

64. Mroz, Z. "An Attempt to Describe the Behavior of Metals under Cyclic Loads Using a More General Workhardening Model", ACTA Mechanica, 7, p. 199, 1967.

65. Lamba, H.S. "Nonproportional Cyclic Plasticity", TAM Report No. 413, Department of Theoretical and Applied Mechanics, University of Illinois at Urbana-Champaign, 1976.

66. Lamba, H.S. and Sidebottom, O.M. "Proportional Biaxial Cyclic Hardening of Annealed Oxygen-Free High-Conductivity Copper", ASTM, Journal of Testing and Evaluation, 6, No. 4, p. 260, 1978.

67. McDowell, D.L. "On the Path Dependence of Transient Hardening and Softening to Stable States under Biaxial Cyclic Loading", Proceedings of the International Conference on Constitutive Laws for Engineering Materials, Desai and Gallagher, eds., Tucson, Arizona, p. 125, 1983.

68. McDowell, D.L., Socie, D.F., and Lamba, H.S. "Multiaxial Nonproportional Cyclic Deformation", ASTM STP770, p. 500, 1982.

69. Nouailhas, D., Policella, H., and Kaczmarck, H. "On the Description of Cyclic Hardening under Complex Loading Histories", Proceedings of the International Conference on Constitutive Laws for Engineering Materials, Desai and Gallagher, eds., Tucson, Arizona, p. 45, 1983.

70. McDowell, D.L. "Transient Nonproportional Cyclic Plasticity", University of Illinois at Urbana-Champaign, Report No. 107, UILU-Eng-83-4003, 1983.

71. McDowell, D.L., Payne, R.K., Stahl, D., and Antolovich, S.D. "Effects of Nonproportional Cyclic Loading Histories on Type 304 Stainless Steel", Proceedings of the International Spring Meeting of Societe Francaise de Metallurgie, Paris, p. 53, 1984.

72. Kaufman, A., Laflen, J.H., and Lindholm, U.S. "Unified Constitutive Material Models for Nonlinear Finite Element Structural Analysis", NASA TM 86985, presented at the Twenty-first Joint Propulsion Conference, Monterey, California, 1985.

73. McDowell, D.L. "A Two Surface Model for Transient Nonproportional Cyclic Plasticity", Trans. ASME, Journal of Applied Mechanics, 85-APM-10, 1985.

74. Leis, B.N. and Laflen, J.H. "Fatigue and Creep Fatigue Damage Analysis under Nonproportional Cycling", Battelle Columbus Laboratories Report SMT-TN-7801.

75. Gell, M., Leverant, G.R., and Wells, C.H. "Achievement of High Fatigue Resistance in Metals and Alloys", ASTM STP467, p. 113, 1970.

76. Kumar, V., Morjaria, M., and Mukherjee, S. "Numerical Integration of Some Stiff Constitutive Models of Inelastic Deformation", Journal of Engineering Materials and Technology, 102, p. 92, 1980.

77. Dame, L.T., Stouffer, D.C., and Abuelfoutouh, N. "Finite Element Analysis of Notch Behavior Using a State Variable Constitutive Equation", Proceedings of the Second Symposium on Nonlinear Constitutive Relations for High Temperature Applications, NASA Lewis, June 1984.

78. Sotolongo, W. and McDowell, D.L. "An Evaluation of Several Constitutive Model Structures for Transient Nonproportional Cyclic Plasticity", submitted for publication to ASME Journal of P.V. Technology, April 1985.

79. Sotolongo, W. and McDowell, D.L. "On the Numerical Integration of Elasto-Plastic Constitutive Model Structures for Nonproportional Cyclic Loading", submitted for publication to Computers and Structures, April 1985.

1. Report No. NASA CR-3998	2. Government Accession No.	3. Recipient's Catalog No.
4. Title and Subtitle A Constitutive Model for the Inelastic Multiaxial Cyclic Response of a Nickel Base Superalloy René 80		5. Report Date July 1986
		6. Performing Organization Code
7. Author(s) V. G. Ramaswamy		8. Performing Organization Report No. None
		10. Work Unit No.
9. Performing Organization Name and Address University of Cincinnati Dept. of Aerospace Engineering and Engineering Mechanics College of Engineering Cincinnati, Ohio 45221		11. Contract or Grant No. NAS3-23927
		13. Type of Report and Period Covered Contractor Report
12. Sponsoring Agency Name and Address National Aeronautics and Space Administration Washington, D.C. 20546		14. Sponsoring Agency Code 533-04-11 (E-3069)

15. Supplementary Notes

Final report. Project Manager, Albert Kaufman, Structures Division, NASA Lewis Research Center, Cleveland, Ohio 44135. This report was a dissertation submitted to the Dept. of Aerospace Engineering and Engineering Mechanics, College of Engineering, Division of Graduate Education and Research, University of Cincinnati, in partial fulfillment of the requirement for the degree of Doctor of Philosophy in 1985.

16. Abstract

The objective of this research was to develop unified constitutive equations which can model a variety of nonlinear material phenomena observed in René 80 at elevated temperatures. A new constitutive model was developed based on back stress and drag stress. The tensorial back stress was used to model directional effects; whereas, the scalar drag stress was used to model isotropic effects and cyclic hardening or softening. A flow equation and evolution equations for the state variables were developed in multiaxial form. Procedures were developed to generate the material parameters. The model predicted very well the monotonic tensile, cyclic, creep and stress relaxation behavior of René 80 at 982 °C. The model was then extended to 871°, 760°, and 538 °C. It was shown that strain rate dependent behavior at high temperatures and strain rate independent behavior at the lower temperatures could be predicted very well. A large number of monotonic tensile, creep, stress relaxation and cyclic experiments were predicted. The multiaxial capabilities of the model were verified extensively for combined tension/torsion experiments. The prediction of the model agreed very well for proportional, nonproportional and pure shear cyclic loading conditions at 982° and 871 °C.

17. Key Words (Suggested by Author(s)) Constitutive modeling; Finite element modeling; Nickel-base alloys; Nonlinear unified theory; Structural analysis	18. Distribution Statement Unclassified – unlimited STAR Category 39		
19. Security Classif. (of this report) Unclassified	20. Security Classif. (of this page) Unclassified	21. No. of pages 243	22. Price* A11